



HAL
open science

Numerical methods applied to Facial Reconstruction : from the segmentation of medical images to the global automation of the optimization process

Lydie Uro

► **To cite this version:**

Lydie Uro. Numerical methods applied to Facial Reconstruction : from the segmentation of medical images to the global automation of the optimization process. Modeling and Simulation. Sorbonne Université, 2019. English. NNT : 2019SORUS671 . tel-03616246

HAL Id: tel-03616246

<https://theses.hal.science/tel-03616246>

Submitted on 22 Mar 2022

HAL is a multi-disciplinary open access archive for the deposit and dissemination of scientific research documents, whether they are published or not. The documents may come from teaching and research institutions in France or abroad, or from public or private research centers.

L'archive ouverte pluridisciplinaire **HAL**, est destinée au dépôt et à la diffusion de documents scientifiques de niveau recherche, publiés ou non, émanant des établissements d'enseignement et de recherche français ou étrangers, des laboratoires publics ou privés.

Thèse de Doctorat de Sorbonne Université

pour l'obtention du grade de
Docteur de Sorbonne Université
Spécialité : Mathématiques Appliquées

par

Lydie Uro

sous la direction de
Yvon Maday

et

Thomas Schouman

**Méthodes Numériques appliquées à la Reconstruction Faciale :
de la segmentation des images médicales à l'automatisation
globale du processus d'optimisation**

après avis des rapporteurs

M. Theodore Papadopoulos, M. Paolo Scolozzi & M. Stefan Zachow

devant le jury composé de

Mme. Maya de Buhan	Examinatrice
M. Patrick Goudot	Directeur de Thèse
M. Antoine Gloria	Examineur
M. Yvon Maday	Directeur de Thèse
M. Theodore Papadopoulos	Rapporteur
Mme. Isabelle Plu	Examinatrice
M. Thomas Schouman	Directeur de Thèse
M. Stefan Zachow	Rapporteur





Table des matières

Remerciements	7
Introduction - En français	11
Introduction - In English	39

I

First Part : Preliminary work

Introduction	69
1 Cephalometry and Masseter	71
1.1 Introduction	72
1.2 Materials and Methods	73
1.2.1 Subjects	73
1.2.2 CT Imaging	73
1.2.3 Statistical Analysis	74
1.3 Results	75
1.3.1 Masseter measurements and Cephalometry	75
1.3.2 Correlation between Masseter and Cephalometry	75
1.4 Discussion	76
1.5 Conclusion	78
2 Reduced Basis of 3D shape	79
2.1 Introduction	80

2.2	Preprocessing	82
2.2.1	Data Acquisition : Segmentation of CT-Scan	82
2.2.2	Mesh Generation : 3D surface reconstruction	83
2.2.3	Mesh and remesh	84
2.2.4	Alignment	85
2.3	Function-to-shape representation	89
2.3.1	Warping (if necessary)	89
2.3.2	Morphing	90
2.3.3	Parametrization : Dimension Reduction	91
2.4	Application of reduces basis of 3D shapes	95
2.4.1	Shape prediction of anatomical element	95
2.4.2	Segmentation and reconstruction	95
2.5	Conclusion	95

II

Second Part : Segmentation

	Introduction	99
3	Proof-of-Concept in 2D	101
3.1	Introduction : State of the art	101
3.2	Notation and problem setting.	104
3.3	Numerical experiments in 2D	105
3.3.1	Reference configuration	105
3.3.2	Generation of the database set	106
3.3.3	Singular Values Decrease	106
3.3.4	Application and results	107
3.3.5	Reconstruction error	108
3.4	First 3D numerical exploration	108
3.4.1	Spherical harmonics - Definition in 3D	109
3.4.2	Parameterization of shapes	110
3.4.3	Reconstruction of a new shape	112
3.4.4	Analytic error	112
3.5	Conclusions and Perspectives.	113
4	Semi-automatic segmentation method in 3D	115
4.1	Introduction	116
4.2	Modes in the reference configuration	116
4.3	Overview of the method for 3D segmentation in a real case	117
4.3.1	Notation	117
4.3.2	Pipeline	117
4.4	Application in a real case : the masseter segmentation	118
4.4.1	Graphical interface development	118
4.4.2	Coordinates Change	120
4.4.3	Reconstruction	122
4.4.4	Visualisation	124

4.5	Discussion and Conclusion	126
5	Practical Application	127
5.1	Introduction	128
5.2	Materiels and Methods	128
5.2.1	Medical Image Data	128
5.2.2	Segmentation process	129
5.3	Results	130
5.4	Discussion	131
5.5	Conclusion	133

III

Third Part : Application to facial reconstruction

	Introduction	137
6	Shape matching	139
6.1	Introduction	140
6.2	A shape optimization framework	141
6.2.1	Shape sensitivity analysis : Hadamard's shape derivative	141
6.2.2	General procedure for the minimization of a shape functional	143
6.3	Two functionals for shape matching	144
6.3.1	Shape matching without constraint on the displacement	144
6.3.2	Shape matching with extension and regularization of the descent direction	145
6.4	Numerical issues and examples	146
6.4.1	Boundary functional P	146
6.4.2	Volume functional J	148
6.4.3	Comparison of the proposed methods	149
7	Facial Reconstruction	155
7.1	Introduction	156
7.2	Anatomy	157
7.2.1	Link between the skull and the face	157
7.2.2	The masseter muscle	158
7.3	Facial reconstruction process	158
7.3.1	The Database : from CT-scan to 3D shape	159
7.3.2	Reconstruction of the masseter muscle	160
7.3.3	Results presentation : combinaison with a general method of facial reconstruction	165
7.4	Validation	168
7.4.1	Protocol description of the survey	169
7.4.2	Results	170
7.5	Discussion and Conclusion	170
	Conclusion and perspectives	173

A	Annexe Proof-of-Concept in 2D	179
A.1	Introduction	180
A.2	Notation and problem setting.	180
A.3	Numerical Experiments	182
A.4	Conclusions and Perspectives.	183
B	Annexe Facial Reconstruction Software	185
B.1	Installation	185
B.1.1	Github	186
B.1.2	Python Librairies	186
B.1.3	Executables	186
B.1.4	Installation testing	186
B.2	Creation of the database	187
B.3	Facial reconstruction from a new skull	187
B.4	How to add step?	187
B.4.1	Script python stand-alone	187
B.4.2	Incorporate an external program	187
B.4.3	Run several functions or scripts in parallel	188
B.4.4	Handle and edit a step	188
B.5	Independent use of the scripts	188
C	Annexe Anthropological Application	193
C.1	Context	193
C.2	The test case	194
C.3	Numerical results	195
C.3.1	Toothless skull with no nasal bone	195
C.3.2	Skull with the teeth and without the nasal bone	195
C.3.3	Skull with the teeth and the nasal bone	195
C.4	Conclusion	197
	List of Tables	199
	List of Figures	205
	Bibliography	207
	Books	207
	Articles	208
	Phd Thesis	223
	Misc	223



Contexte scientifique

Création de la chaire FaciLe

La chaire thématique FaciLe, soutenue par Sorbonne Université et portée par l'Institut des Sciences du Calcul et des Données, a été créée en 2014, avec une équipe composée de médecins légistes, d'anthropologues, de mathématiciens, d'informaticiens, et de chirurgiens maxillo-faciaux, autour d'un projet pluridisciplinaire : la reconstruction d'un visage à partir d'un crâne dans un objectif d'identification.

Le projet FaciLe s'inscrit dans le contexte plus précis d'apporter des éléments de preuve à un cas particulier : la reconstruction du visage d'un chef guerrier néo-calédonien Ataï, tué par des colons français au 19^{ème} siècle, à partir de son crâne (Figure 1). La remise de son crâne à son pays natif, jusqu'alors conservé au Musée de l'Homme à Paris, a eu lieu le 28 Août 2014 [147]. La confirmation de l'identité de l'individu à qui ce crâne a appartenu, via une reconstruction faciale avait alors suscité un fort intérêt de la communauté scientifique.



FIGURE 1 – Deux représentations d'Ataï (a) une gravure et (b) un moulage de son visage

Dès lors une chaire sénior (Fabrice Déméter, anthropologue, en 2014, puis Peter Deuffhard, mathématicien, en 2015), une chaire junior (Maya de Buhan, mathématicienne, 2014-2015) et deux thèses (celle de Chiara Nardoni [158] et la mienne) sont lancées, en parallèle d'un partenariat regroupant des acteurs des différentes disciplines impliquées sur le sujet.

La reconstruction faciale

La reconstruction faciale est un procédé qui consiste à reconstituer le visage d'une personne à identifier, à partir uniquement de son crâne sec, dans le cadre d'une enquête judiciaire par exemple.

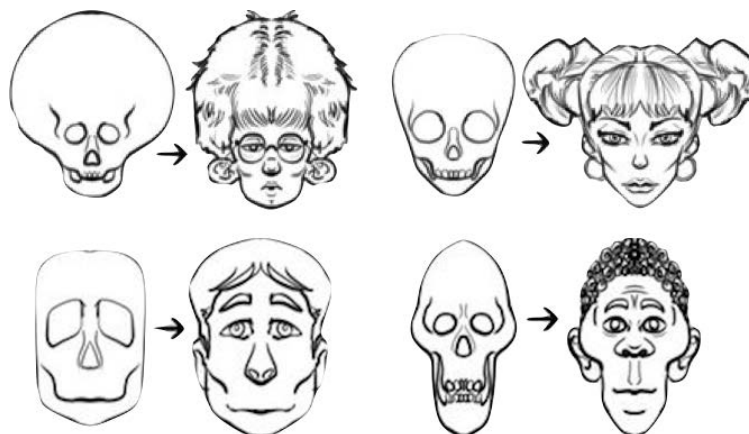


FIGURE 2 – Définition de la reconstruction faciale

Il s'agit d'une application extrêmement précise mais qui peut déboucher sur un grand nombre d'avancées dans différents domaines : l'anthropologie, pour affiner les recherches permettant de connaître et comprendre le visage des autres membres de la lignée humaine, la médecine légale, afin d'identifier des restes humains dans le cadre d'une enquête, ou encore la chirurgie maxillo faciale, pour assister les cliniciens dans leur pratique via des planifications d'opérations assistées par ordinateur.

Bref historique

Il est important de souligner, tout d'abord, que ce problème est mal posé : en effet à une forme de crâne ne correspond pas un unique visage. Différents paramètres, tels que l'âge et le sexe, sont difficiles à déterminer avec certitude et apportent une première variabilité dans le résultat. D'autres comme la corpulence, ne sont simplement pas des informations qu'il est possible de retrouver sur les os du crâne.

Malgré cela, la forte corrélation entre le visage et le crâne est connue depuis plusieurs milliers d'années [111]. La reconstruction faciale n'émerge cependant comme méthode d'usage dans des situations d'identification judiciaires qu'au 19^{ème} siècle, apportant alors un flot de questions éthiques, remettant en cause la fiabilité des méthodes utilisées [252]. Les techniques traditionnelles développées à cette période reposent sur des procédures manuelles, portraits en deux dimensions ou moulages en trois dimensions, réalisées par des artistes experts en anatomie faciale. Le résultat était alors très lié aux compétences et à la subjectivité de l'artiste.

Plus récemment, avec l'essor des ordinateurs et de l'imagerie médicale, de nombreuses méthodes digitales sont apparues à leur tour, avec pour objectif d'éliminer la part de subjectivité intrinsèque aux méthodes précédemment citées et de tirer profit de la possibilité de tester plusieurs hypothèses rapidement. Actuellement la plupart de ces méthodes utilisent l'étude statistique des observations d'un jeu de données comportant un crâne et son visage associé. Les observations prises en considération sont le plus souvent fondées sur des mesures effectuées en des points

anthropologiques connus pour leur constance évolutive, nommés landmarks [30]. Ces mesures peuvent par exemple caractériser des épaisseurs de tissus mous, ou d'autres marqueurs décrivant la variabilité de ces tissus [44, 252]. Toutefois bien que l'identification de ces landmarks soit rendue possible par un expert, leurs propriétés géométriques sont floues et ne permettent pas de les identifier automatiquement via un ordinateur.

Le projet FaciLe se démarque de ces méthodes par deux aspects :

- en basant son approche de la reconstruction faciale tridimensionnelle non pas sur les statistiques mais sur une méthode déterministe, utilisant des équations aux dérivées partielles (EDP), de l'analyse numérique et de la modélisation géométrique 3D.
- en rendant l'entièreté du processus complètement automatique et sans intervention humaine, après acquisition des données du crâne.

Objectif principal de cette thèse

La thématique de la reconstruction faciale est le « fil rouge » de cette thèse, qui décrit l'ensemble de la réflexion scientifique : de l'acquisition et du traitement des données, aux résultats en sciences légales. L'objectif est de développer une méthode complémentaire à celle développée dans le cadre de la thèse de Chiara Nardoni [158], valorisant l'ensemble du projet, tout en apportant des précisions anatomiques dans le processus. Différents problèmes relatifs à cette nouvelle méthodologie, ont été soulevés, occasionnant durant ce travail des études parallèles pour le compléter. Il s'agit par exemple de l'automatisation complète du processus, ou encore la segmentation de tissus mous dans des images médicales.

Démarche scientifique : une application des mathématiques

Les mathématiques appliquées, branche des mathématiques, s'intéressent à l'étude et l'application de modèles à d'autres disciplines, telle que la physique, la chimie, la biologie, l'économie, ou encore la médecine. Elles regroupent toutefois un grand nombre de sous-domaines, en partie indépendants des applications elles-mêmes, comme l'analyse numérique, le contrôle, l'optimisation, la théorie des jeux, ou encore les probabilités.

C'est dans cette vaste discipline que s'inscrit cette thèse de mathématiques appliquées dédiée à la reconstruction faciale tridimensionnelle pour la médecine légale. Différents aspects du problème nous amèneront à utiliser des outils mathématiques variés, tels que les équations différentielles, la réduction de dimensionnalité, les éléments finis...

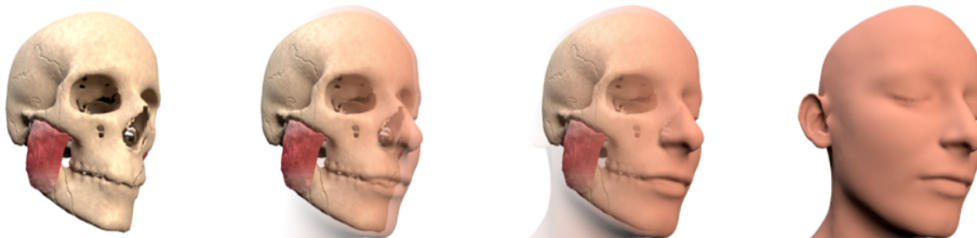


FIGURE 3 – Reconstruction faciale tridimensionnelle

Modélisation et visage

Un modèle

Une des premières étapes en mathématiques appliquées est la modélisation du problème posé. On entend ici par modélisation, l'ensemble du processus permettant l'intervention des mathématiques dans une science basée sur l'expérience ou l'observation, afin d'expliquer, de décrire ou de prédire un phénomène. Un modèle mathématique est donc l'identification de quantités ad'hoc qui décrivent bien la situation étudiée, et un ensemble d'équations sur ces quantités afin d'y appliquer des outils, techniques et théories mathématiques.

La première étape est donc d'identifier le problème, la question que l'on se pose ou l'objet que l'on veut décrire, afin de pouvoir effectuer la traduction mathématique des hypothèses posées suite à cette question, et ainsi de construire notre modèle.

Dans notre cas, la question est la suivante : comment reconstruire le visage d'un individu à partir de la seule connaissance de son crâne, dans un objectif d'identification légale ? Nous posons comme hypothèse le fait qu'un crâne et qu'un visage peuvent être définis comme des formes en trois dimensions. Ils seront donc décrits tout au long du manuscrit par des maillages tridimensionnels (voir un exemple Figure 4).

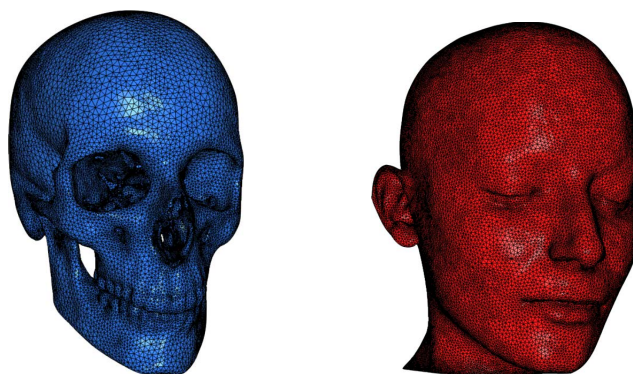


FIGURE 4 – Maillage 3D (a) d'un crâne et (b) d'un visage

L'élasticité

Le premier projet du groupe FaciLe a consisté à considérer un nouvel objet nommé « masque » comme le maillage volumique entre les maillages surfaciques du crâne et du visage associés, représentant les tissus mous pour chaque individu dans notre base de données (Figure 5). Puis lors de l'arrivée d'un nouveau crâne, de reconstruire son visage à partir de la déformation élastique d'un des masques de la base vers ce crâne [35].

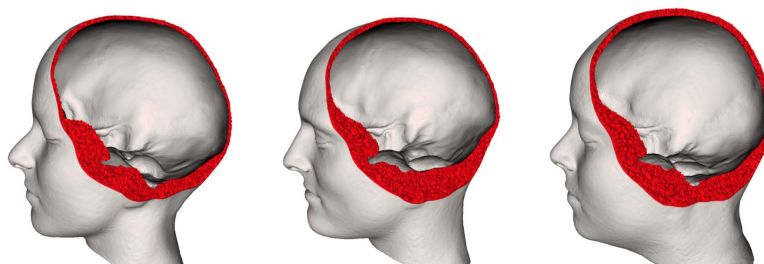


FIGURE 5 – Trois exemples de masques, extrait de [158]

Cette déformation élastique est une méthode de « shape matching » ou « morphing » consistant,

pour un couple de forme 'départ' et 'cible' Ω_0 et Ω_T dans \mathbb{R}^d ($d = 2, 3$) donné, à trouver un moyen de transformer Ω_0 en Ω_T . Ce type de méthode joue un rôle important dans des applications en modélisation géométrique et en analyse de formes [244]. Beaucoup de chercheurs des communautés mathématique et infographique s'y sont intéressés [13, 21, 22, 67, 130, 193]. Une telle déformation peut servir à mesurer à quel point les deux formes diffèrent ou aussi à simplement accomplir la transformation d'un objet en un autre. Ici nous mesurons la différence entre la forme de 'départ' et celle 'cible' selon la fonctionnelle de forme suivante :

$$J(\Omega) = \int_{\Omega} d_{\Omega_T}(x) dx,$$

impliquant la fonction distance signée d_{Ω_T} de $\partial\Omega_T$. La fonction distance signée est une fonction « level set » d'un domaine : qui pour chaque point x de l'espace retourne la distance Euclidienne $d(x, \partial\Omega_T)$ au bord $\partial\Omega_T$, le signe associé à cette distance est positif si le point se situe à l'intérieur du domaine, négatif si non. Le « mapping » global entre Ω_0 et Ω_T est obtenu par un procédé itératif qui minimise $J(\mathcal{E}(\Omega_0))$ (avec \mathcal{E} la déformation élastique), inférant à chaque étape une direction de descente, via un algorithme de gradient, pour la fonctionnelle J . Les conditions optimales associées à ce problème d'optimisation de forme sont calculées en utilisant le cadre de la dérivée de forme d'Hadamard [3, 41, 96]. En pratique, l'espace admissible des déformations est restreint par une paramétrisation élastique du déplacement. Les équations de l'élasticité ont été implémentées avec la méthode des éléments finis.

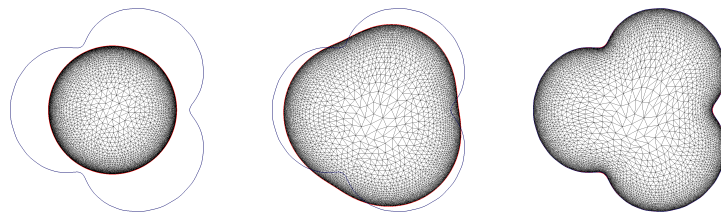


FIGURE 6 – Exemple 2D simple de morphing

Cette première phase du travail a été principalement portée par la thèse de Chiara Nardoni [158], encadrée par Maya de Buhan et Pascal Frey. Nous avons effectué certains de ces travaux ensemble : particulièrement le morphing dit surfacique et sa comparaison avec celui dit volumique (détaillé dans le Chapitre 6). A l'issue de cette thèse dont j'ai repris le travail sur la reconstruction faciale, j'ai développé une méthode complémentaire présentée ci-dessous, et détaillée dans le Chapitre 7, se concentrant sur l'objectif principal de cette thèse, la reconstruction faciale.

Anatomie de la face

Toutefois, cette méthode élastique ne tient pas compte pas de l'anatomie sous jacente du visage, et donc, plus précisément, des composantes fonctionnelles du masque de tissus mous évoqué ci-dessus. Des articles comme celui de [31], nous rappellent pourtant l'importance des connaissances anatomiques, accumulées dans diverses disciplines, sur le visage et dont le domaine de la reconstruction faciale ne prend que très peu en compte et de manière non systématique. Nous nous sommes donc tournés vers nos collègues anthropologues et chirurgiens, participant au projet, afin d'améliorer ce premier modèle, en prenant mieux en compte l'anatomie du visage.

Le muscle masséter

Le visage est principalement, en terme de volume, constitué de muscles et de graisse, recouverts de peau. La graisse étant une composante dont nous ne retrouvons pas d'information sur le crâne, il a été décidé de la considérer à la fin du processus comme une variable à ajuster une fois la forme du visage identifiée. On peut en revanche facilement identifier jusqu'à 100 muscles sur un visage. Deux d'entre eux, plus volumineux que les autres, ont attiré notre attention : le muscle masséter (Figure 7 numéro 1) et le muscle temporal (Figure 7 numéro 2).

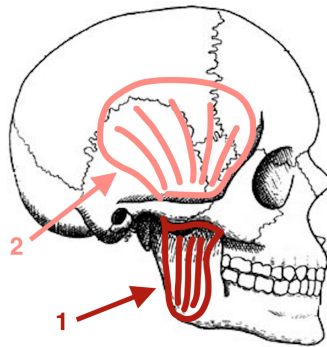


FIGURE 7 – Situation anatomique (1) du muscle masséter, (2) du muscle temporal

Du fait de leur importance fonctionnelle et morphologique respective, nous avons décidé de nous concentrer plus particulièrement sur le masséter du fait de son impact sur la forme du visage. Comme on peut le voir sur la Figure 7, le muscle masséter se situe au niveau de la joue, en avant de l'oreille, le long de la branche de la mandibule. Alors que le muscle temporal, qui se situe lui au niveau des tempes, au dessus de l'arcade zygomatique, est souvent plus fin et couvert par les cheveux, ayant donc dans notre problème un impact moins important dans un premier temps.

Base de données et réduction de dimensionnalité

Il nous faut alors créer un modèle de ce muscle masséter. Afin de le décrire au mieux, aussi simplement que possible, nous utilisons une méthode de réduction de complexité, l'analyse en composantes principales. Décrire la forme du masséter ne nécessite alors plus les 5000 coordonnées 3D des points qui constituaient son maillage, mais seulement $n = 5$ à 20 coefficients bien choisis, selon le niveau de précision souhaité (Figure 8) :

$$\sum_{j=1}^n \alpha_j^k \phi_j, \text{ avec } \alpha \text{ coefficient s'appliquant à la } j\text{-ième composante principale } \phi,$$

pour un individu k donné.

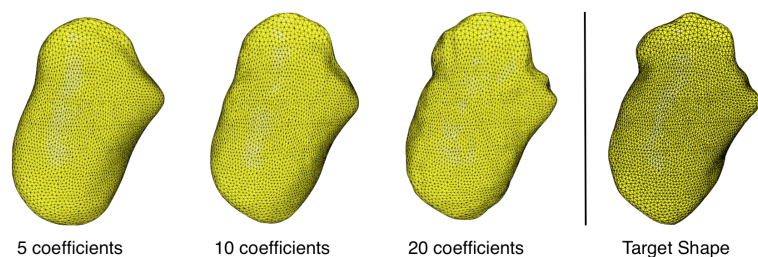


FIGURE 8 – Reconstruction d'un muscle masséter via ACP avec 5 coefficients, 10, et 20, face au vrai muscle

Une fois la reconstruction du masséter (et à terme, du temporal) effectuée, la méthode de déformation élastique exposée dans la section précédente est appliquée, cette fois-ci non pas à partir d'un masque crâne/visage mais crâne+muscles/visage. Cela intégrant des informations plus précises dans ce procédé, tenant compte de l'anatomie, et mettant l'accent sur le lien entre forme et fonction, idée fondatrice de cette thèse.

Acquisition des données

L'ensemble des travaux présentés ci-dessus a été rendu possible grâce à la mise en place d'une base de données associant crâne, visage et muscles pour un même individu comme mentionné auparavant. Cette base de données est constituée d'images médicales 3D qui permettent l'extraction de toutes les informations nécessaires à l'application de cette méthode. Toutes les imageries scanner utilisées dans ce travail de thèse proviennent du service de Chirurgie Maxillo-Faciale de l'Hôpital de La Pitié Salpêtrière à Paris. Cette base de données ne recoupe en rien celle utilisée par Chiara Nardoni avant moi, qui avait obtenu ses données d'un autre projet, sans lien académique avec le projet FaciLe, sur la reconstruction faciale menée par Françoise Tilotta et Yves Rozenholc [225, 226]. Il semblait plus pertinent à cette phase du projet FaciLe de constituer notre propre base de donnée.

Scanner : précision et difficultés

Le choix du type d'imagerie n'est pas anodin. En effet bien que l'IRM présente une meilleure précision en ce qui concerne les tissus mous, la donnée d'entrée de notre problème reste le crâne seul. La meilleure imagerie 3D pour visualiser les os avec précision est, à l'heure actuelle, la tomodensitométrie ou encore appelé scanner, dont on peut voir un exemple Figure 9.

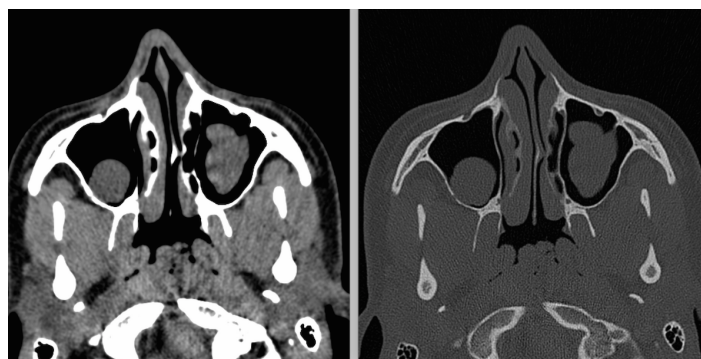


FIGURE 9 – Image de scanner (a) fenêtre d'acquisition "tissus mous", et (b) "osseuse"

Malgré les avantages liés à l'ensemble des informations connues par les images de scanner, il faut garder à l'esprit que de nombreux problèmes intrinsèques aux images altèrent l'acquisition et la visualisation des données en trois dimensions, comme c'est le cas des artefacts créés par le métal utilisé pour soigner les dents (braquettes, couronnes...).

En plus de ces difficultés, certaines contraintes, venant cette fois du modèle, compliquent d'autant plus le pré-traitement des données, par exemple : ne pas tenir compte de la colonne vertébrale dans notre modèle de crâne 3D.

La Segmentation semi-automatique

On appelle segmentation, l'identification sur les images des voxels (pixels en deux dimensions) appartenant à un même objet d'intérêt. Dans notre cas trois objets : le crâne, le visage et le muscle masséter.

La segmentation du crâne et du visage peut être effectuée rapidement à l'aide des niveaux de gris. En effet, il est facile de réaliser automatiquement la segmentation des éléments qui ont un fort

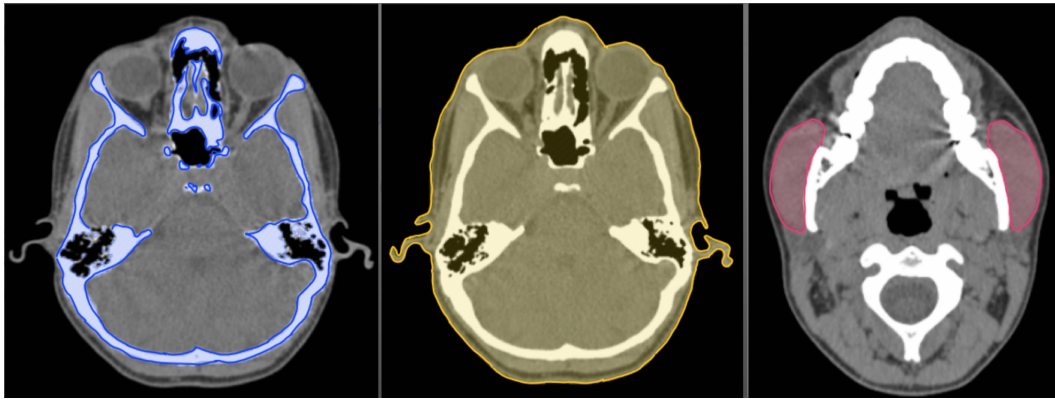


FIGURE 10 – Segmentation (a) du crâne, (b) du visage, et (c) des muscles masséters

contraste. On obtient alors les résultats exposés dans le Figure 10 (a) et (b). La délimitation des tissus mous est plus délicate : en effet la Figure 10 (c), qui montre la segmentation des muscles masséters droit et gauche d'un individu n'a pas pu être obtenue automatiquement. Il a fallu les délimiter manuellement, malheureusement cette procédure est extrêmement chronophage.

Ce problème lié à la segmentation d'images médicales est récurrent dans bien des domaines qui ont besoin d'utiliser comme pré-requis des bases de données 3D d'organes. Une des principales limites est le temps consacré à l'acquisition des données, qui ne sont obtenues qu'en petite quantité, et qui limite d'autant plus la qualité des résultats présentés dans ces différents travaux. C'est dans ce contexte où le peu de données a entravé nos résultats, que nous avons été amenés à développer une application de segmentation semi-automatique pour les tissus mous. A l'aide de la base réduite décrite précédemment, nous connaissons a priori la forme de l'objet à identifier sur les images, dans notre cas le muscle masséter. Il suffit d'identifier les coefficients associés à l'objet d'intérêt, via la résolution d'un système prenant en entrée les coordonnées de quelques points sélectionnés sur l'image $\xi_*^{(j)}$, $j = 1, \dots, m$, avec m le nombre de points sélectionnés :

$$\mathbf{x}^{(j)} = \xi_*^{(j)} + \sum_{i=1}^n \alpha_i \varphi_i(\xi_*^{(j)}), \quad j = 1, \dots, m.$$

Cette méthode est indépendante des niveaux de gris de l'image, et peut donc être appliquée sur tous objets et toutes imageries.

Validation des méthodes développées

L'ensemble des méthodes présentées ont été validées d'un point de vue mathématique, mais pour certifier de leur efficacité pratique dans les disciplines où elles ont pour objectif d'être utilisées, nous avons mis en place des validations expérimentales.

Reconstruction et médecine légale

Pour la reconstruction d'un visage à partir d'un crâne, la façon la plus simple de certifier si la méthode est une réussite, est de vérifier si un individu est en mesure de reconnaître ce visage. C'est pourquoi nous avons mis en place une application de sondage : un utilisateur à qui on présente une photo doit choisir parmi 5 propositions, le visage, décrit par un maillage surfacique, qui lui semble être celui de la personne sur la photo (Figure 11).

Cette opération est réalisée en double aveugle et randomisée pour 4 catégories : la surface 3D du visage segmentée directement, la surface 3D de la reconstruction élastique simple, la surface 3D de la reconstruction avec le masséter segmenté directement et la surface 3D de la reconstruction avec le masséter lui-même reconstruit.

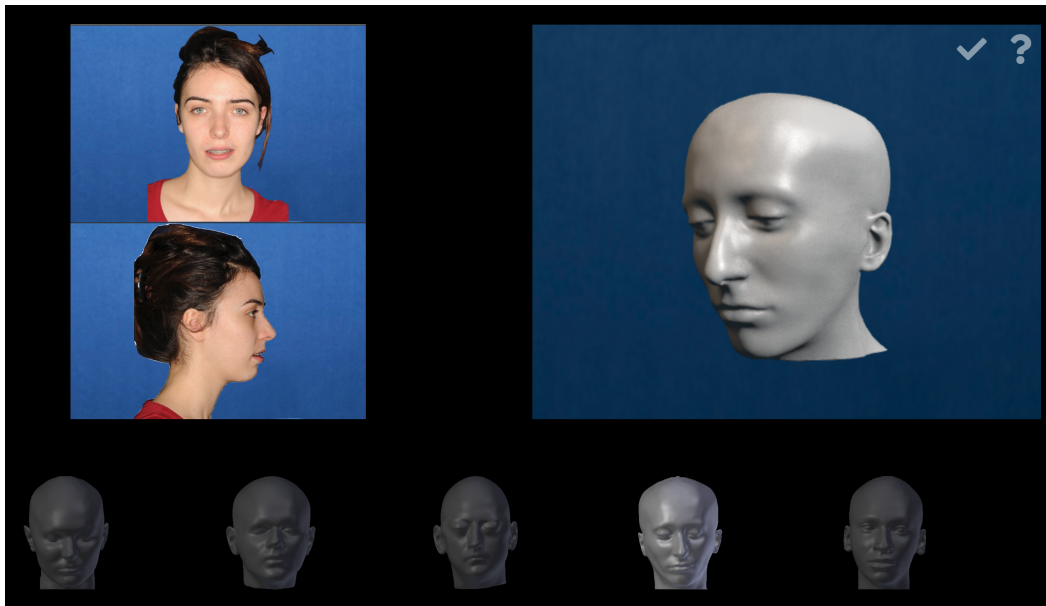


FIGURE 11 – Application de validation de la reconstruction faciale

Cette application permet donc de comparer les résultats de différentes méthodes sur un même jeu de données. En effet, les données utilisées en reconstruction faciale sont souvent extraites de données médicales qui ne sont pas cessibles à d'autres équipes, limitant les comparaisons possibles sur les méthodes à proprement parler.

Segmentation

Dans le cas de la segmentation semi-automatique, l'application développée dans cet objectif étant l'utilisation par des cliniciens ou des chercheurs, nous avons mis en place une étude pour comparer le temps et l'erreur de segmentation avec cette méthode contre la segmentation manuelle de deux praticiennes.

La segmentation manuelle demande d'être précis sur l'ensemble des coupes de scanner où se situe le masséter, alors que la segmentation semi-automatique ne nécessite d'identifier qu'une cinquantaine de points, tel que présenté dans la Figure 12.

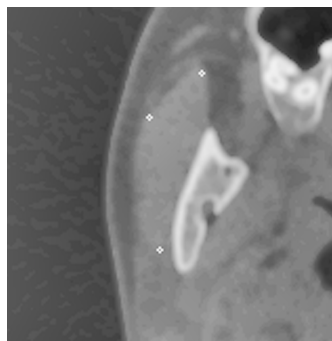


FIGURE 12 – Identification de points à la bordure du masséter avec l'application semi-automatique de segmentation

Principales contributions

Les principales contributions de cette thèse ont été :

- La gestion d'une base réduite de formes en 3D totalement automatique,
- Une nouvelle méthode anatomique de reconstruction faciale,
- Un outil de validation et de comparaison des méthodes de reconstruction,
- Une méthode de segmentation semi-automatique.

Résumé et état de l'art

Ce manuscrit se divise en 3 parties distinctes, chacune composée de 2 à 3 articles soumis ou en cours de soumission. Ci-dessous se trouve un descriptif détaillé de chacun de ces articles, ainsi que l'état de l'art et les résultats qui lui sont associés.

Partie I - Travail préliminaire

Cette première partie regroupe un travail préliminaire sur les relations anatomiques entre le crâne et le muscle masséter, qui nous ont permis de faire l'hypothèse selon laquelle il est possible de déduire la forme du masséter uniquement à partir de celle du crâne. Et le travail sur la gestion d'une base réduite de formes 3D, qui nous permet effectivement de faire les reconstructions du masséter.

Corrélation entre céphalométrie et muscle masséter

Ce travail a été effectué en collaboration avec Adeline Kerbrat, Patrick Goudot et Thomas Schouman.

Bibliographie

La céphalométrie est l'étude des mesures effectuées sur un crâne. Elle permet en clinique de détecter et de caractériser, via l'imagerie médicale, des anomalies présentes sur le crâne de certains patients. Ces mesures sont linéaires ou angulaires. Elles s'effectuent entre différents repères anatomiques identifiés sur le crâne. Ces repères sont des points anatomiques faciles à identifier d'un patient à l'autre. En anthropologie ils sont aussi appelés « landmarks ». Sur la Figure 13, on peut en visualiser plusieurs exemples fréquemment utilisés.

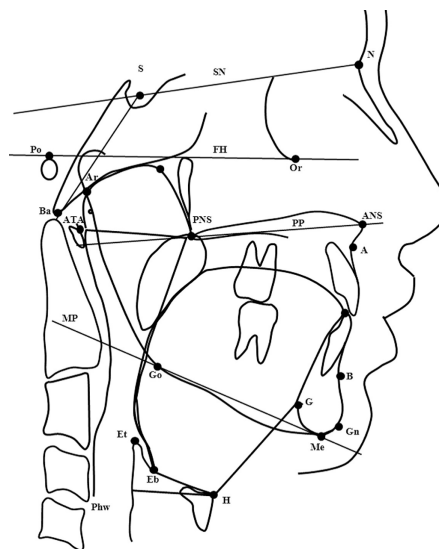


FIGURE 13 – Exemple de différents landmarks céphalométriques

Les études céphalométriques des dernières décennies ont permis de classifier différents phénotypes [195] de longueur faciale [75] ou de classes dentaires [7, 107], qui ont aidé les cliniciens à

mieux caractériser et traiter de nombreuses pathologies comme l'apnée du sommeil [135, 160], la malocclusion [140, 194], ou encore les malformations faciales [73, 95, 162]...

Les muscles élévateurs de la mandibule, du fait de leurs insertions sur les os du crâne, et plus particulièrement la mandibule, sont très liés au développement et donc à la forme du crâne. Parmi ces muscles, le muscle masséter est un des muscles les plus volumineux du visage [260]. Son importance tant fonctionnelle que volumique, lui confère un intérêt tout particulier aux yeux des médecins ou des anatomistes. Il nous a particulièrement intéressé, dans le contexte de la reconstruction faciale, du fait de son impact sur la forme du visage au vu de son emplacement, à l'arrière de la joue. On peut le localiser au bout de la flèche bleue sur la Figure 14.

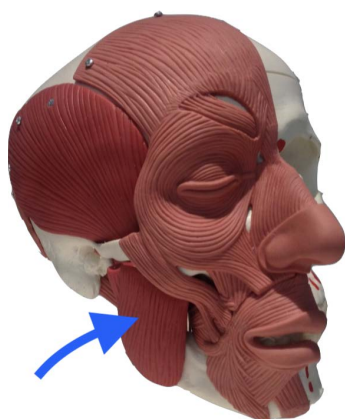


FIGURE 14 – Maquette 3D du crâne et des muscles du visage, au bout de la flèche bleue le muscle masséter

Le muscle masséter est court, épais et quadrilatéral [29]. Il est composé de 3 parties distinctes, ordonnées en faisceaux, que l'on peut visualiser sur la Figure 15 (photo d'une dissection à gauche et schéma à droite) :

- un faisceau superficiel de deux couches, une interne et une externe,
- un faisceau médian avec une seule couche,
- un faisceau profond séparé en trois couches différentes.

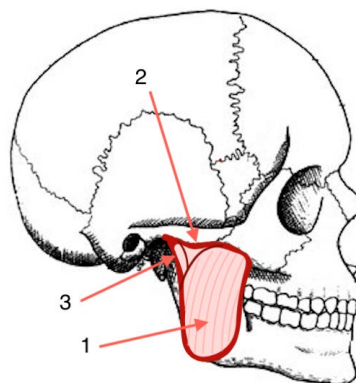
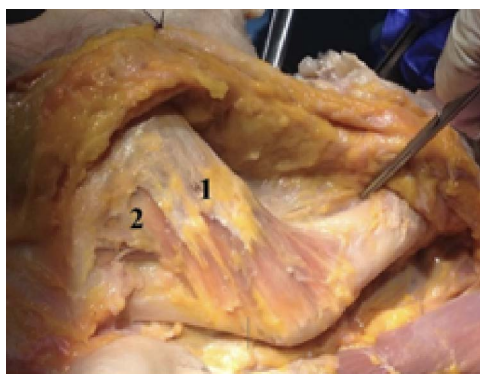


FIGURE 15 – Les faisceaux du muscle masséter (1) superficiel (2) médian, et (3) profond

Notre étude et ses résultats

Cette étude cherche à mettre en lumière le lien morphologique qui existe entre les mesures effectuées sur le crâne et celles effectuées sur le masséter chez des patients dysmorphiques. On

retrouve déjà cette idée dans la littérature avec [12], toutefois notre approche a pour but de compléter leurs résultats en s'intéressant à des morphologies plus variées et à des mesures souvent peu mises en valeur.

Dans le cadre de ce travail et parmi les très nombreuses mesures céphalométriques qui existent, nous en avons sélectionné cinq qui permettent de compléter au mieux la littérature déjà existante sur le sujet [10, 12, 31, 56]. Il s'agit des angles SNA, SNB, ANB, FMA et entre le plan Bispinal et Mandibulaire, que l'on peut visualiser sur la Figure 16.

Pour ce qui est des mesures effectuées sur le masséter, la communauté s'accorde à dire que les paramètres les plus à propos pour le décrire sont sa hauteur, sa largeur, son épaisseur et son volume [31].

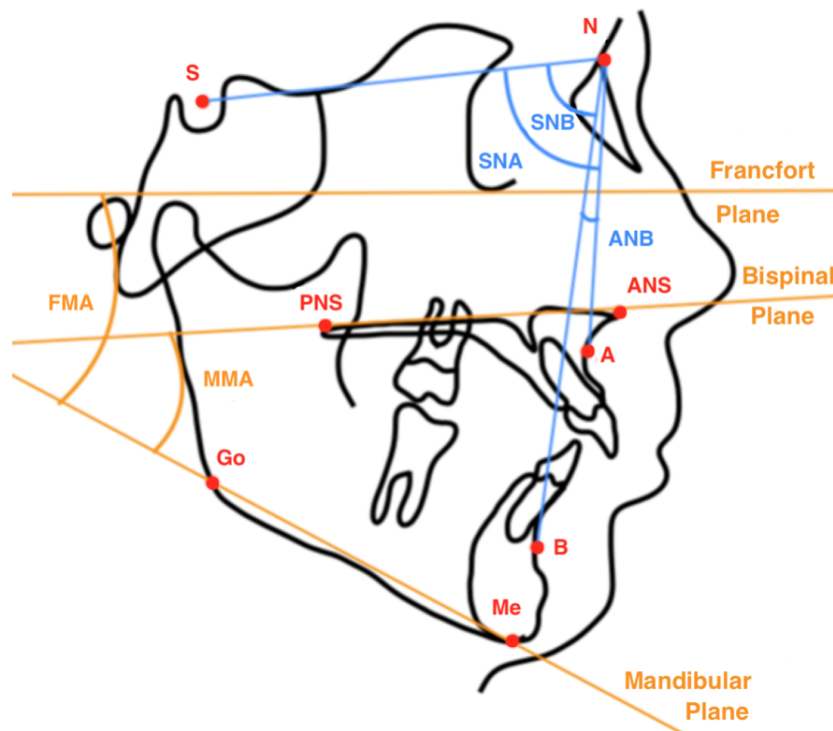


FIGURE 16 – Les mesures céphalométriques que nous avons utilisées pour notre étude

L'étude a été menée sur 51 patients du service de chirurgie maxillo-faciale de l'hôpital de La Pitié Salpêtrière, à Paris. Nous avons identifié plus en détail les corrélations présentes entre la forme du crâne et celle du muscle masséter.

Le FMA est dans notre étude le paramètre de mesure angulaire osseuse, qui présente plus de corrélation avec les mesures massétériques. En effet, il est inversement corrélé aux 4 mesures du masséter testées (hauteur, largeur, épaisseur et volume). Ce qui signifie qu'un muscle masséter long, large, épais et volumineux est associé à un phénotype dit de « face courte » avec un angle mandibulaire fermé. Ce résultat est similaire à ceux trouvés dans [12, 56, 116].

Toutefois peu d'études abordent ce problème selon la position antéropostérieure du maxillaire, ici nous montrons une corrélation du SNA avec l'épaisseur et le volume du masséter et du SNB avec sa hauteur et son volume, contrairement à [125].

Du fait de la présence de ces corrélations significatives, ces conclusions nous ont donc permis de poser comme hypothèse, pour notre méthode de reconstruction faciale, qu'il serait possible de déduire à partir de la forme des os du crâne, celle du muscle masséter.

Processus ingénierique de la constitution d'une base réduite de formes 3D

Ce travail a été effectué en collaboration avec Yvon Maday et Chiara Nardoni.

Il s'agit ici d'un processus complet de traitement d'une base de données de formes 3D. Toutes les méthodes mathématiques utilisées ont déjà été présentées individuellement dans la littérature. Cependant, elles sont ici assemblées et ajustées pour répondre aux caractéristiques de nos applications : reconstruction faciale et segmentation semi-automatique. Il est toutefois tout à fait envisageable d'utiliser le même procédé de traitement et de gestion d'une base réduite de données 3D, dans des objectifs et applications différents tels que les jeux vidéos, la biologie moléculaire, etc.

Les étapes

Plusieurs étapes utilisant des outils mathématiques variés sont nécessaires afin de pouvoir utiliser notre base de données de forme.

1. *Acquisition des données* : dans notre contexte, il s'agit de la segmentation des images médicales. La seconde partie de ce manuscrit est entièrement consacrée à ce problème épineux. La bibliographie et la présentation des méthodes mises en place sont proposées dans la section suivante. L'ensemble des données de scanner collectées pour créer cette base de formes provient du service de Chirurgie Maxillo-Faciale de l'hôpital de La Pitié Salpêtrière, à Paris. Ils ont été acquis avec deux types de fenêtres : tissus mous et os (Figure 17).

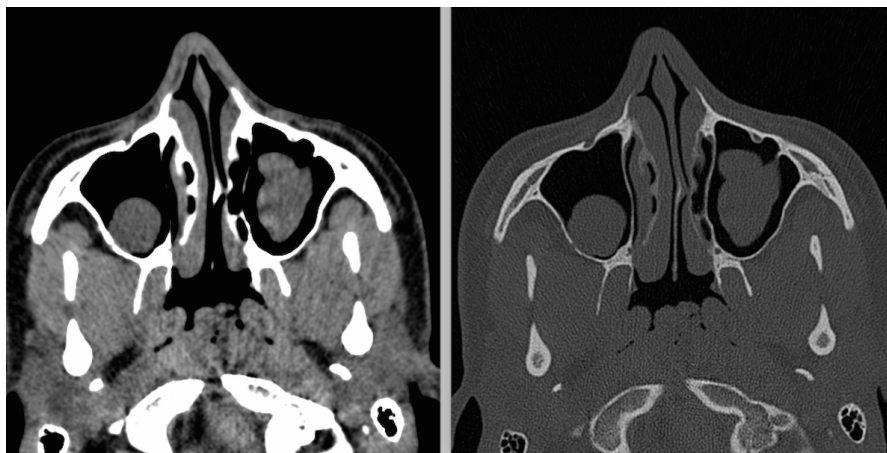


FIGURE 17 – Les deux fenêtres d'acquisition des images scanner (a) tissus mous, et (b) os

2. *Maillage 3D des objets* : passer des coupes d'images médicales segmentées à un maillage en trois dimensions demande la mise en place d'un algorithme d'extraction d'isosurfaces [32] comme les « Marching Cubes », introduit par [134]. Ce dernier permet de créer une triangulation surfacique à partir d'un volume de voxels (pixels en 3D), toutefois ils sont aussi connus pour laisser des artefacts et des éléments invalides dans le maillage, pour des simulations réalisées avec des éléments finis. Il est donc nécessaire d'y ajouter une étape de remaillage, permettant de retrouver une géométrie correcte et de contrôler la qualité du maillage souhaité. Pour cela nous avons utilisé mmg [50, 57], qui nous permet de contrôler la distance de Hausdorff entre le maillage d'entrée et le maillage de sortie, ainsi que d'autres paramètres comme la longueur maximale et minimale des arêtes des triangles du maillage. Les résultats de l'algorithme de Marching Cubes et celui du remaillage sont donnés dans la Figure 18.

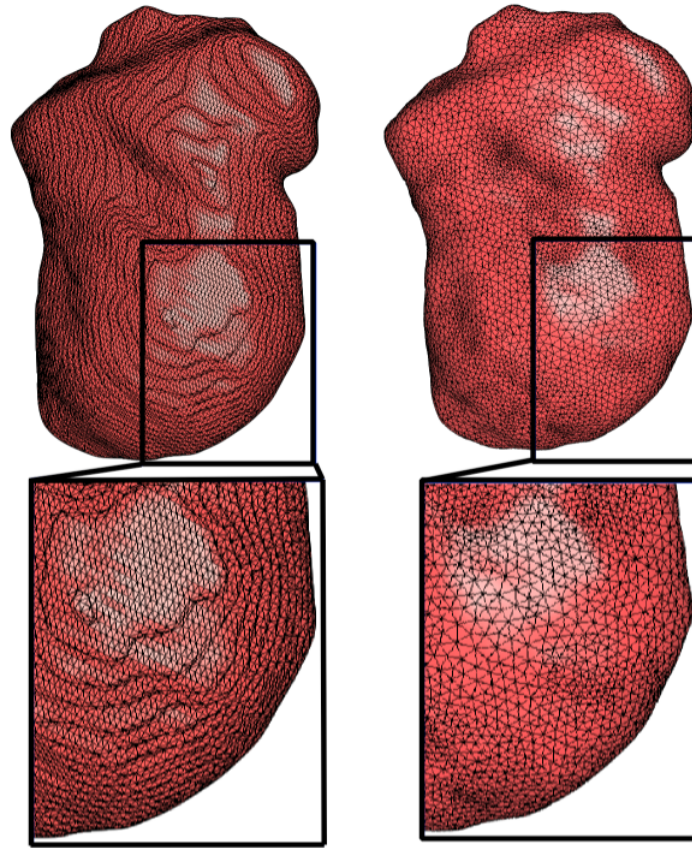


FIGURE 18 – Maillage d’un muscle masséter après l’algorithme du marching cubes à gauche et après remaillage à droite

3. *Alignement* : Souvent sous-estimé, l’alignement cohérent des objets de la base de données entre eux, peut avoir un fort impact sur la suite du processus. Effectivement, si les données sont acquises de plusieurs sources qui n’ont pas les mêmes paramètres d’acquisition, les objets peuvent différer à un seul mouvement rigide et/ou une homothétie près. Il faut donc corriger les translations, rotations et homothéties qui influent sur les données. La première phase consiste à centrer les objets Ω en l’origine du repère à l’aide du calcul de leur barycentre x^G respectif défini par :

$$x^G = \frac{1}{|\Omega|} \int_{\Omega} \vec{x} d\vec{x}$$

avec $\vec{x} \in \Omega$ et $|\Omega|$ le volume d’ Ω . On obtient après discrétisation sur le maillage de l’objet (détaillé dans le chapitre 2, page 49) :

$$x^G = \frac{1}{2|\Omega|} \sum_i x_i^2 n_i d\sigma_i$$

avec n la normale extérieure à la surface de l’objet Ω .

Si nécessaire, c’est à ce moment qu’une mise à l’échelle peut être mise en place.

Pendant la deuxième phase, nous calculons les axes d’inertie pour pouvoir les aligner sur ceux d’un objet de référence, grâce à la matrice d’inertie I_{Ω} :

$$I_{\Omega} = \int_{\Omega} (|\vec{x}|^2 Id - \vec{x} \otimes \vec{x}) d\vec{x}$$

avec Id la matrice identité, et $\vec{x} \otimes \vec{x}$ la matrice $\vec{x} \cdot \vec{x}^T$. Ces deux étapes permettent d'identifier tous les objets de la Figure 19 comme identiques en forme, si on aligne les axes d'inertie et que l'on compare les maillages.

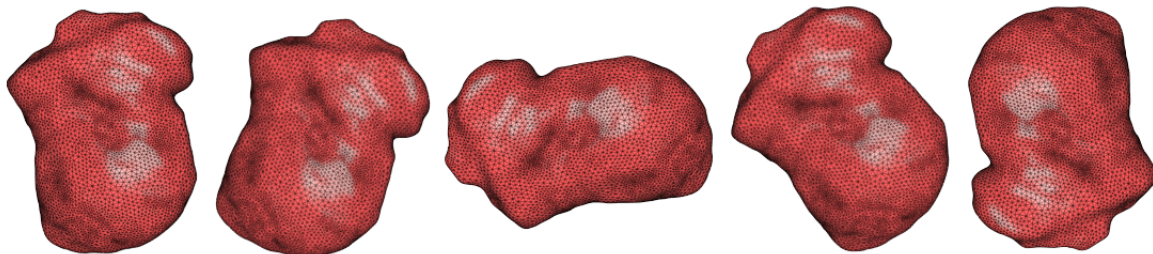


FIGURE 19 – Cinq muscles masséter identiques à un mouvement rigide près

Il est important de noter que notre méthode s'attache particulièrement à ne pas sélectionner de points spécifiques à mettre en correspondance, même pour l'alignement, car nous souhaitons un processus totalement automatique. Cela est rendu possible par la méthode décrite précédemment combinée aux étapes 4 et 5 (warping et morphing) décrites ci-dessous.

4. *Warping* (facultatif) : Cette étape n'est nécessaire que lorsque l'objet dont on veut créer une base réduite de forme n'est pas topologiquement fermé. L'algorithme qui consiste à utiliser les équations de l'élasticité pour déformer un maillage template fermé sur un objet ouvert, a été développé dans [158]. L'idée principale est présentée dans la Figure 20.

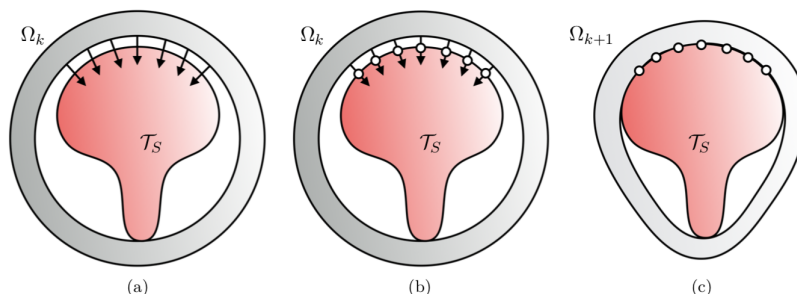


FIGURE 20 – Description schématique du warping : (a) Calcul du champ de déplacement (flèche noire) sur le template Ω_k (en gris) entourant le modèle source (en rouge), (b) Identification des points d'intersection entre le champ de déplacement et le modèle source (points en blanc), et (c) Actualisation de la forme selon le déplacement calculé. Schéma extrait de [158].

5. *Morphing* : Le principe de cette étape est de déformer une forme de référence Ω_0 , dans notre cas une ellipsoïde, vers une forme objectif Ω_k , ici chaque muscle masséter de notre base de données. Cela nous permet de considérer tous les objets de la base comme des déplacements u_k d'un même maillage de référence, ce qui rend toute comparaison entre eux bien plus facile à mettre en place. Cela permet aussi de s'affranchir de la mise en correspondance de « landmarks », à identifier sur tous les objets de la base de données. Un chapitre complet de cette thèse est dédié à l'explication détaillée de cette méthode et de sa bibliographie dans la troisième partie.

6. *Réduction de dimension* : Pour extraire les principales informations dans notre base de données, et afin de représenter au mieux les formes qu'elle contient aussi simplement que possible, nous réalisons une réduction de dimension : une analyse en composantes principales (ACP) ou un algorithme Greedy. Pour cela nous calculons les modes qui permettent de représenter tous les éléments de la base de données par quelques coefficients. On peut alors les représenter par une combinaison linéaire telle que $u_n = \sum_{\ell=1}^n \alpha_{\ell}^k P_{\ell}$, où P_{ℓ} correspond aux modes. On peut visualiser les P_{ℓ} de l'ACP avec ℓ compris entre 1 et 5, sur la Figure 21.

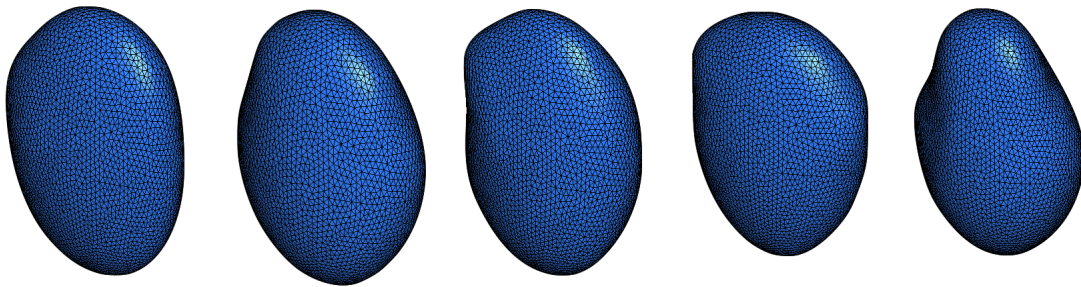


FIGURE 21 – Les 5 premières composantes principales de notre base de données qui permet de reconstruire un nouveau muscle masséter

7. *Apprentissage* : la reconstruction du muscle à partir de mesures anthropologiques est envisageable, en apprenant, via des algorithmes type réseaux de neurones, les coefficients de l'ACP associés à ces mesures. Nous nous sommes toutefois heurtés ici au manque de données de muscles masséters segmentés, car leur acquisition est chronophage. C'est ce qui a motivé les travaux entrepris sur la segmentation semi-automatique au cours de ma thèse, présentés dans la partie II.
8. *Applications* : de nombreuses applications utilisant cette base réduite de formes peuvent être développées. Ici nous avons développé un atlas anatomique pour le muscle masséter, le visage et le crâne, qui nous a servi à créer des algorithmes en segmentation d'images et en reconstruction faciale. Ces points sont l'objet des deux parties suivantes de cette thèse.

Partie II - Acquisition et traitement des données - Segmentation

Dans cette deuxième partie, nous allons nous intéresser à l'acquisition des données et donc à la segmentation, plus spécifiquement des tissus mous, comme le muscle masséter sur les images de scanner, qui s'est révélée être un problème durant nos travaux sur la reconstruction faciale. En effet, pour être en mesure de reconstruire les muscles, puis le visage, à partir du crâne, il nous a fallu constituer une base de données de formes 3D grâce à la méthode présentée précédemment (Partie I - Chapitre 2). La première étape de cette méthode est l'acquisition des données, la segmentation d'images médicales. Nous avons donc cherché à mettre en place une méthode semi-automatique qui nous permettait d'accélérer le processus sans augmenter l'erreur.

Cette partie est divisée en trois chapitres, qui portent sur le sujet commun de la segmentation des tissus mous. Le premier est une brève preuve de concept en 2D et en 3D, le second le développement de cette méthode en détails dans le cas particulier du muscle masséter, et le dernier est une application pratique qui compare la méthode de référence actuelle, la segmentation manuelle, à notre méthode semi-automatique développée dans les deux articles précédents.

L'état de l'art étant très lié pour ces trois chapitres, une présentation commune est faite ci-dessous. Les résultats de ces trois articles sont ensuite présentés chacun à leur tour.

Bibliographie

La segmentation d'images médicales consiste à identifier et labelliser les voxels (pixels 3D) de l'ensemble de l'image ou d'un objet d'intérêt. Dans notre cas, nous nous sommes intéressés au muscle masséter dans le contexte d'une application spécifique : la reconstruction faciale.

Cependant, les méthodes de segmentation automatiques ou semi-automatiques ont un plus vaste champ d'application. Elles sont par exemple très largement utilisées dans le « diagnostic assisté par ordinateur », qui est devenu un des sujets principaux de recherche en imagerie médicale et en radiologie [59, 60, 62, 70, 217] dans les dernières décennies. Dans les années 80, le concept de diagnostic automatique ou assisté par ordinateur était déjà connu depuis des études datant des années 60 [19, 132, 150], mais ces premières tentatives n'étaient pas un réel succès. En effet, la détection automatique d'organes ou de lésions s'est révélée extrêmement difficile.

De nos jours, les techniques se sont de plus en plus nombreuses, en partie grâce au développement technologique des ordinateurs et des méthodes d'acquisition. Certains tissus, dont le contraste avec le tissu voisin est suffisamment important, comme les os, sont facilement détectables automatiquement [115, 175, 262]. Il en va de même pour les organes majeurs du corps humain et les pathologies qui leur sont associées, comme le cerveau et le coeur [16, 33, 196], qui ont toujours suscité un grand intérêt pour les soignants. Les méthodes d'utilisation communes pour ces types d'applications sont les méthodes dites de seuillage ou de détection des bords. La première consiste à regrouper dans un même label les pixels qui ont un niveau de gris proche ou plus exactement contenu par une ou plusieurs valeurs seuils [176]. La seconde, qui s'appuie aussi sur la détection des niveaux de gris, cherche les frontières des régions anatomiques en analysant les transitions rapides de ces niveaux, et assemble les voxels homogènes dans un même label [133]. Ces deux méthodes sont fondées sur la détection des niveaux de gris, c'est ce qui permet, entre autres, aux experts de différencier deux régions anatomiques et de réaliser une segmentation manuelle [170]. Ce type de stratégie, mimant la connaissance des experts ont été les premières à être mises en place [61, 63]. Différentes classifications de ces méthodes existent, on peut par exemple citer [258].

Toutefois, plus récemment, d'autres types de méthodes, fondées au moins en partie sur les statistiques, se sont progressivement développées, comme les atlas guidés, les modèles déformables ou encore l'utilisation massive de l'apprentissage. Elles se différencient entre autres par la quantité de connaissances a priori injectée dans la méthode [40].

Les atlas statistiques utilisent comme référence une ou plusieurs structures d'intérêt déjà segmentées, appelées atlas, comme connaissance préalable pour de nouvelles segmentations [105, 180]. La segmentation d'une nouvelle image repose alors sur un alignement et une déformation qui permet de définir la transformation optimale entre l'atlas et la nouvelle image. Différents types d'algorithmes existent pour optimiser le déplacement [173, 223], ou l'utilisation de l'atlas lui-même [2, 45, 259]. Ces méthodes de segmentation se sont révélées efficaces lors des grands concours de segmentation, organisés par « the American Association of Physicists in Medicine », ou « the Medical Image Computing and Computer-Assisted Intervention Society ».

Les modèles déformables nécessitent quand à eux plus d'informations a priori. Lorsque ces dernières sont disponibles, les variations caractéristiques de la forme de la structure d'intérêt peuvent être utilisées pour former des modèles statistiques de forme. Cela limite les résultats obtenus des segmentations, à des formes anatomiquement plausibles [94]. Toutefois, ces méthodes sont aussi moins flexibles pour la raison précédemment citée. Par ailleurs, la taille et le contenu des données d'entraînement limitent aussi la performance des résultats. Cette méthode reste cependant fréquemment utilisée pour les structures anatomiques pelviennes [72, 127, 187].

L'apprentissage statistique, appliqué à la segmentation d'images, regroupe à lui tout seul un large panel de méthode en plein essor, telle que le support vecteur machine, les arbres de décisions, le deep learning ou encore les réseaux de neurones [110]. Ces derniers sont déjà retrouvés dans de multiples applications comme la segmentation de tumeur dans le cerveau, ou dans le foie, etc

[126, 143, 151, 183]. Les résultats obtenus par ces algorithmes sont prometteurs dans le cadre des applications pour lesquels ils sont développés. Mais il n'est pas toujours évident de les étendre à tous les types d'images et cela nécessite souvent un jeu de données important au vu de la variabilité humaine sous-jacente aux données médicales [110].

La méthode que nous proposons s'appuie sur ces dernières techniques (modèle déformable, atlas statistique et apprentissage) et emprunte certains outils à chacune d'entre elles, pour les combiner de manière à réaliser notre objectif. Elle est comparable à [25], mais avec une vision déterministe du problème, et une application pratique dans des cas réels de segmentation par des praticiens. En effet le plus souvent les méthodes de segmentation sont développées dans un but spécifique, et il est important de noter qu'il n'y a, pour le moment tout du moins, pas de méthode universelle de segmentation. Chaque algorithme répond à un ensemble unique de contraintes et d'objectifs, rendant la méthode mise en place particulièrement intéressante pour une application précise et parfois moins pour d'autres.

Les objectifs plus précis que nous nous sommes donnés pour le cadre de ce travail sont :

- une méthode rapide,
- utilisable par des cliniciens,
- plus spécifiquement pour la segmentation des tissus mous, tels que des muscles,
- et dont les limites sont parfois difficiles à percevoir sur scanner.

Nous nous sommes limités ici à explorer les grandes méthodes existantes, cependant pour plus de détails, il est possible de se référer à [62, 94, 105, 131].

Introduction du concept

Ce travail a été effectué en collaboration avec Damiano Lombardi et Yvon Maday. Le bref article qui en est extrait est présenté dans l'appendice A.

Nous présentons ici une méthode de segmentation d'imagerie médicale semi-automatique fondée sur un modèle, minimisant l'intervention d'un expert. A l'aide d'une base réduite de formes 3D (constituée selon la méthode exposée dans le chapitre précédent, et donc représentées comme des déformations élastiques), nous pouvons approximer la forme de l'objet à identifier sur les images, comme un muscle sur un scanner. Il suffit d'identifier les coefficients associés à l'objet d'intérêt, via la résolution d'un système linéaire prenant en entrée les coordonnées de quelques points sélectionnés sur l'image. Cette méthode est indépendante des niveaux de gris de l'image, et peut donc être appliquée sur tous objets et toutes imageries.

Soit $E \subset \mathbb{R}^3$ notre forme de référence, ξ un point de E et $x \in F \subset \mathbb{R}^3$ avec F le bord de l'objet segmenté. On peut extraire de l'ACP de l'ensemble des objets de notre base de données, représenté par des déplacements u de la forme de référence sur ces objets, les modes ϕ_i . On obtient alors :

$$u \approx u_n = \sum_{i=1}^n \alpha_i \phi_i.$$

On sélectionne un certain nombre de points $x^{(j)}$ sur notre image, et on peut alors écrire que :

$$\mathbf{x}^{(j)} = \xi_*^{(j)} + \sum_{i=1}^n \alpha_i \phi_i(\xi_*^{(j)}), \quad j = 1, \dots, m.$$

En choisissant les $\xi_*^{(j)}$ tels qu'ils soient les points de E les plus proches de $x^{(j)}$, on obtient le système linéaire suivant à résoudre :

$$\begin{cases} \Phi\alpha &= d, \\ \Phi_{jik} &= \varphi_{i,k}(\xi_*^{(j)}), \\ d_{j,k} &= \mathbf{x}_k^{(j)} - \xi_{*k}^{(j)}, \end{cases} \quad (1)$$

Un exemple implémenté en 2D est proposé Figure 22. À gauche de la figure, on peut voir la forme de référence qui est transportée vers différentes formes cibles, constituant ainsi notre base de données de formes 3D représentée par des champs de déplacement. À droite, la reconstruction (en rouge) d'une image générée aléatoirement (en bleu) par la résolution d'un système linéaire, permettant d'identifier les coefficients de notre base réduite.

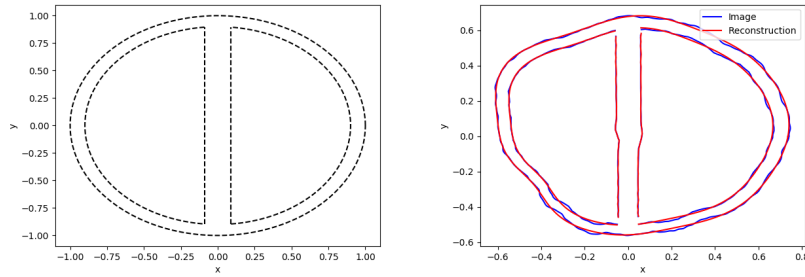


FIGURE 22 – Template non déformé à gauche et une déformation et sa reconstruction à droite

Dans l'idée de tester notre concept en 3D, brièvement exposé dans la section précédente en 2D, nous avons décidé d'utiliser la paramétrisation suivante, appliquée aux harmoniques sphériques, afin de créer 100 formes 3D nous servant de bases de reconstruction :

$$\begin{cases} a_k^{Real} = \frac{\sqrt{\mu_3}}{(l+1)^\beta} \cos(2\pi\kappa\sqrt{\mu_1}) \cos(2\pi\kappa\sqrt{\mu_2}) \\ a_k^{Imag} = \frac{\sqrt{\mu_3}}{(l+1)^\beta} \sin(2\pi\kappa\sqrt{\mu_1}) \sin(2\pi\kappa\sqrt{\mu_2}) \end{cases}$$

avec $(\mu_1, \mu_2, \mu_3) \in [0, 1]^3$, $\beta = 1.5$, et $\kappa = l(m+1)$.

Il suffit d'un simple graphe, Figure 23, pour voir l'utilité de cette paramétrisation sur la décroissance des valeurs propres après l'ACP, par rapport à une ACP faite directement sur les harmoniques sphériques.

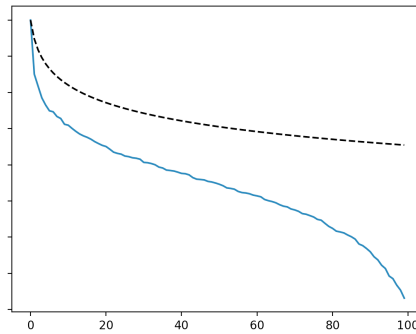


FIGURE 23 – Décroissance des valeurs propres après ACP, avec (en bleu) et sans (en noir) paramétrisation

Un certain nombre de points est sélectionné au hasard sur une nouvelle forme, générée aléatoirement à l'aide des harmoniques sphériques, que nous souhaitons reconstruire. Après résolution du système linéaire A.6 permettant d'identifier les coefficients α de l'ACP : il est possible de reconstruire par la combinaison linéaire de ces coefficients et des modes ACP, la forme d'intérêt. On peut alors comparer l'erreur faite entre notre reconstruction et la véritable forme, à l'erreur de projection due au fait qu'on n'utilise qu'un nombre restreint de modes et que donc nous faisons une approximation. Dans ce cadre, les deux erreurs retrouvées sont du même ordre de grandeur et diffèrent peu.

Application à la segmentation du muscle masséter

Ce travail, en cours de développement, a été effectué en collaboration avec Damiano Lombardi et Yvon Maday.

Cette fois, la base réduite de formes 3D utilisée est celle de muscles masséter générée à l'aide de la section 2 de la partie I. L'idée est que les masséters ne sont pas des formes aléatoires (comme dans le cas sans paramétrisation évoqué précédemment), ils font partie de la famille des muscles masséter qui a une petite dimension de Kolmogorov (comme dans le cas paramétré).

1. *Sélection des points* : La première étape est la sélection de points sur les images scanner à la frontière du muscle (Figure 24).

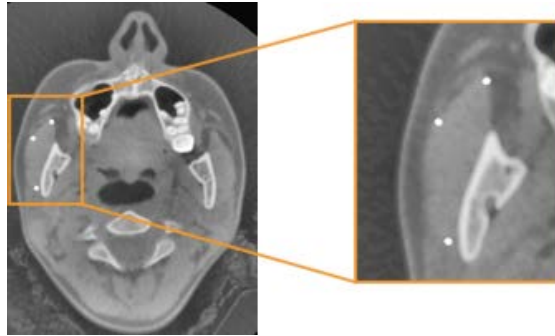


FIGURE 24 – Sélection des points à la frontière du muscle masséter

2. *Changement de Coordonnées* : des images dicom à notre espace de base réduit $[0, 1]^3$. Une transformation affine est construite, telle que :

$$\mathcal{X} : \begin{cases} \Omega_m \rightarrow [0, 1]^3 \\ x \mapsto \xi. \end{cases} \quad (2)$$

Nous avons $\xi = \mathcal{X}(x)$, et, puisque la transformation est inversible, $x = \mathcal{X}^{-1}(\xi)$.

Les points sont transportés dans $[0, 1]^3$, que nous appelons la configuration de référence, où les modes sont définis et où la reconstruction a lieu.

3. *La reconstruction d'un masséter en 3D* : à partir des points sélectionnés, nous identifions les meilleurs coefficients α qui permette d'optimiser au mieux la reconstruction au nuage de points.

En exploitant les points, un maillage constitué de $\mathcal{N} \in \mathbb{N}^*$ degrés de liberté est reconstruit : $v^{(i)}, i = 1, \dots, \mathcal{N}$.

Ces deux dernières étapes diffèrent sensiblement de la méthode décrite au chapitre 3.

4. *Visualisation et Validation* : le maillage est transporté dans la configuration de l'image en utilisant $u^{(i)} = \mathcal{X}^{-1}(v^{(i)})$ et un fantôme est calculé sur cette base, qui est :

$$\tilde{\mathcal{F}} : \begin{cases} \Omega \rightarrow \mathbb{R} \\ x \mapsto \tilde{\mathcal{F}}(x_1, x_2, x_3). \end{cases} \quad (3)$$

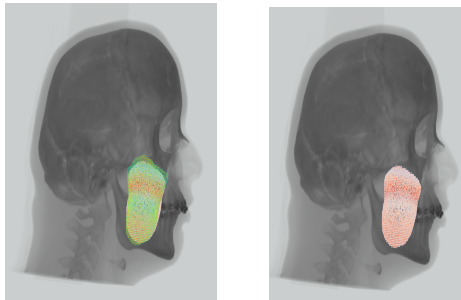


FIGURE 25 – Représentation 3D d'un crâne et de son visage associé : (a) et la superposition des masséters segmentés manuellement et semi-automatiquement, (b) et du muscle masséter reconstruit après segmentation semi-automatique uniquement

Application pratique de cette méthode semi-automatique

Ce travail a été effectué en collaboration avec Camille Cardot, Damiano Lombardi, Thomas Schouman et Wided Siai.

Le propos de cet article est de comparer l'utilisation de notre méthode semi-automatique, exposée ci-dessus, à la méthode de référence manuelle actuelle, par des praticiens. Il s'agit donc entre autres d'une remise en contexte pratique de cette méthode.

Deux opérateurs avec des connaissances anatomiques de la région du muscle masséter, mais pas d'expertise poussée en radiologie ou en segmentation, ont chacun segmenté 20 masséters : une première fois manuellement, puis une seconde fois avec la méthode semi-automatique, au moins un mois plus tard. Pour la segmentation manuelle, nous avons utilisé le logiciel Amira [197]. Pour celle semi-automatique, une interface graphique pour des cliniciens a été mise en place (Figure 26).

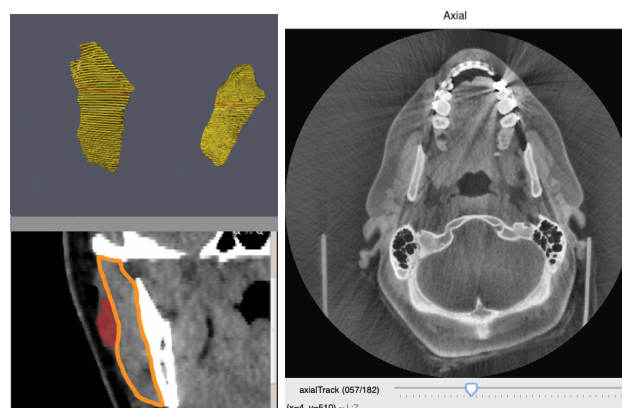


FIGURE 26 – Les deux logiciels de segmentation utilisés : à droite, Amira, et à gauche, la méthode semi-automatique

Les nombreuses difficultés rencontrées lors des segmentations manuelles sont celles exposées dans la bibliographie ci-dessus. Cela rend le travail extrêmement long et fastidieux, puisqu'il faut en moyenne 1h45 pour segmenter un seul muscle. Pour la segmentation semi-automatique, bien que certaines complications liées intrinsèquement à l'exercice de la segmentation étaient toujours présentes, la rapidité et la simplicité du processus, rend l'ensemble de l'acquisition plus agréable et plus rapide (en moyenne 9m30 par muscle). Une difficulté associée plus spécifiquement à cette méthode a tout de même perturbé les opérateurs : il s'agit de l'impossibilité de visualiser en temps réel le modèle 3D de la segmentation. Cela reste toutefois bien plus rapide et moins pénible pour un praticien, et on peut sans mal espérer améliorer l'algorithme nous permettant de calculer l'alignement, qui est le plus chronophage.

Par ailleurs une brève étude de reproductibilité inter-opérateur a été menée. Que ce soit en terme de temps de segmentation ou d'erreur de segmentation, notre méthode semi-automatique de segmentation est reproductible d'un opérateur à l'autre. Tandis que la segmentation manuelle n'est, en terme de temps, pas reproductible. Il y a donc un gain dans la fiabilité des résultats avec notre méthode.

Partie III - Reconstruction faciale

La dernière partie présente d'abord le « morphing », outil dont nous nous sommes déjà servis dans le processus permettant de créer une base réduite de formes 3D, et que nous allons maintenant aussi appliquer à la reconstruction faciale, dans le second chapitre de cette partie.

Le morphing

Ce travail a été effectué en collaboration avec Maya de Buhan et Chiara Nardoni, il a en partie déjà été présenté dans les travaux de thèse de cette dernière, et va donner suite à une publication commune.

L'objectif général du morphing est de trouver une transformation d'une forme de référence donnée vers un objet cible. Ici nous proposons de définir cette transformation comme une déformation élastique obtenue en minimisant une fonctionnelle fondée sur la distance entre les deux formes. Pour accomplir cet objectif, nous utilisons des méthodes d'optimisation de forme.

L'optimisation de forme consiste à optimiser une fonctionnelle de coût $F(\Omega)$ dans un ensemble de forme admissible O_{ad} . Un problème générique d'optimisation de forme peut s'écrire :

$$\min_{\Omega \in O_{ad}} F(\Omega), \text{ ou } \max_{\Omega \in O_{ad}} F(\Omega).$$

Les applications de ce type de problème sont vastes et amènent des problèmes aussi bien théoriques que numériques à résoudre : la définition du domaine admissible, la notion de dérivation dans cet espace, les propriétés géométriques du domaine, etc. De nombreuses notions de dérivation par rapport au domaine sont décrites dans la littérature, nous ferons ici référence à la méthode de variation de bord d'Hadamard [3, 96, 157].

Notre méthode a plus en commun avec *Simon et al.* [192, 193] car elle propose un modèle de déformation inspiré de la physique, et avec *Bacjcy et al.* [14] qui emprunte des techniques au contrôle optimal et à l'optimisation de forme. Pour une bibliographie détaillée de toutes ces méthodes, il est possible de se référer à [244]. Nous présentons ici deux fonctionnelles de forme : une « volumique » J et une « surfacique » P , puis à l'aide de différentes simulations numériques, nous comparons leurs résultats.

Une fonctionnelle volumique

Nous mesurons la différence entre la forme de référence Ω et la cible Ω_T par la fonctionnelle de forme suivante :

$$J(\Omega) = \int_{\Omega} d_{\Omega_T}(x) dx,$$

qui implique d_{Ω_T} la fonction distance signée à Ω_T , définie comme suit :

$$\forall x \in \mathbb{R}^d, d_{\Omega_T}(x) = \begin{cases} -d(x, \partial\Omega_T) & \text{if } x \in \Omega_T, \\ 0 & \text{if } x \in \partial\Omega_T, \\ d(x, \partial\Omega_T) & \text{if } x \in {}^c\overline{\Omega_T}. \end{cases}$$

On peut alors calculer la dérivée de forme de J :

$$\forall \theta \in W^{1,\infty}(\mathbb{R}^d, \mathbb{R}^d), J'(\Omega)(\theta) = \int_{\partial\Omega} d_{\Omega_T} \theta \cdot n ds.$$

avec $\theta : \mathbb{R}^d \mapsto \mathbb{R}^d$ un petit difféomorphisme.

Puis trouver la direction de descente associée, et à l'aide d'un algorithme itératif qui minimise J . On obtient alors une séquence de forme de plus en plus proche de Ω_T . Cet algorithme a été implémenté avec la méthode des éléments finis en 2D et en 3D.

On peut voir avec la Figure 27, la déformation d'un disque en un lapin, obtenu avec la minimisation de J :

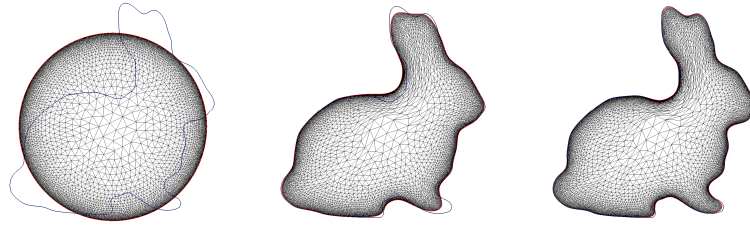


FIGURE 27 – Morphing 2D d'un disque en un lapin

Comparaison avec une fonctionnelle surfacique

Nous avons aussi comparé la fonctionnelle J avec une fonctionnelle plus classique de surface P , telle que :

$$P(\Omega_0) = \int_{\partial\Omega_0} (d(s, \partial\Omega_T))^2 ds,$$

qui dépend de la distance euclidienne $d(\cdot, \partial\Omega_T)$ à $\partial\Omega_T$, évaluée au bord de Ω_0 . La fonctionnelle P est plus intuitive, puisqu'elle essaie d'aligner deux formes en fonction de leurs bords et a l'avantage d'être bien définie sur une surface et pas une forme. Cependant, en pratique, cette fonctionnelle s'avère numériquement plus difficile à mettre en place. En effet, la dérivée de forme de P implique de calculer la courbure moyenne au bord :

$$\forall \theta \in W^{1,\infty}(\mathbb{R}^d, \mathbb{R}^d), P'(\Omega)(\theta) = \int_{\partial\Omega} \left(\frac{\partial d^2}{\partial n} + \kappa d^2 \right) \theta \cdot n ds,$$

avec κ la courbure moyenne de $\partial\Omega$.

Par ailleurs, pour minimiser P , un point de $\partial\Omega$ doit se déplacer vers le point le plus proche de $\partial\Omega_T$, ce qui peut générer une ambiguïté, menant à des singularités numériques, empêchant la convergence globale de l'algorithme.

On peut voir sur la Figure 28, un premier exemple où la fonctionnelle surfacique parvient au même résultat que la fonctionnelle volumique (Figure 6), mais sur un exemple un peu plus compliqué, des singularités apparaissent.

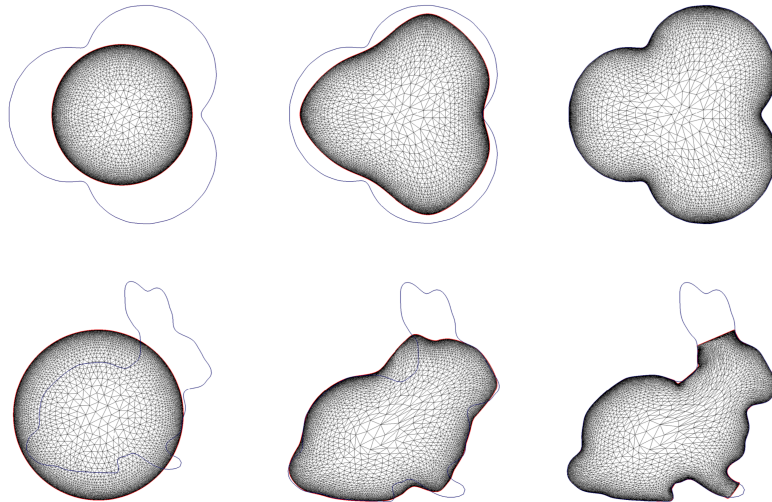


FIGURE 28 – Morphing 2D d'un disque en un lapin

Au vu de ces résultats, c'est la première fonctionnelle qui a été choisie pour l'application de reconstruction faciale, dont le morphing est un ingrédient clé.

Application à la reconstruction faciale

Ce travail a été effectué en collaboration avec Patrick Goudot, Yvon Maday, et Thomas Schouman. Il reprend et développe les travaux d'abord entrepris par Maya de Buhan et Chiara Nardoni.

La reconstruction faciale a pour but d'estimer l'apparence faciale d'un individu à partir de la seule connaissance de son crâne. Cela se base sur l'hypothèse qu'il existe une importante corrélation entre la structure osseuse et celle des tissus mous [102], ce que nous avons aussi confirmé dans le premier chapitre de cette thèse. Toutefois, ce processus reste une approximation de la forme du visage, en effet les caractères secondaires comme les cheveux, la couleur de peau ou des yeux ne sont pas identifiés via ces méthodes. Par ailleurs, d'autres paramètres qui eux influencent la forme même du visage ne sont pas toujours faciles à identifier sur le crâne comme l'âge ou le sexe, voire pas du tout comme la corpulence. Certaines études proposent alors un ensemble de reconstructions possibles pour pallier ce problème [43, 153].

D'un point de vue mathématique, on dit que le problème est mal posé, ce qui va engendrer deux types de difficultés : la caractérisation de la solution qui n'est pas unique, celle du degré de précision obtenu via ces reconstructions, ainsi que la stabilité.

De nos jours, la reconstruction faciale a divers objectifs de la médecine à l'anthropologie. Dans le projet *FaciLe*, l'objectif est la reconstruction d'un visage en médecine légale afin d'identifier la personne décédée.

Une longue histoire

L'histoire de la reconstruction faciale est assez fascinante. En effet, on en retrouve des traces très tôt dans les civilisations humaines, dans les pratiques liées aux ancêtres ou les rites mortuaires. En 1930, une collection de crânes humains plâtrés (Figure 29), datant d'il y a 9000 ans, est retrouvée sous le sol d'une maison néolithique à Jericho [111].



FIGURE 29 – Crânes plâtrés de Jericho (7000 av JC) préservé au British Museum de Londres (à gauche) et Jordan Archeological Museum d’Amman (à droite). Images extraites de [111]

Dans ce contexte la signification symbolique est prépondérante sur l’anatomie. Cependant, on peut considérer ces visages comme une des premières tentatives de reconstruction faciale. On retrouve par la suite ce type de pratique dans de nombreuses civilisations. On peut citer l’Egypte antique et les masques mortuaires pharaoniques par exemple.

Ce n’est toutefois qu’à partir du 15^{ème} siècle, en Europe, que les connaissances en anatomie se développent, en particulier grâce à l’essor de la dissection jusque là interdite. Ce qui va permettre progressivement un gain de connaissances puis d’intérêt pour la reconstruction faciale dans un cadre plus judiciaire. Ce n’est seulement qu’à la fin du 19^{ème} siècle, voir le début du 20^{ème}, que la reconstruction faciale entre à part entière dans les sciences légales. Deux écoles de référence se développent alors, l’école Russe et l’école Américaine.

L’anthropologue russe Mikhail Gerasimov (1907-1970) pensait que la forme des muscles était très liée aux structures osseuses sous-jacentes [76, 77], et qu’il fallait pour faire une reconstruction faciale correcte avoir des connaissances anatomiques et artistiques très poussées. L’école Américaine, dont on peut citer l’anthropologue Wilton Krogman comme pionnier [124], fonde sa méthode non pas sur la reproduction de détails anatomiques mais sur des tables de mesures d’épaisseur de tissus mous. Dans les années 80, on voit apparaître une troisième école, qui s’inspire des deux précédentes, et qui est développée par Richard Neave et Carolin Wilkinson. Cette méthode traditionnelle se fonde sur des procédures manuelles telles que : des reconstructions 2D sous forme de portraits [91, 220], ou 3D sous forme de bustes (Figure 30).



FIGURE 30 – Méthode manuelle 2D (en haut) et 3D (en bas) de reconstruction faciale. Images extraites de [253]

Ces méthodes manuelles, bien qu'obtenant souvent des résultats plausibles, sont rapidement critiquées, principalement pour leur manque de standardisation et leur trop grande subjectivité liée à l'artiste anatomiste lui-même [91]. Par ailleurs ce type de reconstruction pouvait prendre jusqu'à plusieurs jours de travail à un expert avant d'obtenir un visage.

L'apparition des ordinateurs, des méthodes numériques et de visualisation donne une nouvelle opportunité à la reconstruction faciale. Celle de l'automatisation du processus, permettant un gain de temps et une moindre subjectivité des méthodes. De nos jours, la plupart des méthodes digitales existantes associent modèles statistiques et bases de données.

Une méthode qui tient compte de l'anatomie

C'est dans ce vaste contexte, que les méthodes développées au sein du projet FaciLe prennent racines. Notre méthode de reconstruction faciale, s'appuie sur le travail préliminaire de Chiara Nardoni et Maya de Buhan au sein du projet.

La méthode que nous proposons s'inspire largement de l'histoire de la reconstruction faciale, en prêtant une attention particulière à l'anatomie musculaire, qui a toutefois été délaissée dans les méthodes automatiques actuelles [203]. Elle complète la méthode originale développée dans [35], qui se détachait déjà des méthodes statistiques en se fondant sur la déformation élastique d'un masque de parties molles.

Dans un premier temps, et avant de pouvoir mettre en place toute reconstruction, il nous faut constituer une base de données 3D avec des crânes, des visages et des muscles masséters associés pour une même personne. La constitution de cette base se fait comme indiqué dans le chapitre 2 de cette thèse, cela nous permet de relier entre eux l'ensemble des éléments de la base (Figure 31).

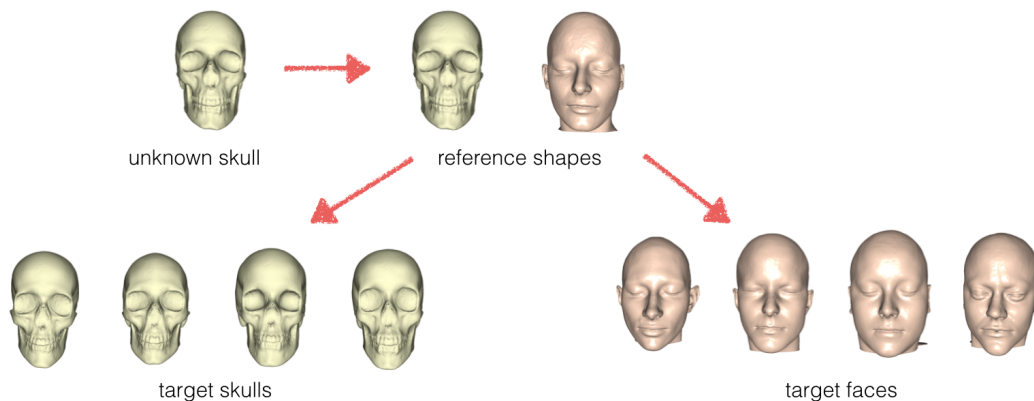


FIGURE 31 – Chaque crâne de la base est relié à un crâne de référence après l'étape du « morphing », et chaque visage au visage associé à ce crâne de référence, par la même méthode. Il en va de même pour les muscles, et ainsi chaque élément de notre base de données est relié. Image extraite de [35]

Une dernière étape est nécessaire avant de pouvoir faire la reconstruction d'un visage à partir d'un crâne inconnu, celle de créer, pour chaque couple crâne/visage de la base, un masque qui représente les tissus mous (Figure 32). C'est à partir de ces masques que la reconstruction d'un nouveau visage est générée. On applique la déformation élastique d'un crâne de la base, identifié comme proche du crâne inconnu, vers ce crâne inconnu, au masque de tissu mou associé au crâne de la base choisie.

Il est maintenant possible de mettre en place une reconstruction. A l'aide de la base réduite de

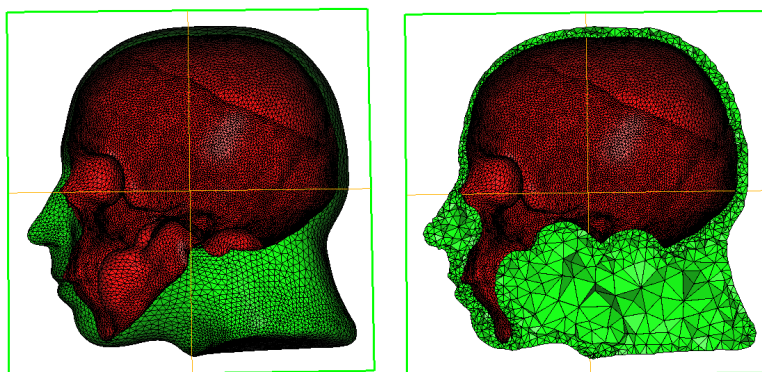


FIGURE 32 – Assemblage des deux surfaces crâne et visage d’un même individu (à gauche), maillage tétraédrique de l’espace entre le crâne et le visage, appelé masque (à droite).

forme 3D mise en place pour le muscle masséter, nous commençons par ajouter sur le crâne inconnu la reconstruction de ce muscle. Puis le crâne est fermé, à l’aide de la technique de « warping » décrit dans le chapitre 2 (Figure 33).

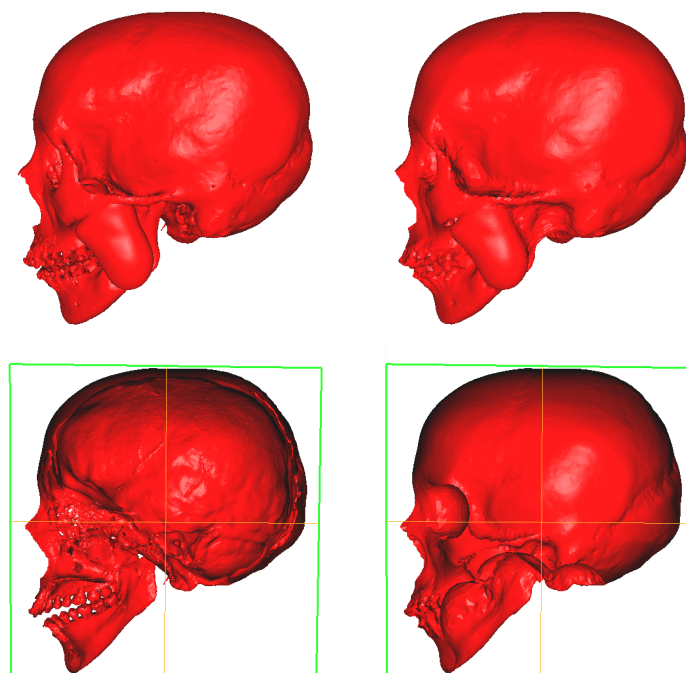


FIGURE 33 – Exemple de crânes avec masséters reconstruits (à gauche) puis fermés par warping (à droite), en dessous section médiale de ces mêmes crânes

Il faut garder à l’esprit qu’il est possible de mettre en place cette même méthode pour d’autres éléments du visage et que le muscle masséter est une première illustration de ce procédé.

Il ne reste plus que l’étape de déformation d’un masque de la base de données vers notre crâne inconnu, qui intègre déjà l’information supplémentaire contenue dans le muscle masséter. Nous obtenons ainsi un visage pour notre crâne inconnu, Figure 34.

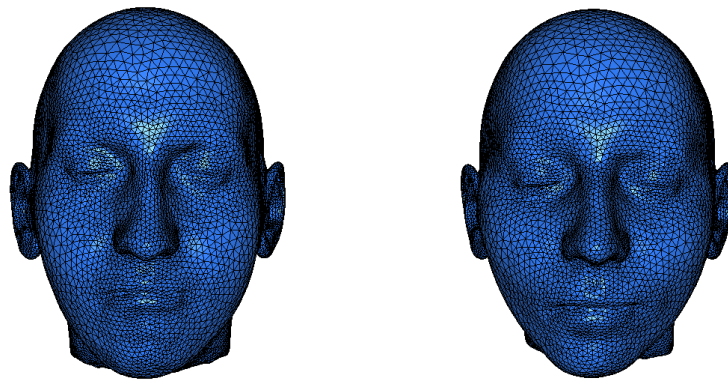


FIGURE 34 – Reconstruction d’un visage à partir de son crâne (à gauche), à comparer avec le vrai visage 3D (à droite).

Validation

Les méthodes de reconstruction faciale sont particulièrement difficiles à évaluer, à comparer et à valider. En effet, chaque équipe qui propose une solution à ce problème a travaillé sur un jeu de données restreint, souvent de provenance médicale, et qui n’a donc pas la possibilité d’être transféré à d’autres équipes pour comparaison. Qui plus est, l’objectif in fine des reconstructions faciales en médecine légale est la reconnaissance et l’identification d’une personne décédée. Il nous a donc paru important et intéressant de mettre en place une méthode de validation reproductible qui permette de comprendre et comparer ces méthodes.

Pour cela nous avons développé une application, permettant à des utilisateurs d’identifier à partir de deux photos d’un même individu (face et profil), le visage 3D qui leur paraît correspondre. Quatre types de tests sont proposés, à l’aveugle, où l’opérateur doit identifier à partir d’une photo :

1. des vrais visages segmentés en 3D,
2. des reconstructions effectuées avec la méthode de [35],
3. des reconstructions effectuées avec la méthode exposée précédemment mais où le vrai muscle masséter a été ajouté,
4. des reconstructions effectuées avec la méthode exposée précédemment avec le masséter reconstruit.

Une capture d’écran de l’application est visible Figure 11.

Annexes

Je présente dans ces annexes :

- la courte note, extraite du Chapitre 3 de cette thèse, publiée dans les Comptes Rendus Mathématique de l’Académie des Sciences, avec Damiano Lombardi et Yvon Maday,
- le « Read Me » (notice explicative) du logiciel de reconstruction faciale mis en place pendant ma thèse qui permet de rendre l’ensemble du processus totalement automatique,
- une application pratique de reconstruction faciale qui a permis des simulations en anthropologie, en collaboration avec Martin Friess.



Scientific context

Creation of the "FaciLe" project

The FaciLe project, supported by Sorbonne University and hosted by the Institute of Computational and Data Sciences, was created in 2014, with a team composed of forensic physicians, maxillofacial surgeons, anthropologists, mathematicians, and computer scientists, around a multi-disciplinary project : the reconstruction of a face from a dry skull with the aim, e. g., of identifying the deceased one.

The creation of this project occurred in the specific context of providing evidence in a particular case : the facial reconstruction of a New Caledonian Atai warrior leader, killed by French settlers in the 19th century, from his skull (Figure 35). The handing over of his skull to his native country, until then kept at the Musée de l'Homme in Paris, took place on 28 August 2014 [147]. The confirmation of the identity of the individual to whom this skull belonged, with the facial reconstruction process, had then aroused strong interest from the scientific community.



FIGURE 35 – Two representations of Atai (a) an engraving and (b) a casting of his face

Since then, a senior chair (Fabrice Déméter, anthropologue, in 2014, and then Peter Deuffhard,

mathematician, in 2015), a junior chair (Maya de Buhan, mathematician, 2014-2015) and two thesis (Chiara Nardoni [158], and that very one) have been initiated, alongside a partnership involving stakeholders from the different disciplines involved on this topic.

Facial Reconstruction

Facial reconstruction is a process that consists of reconstructing the face of a person to be identified, based solely on his dry skull, in the context of a judicial inquiry for example.

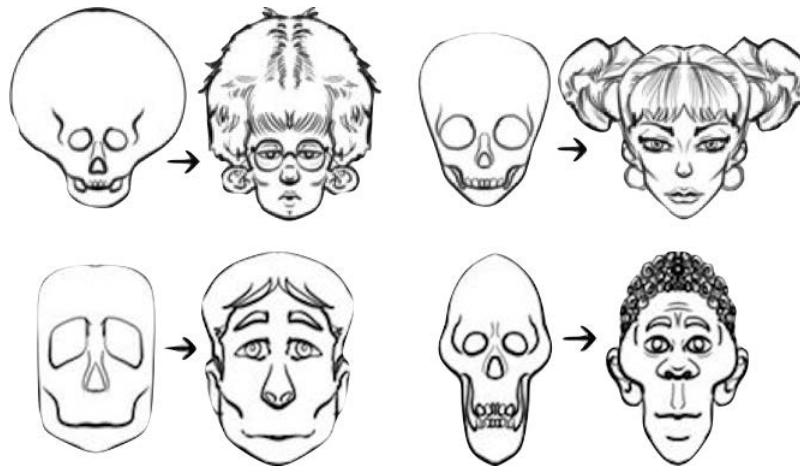


FIGURE 36 – Facial reconstruction definition

This is an extremely specific application but it can lead to a large number of breakthroughs in different fields : anthropology, to refine research about knowing and understanding the face's shapes of other members of the human lineage, forensic medicine, to identify human remains in the context of an investigation, or maxillofacial surgery, to assist clinicians in their practices through computer-assisted operation planning.

A brief history

First of all, it is important to underline, that this problem is not well posed : indeed, a skull shape does not correspond to a single face. Different parameters, such as age and sex, are difficult to determine with certainty and provide initial variability in the result. Other factors, such as stature, are simply not information that can be found on the bones of the skull.

Despite this, the strong correlation between the face and the skull has been known for several thousand years [111]. However, facial reconstruction only emerged as a common method in forensic identification situations in the 19th century, bringing with it a flood of ethical issues, questioning the reliability of the methods used [252]. The traditional techniques developed during this period were based on manual procedures, two-dimensional portraits or three-dimensional casts, carried out by artists who were experts in facial anatomy. The result was then very much linked to the artist's skills and subjectivity.

More recently, with the rise of computers and medical imaging, many digital methods have also emerged, with the aim of eliminating the inherent subjectivity of the methods mentioned above and taking advantage of the opportunity to test several hypotheses quickly. Currently most of these methods use the statistical study of observations from a dataset with a skull and its associated face. The observations taken into consideration are most often based on measurements made at anthropological points known for their evolutionary constancy, called landmarks [30]. These measurements can, for example, characterize soft tissue thicknesses, or other markers describing the variability of these tissues [44, 252]. However, although the identification of these landmarks is made possible by an expert, their geometric properties are unclear and do not allow them to be automatically

identified via a computer.

The FaciLe project differs from these methods in two main ways :

- by basing the proposed approach to three-dimensional facial reconstruction not on statistics but on a deterministic method, using partial differential equations (PDEs), numerical analysis and 3D geometric modelling.
- by making the entire process completely automatic and without human intervention, after the acquisition of skull data.

Main objective of this thesis

The theme of facial reconstruction is the common thread of this thesis, which describes the whole scientific process : from data acquisition and processing to results in the forensic sciences. The goal is to develop a method complementary to the one developed in Chiara Nardoni's thesis [158], enhancing the overall project, while providing anatomical details in the process. Various problems relating to this new methodology were raised, causing parallel studies to be carried out during this work. These include, for example, the complete automation of the process, or the segmentation of soft tissue in medical images.

Scientific approach : an application of mathematics

Applied mathematics, a branch of mathematics, focuses on the study and application of models to other disciplines, such as physics, chemistry, biology, economics, or medicine. However, they include a large number of sub-domains, partly independent of the applications themselves, such as numerical analysis, control, optimization, game theory and probability.

It is in this vast field that this thesis of applied mathematics dedicated to three-dimensional facial reconstruction for forensic medicine is part of. Different aspects of the problem will lead us to use various mathematical tools, such as differential equations, dimensionality reduction, finite elements...

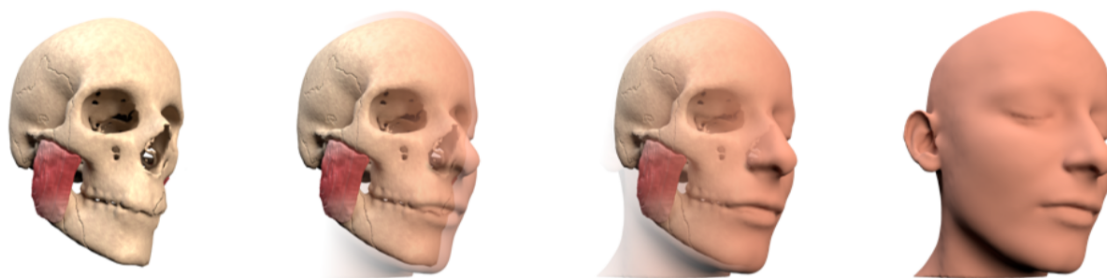


FIGURE 37 – Three-dimensional facial reconstruction

Modeling and face

A model

One of the first steps in applied mathematics is the modelling of the problem posed. Modelling here refers to the entire process by which mathematics can be used in an experiment-based or observational science to explain, describe or predict a phenomenon. A mathematical model is therefore the identification of ad'hoc quantities that describe well the state under investigation and a set of equation on theses quantites in order to apply mathematical tools, techniques and theories to those.

The first step is therefore to identify the problem, the question you are asking yourself or the object you want to describe. In order to be able to carry out the mathematical translation of the hypotheses put forward following this question, and thus to build our model.

In our case, the question is as follows : How to reconstruct an individual's face from the sole knowledge of his skull, for the purpose of legal identification ? We assume that a skull and a face can be defined as three-dimensional shapes. They will therefore be described throughout the manuscript by three-dimensional meshes (see an example Figure 38).

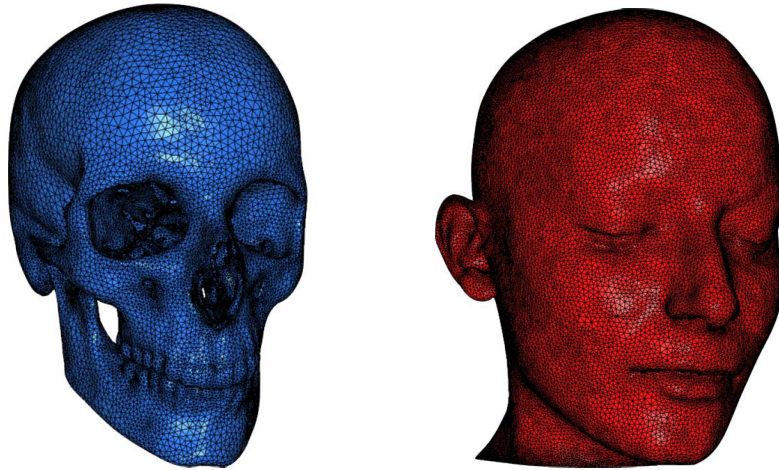


FIGURE 38 – 3D surfacic mesh (a) of a skull and (b) of a face

Elasticity

The first project of the FaciLe group consisted in considering a new object name « mask » as the volume mesh between the surfacic meshes of the skull and the associated face, representing soft tissues for each individual in our database (Figure 39). Then when a new skull is introduced, to reconstruct its face from the elastic deformation of one of the masks from the database to this skull [35].

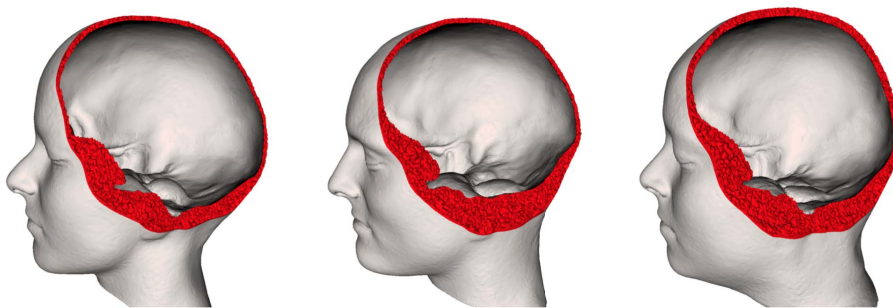


FIGURE 39 – Three examples of masks, from [158]

This elastic deformation is a method of « shape matching » or « morphing » consisting, for a couple of given 'starting' and 'target' shape, Ω_0 and Ω_T , in $\mathbb{R}^d (d = 2, 3)$, to figure out a way to convert Ω_0 into Ω_T . This type of method plays an important role in geometric modelling and shape analysis applications [244]. Many researchers from the mathematical and computer graphics communities have been interested in it [13, 21, 22, 67, 130, 193]. Such a deformation can be used to measure how different the two shapes are or simply to accomplish the transformation from

one shape to another. Here we measure the difference between the 'starting' and 'target' shapes according to the following functional shape :

$$J(\Omega) = \int_{\Omega} d_{\Omega_T}(x) dx,$$

involving the signed distance function d_{Ω_T} to $\partial\Omega_T$. The signed distance function is a « level set » function of a domain : which for each point x of the space returns the Euclidean distance $d(x, \partial\Omega_T)$ to the edge $\partial\Omega_T$, the sign associated with this distance is positive if the point is located inside the domain, negative if not. The overall « mapping » between Ω_0 and Ω_T is obtained by an iterative process that minimizes $J(\mathcal{E}(\Omega_0))$ (with \mathcal{E} the elastic deformation), inferring at each step a direction of descent, via a gradient algorithm, for the functional J . The optimal conditions associated with this shape optimization problem are calculated using the Hadamard shape derivative framework [3, 41, 96]. In practice, the permissible deformation space is restricted by elastic displacement parameterization. The elasticity equations were implemented using the finite element method.

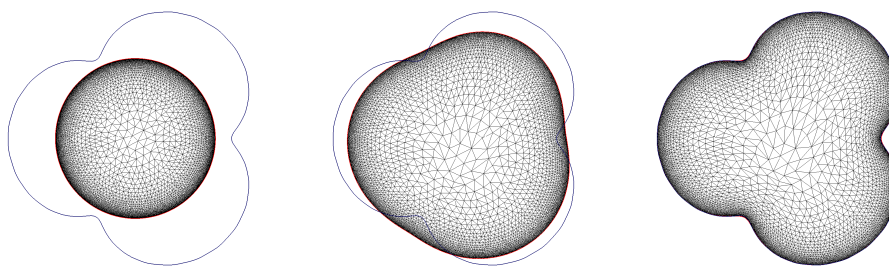


FIGURE 40 – Simple 2D morphing example

This first phase of the work was mainly carried out by Chiara Nardoni's thesis [158], supervised by Maya de Buhan and Pascal Frey. We have carried out some of these studies together with her : particularly the so-called boundary morphing and its comparison with the so-called volumic morphing (detailed in Chapter 6). At the end of this thesis, I have developed a complementary method presented below (and detailed in Chapter 7), focussing on the main aim of this thesis the facial reconstruction.

Anatomy of the Face

However, this elastic method does not take into account the underlying anatomy of the face, and therefore, more precisely, the functional components of the soft tissue mask mentioned above. Articles such as the one in [31], however, remind us of the importance of anatomical knowledge, accumulated in various disciplines, on the face and of which the field of facial reconstruction takes little account and in a non systematic way. We therefore turned to our anthropological and surgical colleagues involved in the project to improve this first model, taking better into account the anatomy of the face.

The masseter muscle

The face is mainly, in terms of volume, made up of muscles and fat, covered with skin. Since fat is a component for which there is no information on the skull, it was decided to consider it at the end of the process as a variable to be adjusted once the shape of the face has been identified.

On the other hand, it is easy to identify up to 100 muscles on a face. Two of them, larger than the others, caught our attention : the masseter muscle (Figure 41 number 1) and the temporal muscle (Figure 41 number 2).

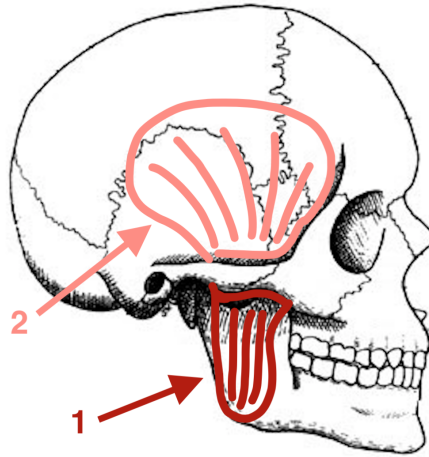


FIGURE 41 – Anatomical situation (1) of the masseter muscle, (2) of the temporal muscle

Due to its respective functional and morphological importance, we have decided to focus more specifically on the masseter because of its impact on the shape of the face. As can be seen in Figure 41, the masseter muscle is located at the cheek, in front of the ear, along the branch of the mandible. While the temporal muscle, which is located at the temples, above the zygomatic arch, is often thinner and covered by the hair, thus having a less significant impact on our problem at first.

Database and reduction of dimensionality

We then need to create a model of this masseter muscle. In order to best describe it, as simply as possible, we use a method of complexity reduction, a principal component analysis (PCA). Describing the shape of the masseter no longer requires the 5,000 3D coordinates of the points that constituted its mesh, but only $n = 5$ to 20 well chosen coefficients, depending on the desired level of precision (Figure 42) :

$$\sum_{j=1}^n \alpha_j^k \phi_j, \text{ with } \alpha \text{ coefficient applying to the } j\text{-ième principale component } \phi,$$

for a given individual k .

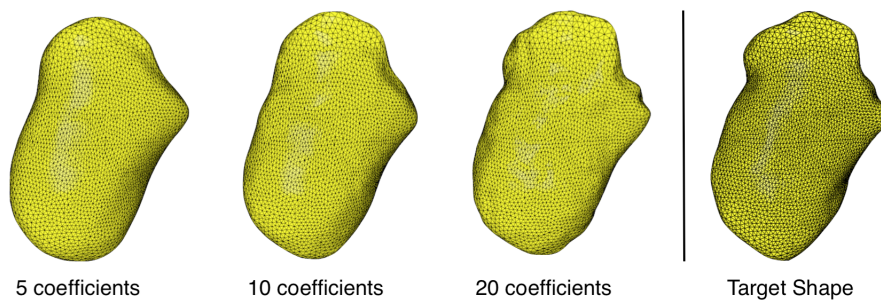


FIGURE 42 – Reconstruction of a masseter muscle via PCA with 5 coefficients, 10, and 20, facing the real muscle

Once the reconstruction of the masseter (and possibly, of the temporal) has been completed, the elastic deformation method exposed in the previous section is applied, this time not from a skull/face mask but from a skull+muscles/face mask. This incorporates more precise information into this process, taking into account anatomy, and emphasizing the link between form and function, the founding idea of this thesis.

Data acquisition

All the work presented above was made possible thanks to the implementation of a database combining skull, face and muscles for the same individual as mentioned above. This database consists of 3D medical images that allow the extraction of all the information necessary for the application of this method. All the scanner data collected to create this shape database comes from the Maxillo-Facial Surgery department of La Pitié Salpêtrière Hospital in Paris. This database does not in any way overlap with the one used by Chiara Nardoni before me, who had obtained her data from another project, with no academic link to the FaciLe project, on the facial reconstruction carried out by Françoise Tilotta and Yves Rozenholc [225, 226]. Indeed it seemed more relevant to this phase of the FaciLe project to build our own database.

CT-scan : precision and difficulties

The choice of the type of imaging is not insignificant. Indeed, although MRI has a better precision for soft tissue, the input to our problem is the skull alone. The best 3D imaging to precisely visualize bones is currently the CT scanner, an example of which can be seen in Figure 43.

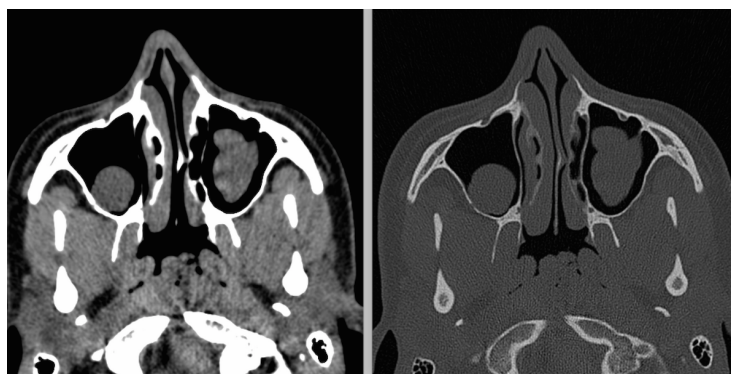


FIGURE 43 – Scanner images (a) "soft tissue" acquisition window, and (b) "bone" acquisition window

Despite the advantages associated with all the information known by scanner images, it should be kept in mind that many problems inherent to images affect the acquisition and visualization of data in three dimensions, as is the case with artifacts created by the metal used to treat teeth (brackets, crowns...).

In addition to these difficulties, some constraints, this time coming from the model, further complicate the pre-processing of the data, for example : not taking the spine into account in our 3D skull model.

Semi-automatic Segmentation

Segmentation is the identification on images of voxels (three-dimensional pixels) belonging to the same object of interest. In our case three objects : the skull, the face and the masseter muscle.

Segmentation of the skull and face can be done quickly using grey levels. Indeed, it is easy to automatically segment elements that have a high contrast. The results shown in Figure 44 (a) and (b)



FIGURE 44 – Segmentation (a) of the skull, (b) of the face, and (c) of the masseter muscles

are then obtained. The delimitation of soft tissues is more delicate : Figure 44 (c), which shows the segmentation of an individual's right and left masseter muscles, could not be obtained automatically. They had to be delimited manually, unfortunately, this procedure is extremely time-consuming.

This problem of segmentation of medical images is found in many research fields, which need to use 3D organ databases as a prerequisite. A main limitation is the time devoted to the acquisition of data, which is therefore obtained in limited quantities, and which limits the quality of the results presented in these various studies. It is in this context, where the limitation of data has compromised our results, that we have proposed and developed a semi-automatic segmentation application for soft tissues. Using the reduced basis described above, we know a priori the shape of the object to be identified on the images, in our case the masseter muscle. It is only necessary to identify the coefficients associated with the object of interest, via the resolution of a system taking as input the coordinates of a few points selected on the image $\xi_*^{(j)}$, $j = 1, \dots, m$, with m the number of selected points :

$$\mathbf{x}^{(j)} = \xi_*^{(j)} + \sum_{i=1}^n \alpha_i \varphi_i(\xi_*^{(j)}), \quad j = 1, \dots, m.$$

This method is independent of the grayscale of the image, and can therefore be applied to all objects and images.

Validation of the methods developed

All the methods presented have been validated from a mathematical point of view. We also have set up experimental validations, in order to certify their practical effectiveness in the disciplines where they are to be used.

Reconstruction and Forensic Medicine

For the reconstruction of a face from a skull, the easiest way to certify that the method is successful is to check if an individual is able to recognize this face. This is why we have set up a survey application : a user to whom a photo is presented must choose among 5 proposals, the face, described by a surface mesh, which seems to him to be the one of the person in the photo (Figure 45).

This operation is performed in double blind and randomized for 4 categories : the 3D surface of the true face directly segmented, the 3D surface of the simple elastic reconstruction, the 3D surface of the reconstruction with the directly segmented masseter and the 3D surface of the reconstruction with the reconstructed masseter itself.

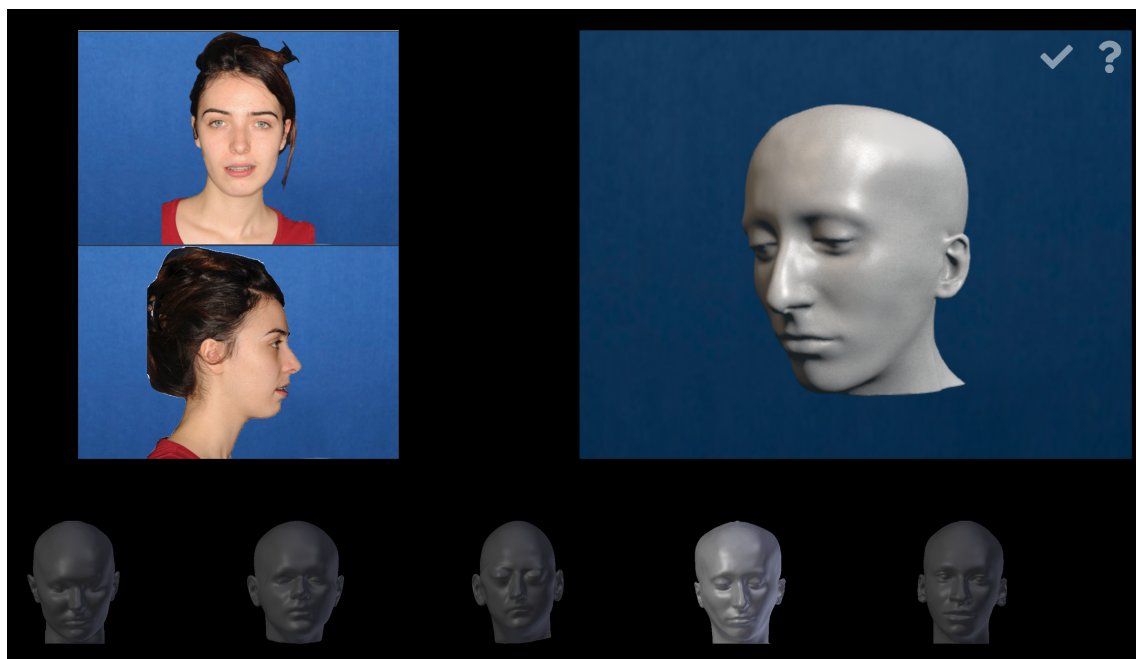


FIGURE 45 – Facial reconstruction validation application

This application therefore allows to compare the results of different methods on the same dataset. Indeed, the data used in facial reconstruction are often extracted from medical data that are not transferable to other teams, limiting possible comparisons on the methods themselves.

Segmentation

In the case of semi-automatic segmentation, the application developed for this purpose being the use by clinicians or researchers, we have set up a study to compare the time and error of segmentation with this method against the manual segmentation of two practitioners.

Manual segmentation requires accuracy on all scanner sections where the masseter is located, while semi-automatic segmentation requires only about 50 points to be identified, as shown in Figure 46.

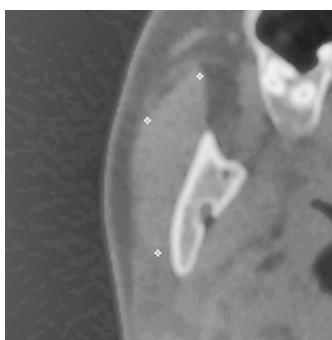


FIGURE 46 – Points identification at the edge of the masseter with semi-automatic segmentation application

Main Contributions

The main contributions of this thesis are :

- Management of a reduced 3D shapes database fully automatic,

- A new anatomical method of facial reconstruction,
- A tool for validating and comparing reconstruction methods,
- A semi-automatic segmentation method.

Summary and state of the art

This manuscript is divided into 3 distinct parts, each composed of 2 to 3 articles submitted or in the process of being submitted. Below is a detailed description of each of these articles, as well as the state of the art and the results associated with it.

Part I - Preliminary Work

This first part includes preliminary work on the anatomical relationships between the skull and the masseter muscle, which allowed us to make the hypothesis that it is possible to deduce the shape of the masseter only according to that of the skull. And the work on the management of a reduced 3D shape base, which effectively allows us to propose the reconstructions of the masseter.

Correlation between cephalometry and muscle masseter

This work was conducted in collaboration with Adeline Kerbrat, Patrick Goudot and Thomas Schouman.

Bibliography

Cephalometry is the study of measurements taken on a skull. It allows in the clinic to detect and characterize, via medical imaging, anomalies present on the skull of certain patients. These measurements are linear or angular. They are performed between different anatomical landmarks identified on the skull. These landmarks are anatomical points that are easy to identify from one patient to another. In anthropology they are also called "landmarks". In Figure 47, we can visualize several frequently used examples.

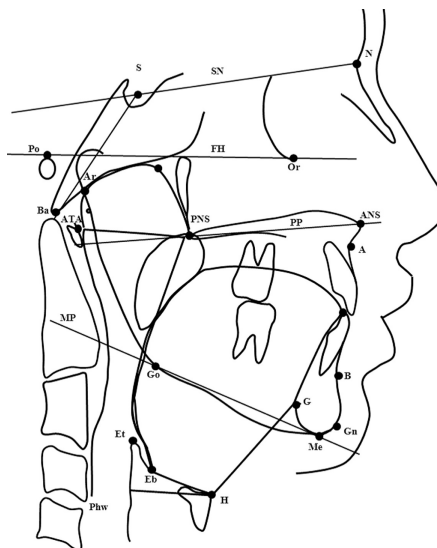


FIGURE 47 – Example of different cephalometric landmarks

Cephalometric studies in recent decades have made it possible to classify different phenotypes [195] of facial length [75] or dental classes [7, 107], which have helped clinicians better characterize and treat many conditions such as sleep apnea [135, 160], malocclusion [140, 194], or facial

malformations [73, 95, 162]...

The elevating muscles of the mandible, because of their insertions on the bones of the skull, and more particularly the mandible, are closely related to development and therefore to the shape of the skull. Of these muscles, the masseter muscle is one of the largest muscles on the face [260]. Its functional and volumetric importance gives it a particular interest in the eyes of doctors or anatomists. We were particularly interested, in the context of facial reconstruction, because of its impact on the shape of the face due to its location, behind the cheek. We can locate it at the end of the blue arrow in Figure 48.

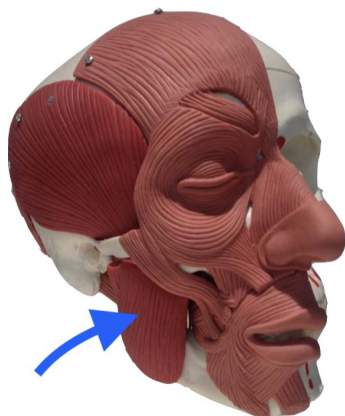


FIGURE 48 – 3D model of the skull and facial muscles, at the end of the blue arrow the muscle massage

The masseter muscle is short, thick and quadrilateral [29]. It is composed of 3 distinct parts, ordered in beams, which can be visualized in Figure 49 (picture of a dissection on the left and schema on the right) :

- a superficial beam of two layers, one internal and one external,
- a single-layer median beam,
- a deep beam separated into three different layers.

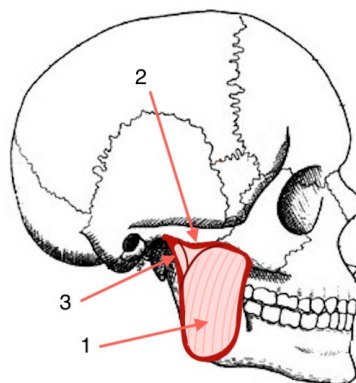
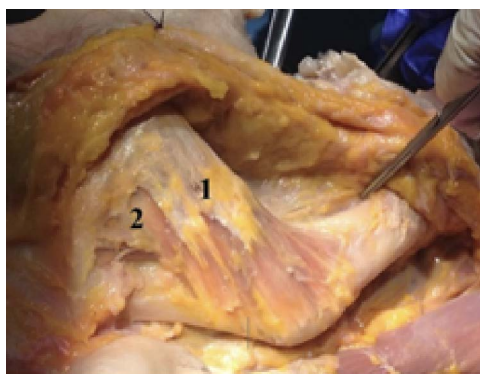


FIGURE 49 – The beams of the (1) superficial (2) medium, and (3) deep masseter muscle

Our study and its results

This study seeks to highlight the morphological link between measurements on the skull and those on the masseter in dysmorphic patients. We already find this idea in the literature with [12],

however our approach aims to complete their results by focusing on more varied morphologies and measures that are often undervalued.

Within the framework of this work and among the very numerous cephalometric measurements that exist, we have selected five that best complement the existing literature on the subject [10, 12, 31, 56]. These are the angles SNA, SNB, ANB, ANB, FMA and between the Bispinal and Mandibular plane, which can be seen in Figure 50.

As for the measurements taken on the masseter, the community agrees that the most appropriate parameters to describe it are its height, width, thickness and volume [31].

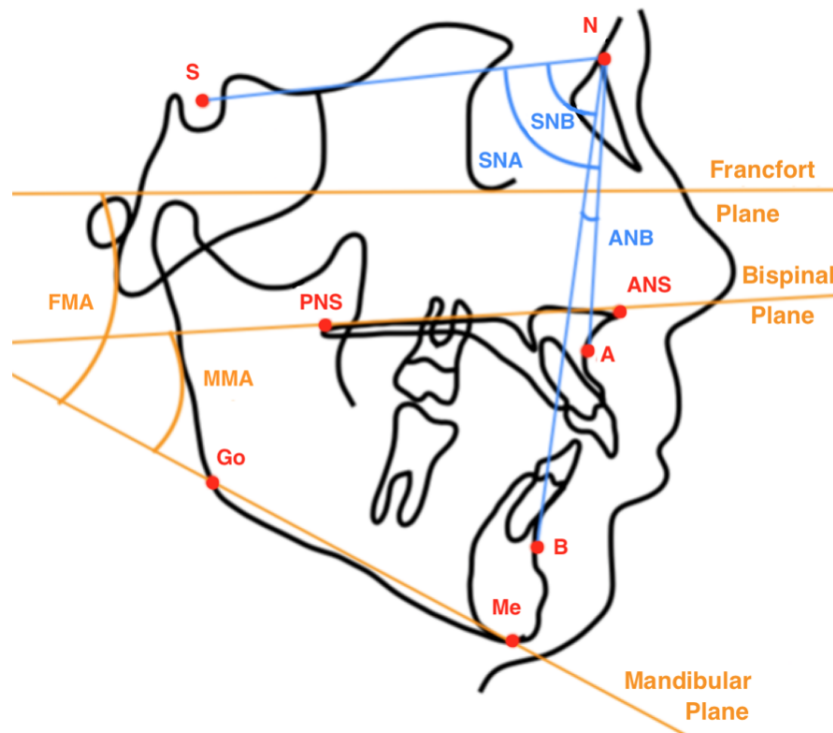


FIGURE 50 – The cephalometric measurements we used for our study

The study was conducted on 51 patients in the maxillofacial surgery department of La Pitié Salpêtrière Hospital in Paris. We have identified significant correlation between the shape of the skull and the shape of the masseter muscle.

In our study, the FMA is the bone angle measurement parameter, which is more correlated with masseter measurements. Indeed, it is inversely correlated to the 4 masseter measurements tested (height, width, thickness and volume). This means that a long, wide, thick and voluminous masseter muscle is associated with a phenotype called « short face » with a closed mandibular angle. This result is similar to those found in [12, 56, 116].

However, few studies address this problem according to the anterior posterior position of the maxilla, here we show a correlation of the SNA with the thickness and volume of the masseter and the SNB with its height and volume, unlike [125].

Because of the presence of these significant correlations, these conclusions have therefore allowed us to hypothesize, for our facial reconstruction method, that it would be possible to deduce the shape of the masseter muscle from the skull bones.

Engineering process of building a reduced base of 3D shapes

This work was conducted in collaboration with Yvon Maday and Chiara Nardoni.

This is a complete methodology for processing a 3D shape database. All the mathematical methods used have already been individually presented in the literature. However, they are here assembled and adjusted to meet the characteristics of our applications : facial reconstruction and semi-automatic segmentation. However, it is entirely possible to use the same process for processing and managing a reduced 3D database, for different purposes and applications such as video games, molecular biology, etc.

The steps involved

Several steps using various mathematical tools are necessary in order to be able to use our 3D shape database.

1. *Data acquisition* : in our context, it is the segmentation of medical images. The second part of this manuscript is entirely devoted to this thorny problem. The bibliography and presentation of the methods implemented are proposed in the following section. All the scanner data collected to create this shape database comes from the Maxillo-Facial Surgery department of La Pitié Salpêtrière Hospital in Paris. They were acquired with two types of windows : soft tissue and bone (Figure 51).

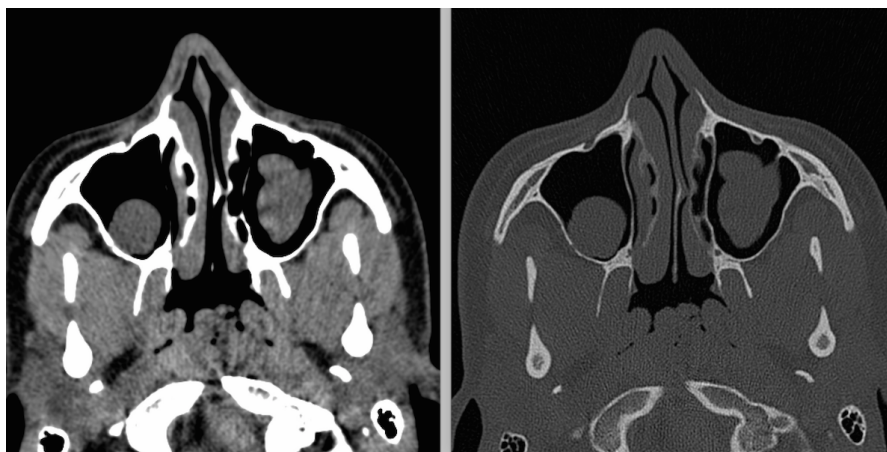


FIGURE 51 – The two scanner image acquisition windows (a) soft tissue, and (b) bone

2. *3D mesh of objects* : moving from segmented medical image sections to a three-dimensional mesh requires the implementation of an isosurface extraction algorithm [32] such as the « Marching Cube », first introduced by [134]. The latter allows to create a surface triangulation from a volume of voxels (3D pixels), however they are also known to leave artifacts and invalid elements in the mesh for finite element simulations. It is therefore necessary to add a remeshing step, allowing to find a correct geometry and to control the quality of the desired mesh size. For that we used *mmg* [50, 57], which allows us to control the Hausdorff distance between the input mesh and the output mesh, as well as other parameters such as the maximum and minimum length of the edges of the mesh triangles. The result of the Marching Cube algorithm and the remeshing algorithm is given in Figure 52.
3. *Alignment* : often underestimated, the coherent alignment of database objects can have a strong impact on the rest of the process. Indeed, if the data are acquired from several sources

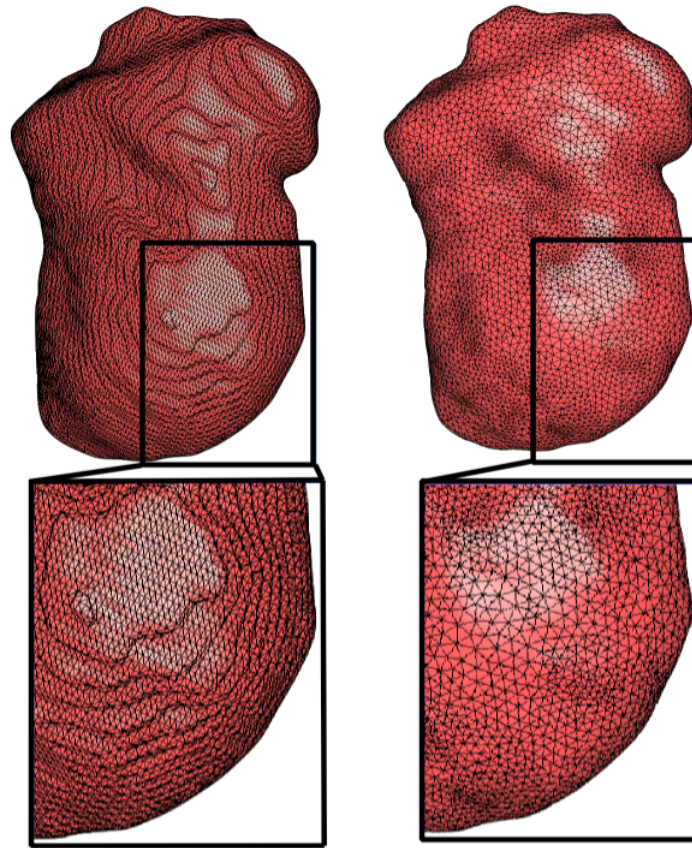


FIGURE 52 – Mesh of a masseter muscle after the marching cube algorithm on the left and after remeshing on the right

that do not have the same acquisition parameters, the objects may differ from only a rigid movement and/or homothety. It is therefore necessary to correct the translations, rotations and homoteties that affect the data. The first phase consists in centering the objects Ω in the origin of the reference system using the calculation of their respective barycenter x^G defined by :

$$x^G = \frac{1}{|\Omega|} \int_{\Omega} \vec{x} d\vec{x}$$

with $\vec{x} \in \Omega$ and $|\Omega|$ the volume of Ω . After discretization on the mesh of the object (detailed in chapter 2, page 49) :

$$x^G = \frac{1}{2|\Omega|} \sum_i x_i^2 n_i d\sigma_i$$

with n the external normal on the surface of the object Ω .

If necessary, this is when a scaling can be done. During the second phase, we calculate the axes of inertia to be able to align them with those of a reference object, using the inertia matrix I_{Ω} :

$$I_{\Omega} = \int_{\Omega} (|\vec{x}|^2 Id - \vec{x} \otimes \vec{x}) d\vec{x}$$

with Id the identity matrix, and $\vec{x} \otimes \vec{x}$ the matrix $\vec{x} \cdot \vec{x}^T$. These two steps allow to identify all the objects in Figure 53 as identical in shape, if the axes of inertia are aligned and the meshes are compared.

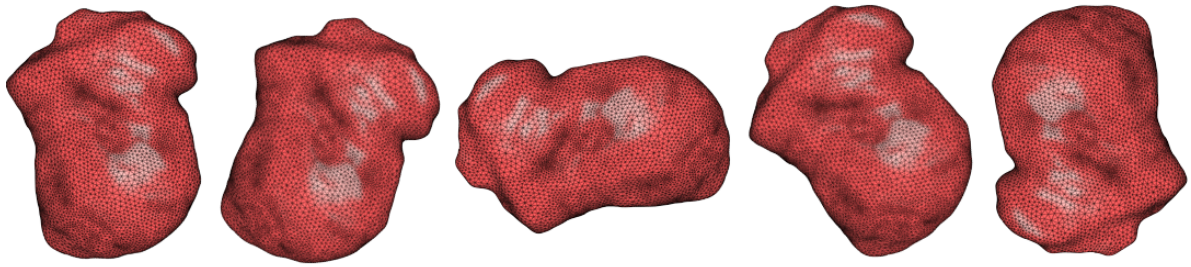


FIGURE 53 – Five masseter muscles identical with the exception of a rigid movement

It is important to note that our method is particularly attentive not to select specific points to be mapped, even for alignment, because we wanted a fully automatic process. This is made possible by the method described above combined with steps 4 and 5 (warping and morphing) described below.

4. *Warping* (optional) : This step is only necessary when the object to be created as a reduced shape base is not topologically closed. The algorithm which consists in using the elasticity equations to deform a closed template mesh on an open object, was developed in [158]. The main idea is presented in Figure 54.

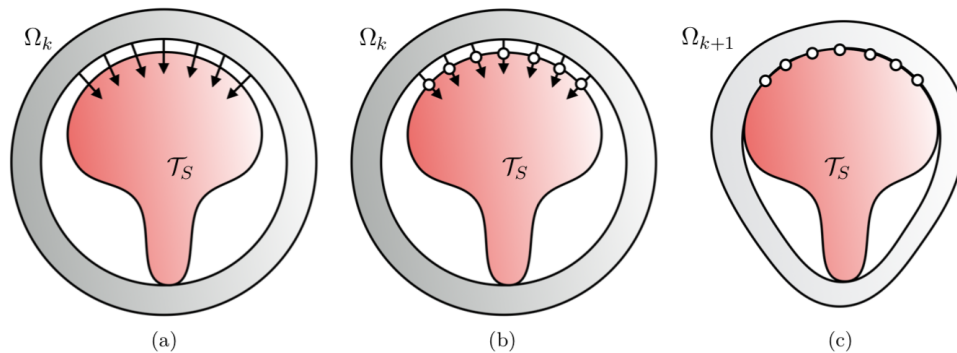


FIGURE 54 – Schematic description of the warping algorithm : (a) Computation of the displacement field (black arrow) on the template Ω_k (in grey) surrounding the source model (in red), (b) Identification of the intersection points between the displacement field and the source model (white points), and (c) Update of the shape according to the calculated displacement. Schema from [158].

5. *Morphing* : The idea of this step is to deform a reference form Ω_0 , in our case an ellipsoid, into an objective form Ω_k , here each muscle masseter from our database. This allows us to consider all the objects in the database as u_k displacements of the same reference mesh, which makes any comparison between them much easier to set up. It also eliminates the need to match landmarks, to label on all objects in the database. A complete chapter of this thesis is dedicated to the detailed explanation of this method and its bibliography in the third part.
6. *Reduction dimension* : In order to extract the main information from our database, and to best represent the shapes it contains as simply as possible, we perform a reduction dimension : a principal component analysis (PCA) or a greedy algorithm. For this purpose we calculate the modes that allow us to represent all the elements of the database by a few coefficients.

We can then represent each object by a linear combination such as $u_n = \sum_{\ell=1}^n \alpha_\ell^k P_\ell$, with P_ℓ the modes. You can view the P_ℓ for the PCA with ℓ between 1 and 5, on Figure 55.

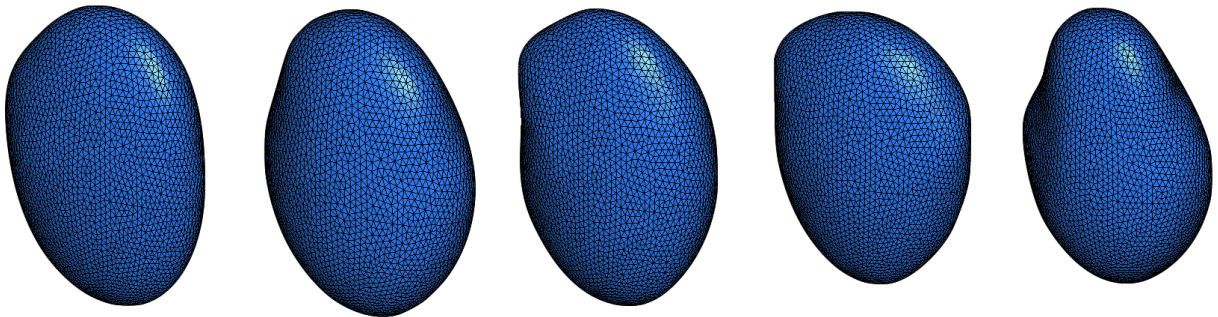


FIGURE 55 – The first 5 main components of our database that allows us to rebuild a new muscle masseter

7. *Machine Learning* : muscle reconstruction based on anthropological measurements is possible, by learning, via neural network algorithms, the PCA coefficients associated with these measurements. However, we have encountered here the lack of data on segmented masseter muscles, because their acquisition is time-consuming. This is what motivated the work undertaken on semi-automatic segmentation during my thesis, presented in Part II.
8. *Applications* : many applications using this reduced shape base can be developed. Here we have developed an anatomical atlas for the masseter muscle, face and skull, which has been used to create algorithms for image segmentation and facial reconstruction. These points are the subject of the following two parts of this thesis.

Part II - Data Acquisition and Processing - Segmentation

In this second part, we focus on data acquisition and therefore segmentation, more specifically of soft tissues, such as masseter muscle on scanner images, which has been an issue during our work on facial reconstruction. Indeed, to be able to reconstruct the muscles, then the face, from the skull, we had to build a database of 3D shapes using the method presented above (Part I - Chapter 2). The first step of this method is the acquisition of data, the segmentation of medical images. So we tried to set up a semi-automatic method that allowed us to speed up the process without increasing the error. Allowing us to overcome two main difficulties in soft tissue segmentation : the impossibility of relying solely on grey levels and the impossibility of properly discerning on the CT-Scan image, even for an expert, muscle insertion (on the zygomatic arch in the case of the masseter muscle).

This section is divided into three chapters, which focus on the common topic of soft tissue segmentation. The first is a brief proof of concept in 2D and in 3D, the second is the development of this method in detail in the specific case of the masseter muscle, and the last is a practical application that compares the current reference method, manual segmentation, to our semi-automatic method developed in the two previous articles.

As the state of the art is closely linked for these three chapters, a common presentation is made below. The results of these three articles are then presented in sequence.

Bibliography

The segmentation of medical images consists in identifying and labelling the voxels (3D pixels) of the entire image or object of interest. In our case, we were interested in the muscle masseter in

the context of a specific application : facial reconstruction.

However, automatic or semi-automatic segmentation methods have a wider scope of application. For example, they are widely used in « computer-assisted diagnosis », which has become one of the main research topics in medical imaging and radiology [59, 60, 62, 70, 217] in recent decades. In the 1980s, the concept of automatic or computer-assisted diagnosis was already known from studies dating back to the 1960s : [19, 132, 150], but these first attempts were not a real success. Indeed, the automatic detection of organs or lesions has proven extremely difficult.

Nowadays, techniques are more and more numerous, partly thanks to the technological development of computers and acquisition methods. Some tissues, whose contrast with the neighbouring tissue is sufficiently important, such as bones, are easily detected automatically [115, 175, 262]. The same is true for the major organs of the human body and the pathologies associated with them, such as the brain and heart [16, 33, 196], which have always aroused great interest among carers. The common methods of use for these types of applications are the so-called thresholding or edge detection methods. The first consists in grouping in the same label the pixels which have a close grey level or more exactly contained by one or more threshold values [176]. The second, which also relies on the detection of grey levels, looks for the boundaries of anatomical regions by analyzing the rapid transitions of these levels, and assembles the homogeneous voxels into a single label [133]. These two methods are based on the detection of grey levels, which allows experts to differentiate two anatomical regions and perform manual segmentation [170]. This type of strategy, mimicking the knowledge of experts, is the first to be implemented. Different classifications of these methods exist, for example, we can quote [258].

However, more recently, other types of methods have gradually developed, such as deformable models, guided atlases or the massive use of machine learning. They differ, among other things, by the amount of knowledge a priori injected into the method [40].

Statistical atlases use as a reference one or more already segmented structures used as prior knowledge for new segmentations [105, 180]. The segmentation of a new image is then based on a registration and deformation that allows to define an optimal transformation between the atlas and the new image. Different types of algorithms exist to optimize the deformation [173, 223], or the use of the atlas itself [2, 45, 259]. These segmentation methods have proven effective in major segmentation competitions organized by « the American Association of Physicists in Medicine », or « the Medical Image Computing and Computer-Assisted Intervention Society ».

Deformable models require more information a priori. When the latter are available, characteristic variations in the interest structure shape can be used to statistical shape models. This limits the results obtained from segmentations to anatomically plausible shapes [94]. However, these methods are also less flexible for the reason mentioned above. In addition, the size and content of the training data also limits the performance of the results. However, this method is still frequently used for pelvic anatomical structures [72, 127, 187].

Statistical learning, applied to image segmentation, groups together a wide range of methods in full swing, such as machine vector support, decision trees, deep learning or neural networks [110]. These are already found in multiple applications such as tumor segmentation in the brain, or in the liver, etc. [126, 143, 151, 183]. The results obtained by these algorithms are promising for the applications for which they are developed. But it is not always obvious to extend them to all types of images and often requires a large dataset in view of the human variability underlying the medical data [110].

The method we propose is based more on these last techniques and borrows some tools from each of them, to combine them in order to achieve our objective. It is comparable to [25], but with a deterministic view of the problem, and a practical application in real cases of segmentation by practitioners. Indeed, most often segmentation methods are developed for a specific purpose, and it

is important to note that there is, at least for the moment, no universal segmentation method. Each algorithm responds to a unique set of constraints and objectives, making the method implemented particularly interesting for a specific application and sometimes less so for others.

The more specific objectives that we have set for the framework of this work are :

- a fast method,
- suitable for clinicians,
- more specifically for the segmentation of soft tissues, such as muscles,
- and whose limits are sometimes difficult to perceive on a scanner.

We have limited ourselves here to explore the main existing methods, however for more details, it is possible to refer to [62, 94, 105, 131].

Introduction of the concept

This work was conducted in collaboration with Damiano Lombardi and Yvon Maday. The brief article that is extracted from this work is presented in appence A.

We present here a model-based semi-automatic medical imaging segmentation method, minimizing the intervention of an expert. Using a reduced basis of 3D shapes (constituted according to the method described in the previous chapter, and therefore represented as elastic deformations), we can approximate the shape of the object to be identified on the images, like a muscle on a scanner. It is enough to identify the coefficients associated with the object of interest, via the resolution of a linear system taking as input the coordinates of some selected points on the image. This method is independent of the grayscale of the image, and can therefore be applied to any object and any image.

Let $E \subset \mathbb{R}^3$ be our reference shape, ξ a point of E and $x \in F \subset \mathbb{R}^3$ with F the boundary of the segmented object. We can extract from the PCA of all the objects in our database, represented by displacements u of the reference shape on these objects, the modes ϕ_i . We then obtain :

$$u \approx u_n = \sum_{i=1}^n \alpha_i \phi_i.$$

We select a certain number of points $x^{(j)}$ on our image, and we can then write that :

$$\mathbf{x}^{(j)} = \xi_*^{(j)} + \sum_{i=1}^n \alpha_i \phi_i(\xi_*^{(j)}), \quad j = 1, \dots, m.$$

By choosing the *boldsymbol* $\xi_*^{(j)}$ such that they are the closest points of E to $x^{(j)}$, we obtain the following linear system to solve :

$$\begin{cases} \Phi \alpha & = d, \\ \Phi_{jik} & = \phi_{i,k}(\xi_*^{(j)}), \\ d_{j,k} & = \mathbf{x}_k^{(j)} - \xi_{*k}^{(j)}, \end{cases} \quad (4)$$

An example implemented in 2D is proposed Figure 56. To the left of the figure, we can see the reference shape that is transported to different target shapes, thus constituting our database of 3D shapes represented by displacement fields. On the right, is the reconstruction (in red) of an image randomly generated (in blue) by the resolution of a linear system, allowing us to identify the coefficients of our reduced base.

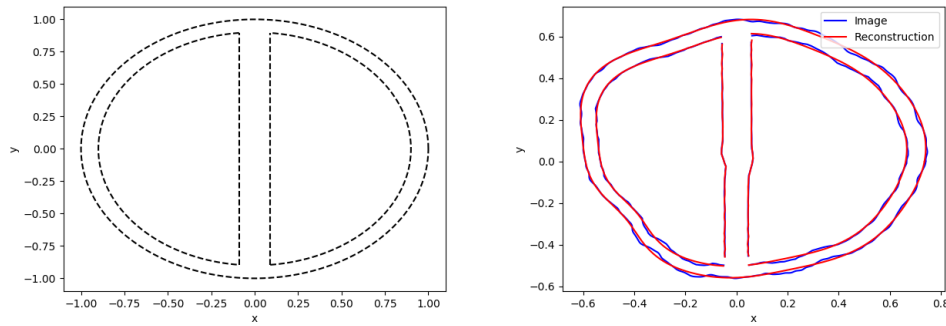


FIGURE 56 – Template undeformed on the left and deformation and reconstruction on the right

In order to test our 3D concept, briefly explained in the previous 2D section, we decided to use the following parameterization, applied to spherical harmonics, to create 100 3D shapes as a basis for reconstruction :

$$\begin{cases} a_k^{Real} = \frac{\sqrt{\mu_3}}{(l+1)^\beta} \cos(2\pi\kappa\sqrt{\mu_1}) \cos(2\pi\kappa\sqrt{\mu_2}) \\ a_k^{Imag} = \frac{\sqrt{\mu_3}}{(l+1)^\beta} \sin(2\pi\kappa\sqrt{\mu_1}) \sin(2\pi\kappa\sqrt{\mu_2}) \end{cases}$$

with $(\mu_1, \mu_2, \mu_3) \in [0, 1]^3$, $\beta = 1.5$, and $\kappa = l(m+1)$.

A simple graph, Figure 57, is sufficient to see the utility of this parameterization on the decay of eigenvalues after the PCA, compared to an PCA made directly on spherical harmonics.

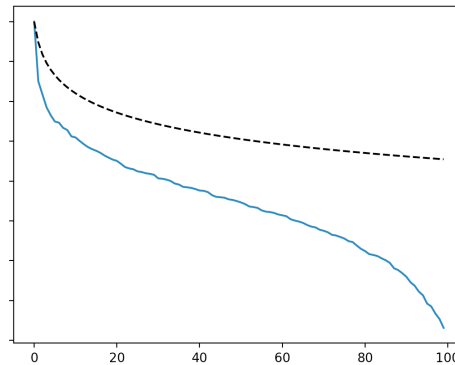


FIGURE 57 – Decrease of eigenvalues after PCA, with (in blue) and without (in black) parameterization

A certain number of points are randomly selected on a new shape, randomly generated using spherical harmonics, which we wish to reconstruct. After resolution of the linear system 4 allowing to identify the coefficients α of the PCA : it is possible to reconstruct by the linear combination of these coefficients and the PCA modes, the shape of the interest. We can then compare the error made between our reconstruction and the real form, to the projection error due to the fact that we only use a limited number of modes and that we therefore make an approximation. In this context, the two errors found are of the same order of magnitude and differ little.

Application to masseter muscle segmentation

This work, still in progress, was conducted in collaboration with Damiano Lombardi and Yvon Maday.

This time, the reduced basis of 3D shapes used is that of masseter muscles generated using section 2 of Part I. The idea is that the masseters are not random shapes (as in the previous case without parametrisation mentioned above), they are part of the masseter muscle family which has a small Kolmogorov dimension (as in the parametric case).

1. *Selection of points* : The first step is the selection of points on the scanner images at the muscle boundary (Figure 58).

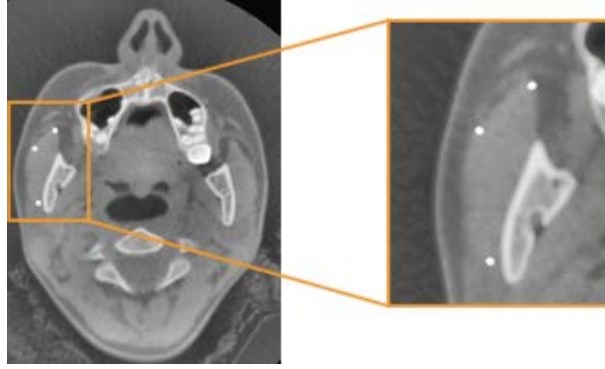


FIGURE 58 – Selection of points at the muscle masseter boundary

2. A **coordinate change** from dicom images to our reduced basis space $[0, 1]^3$. An affine transformation is built, such that :

$$\mathcal{X} : \begin{cases} \Omega_m \rightarrow [0, 1]^3 \\ x \mapsto \xi. \end{cases} \quad (5)$$

We have $\xi = \mathcal{X}(x)$, and, since the transformation is invertible, $x = \mathcal{X}^{-1}(\xi)$.

The points are transported into $[0, 1]^3$, that we call the reference configuration, where the modes are defined and where the reconstruction takes place.

3. The **reconstruction** of the 3D masseter from the selected points, i.e. the identification of the best coefficient a to fit those points in our reduced basis.

By exploiting the points, a mesh consisting of $\mathcal{N} \in \mathbb{N}^*$ degrees of freedom is reconstructed : $v^{(i)}, i = 1, \dots, \mathcal{N}$.

These two last step differ significantly from the method described in Chapter 3.

4. **Visualisation** and **validation** of our segmentation on the dicom images.

The mesh is transported into the image configuration by using $u^{(i)} = \mathcal{X}^{-1}(v^{(i)})$ and a phantom is computed based on them, which is :

$$\tilde{\mathcal{F}} : \begin{cases} \Omega \rightarrow \mathbb{R} \\ x \mapsto \tilde{\mathcal{F}}(x_1, x_2, x_3). \end{cases} \quad (6)$$

Practical application of this semi-automatic method

This work was conducted in collaboration with Camille Cardot, Damiano Lombardi, Thomas Schouman and Wided Siai.

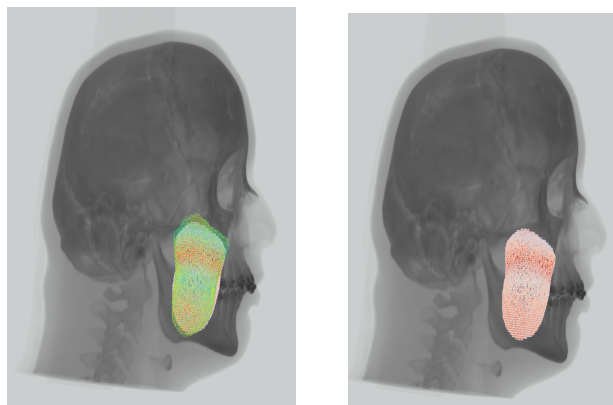


FIGURE 59 – 3D representation of a skull and its associated face : (a) and the superposition of manually and semi-automatically segmented masseters, (b) and the reconstructed masseter muscle after semi-automatic segmentation only

The purpose of this article is to compare the use of our semi-automatic method, described above, with the current manual reference method by practitioners. It is therefore, among other things, a practical contextualization of this method.

Two operators with anatomical knowledge of the muscle masseter region, but no extensive expertise in radiology or segmentation, each segmented 20 masseters : first manually, then semi-automatically, at least one month later.

For manual segmentation, we used the Amira software [197]. For semi-automatic segmentation, a graphical interface that can be used by clinicians has been implemented (Figure 60).

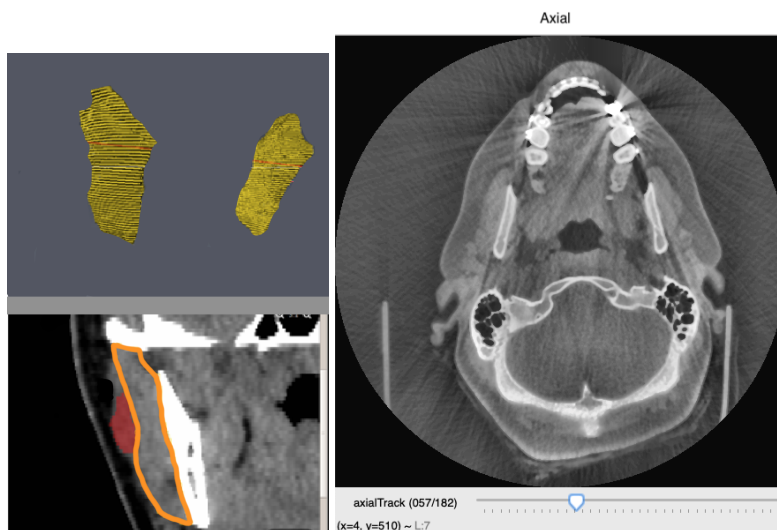


FIGURE 60 – The two segmentation software used : on the right, Amira, and on the left, the semi-automatic method

The many difficulties encountered during manual segmentation are those described in the bibliography above. This makes the work extremely long and tedious, since it takes on average 1h45 to segment a single muscle. For semi-automatic segmentation, although some complications intrinsically linked to the exercise of segmentation were still present, the speed and simplicity of the process makes the whole acquisition more pleasant and faster (on average 9m30 per muscle). A difficulty associated more specifically with this method has nevertheless disturbed the operators :

it is the impossibility of visualizing in real time the 3D model of the segmentation. However, it remains much faster and less painful for a practitioner, and one can easily hope to improve the algorithm allowing us to calculate the alignment, which is the most time-consuming.

In addition, a brief inter-operator reproducibility study was conducted. Either in terms of segmentation time or segmentation error, our semi-automatic segmentation method is reproducible from one operator to another. While manual segmentation, in terms of time, is not reproducible. There is therefore a gain in the reliability of the results with our method.

Partie III - Facial Reconstruction

The last part first presents the « morphing », a tool that we have already used in the process of creating a reduced base of 3D shapes, and that we will now also apply to facial reconstruction, in the second chapter of this part.

Morphing Algorithm

This work was conducted in collaboration with Maya de Buhan and Chiara Nardoni, it has already been partly presented in the latter's thesis work, and will follow up on a joint publication.

The general objective of morphing is to find a transformation from a given reference shape to a target object. Here we propose to define this transformation as an elastic deformation obtained by minimizing a functional one based on the distance between the two shapes. To achieve this objective, we use shape optimization methods.

Shape optimization consists in optimizing a functional with a cost of $F(\Omega)$ in an eligible shape set O_{ad} . A generic shape optimization problem can be written :

$$\min_{\Omega \in O_{ad}} F(\Omega), \text{ ou } \max_{\Omega \in O_{ad}} F(\Omega).$$

The applications of this type of problem are vast and lead to both theoretical and numerical problems to be solved : the definition of the admissible domain, the notion of derivation in this space, the geometric properties of the domain, etc. Many notions of derivation in relation to the domain are described in the literature, we will refer here to Hadamard's method of edge variation [3, 96, 157].

Our method has more in common with *Simon et al.* [192, 193] because it proposes a deformation model inspired by physics, and with *Bajcsy et al.* [14] which borrows techniques from optimal control and shape optimization. For a detailed bibliography of all these methods, we refer to [244]. We present here two functional forms : a « volumetric » J and a « surface » P , then with the help of different numerical simulations, we compare their results.

A volumetric functional

We measure the difference between the reference form Ω and the target Ω_T by the following functional form :

$$J(\Omega) = \int_{\Omega} d_{\Omega_T}(x) dx,$$

which implies d_{Ω_T} the signed distance function at Ω_T , defined as follows :

$$\forall x \in \mathbb{R}^d, d_{\Omega_T}(x) = \begin{cases} -d(x, \partial\Omega_T) & \text{if } x \in \Omega_T, \\ 0 & \text{if } x \in \partial\Omega_T, \\ d(x, \partial\Omega_T) & \text{if } x \in {}^c\overline{\Omega_T}. \end{cases}$$

We can then computed the shape derivative of J :

$$\forall \theta \in W^{1,\infty}(\mathbb{R}^d, \mathbb{R}^d), J'(\Omega)(\theta) = \int_{\partial\Omega} d_{\Omega_T} \theta \cdot n ds.$$

with $\theta : \mathbb{R}^d \mapsto \mathbb{R}^d$ a small diffeomorphism.

Then find the associated descent's direction, and using an iterative algorithm that minimizes J . We then obtain a shape sequence that is closer and closer to Ω_T . This algorithm has been implemented with the 2D and 3D finite element method.

We can see with Figure 61, the deformation of a disc into a rabbit, obtained with the minimization of J :

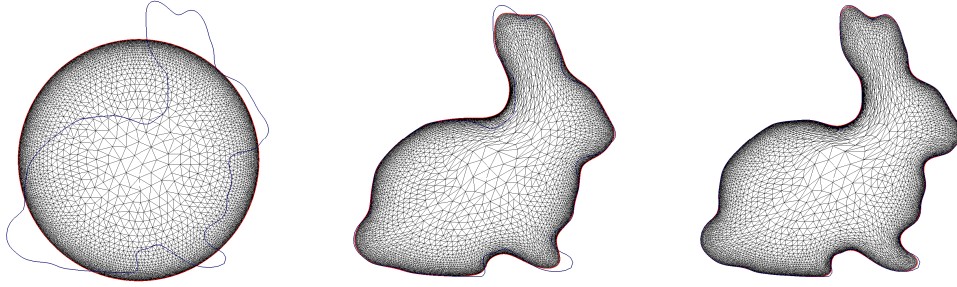


FIGURE 61 – 2D morphing of a disc into a rabbit

Comparison with a boundary functional

We also compared the J functional with a more traditional P boundary functional, such as :

$$P(\Omega_0) = \int_{\partial\Omega_0} (d(s, \partial\Omega_T))^2 ds,$$

which depends on the Euclidean distance $d(\cdot, \partial\Omega_T)$ to $\partial\Omega_T$, evaluated at the edge of Ω_0 . The P functional is more intuitive, since it tries to align two shapes according to their edges and has the advantage of being well defined on a surface and not a shape. However, in practice, this functional is numerically more difficult to implement. Indeed, the shape derivative of P implies calculating the average curvature at the edge :

$$\forall \theta \in W^{1,\infty}(\mathbb{R}^d, \mathbb{R}^d), P'(\Omega)(\theta) = \int_{\partial\Omega} \left(\frac{\partial d^2}{\partial n} + \kappa d^2 \right) \theta \cdot n ds,$$

with κ the mean curvature of $\partial\Omega$.

In addition, to minimize P , a point of $\partial\Omega$ must move to the nearest point of $\partial\Omega_T$, which can generate ambiguity, leading to numerical singularities, preventing the algorithm's global convergence.

We can see on Figure 62, a first example where the functional surface achieves the same result as the functional volume (Figure 40), but on a more complicated test, some singularities appear.

In view of these results, it is the first functional that has been chosen for the facial reconstruction application, of which morphing is a key ingredient.

Application to facial reconstruction

This work was conducted in collaboration with Patrick Goudot, Yvon Maday, and Thomas Schouman. It takes up and develops the work first undertaken by Maya de Buhan and Chiara Nardoni.

The purpose of facial reconstruction is to estimate an individual's facial appearance based solely on knowledge of his or her skull. This is based on the assumption that there is a significant

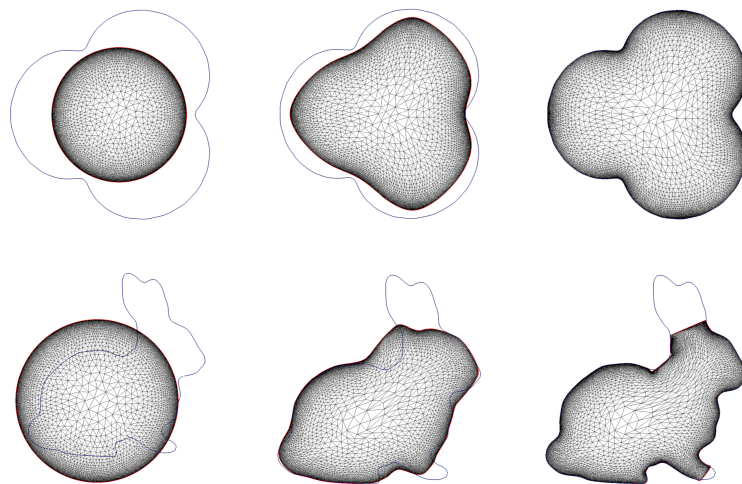


FIGURE 62 – 2D morphing of a disc into a rabbit

correlation between bone structure and soft tissue structure [102], which we also confirmed in the first chapter of this thesis. However, this process remains an approximation of the shape of the face, as secondary characteristics such as hair, skin colour or eyes are not identified by these methods. In addition, other parameters that influence the shape of the face itself are not always easy to identify on the skull, such as age or sex, or even not at all, such as stature. Some studies then propose a set of possible reconstructions to overcome this problem [43, 153].

From a mathematical point of view, it is said that the problem is not well posed, which will generate three types of difficulties : the characterization of the solution, which is not unique, the characterization of the degree of precision obtained through these reconstructions and also the stability of the proposed solutions.

Nowadays, facial reconstruction has various objectives from medicine to anthropology. In the FaciLe project, the objective is to reconstruct a face in forensic medicine in order to identify the deceased person.

A long history

The history of facial reconstruction is quite fascinating. Indeed, traces of it can be found very early in human civilizations, in practices related to ancestors or mortuary rites. In 1930, a collection of flattened human skulls (Figure 63), dating back 9000 years, was found under the ground of a neolithic house in Jericho [111].



FIGURE 63 – Flat skulls of Jericho (7000 BC) preserved at the British Museum in London (left) and the Jordan Archeological Museum in Amman (right). Images from [111]

In this context the symbolic meaning is predominant over anatomy. However these faces can be

considered as one of the first attempts at facial reconstruction. This type of practice is later found in many civilizations, such as ancient Egypt and pharaonic death masks, for example.

However, it was not until the 15th century, in Europe, that anatomical knowledge developed, particularly thanks to the rise of dissection, which had until then been prohibited. This will gradually lead to a gain in knowledge and interest in facial reconstruction in a more judicial context. It is only at the end of the 19th century, or even the beginning of the 20th, that facial reconstruction becomes a full part of the legal sciences. Two reference schools were then developed, the Russian school and the American school.

The Russian anthropologist Mikhail Gerasimov (1907-1970) believed that the shape of the muscles was closely linked to the underlying bone structures [76, 77], and that it was necessary to have very advanced anatomical and artistic knowledge to make a correct facial reconstruction. The American school, whose anthropologist Wilton Krogman can be cited as a pioneer [124], bases its method not on the reproduction of anatomical details but on tables measuring soft tissue thickness. In the 1980s, a third school appeared, inspired by the two previous ones, and developed by Richard Neave and Carolin Wilkinson. This traditional method is based on manual procedures such as : 2D reconstructions in the form of portraits [91, 220], or 3D in the form of a bust (Figure 64).



FIGURE 64 – Manual 2D (top) and 3D (bottom) facial reconstruction method. Images from [253]

These manual methods, although often producing credible results, are quickly criticized, mainly for their lack of standardization and their too great subjectivity related to the anatomist artist himself [91]. In addition, this type of reconstruction could take up to several days for an expert to work before obtaining a face.

The emergence of computers, digital and visualization methods gives a new opportunity to facial reconstruction. The one of process automatization, allowing time savings and less subjectivity of methods. Nowadays, most existing digital methods combine statistical models and databases.

A method that takes anatomy into account

It is in this vast context that the methods developed within the FaciLe project take root. Our facial reconstruction method is based on the preliminary work of Chiara Nardoni and Maya de Buhan within the project.

The method we propose is largely inspired by the history of facial reconstruction, with particular attention to muscle anatomy, which has however been neglected in the current automatic methods [203]. It complements the original method developed in [35], which already differed from statistical methods based on the elastic deformation of a soft tissues mask.

First, and before we can set up any reconstruction, we need to build a 3D database with skulls, faces and masseter muscles associated for the same person. The constitution of this database is done as indicated in chapter 2 of this thesis, this allows us to link all the elements of the database together (Figure 65).

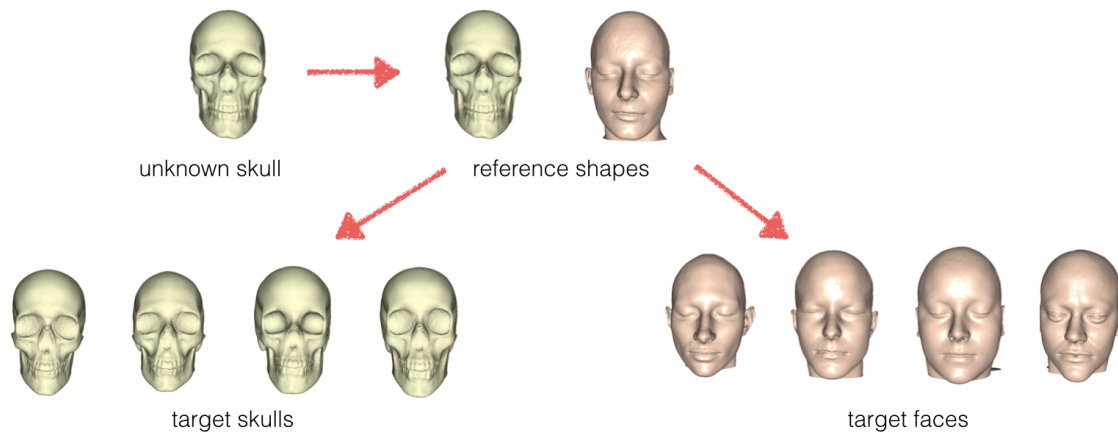


FIGURE 65 – Each skull on the base is connected to a reference skull after the « morphing » step, and each face to the face associated with this reference skull, by the same method. The same applies to muscles, so every element of our database is linked. Image from [35]

A last step is necessary before a face can be reconstructed from an unknown skull, that of creating, for each skull/face pair of the base, a mask that represents the soft tissues (Figure 66). It is from these masks that the reconstruction of a new face is generated. The elastic deformation of a skull from the base, identified as close to the unknown skull, is applied to this unknown skull, using a soft tissue mask associated with the skull of the chosen base.

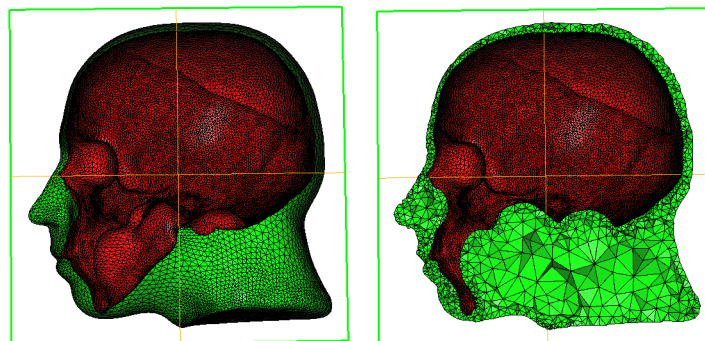


FIGURE 66 – Assembly of the two skull and face surfaces of the same individual (left), tetrahedral mesh of the space between the skull and the face, called a mask (right)

It is now possible to set up a reconstruction. Using the reduced 3D shaped basis set up for the

masseter muscle, we start by adding the reconstruction of this muscle to the unknown skull. Then the skull is closed, using the « warping technique » described in Chapter 2 (Figure 67).

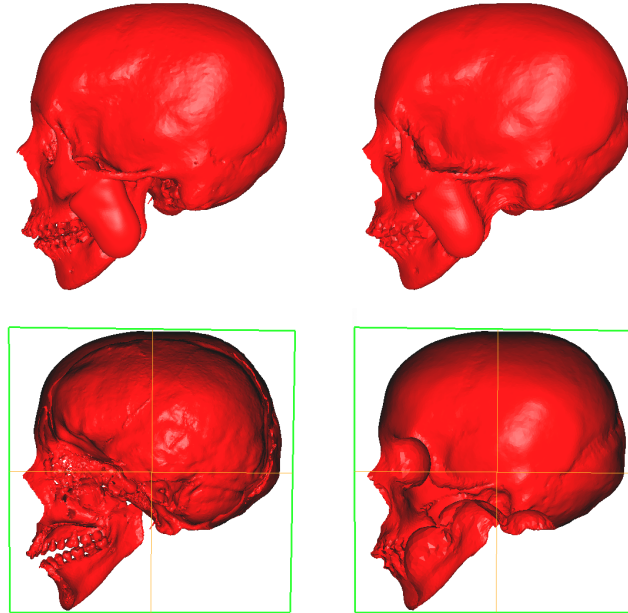


FIGURE 67 – Example of skulls with reconstructed masseters (left) then closed by warping (right), below medial section of the same skulls

It should be kept in mind that it is possible to implement the same method for other facial elements and that the masseter muscle is a first illustration of this process.

All that remains is the step of deforming a mask from the database to our unknown skull, which already integrates the additional information contained in the masseter muscle. This gives us a face for our unknown skull, Figure 68.

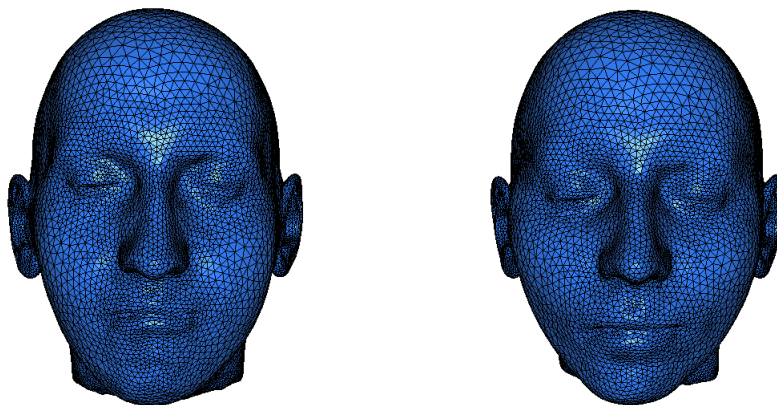


FIGURE 68 – Reconstruction of a face from its skull (left), to be compared with the real 3D face (right)

Validation

Facial reconstruction methods are particularly difficult to evaluate, compare and validate. Indeed, each team which proposes a solution to this problem has worked on a limited set of data, often of medical origin, and which therefore does not have the possibility to be transferred to other teams for comparison. Moreover, the ultimate objective of facial reconstructions in forensic medicine is the recognition and identification of a deceased person. It therefore seemed important and interesting to us to set up a reproducible validation method that would allow us to understand and compare these methods.

For this purpose we have developed an application, allowing users to identify from two pictures of the same individual (face and profile), the 3D face that seems to correspond to them. Four types of tests are proposed, blind, where the operator must identify from a picture :

1. real faces segmented in 3D,
2. reconstructions performed using the [35] method,
3. reconstructions carried out with the method described above but where the real masseter muscle has been added,
4. reconstructions performed with the method previously described with the reconstructed masseter.

A screenshot of the application is shown in Figure 45.

Appendices

In these appendices, I detail :

- the short note, extracted from Chapter 3 of this thesis, published in the *Comptes Rendus Mathématiques de l'Académie des Sciences*, with Damiano Lombardi and Yvon Maday,
- the "Read Me" (explanatory leaflet) of the facial reconstruction software implemented during my thesis, which makes it possible to make the entire process fully automatic,
- a practical application of facial reconstruction that have allowed simulations in anthropology, in collaboration with Martin Friess.



First Part : Preliminary work

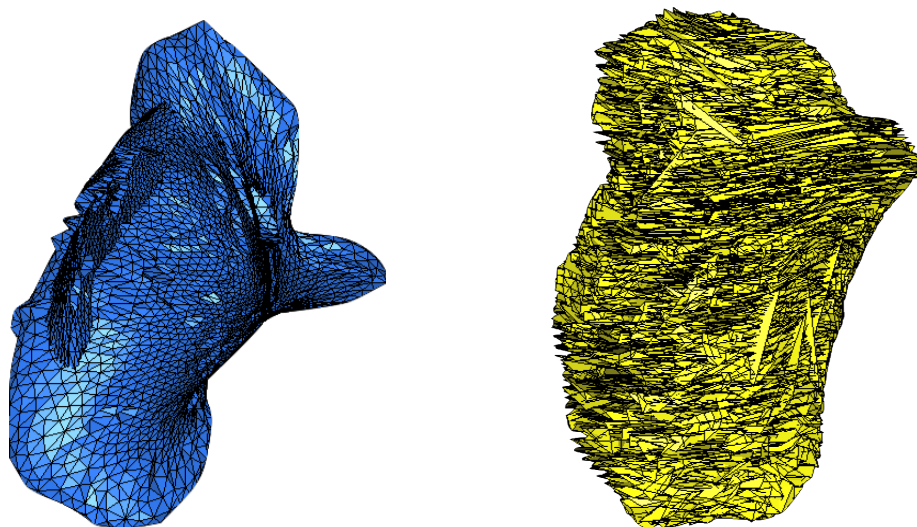
Introduction 69

1 Cephalometry and Masseter 71

- 1.1 Introduction
- 1.2 Materials and Methods
- 1.3 Results
- 1.4 Discussion
- 1.5 Conclusion

2 Reduced Basis of 3D shape 79

- 2.1 Introduction
- 2.2 Preprocessing
- 2.3 Function-to-shape representation
- 2.4 Application of reduces basis of 3D shapes
- 2.5 Conclusion



INTRODUCTION PART I

This first part contains two chapters and is a necessary groundwork for the implementation of the next two parts.

The first chapter presents our working hypothesis that the shape of the facial muscles and that of the underlying bones are highly correlated. Confirming and more precisely quantifying this first step was necessary to implement our facial reconstruction method, which takes into account the underlying anatomy of the face. This chapter focuses on the link between 5 known cephalometric measurements in the literature, and 4 measurements performed on the masseter muscle. The results make precise the strong correlation, which led us to build a 3D database of masseter muscles, which could be reconstructed from these measurements on the skull. This is presented in the next chapter.

The second chapter describes how we have generated the database on which the work of the next two parts is based. We detail the different steps necessary for the creation of a reduced basis of 3D shapes : medical image segmentation, 3D mesh, alignment, warping, morphing, principal component analysis, and machine learning. Note that the first part is the most tedious and time consuming as it requires human treatment contrarily to what happens for all the other ones for which automatic treats has been implemented.

**the nice figures presented above are the results of unfortunate numerical simulations carried out during the work on Chapter 2, and they also illustrate some of the difficulties of numerical implementation work.*



1. Cephalometry and Masseter

Sommaire

1.1	Introduction	72
1.2	Materials and Methods	73
1.2.1	Subjects	73
1.2.2	CT Imaging	73
1.2.3	Statistical Analysis	74
1.3	Results	75
1.3.1	Masseter measurements and Cephalometry	75
1.3.2	Correlation between Masseter and Cephalometry	75
1.4	Discussion	76
1.5	Conclusion	78

Can the shape of the masseter be inferred from that of the skull ?

Work in collaboration with Adeline Kerbrat, Patrick Goudot and Thomas Schouman, to be submitted in International Journal of Oral And Maxillofacial Surgery.

Abstract

Background : The masseter muscle is the largest muscle of the face that significantly influences facial appearance. Its morphological analysis could translate the impact of masticatory function on the shape of the facial skeleton. The aim of this study was to identify correlations between facial typology and masseter muscle dimensions in a sample of dysmorphic patients.

Methods : The CT-scans of 51 dysmorphic patients aged 14 to 47 were collected. SNA, SNB, ANB, Fancfort-mandibular, and maxillo-mandibular angles were measured to describe the

facial types. Masseter muscle width, height, thickness and volume were also measured. Pearson's correlation coefficients between each masseter and facial skeleton variables were calculated.

Results : We found numerous correlations between cephalometric measurements and masseter muscle dimensions in dysmorphic patients. The most strongly correlated parameters was the FMA, with a Pearson's correlation coefficient between -0.440 and -0.340 for all masseter dimensions and always a p-value < 0.01. Some other correlation were proved between the SNA and thickness (p=0.021) and volume (p=0.005) of the masseter, and the SNB and height (p=0.002) and volume (p=0.009) of the masseter.

Conclusion : This study confirmed previously reported correlations between the masseter dimensions and facial vertical proportions in a sample of patients exhibiting a wide range of maxillo-mandibular dysmorphoses, but also demonstrated some correlation with the sagittal proportions of the face.

Key Words

Cephalometric analysis, Masseter muscle.

1.1 Introduction

Human craniofacial skeleton exhibits a wide range of variations [195]. Skull anatomy can be described with different phenotypes mainly defined by vertical and sagittal (antero-posterior) parameters. These parameters allow categorization of most phenotypes into one of the following : short, normal or long face for vertical parameters [75], retruded, normal, or protruded for sagittal parameters [7, 107]. We can describe the different facial typologies according to three categories based on the vertical dimension : long, balanced, and short-face [163, 184], and three categories based on the Francfort-mandibular angle : hyperdivergent (>30°), normodivergent (20° to 30°), and hypodivergent (<20°).

Because they insert onto facial bones, notably the jaws, masticatory muscles influence facial growth patterns, and eventually facial typology. Several authors studied the link between masticatory muscle contraction force, facial typology, and their descriptive anatomy [56, 106, 188]. The masseter is the largest muscle of the face [260]. It is strongly related to the shape of the mandible, due to its major insertions on the mandibular angle. Masseter volume and cross-sectional area (CSA) are significantly associated with vertical dimensions of the face [31]. It has also been demonstrated that masseter thickness presented the most significant correlation with skeletal dimensions in all directions [12]. Masseter muscle volume greatly influences facial morphology and is documented to be strongly related to skeletal anatomy [203, 228]. However, most of these studies used samples of healthy subjects, with regards to jaw discrepancy, or very restrictive definitions of facial typology (e.g. absolute dimensions of the face). Differences were found between the masseter morphology of patients exhibiting mandibular prognathism when compared to healthy subjects but it is unclear how these correlations apply to patients with significant jaw discrepancy.

The aim of this study was to assess the validity of previously reported correlations and to look for other possible correlations between specific masseter shape parameters and facial typology as assessed by cephalometric analysis in a sample of patients representing a wide range of facial phenotypes, including patients with significant jaw discrepancy.

1.2 Materials and Methods

1.2.1 Subjects

Fifty-one patients (17 males / 34 females) aged 26.9 years on average (standard deviation (SD) 9.4 years) referred for orthognathic surgery in one single maxillofacial surgery department, and exhibiting a variety of maxillo-mandibular dysmorphoses, were recruited for this study. All subjects had complete or nearly complete dentition, and presented no temporo-mandibular joint condition. Inclusion in the study required that both masseter muscles be entirely included in the field of acquisition of the CT-scan and that the muscles present no lesions or lesion-related symptoms. All patients were informed that their anonymized data would be used for research purposes, which they were free to oppose.

1.2.2 CT Imaging

All CT-scans were obtained using a Discovery CT750HD system (GE Healthcare, Chicago, Illinois, United States). The reconstructed images had a slice thickness of 0.62 mm for bones, and of 1.25 mm for soft tissues. The patients were trained by their referring surgeon to position their mandible in usual occlusion according to centric relation of the condyles just before the CT-scan.

Cephalometric Analysis

All cephalometric measurements were performed on 3D skull models extracted from CT-scans with Mimics® Innovation Suite 21.0 (Materialise, Leuven, Belgium), Figure 1.1 (a).

We used common cephalometric measurements to describe the dysmorphic phenotype. The cephalometric landmarks and angles used in this study are shown in Figure 1.1 (b).

- SNA : angle between the points sella [S], nasion [N] and subspinale [A],
- SNB : angle between the points sella [S], nasion [N] and supramentale [B],
- ANB : angle between the points subspinale [A], nasion [N] and supramentale [B],
- Francfort-mandibular angle (FMA) : angle between Francfort horizontal plane and mandibular plane,
- Maxillo-mandibular angle (MMA) : angle between the mandibular basilar border plane and the palatal (or bispinal) plane (plane joining the anterior nasal spine and the posterior one).

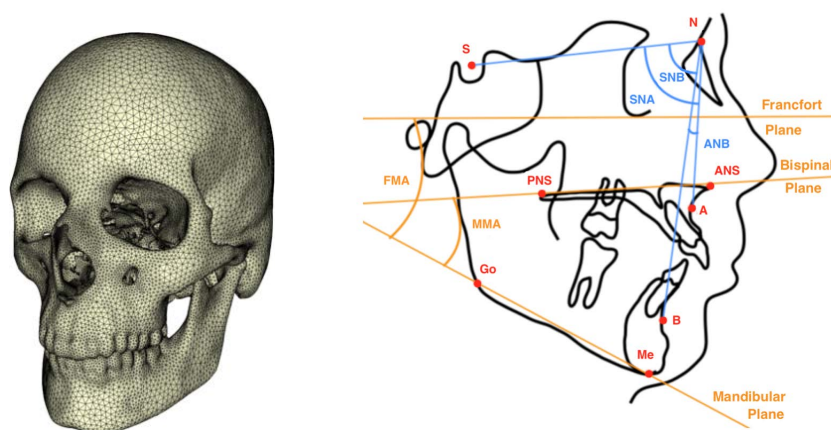


FIGURE 1.1 – (a) 3D mesh of a skull used for performing measurements, and (b) Cephalometric landmarks and measurements - S sella turcica, N nasion, PNS posterior nasal spine, ANS anterior nasal spine, A subspinale, Go gonion, B supramentale, Me menton ; FMA Francfort mandibular angle and MMA maxillo-mandibular angle.

Masseter Measurements

Muscle measurements were performed on axial and coronal reconstructions of the soft tissue window acquisition using Horos® 2.1.1 (Horos Project, GNU Lesser General Public License, Version 3 (LGPL-3.0)).

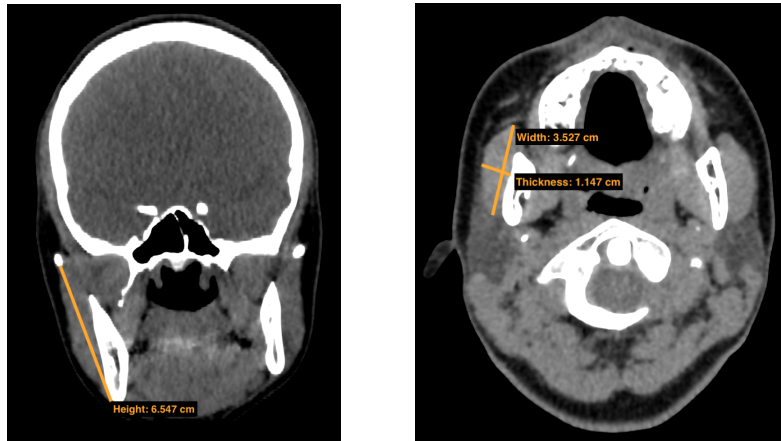


FIGURE 1.2 – Measurement of the masseter dimensions on (a) frontal and (b) axial views.

Muscle measurements were performed on axial and coronal reconstructed sections obtained from the soft tissue window acquisition using Horos® 2.1.1 (Horos Project, GNU Lesser General Public License, Version 3 (LGPL-3.0)). Both the right and left masseters were measured in a first series of 20 patients. As no significant differences were found between both sides in this preliminary series, only the right masseter was measured for the following 31 patients and we used the right masseter measures of the whole sample for further analysis of the correlations.

The CT-scans were first reoriented by aligning the axial views onto the Francfort horizontal plane and the sagittal views onto the midsagittal plane. We chose 3 variables of interest to describe the masseter muscles : width (anteroposterior distance in a horizontal plane), thickness (maximal distance between masseter lateral edge and outer cortex of the mandibular ramus), and height (maximal vertical distance between zygomatic arch and mandibular basilar border). Width and thickness were measured using an axial slice through the lingula. Height was measured using a coronal view aligned on masseter maximum height, Figure 1.2.

We performed manual slice-by-slice segmentation of the masseter using Amira® 2019-05 (Zuse Institute Berlin, Berlin, Germany) [197] (Figure 1.3 (b)). The volume of the 3D mesh generated from the segmentation was computed using a simple algorithm that we developed in C language, using the 3D tetrahedra of the mesh.

1.2.3 Statistical Analysis

All statistical analyses were done with the statistical package of R® (3.5.3, 2019-03-11, The R Foundation for Statistical Computing). The mean value, standard deviation (SD) and range of each measurement were calculated. We checked that the data distribution followed a normal law with a Shapiro-Wilk test. Pearson's correlation coefficients between masseter variables and cephalometric variables were calculated as well as data plots with linear and non linear regressions. The significance threshold used for all tests was $p = 0.05$.

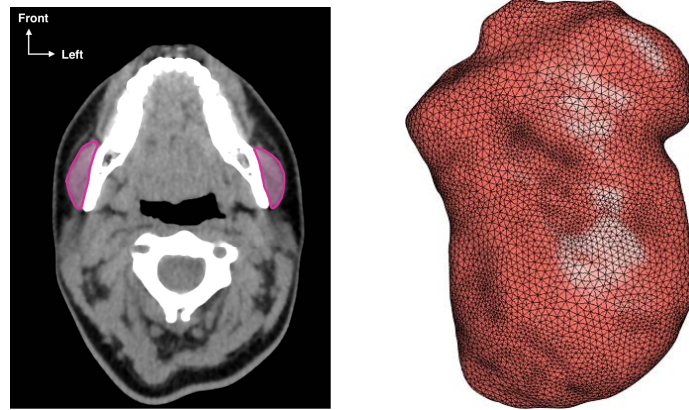


FIGURE 1.3 – (a) CT-scan axial view parallel to the Francfort horizontal plane through the lingula showing the segmentation of the masseters in pink, and (b) 3D mesh of a masseter after segmentation used for computing the volume

1.3 Results

1.3.1 Masseter measurements and Cephalometry

Descriptive statistics for masseter measurements and volumes are given in Table 7.4. All masseter variables were normally distributed. The differences between the right and left measurements were not significantly different (height $p=0.60$, width $p=0.11$, thickness $p=0.30$).

	Mean	SD	Minimum	Maximum
Width	4.02	0.50	3.00	5.40
Thickness	1.23	0.26	0.69	1.97
Height	6.17	0.48	4.85	7.69
Volume	7.88	2.52	3.65	16.85

TABLE 1.1 – Descriptive statistics of masseter measurements

Descriptive statistics of the cephalometric measurements are given in Table 1.2. All cephalometric variables were normally distributed.

	Mean	SD	Minimum	Maximum
SNA	79.9	5.1	68.8	95.2
SNB	75.6	5.7	65.8	91.8
ANB	4.4	3.2	-5.0	10.1
FMA	24.2	10.1	2.2	51.1
Bispi-Mand	23.6	9.4	6.2	52.3

TABLE 1.2 – Descriptive statistics of cephalometric measurements

1.3.2 Correlation between Masseter and Cephalometry

All masseter dimensions showed significant reverse correlations with FMA. Masseter height was the most strongly related to cephalometric measures. It was correlated with SNB, ANB, FMA and MMA. ANB was correlated only with masseter height. The correlation coefficients are given in Table 1.3.

	SNA	SNB	ANB	FMA	MMA
Width	NS	NS	NS	-0.385 <i>p</i> = 0.005	-0.489 <i>p</i> < 0.001
Thickness	0.324 <i>p</i> = 0.021	NS	NS	-0.340 <i>p</i> = 0.01	-0.313 <i>p</i> = 0.025
Height	NS	0.423 <i>p</i> = 0.002	-0.311 <i>p</i> = 0.026	-0.444 <i>p</i> = 0.001	-0.298 <i>p</i> = 0.03
Volume	0.385 <i>p</i> = 0.005	0.362 <i>p</i> = 0.009	NS	-0.345 <i>p</i> = 0.013	NS

TABLE 1.3 – Correlation coefficients between masseter and skeletal measurements (ns : Non-Significant)

In Figure 1.4, the scatter plots of masseter measurements that are significantly correlated to angular bones dimensions are highlighted in blue.

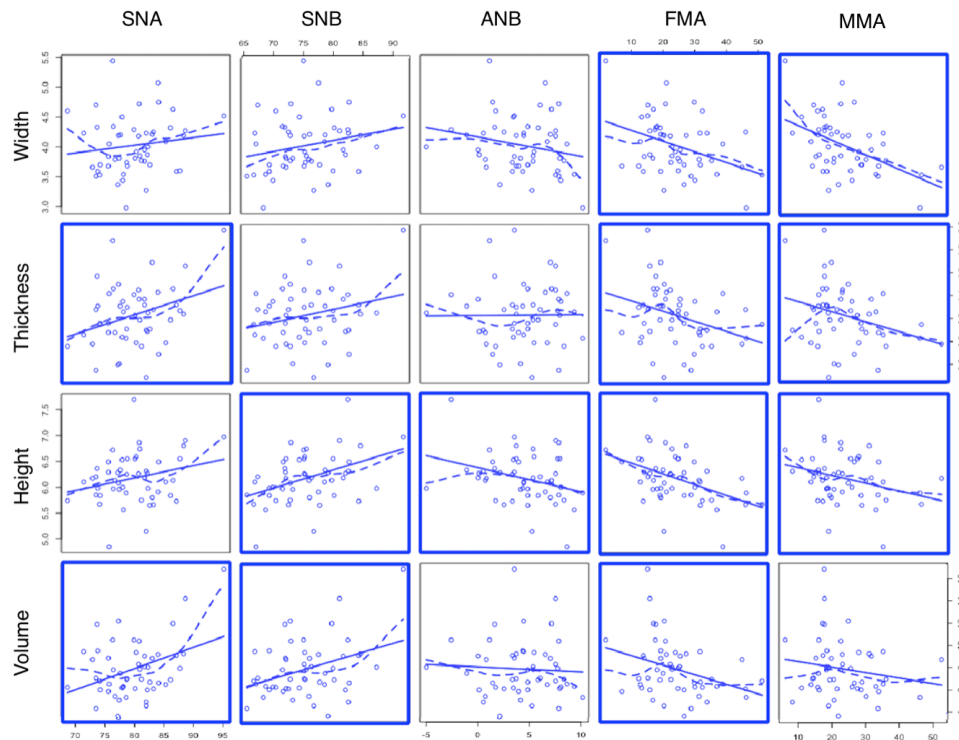


FIGURE 1.4 – Data plots showing significant correlation, highlighted in blue. The continuous straight lines represent linear regressions, which explain the 20% (R^2) average variability of the data, while the discontinuous straight lines represent nonlinear regression.

1.4 Discussion

This study showed that the morphology of the masseter muscle is strongly related to skull cephalometric parameters in a sample of patients exhibiting a wide range of maxillo-mandibular dysmorphoses, the most strongly correlated being the FMA.

We found numerous correlations between cephalometric measurements and masseter muscle

dimensions. Most studies in the literature assessed the relationship between muscle thickness and facial height. In our study, the FMA angle was significantly inversely correlated with masseter length, height, width and volume. Moreover, the MMA was also significantly inversely correlated with muscle length, height and width. These results are similar to those found in the literature [12, 56, 116]. According to the literature and to our study, thick, long and large masseter muscles are associated with short-face phenotypes characterized by closed gonial angles (hypodivergent), while short, thin masseters are related with long-face phenotypes characterized by open gonial angles (hyperdivergent) [23, 125].

In our findings, the SNA angle (describing the relative horizontal position of the maxilla to the cranial base) was significantly correlated with the masseter muscle volume and thickness. This means that the more protruded maxilla, the thicker the masseter is. The SNB angle (horizontal position of the mandible to the cranial base) was significantly correlated with the masseter muscle volume and height. Again, the more protruded mandible, the thicker and longer the masseter is. These results differ from the literature : *Kubota et al* [125] found no association between the masseter muscle dimensions and SNA or SNB. Similarly, *Zepa et al* did not find any significant difference between the masseter muscle dimensions of Class II and Class III patients [261]. The mechanism that could explain the SNA angle correlation with masseter dimensions in our findings is unclear. The masseter muscle inserts onto the mandibular angle and the zygomatic arch. On the lingual side of the mandibular ramus lies the medial pterygoid muscle. It occupies the vast majority of the infratemporal fossa, which is located right behind the maxilla. Along with the masseter, this muscle forms the pterygomasseteric sling around the mandibular angle. Because of this continuity and of their identical function, their dimensions are related. Indeed, **Weijs et al.** evaluated masseter muscle and medial pterygoid muscle morphology of 16 volunteers. They found a strong correlation between the CSAs of the masseter muscle and the medial pterygoid muscle [247]. Therefore, we hypothesize that this correlation between a more anteriorly positioned maxilla and a thicker masseter could be the result of a bulky pterygoid muscle pushing the maxilla forward.

The ANB angle characterizes the horizontal relationship of the maxilla to the mandible. In our study, this angle was significantly inversely correlated only with muscle height. The greater distance between the maxilla and the mandible, the shorter masseter. However, the relevance of such a correlation based on the total range of variations of ANB, including positive and negative values which correspond to two opposite phenotypes, is questionable. A subgroup analysis based on the sign of the ANB value could be more informative but this was not possible in our series because of the limited sample size.

Becht and al. [18] compared masseter muscle length and orientation in a population of 150 patients divided in subgroups according to facial height, anteroposterior skeletal pattern (ANB angle) and symmetry : no significant differences were found between the length of masseter muscle in the three anterior- posterior groups. However, the orientation of the muscle differed according to antero-posterior facial pattern : the orientation of the masseter was more vertical in Class III compared to Classes I and the orientation of the masseter was more horizontal in Class II compared to Class I. ANB is probably related to the orientation of the masseter muscle rather than to the muscle's height.

In addition to the correlation with craniofacial phenotype, masseter dimensions also depend to some extent on genetics and muscle tissue fiber type composition. The vertical dimension of the face mostly is strongly correlated with muscular fiber composition ; a reverse correlation has been demonstrated between masseter's height and the percentage of type II muscular fibers [186]. However, it is still unclear whether the percentage of fiber types in the muscle is the cause or the

consequence of the facial type.

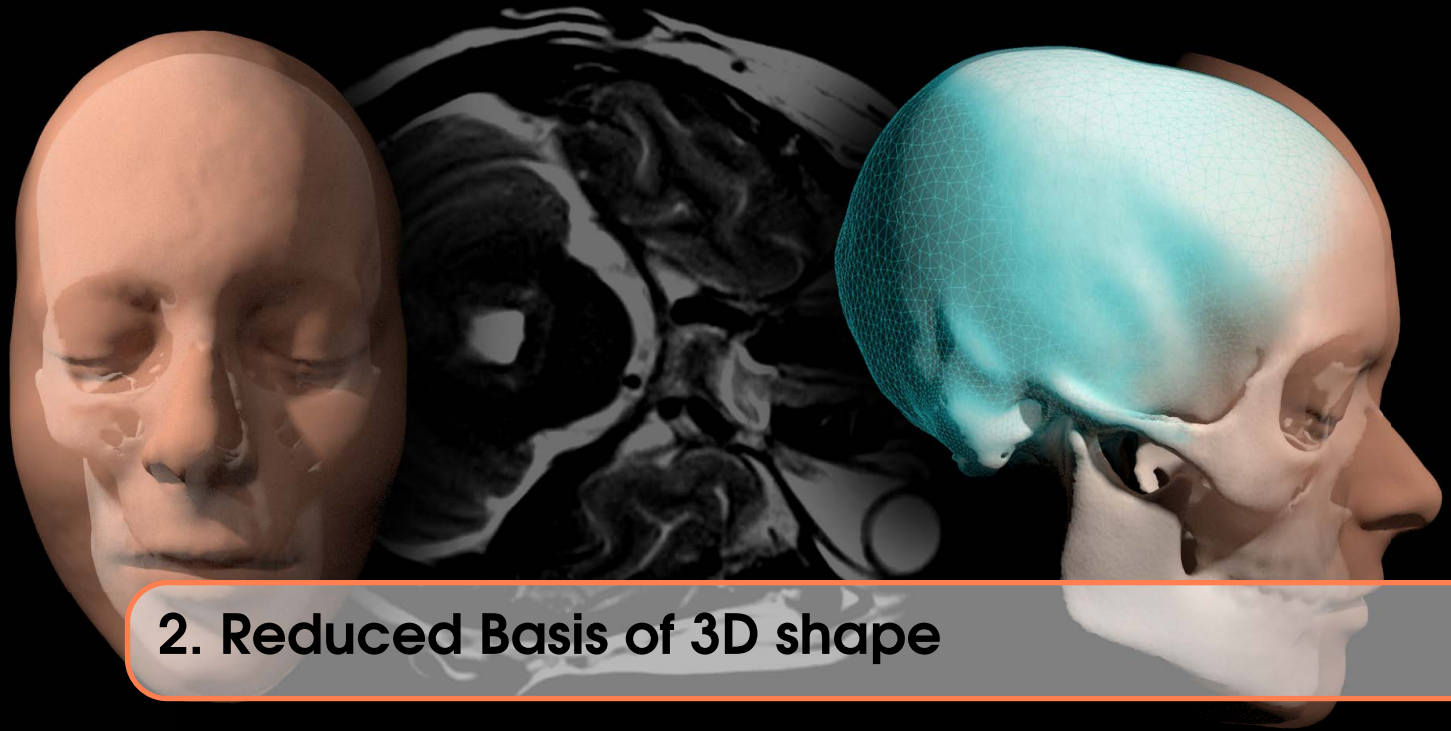
Computed tomography allows qualitative and quantitative analysis of muscle morphology [117, 125]. Although the muscular structures are slightly less clearly visible than with Magnetic Resonance Imaging (MRI), measurements obtained on CT-scans or MRI are comparable [116]. Moreover, CT-scans allow evaluate both craniofacial skeletal morphology and masseter muscle shape. MRI is particularly suitable to analyze muscular tissue. It enables in vivo measurement of many anatomical parameters of the masseter, such as CSA [238, 239, 246] and volume [79, 93, 120]. However, it is less suitable for bone tissue assessment and cephalometric analysis based on MRI is not validated. Ultrasonography allows in vivo measurement of the CSA and volume of the muscle, but the technique requires a trained practitioner. In our study, we also controlled the reproducibility bias risk by splitting bone tissue and soft tissue measurements, which were done by 2 distinct operators.

In this study, we investigated muscular shape and volume in a sample of patients exhibiting facial dysmorphism eligible to surgical treatment. In addition to specific post-operative physical therapy, surgical correction of the jaw discrepancy changes the muscle functional pattern. Therefore, it would be interesting to investigate how these functional changes may translate into dimensional changes in the masseter muscle after surgery, as *Westermarck et al.* hypothesized [249], and to identify a muscular pattern so as to predict relapse.

Although we were able to demonstrate significant correlations, increasing the sample size of our study would allow increase the power of the correlations. This would be especially interesting to investigate separately subgroups based on ANB angle as defined by above or below the norm rather than considering it as a continuous variable. Indeed, increased or reduced ANB angles describe very different facial types which may exhibit specific patterns of correlation with masseter variables. We could thus better describe the link between the morphology of the skull on that of the muscles, which could help predict the shape of one from the other. This could be useful for facial morphology reconstruction or simulation or for computer-assisted surgery applications. A second limitation that can be exposed is the absence of a measurement reproducibility study for the masseter dimensions. This would possibly make it easier to establish strict anatomical criteria that would be comparable from one study to another.

1.5 Conclusion

As a conclusion, we showed in this study that the morphology of the masseter muscle is strongly related to the vertical proportions of the skull and, to some extent, to the sagittal, in a sample of patients exhibiting a wide range of maxillo-mandibular dysmorphoses, suggesting that it is possible to deduce the shape of the masseter from that of the skull.



2. Reduced Basis of 3D shape

Sommaire

2.1	Introduction	80
2.2	Preprocessing	82
2.2.1	Data Acquisition : Segmentation of CT-Scan	82
2.2.2	Mesh Generation : 3D surface reconstruction	83
2.2.3	Mesh and remesh	84
2.2.4	Alignment	85
2.3	Function-to-shape representation	89
2.3.1	Warping (if necessary)	89
2.3.2	Morphing	90
2.3.3	Parametrization : Dimension Reduction	91
2.4	Application of reduces basis of 3D shapes	95
2.4.1	Shape prediction of anatomical element	95
2.4.2	Segmentation and reconstruction	95
2.5	Conclusion	95

Constitution of a reduced basis of 3D shape, application for medical anatomical atlas

Work in collaboration with Yvon Maday and Chiara Nardoni.

Key Words

Reduced Basis, Anatomical Atlas, Segmentation, Alignment, Morphing, PCA

2.1 Introduction

The processing of medical images has always been and remains a difficult task. Different mathematical methods have been put in place to extract as much data as possible as easily as possible. Depending on the desired applications, each of these methods has its own advantages and disadvantages. Our objective in this chapter is to present a method for creating a 3D database of organs that is easy to use for different applications, of which we will detail two examples in Parts II and III, respectively medical image segmentation and facial reconstruction for forensic medicine.

Modeling anatomical elements such as muscles or bones in 3D is now increasingly useful for multiple applications such as reconstruction, simulation or even surgery [64, 156, 177]. Building a database of anatomical organs is the first step in this type of research. This therefore represents a major challenge for physicians and can have significant implications for clinical practice [62, 181]. Indeed, this type of database can be used to improve diagnosis or prognostic processes [62, 119, 152], or even facilitate the identification of anatomical structures for students in training [164].

The set of all variations of a given anatomical element constitutes a huge sampling (based on the total human population, ie about 7.5 billion) of what can be considered as a manifold, \mathcal{M} ie a continuous set that varies in a rather regular way. The complexity of this manifold informs on the diversity of the given element, which, most of the times, is rather low. In order to mathematically apprehend this complexity, the notion of Kolmogorov n-width is rather helpful. It is defined by

$$d_n(\mathcal{M}, X) = \inf_{X_n \subset X} \sup_{f \in \mathcal{M}} \inf_{g \in X_n} \|f - g\|$$

where X denotes the way differences between two elements in \mathcal{M} is measured (it is associated to a Hilbert space that contains \mathcal{M}). The Kolmogorov n-width measure to which extend all elements of \mathcal{M} can be represented as a linear combination of very few basic structures. This mathematical representation is associated in the medical literature to anatomical atlases that is based on a rich enough sample that represents quite well the variability of the given anatomical element.

Several problems emerge from this definition of anatomical atlases for the construction of a digital 3D atlas [11, 154] :

1. how to identify those characteristic structures that best describe stability and anatomical variability ?
2. how to match all the objects in the database in order to compare them as well as possible ?
3. how to model a new structure using this database ?

Currently most of the construction methods of these atlases are largely automatic, so it is more interesting to look at a clearer classification [24]. There are anatomical atlases of different structures : brain, heart, skull, vertebrae, liver, mandible, lungs ; which can be classified according to whether these organs are rigid (bone), elastic (such as brain or liver), or elastic and articulated (such as heart or face) [98]. Here we will be particularly interested in the representation chosen for the elements of the atlas.

An anatomical structure can be represented by different common generic and invariable characteristics : set of points, lines, surfaces or volumes. However, there may be a difference between the representation chosen for the statistical atlas and that used by the mapping method. Finally, some atlases accumulate representations : points and lines, lines and surfaces [26].

The representation by characteristic points, or landmarks, is the representation traditionally used for the anatomy of the head. It is still widely used because the characteristic points allow a simple statistical modeling of the shape to be characterized. There are many cephalometric atlases that have been in place for several decades in 2D and 3D [28, 53, 114, 148, 171]. The automatic detection of cephalometric points has also been the subject of numerous studies, such as those of [47, 104] and more recently of [128]. An example is provided in Figure 2.1.

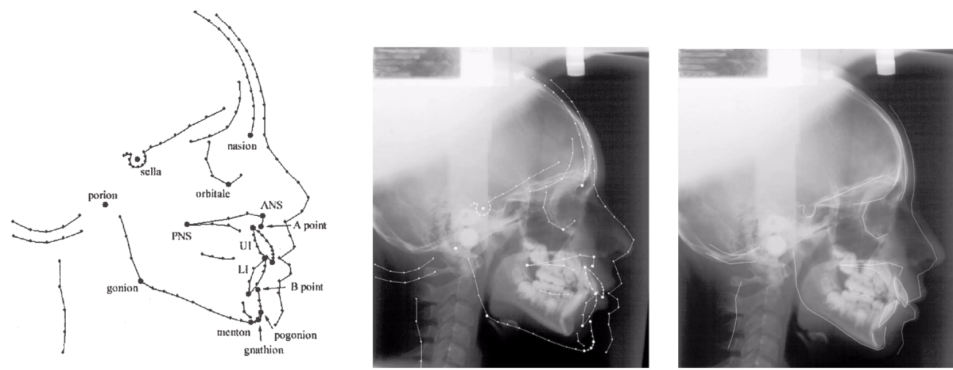


FIGURE 2.1 – 2D cephalometric method, Images extracted from [104]

Landmarks play a fundamental role in computational anthropology and are defined as discrete anatomical loci that can be recognized as homologous in all specimens under investigation. In morphometric practices the sparse set of anatomical landmarks are used to build a statistical shape model and study variations. However, we have decided to drop these landmarks because of the difficulties of acquisition, manual or automatic, but also because these points are only really reliable on the bone, and more difficult to transpose on the skin, and more particularly on the « intermediate » soft tissues like muscles. Some authors have already developed landmark-free, fully automated methods for shape analysis. An example with application in paleontology is presented in [172]. Our choice was therefore based on surface characteristics.

Many atlases or statistical shape models use a representation of the shape by one or more surfaces modeled by meshes. The hypothesis necessary for the statistical modelling step is the following : each vertex of the mesh at the end of the mapping step is a point which, if not characteristic (no biological correspondence), represents the same place on each copy. These points are then called semi-characteristic points, or semi-landmarks, and were introduced by Bookstein [30]. Our objective here is closer to that of [224], whose aim is not to achieve a set of variations around this form but to quantify an individual's anatomical deviation from the copies in the database. The methods used are however very different.

With the development of data science and visualization, especially for 3D objects, it has become increasingly important to consider a way to synthesize information. It also allows us to better represent the data. A good way to represent a family of complex object with only a few coefficients, is to build a reduced base [100, 112], with a so-called Principal Component Analysis (PCA), most of the time. The first analysis of this type, applied to the processing of shapes, is presented in [46, 48]. But in order to be able to perform this kind of analysis, a Procrustes Analysis like first describe in [103], with the aim to performed rigid registration, is needed.

In this chapter we present a method to build a database of 3D shapes, easily representative and useful for modeling. We are developing a threaded example of 3D shape representation in medical imaging, in order to create a 3D anatomical atlas [105]. We choose to present our methodology on specific example, the skull, the face and the masseter muscle, which is the most voluminous muscle of the face, used for mastication.

The first part presents the pre-processing of the data, where we detail the segmentation, the meshing and the alignment process. The second shows how to describe, compare and therefore model each object in the database. The last part describes an application to facial reconstruction and segmentation, note that it is necessary to keep in mind that this procedure can be applied to

many other applications, such as structural classification which is a basic task in molecular biology, or in animation cinema and video game creation, etc. [39].

2.2 Preprocessing

2.2.1 Data Acquisition : Segmentation of CT-Scan

To process data in three dimensions, the first step is to acquire the raw data. This step depends on the type of data needed for a specific problem. In our case, a good way to obtain a 3D representation of anatomical elements is to use medical imaging such as MRI or CT-Scan. The data we collected are CT scans, from the oral surgery department of La Pitié Salpêtrière Hospital, Paris, France.

Segmentation is a necessary step to move from a cross-sectional image to a 3D mesh representation, it corresponds to the process of assigning a label to each voxel (3D pixel) of an image. This step can be done in different ways : manually, semi-automatically or automatically. The choice of method depends on the type of image and the object of interest. In our example, the segmentation of the masseter was first manually segmented by anatomical experts, then semi-automatically using the [137] method. In the Figure 2.2, we can visualize an axial section of a CT-Scan, with the selection of the pink masseter muscle, performed manually.

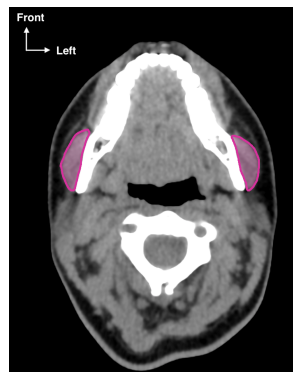


FIGURE 2.2 – Segmentation of the masseter muscle, in pink, on a head CT-Scan

Other objects of interest are easier to segment automatically, such as skull bones or face, on the same scanners. However, most of the time, it is necessary to manually modify the result obtained automatically, using multi-thresholding method, due to the occurrence of artefacts, as is often the case with teeth (Figure 2.3). In addition, in our specific case, other adjustments may be of particular interest, such as the removal of the spine (Figure 2.4), or segmentation of the mandible separately.

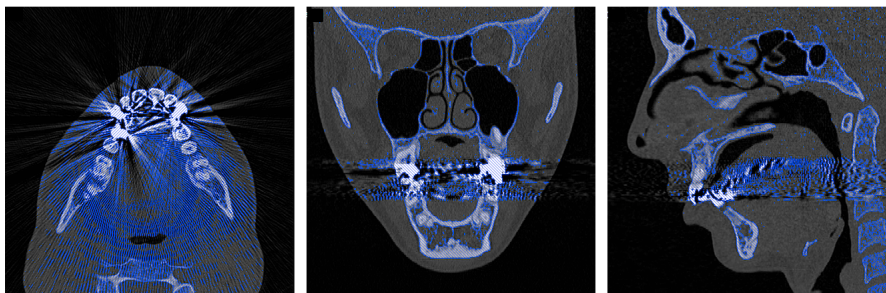


FIGURE 2.3 – Automatic skull segmentation in blue, with thresholding method, in the presence of dental artifacts

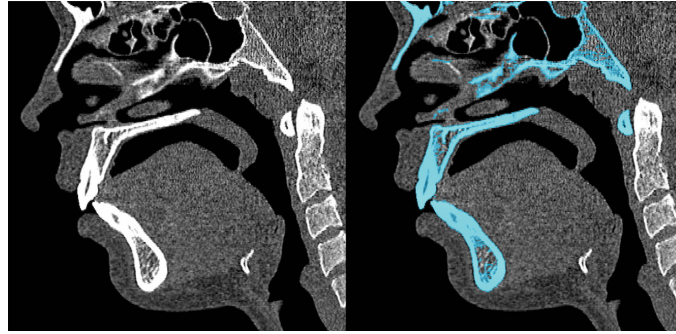


FIGURE 2.4 – Segmentation of the skull after removing the spine

2.2.2 Mesh Generation : 3D surface reconstruction

A CT-Scan is a collection of slices like Figures 2.2, 2.3 or 2.4. From all these 2D images that are manually segmented, we can obtain a 3D representation of an object of interest, here the skull, the face and the masseter muscle.

The generation of a 3D triangular mesh from discrete volumetric data is generally called *isosurface extraction* [32]. The standard tool used for isosurface extraction is the « Marching Cubes » algorithm, introduced in [134]. The algorithm takes as input a cubic lattice T with an implicit function ϕ defined at each T vertex. In our context, the lattice is given by the set of voxels in which the discrete volumetric data are placed. The binary function ϕ is defined to be positive at a given vertex if it belongs to the considered label, negative otherwise. First, when a T edge is composed of two opposite sign ends, a mesh vertex is created along the edge. Secondly, the previously defined mesh vertices are connected by triangles.

Despite the simplicity of this classic method of « Marching Cubes », it is well known that sometimes it can produce topologically ambiguous configurations or artificial holes, leading to invalid triangulation. To address these problems, several variants have been developed [58, 122, 149, 155, 161, 248, 250]. For this work, we used the algorithm available in the Amira software [197].

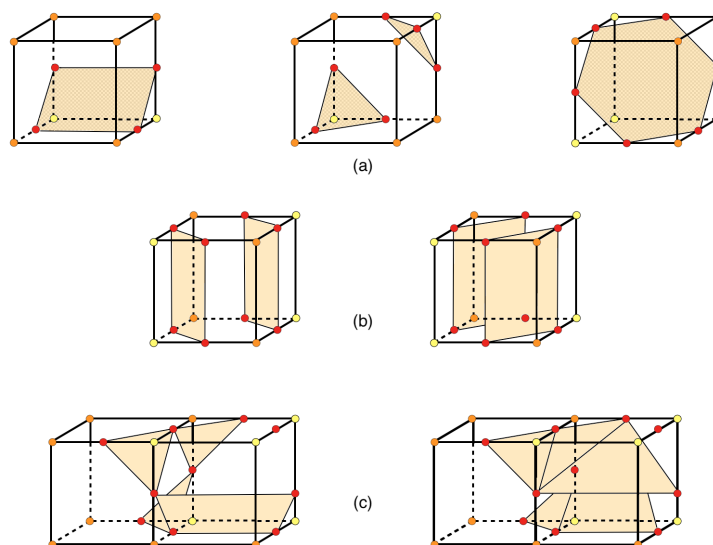


FIGURE 2.5 – Some example of isosurface-cell intersection in the Marching Cubes algorithm.

In Figure 2.5, we show some example of isosurface-cell intersection in the Marching Cubes algorithm. The yellow (respectively orange) dots correspond to positive (respectively negative) values of ϕ . The orange zone corresponds to the reconstructed surface patch. The whole isosurface is constructed by gluing the local patches. The first line of the Figure 2.5 (a) show some examples of configurations from the look-up table of Marching Cubes algorithm [134]. The second line (b) present a configuration from the look-up table of Marching Cubes algorithm [134] presenting a topological ambiguity. The grey zones correspond to two possible connections associated to the same configuration. At last, the bottom line (c) Topological incoherence generated from the look-up table of Marching Cubes original algorithm [134] (left) and repairing (right).

2.2.3 Mesh and remesh

To represent a 3D object, we thus use a triangular surface mesh. As pointed out in the previous section, triangulations obtained from « Marching Cubes » procedure contain, in general, a lot of ill-shaped elements which are redundant and oversampled to correctly describe the geometry of the model for computation. We are thus confronted with a problem of surface remeshing. The quality of a triangulation is strongly related to the targeted application and can involve vertex sampling, regularity, complexity, size of the elements or shape. Very often, the initial triangulation provided as a support for the geometry knowledge is not appropriate for a numerical computation due to very poor quality elements. It is therefore important to assure that each item of the database has a valid mesh.

Generally, the remeshing procedure aims at providing a correct and accurate geometric approximation of the underlying 3D model, and a computational mesh of high quality elements suitable for finite elements simulations. We discuss here only some basic ideas, see [5] for further references.

Software like *mmg* [50, 57] for the remeshing process can be used with the appropriate parameters, in order to obtain a valid mesh with a computable number of triangles. The parameters we considered were :

- the minimum (h_{min}) and maximum (h_{max}) size of an element that can be used for remeshing,
- the Hausdorff distance (h_{hausd}), which controls the proximity authorized between the original mesh and its remeshing,
- the mesh gradation (h_{grad}), i.e. the size variation between neighboring elements.

One of the most important parameter is the Hausdorff distance, which defines the tolerance we accept between the input and the output mesh.

Let (X, d) be a complete metric space, and $K(X)$ all the compacts set of X . Let A and B be compacts set of $K(X)$, we use $d_A(x) = \inf_{a \in A} d(a, x)$ the distance at A . We define their Hausdorff distance by :

$$\partial(A, B) = \max(\sup_{a \in A} d_B(a), \sup_{b \in B} d_A(b)).$$

According to the inferred geometric information and the input defined by the user parameters the method constructs an isotropic metric size map, to which the final mesh is adapted.

Figure 2.6 illustrates the remeshing process and influence of the Hausdorff distance parameter over the remeshing procedure. This value is chosen according to the tolerance allowed in the segmentation process. As illustrated in this same figure, the remeshing procedure also removes the « staircases » artefacts due to the spatial discretization and connectivity.

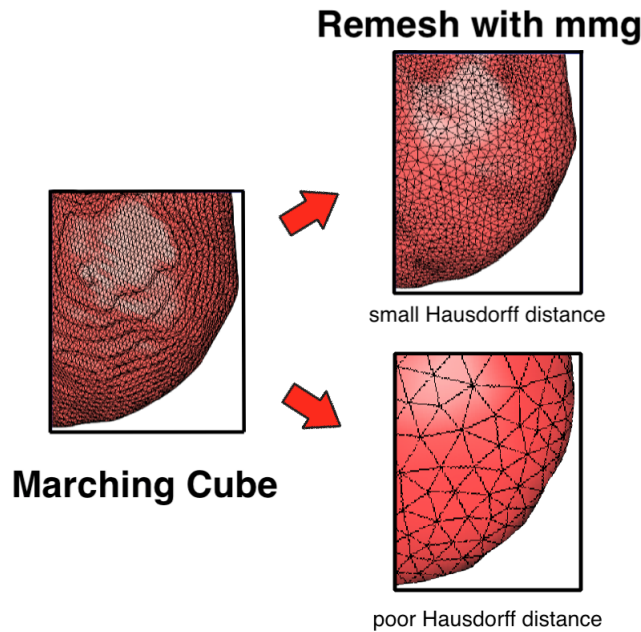


FIGURE 2.6 – A part of a 3D mesh of a masseter muscle, extracted from Amira Software with the marching cube algorithm, on the right; and remesh with mmg, on the left, with a small Hausdorff distance parameters (top), or with a poor Hausdorff distance parameters (bottom).

2.2.4 Alignment

A recurring problem in areas that use three-dimensional object databases, the alignment step is really important to « standardise » data and to be able to provide a better model. Indeed to compare our data we first need to realize that there is no identical data up to a rigid movement and an homothety.

A rigid movement is defined as a transformation that, when acting on a vector v , produces a transformed vector $T(v)$ of the form :

$$T(v) = Rv + L \text{ where } R^T = R^{-1} \text{ is a rotation,} \quad (2.1)$$

with L a vector representing a translation of the origin.

An homothety can be defined as a transformation of an affine space determined by a point S that refers to its center and a nonzero number λ that refers to its ratio, which gives

$$\forall M, M \mapsto S + \lambda \overrightarrow{SM}. \quad (2.2)$$

These transformations : rotation, translation and homothety are called similarities, and do not modify the shape of the object. Thus, once we have eliminated, the uncertainty generated by those similarities, we are certain to compare the shape of each object of the database. Therefore in practice, to be able to compare the shape of two 3D objects, we first need to center, scale and give them the right orientation accordingly.

Centering the objects at the origin

We call « centering the object », the translation of the object to the origin point $\vec{O} = (0, 0, 0)$.

In order to do that, we choose to compute the barycentric coordinates. And subtract them from the coordinates of all the object's points.

We write \vec{x} a point of \mathbb{R}^3 , with components (x_1, x_2, x_3) . Let \vec{x}^G be the barycenter of the object of interest Ω , we write (x_1^G, x_2^G, x_3^G) its coordinates. We have :

$$\vec{x}^G = \frac{1}{|\Omega|} \int_{\Omega} \vec{x} dx, \quad (2.3)$$

with $\vec{x} \in \Omega$ and $|\Omega|$ the volume of Ω .

With the consideration of the first component of \vec{x}^G , and we note that $x_1 = \text{div}((\frac{x_1^2}{2}, 0, 0))$, then from the divergence-formula we have $\int_{\Omega} \text{div}(\vec{u}) d\vec{x} = \int_{\partial\Omega} \vec{u} \cdot \vec{n} d\sigma$ with \vec{n} being the exterior normal to the surface of Ω , with components (n_1, n_2, n_3) , allows to transform a volumetric integral to a surfacic one. We have :

$$x_1^G = \frac{1}{2|\Omega|} \int_{\partial\Omega} x_1^2 n_1 d\sigma. \quad (2.4)$$

By discretizing on our mesh, and we get :

$$x_1^G = \frac{1}{2|\Omega|} \sum_i x_{i,1}^2 n_{i,1} d\sigma_i, \quad (2.5)$$

with $d\sigma_i$ the area of the triangle of interest.

We proceed similarly for x_2^G and x_3^G . We thus obtain the barycentric coordinates of Ω , which we can subtract from the coordinates of all the points x of Ω to center up our object at the origin.

Rotation : alignment of inertia axes

In a second step, we wish to orient all our objects accordingly. The goal is to be able to identify as a unique object two surface-meshes which would only differ from a rotation.

Let Ω be a domain containing the origin \vec{O} as barycenter. The angular momentum of Ω in relation to a direction axis \vec{d} when the solid is rotating around \vec{d} is given by :

$$M(\vec{d}) = \int_{\Omega} \vec{x} \wedge \omega(\vec{x})(\vec{d} \wedge \vec{x}) d\vec{x} \quad (2.6)$$

with ω being the angular velocity, $\vec{d} \wedge \vec{x}$ being the direction vector of the displacement of the particle \vec{x} (instantaneous direction). This is a generalisation of the formula giving the angular velocity of a sum of particles. Therefore :

$$M(\vec{d}) = \omega I_{\Omega} \vec{d}, \quad (2.7)$$

where I_{Ω} is the inertia matrix.

$$I_{\Omega} = \int_{\Omega} (|\vec{x}|^2 Id - \vec{x} \otimes \vec{x}) d\vec{x}, \quad (2.8)$$

with Id the identity matrix, and $\vec{x} \otimes \vec{x}$ the matrix $\vec{x} \cdot \vec{x}^T$.

Proposition 2.2.1 The inertia matrix I_{Ω} is symmetric, positive definite, therefore diagonalisable in an orthogonal basis.

Along the components, the inertia matrix is written as :

$$I_{\Omega_{3,3}} = \int_{\Omega} (x_1^2 + x_2^2 + x_3^2) - x_3^2 dx_1 dx_2 dx_3, \quad (2.9)$$

$$= \int_{\Omega} (x_1^2 + x_2^2) dx_1 dx_2 dx_3. \quad (2.10)$$

Then we obtain :

$$I_{\Omega_{1,1}} = \int_{\Omega} (x_2^2 + x_3^2) dx_1 dx_2 dx_3, \quad (2.11)$$

$$I_{\Omega_{2,2}} = \int_{\Omega} (x_1^2 + x_3^2) dx_1 dx_2 dx_3, \quad (2.12)$$

$$(2.13)$$

And :

$$I_{\Omega_{1,2}} = - \int_{\Omega} x_1 x_2 dx_1 dx_2 dx_3, \quad (2.14)$$

$$I_{\Omega_{1,3}} = - \int_{\Omega} x_1 x_3 dx_1 dx_2 dx_3, \quad (2.15)$$

$$I_{\Omega_{2,3}} = - \int_{\Omega} x_2 x_3 dx_1 dx_2 dx_3. \quad (2.16)$$

$$(2.17)$$

Computation of the coefficients of I_{Ω} : we transform the expressions below using the Green formula, similarly as the barycenter.

For instance :

$$I_{\Omega_{1,2}} = - \int_{\Omega} \operatorname{div} \begin{pmatrix} 0 \\ 0 \\ x_1 x_2 x_3 \end{pmatrix} dx_1 dx_2 dx_3 \quad (2.18)$$

$$= - \int_{\partial\Omega} x_1 x_2 x_3 n_3 dx_1 dx_2 dx_3. \quad (2.19)$$

The same holds for the other components.

After discretization, as for the barycenter, we obtain for (2.19) :

$$I_{\Omega_{x_i,1x_i,2}} = \sum_i x_{i,1} x_{i,2} x_{i,3} n_{i,3} d\sigma_i \quad (2.20)$$

Using these discretized formula, we implemented this procedure on a simple case first (Figure 2.7). The same 3D brick has been rotated in three different orientations on the right of first line of this figure and, after using our algorithm, they are all set back the same direction as the brick of the left of the figure, on the bottom line.

In Figure 2.8 we give another exemple, more specific to our problem and a less obvious than the previous one : the masseter muscle.

This whole process is quite useful to detect rigid motion differences between two objects and align them. However in some cases, depending on the goal, we need more accuracy on a specific part of the object. For example on our CT-Scan, we are interested in aligning more specifically the eyes, the nose, or/and the mouth more than the whole head, especially when the acquisition parameters or the position of the patients are not all the time the same, hence affecting the data. In this case, we can add a last step, presented below.

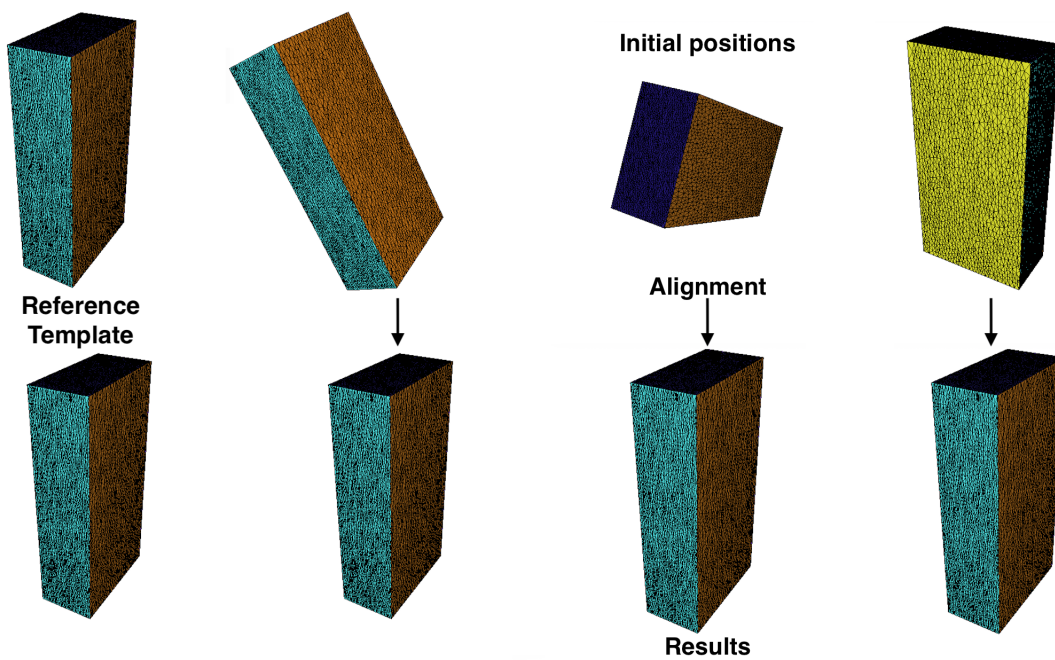


FIGURE 2.7 – Alignment of a 3D pavement after using this method

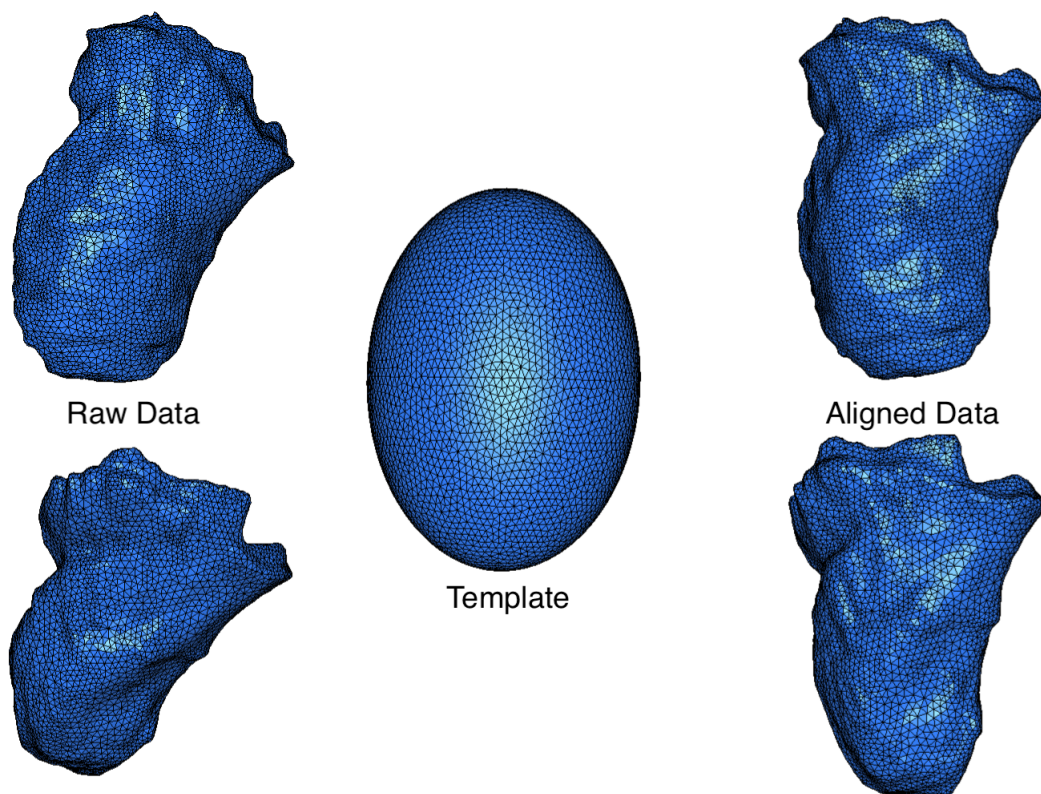


FIGURE 2.8 – Alignment of 2 masseters with an ellipsoid template : on the left column the raw muscles after remeshing ; on the right after the alignment process on the ellipsoid template (in the middle).

Iterative closest point (ICP)

This algorithm (ICP) is employed to minimise the difference between two clouds of points. One is the fixed target, while the other one (the source) is aligned to best match the reference. This algorithm iteratively transforms (through translations and rotations) the clouds of points of the source to minimise the distance between two clouds i.e. the sum of the squared differences between the coordinates of the matched pairs is minimised.

This method was first introduced by [27]. As suggested in the section above, we can use the ICP algorithm to obtain a better accuracy : indeed for the same « face » example we can only select the points of the region of interest, and make the others follow the same transformation.

However, if the first two steps are not performed before, i.e. the translation and the rotation, this algorithm may fail. Indeed, a first good initialization is essential to the ICP algorithm for an pertinent result. Most of the time this is done via landmarks selection (semantically identifiable point on the object), but in our facial reconstruction and segmentation applications, it was precisely important to get rid of it. This is one of the interesting points of this fully automatic method of processing 3D data for a reduced shape basis : the matching of shapes is not done by a selection of landmarks.

2.3 Function-to-shape representation

In order to make the link between the items of our database and to be able to summarize information, we need a way to compare them. The preprocessing of the data was needed to eliminate identical cases which differ only from size or alignment, and obtain a smaller Kolmogorov dimension of the object family. This being done, in order to find a way to summarize the information, we need comparable meshes with the same number of points, triangles, and with the same topology for each object of the database.

The idea being to be able to match all objects of the same type in the database, such as skulls for example. As we have decided not to select landmarks, we will define semi-landmarks, via a dense mesh used as a deformed template on all objects in the database. For that we propose as a model an elastic shape matching from a reference shape Ω_0 to each object of the database Ω_{T_j} . A supplementary step is needed before if the object is not closed. This case does not appear in the face or muscle case, but for creating a database of skull one would need to perform this first warping step.

2.3.1 Warping (if necessary)

As mentioned above, if the object of interest is not closed, this step is mandatory before performing the elastic shape matching. A relevant example of this problem, in our case, is the skull (Figure 2.9).

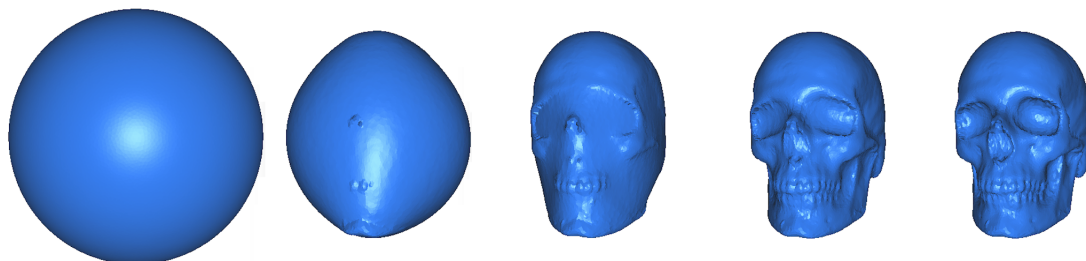


FIGURE 2.9 – Warping a skull from a sphere

Warping, as described in [158], is a tool allowing to define a closed surface model from an unorganized source model. In this context, we focus on the reconstruction of a connected shape starting from the discrete data of a source triangulation. Such a triangulation could present one or more undesirable particularities : invalid, not closed, or topologically intersected, etc. Here we use an algorithm based on mesh deformation techniques, where a closed surface mesh model is iteratively deformed, producing a sequence of surfaces which are "closer and closer" to the source triangulation, in the sense of the Hausdorff distance.

2.3.2 Morphing

This step really enables us to describe and put in correspondance every object of the database. Once performed, we will no longer consider a database of 3D mesh objects but of displacement a function with the same number of components for every object.

The aim of a morphing algorithm is to transport a template to a source object by minimising a shape functional, as described in more details [34, 158], and also in the Chapter 6 of this thesis.

For reasons detailed in Chapter 6, this algorithm need a volumic mesh to be processed. Indeed, we have shown that surfaced morphing is not very reliable for complex shapes and is difficult to implement in 3D, so choosing volume morphing is simpler and faster. Thus we add a brief step of 3D meshing of the surface shape database. We can briefly described the used method as follow.

Let Ω_0 and $\Omega_T \subset \mathbb{R}^d$ be respectively our ellipsoid template E (Figure 2.10) and one "target" masseter of our data T_i . As they share the same topology, our purpose is to map Ω_0 onto Ω_T by minimising an energy functional which measures the discrepancy between the shapes. In order to achieve our goal, we introduce the following functional $J(\Omega)$:

$$J(\Omega) = \int_{\Omega} d_{\Omega_T} dx, \quad (2.21)$$

where $\Omega = F(\Omega_0)$ the ensemble of eligible shapes for F the elastic transformation, and d_{Ω_T} is the signed distance function to Ω_T , defined as :

$$\forall x \in \mathbb{R}^d, d_{\Omega_T}(x) = \begin{cases} -d(x, \partial\Omega_T) & \text{if } x \in \Omega_T, \\ 0 & \text{if } x \in \partial\Omega_T, \\ d(x, \partial\Omega_T) & \text{if } x \in {}^c\Omega_T. \end{cases} \quad (2.22)$$

In order to decrease the value of $J(\Omega)$, the domain Ω must expand in the regions of the ambient space \mathbb{R}^d where d_{Ω_T} is negative, and to retract in those where it is positive. By deforming the template shape as above we can always obtain better values for J until the deformed template shape reaches the target shape Ω_T .

Using a classical calculation (see [3, 96]), the functional (2.21) is shape differentiable at any masseter shape $\Omega \in O_{ad}$, with O_{ad} a set of admissible shape, and the associated shape derivatives reads :

$$\forall \theta \in W^{1,\infty}(\mathbb{R}^d, \mathbb{R}^d), J'(\Omega)(\theta) = \int_{\partial\Omega} d_{\Omega_T} \theta \cdot n ds. \quad (2.23)$$

Then a descent direction is inferred from previous formulas and an iterative algorithm devoted to the minimisation of J produces a sequence of shapes which are 'closer and closer' to Ω_T .

First we fill all the considered shapes Ω with a linear elastic material. Then, we assume that any such shape Ω contains a given subset $\omega \Subset \Omega$ on which it is clamped. We now obtain a descent direction for $J(\Omega)$ as the unique solution u_{Ω} belonging to $H_{\omega}^1(\Omega)^d := \{v \in H^1(\Omega)^d, v = 0 \text{ on } \omega\}$

the variational problem :

$$\forall v \in H_{\omega}^1(\Omega)^d, \int_{\Omega} \sigma(u_{\Omega}) : \varepsilon(v) dx = -J'(\Omega)(v) = - \int_{\partial\Omega} d_{\Omega_T} v \cdot n ds. \quad (2.24)$$

where $\varepsilon(v) = \frac{1}{2}(\nabla v + \nabla v^T)$ is the linearised strain tensor and σ is the associated stress tensor via the Hooke's law with Lamé coefficients λ, μ :

$$\sigma(u) = 2\mu\varepsilon(u) + \lambda \operatorname{tr}(\varepsilon(u))I. \quad (2.25)$$

Figure 2.10 shows our ellipsoid template E which is deformed on 3 target shape T_1, T_2, T_3 , and we obtain three result shapes F_1, F_2, F_3 described by their displacement function u_1, u_2, u_3 .

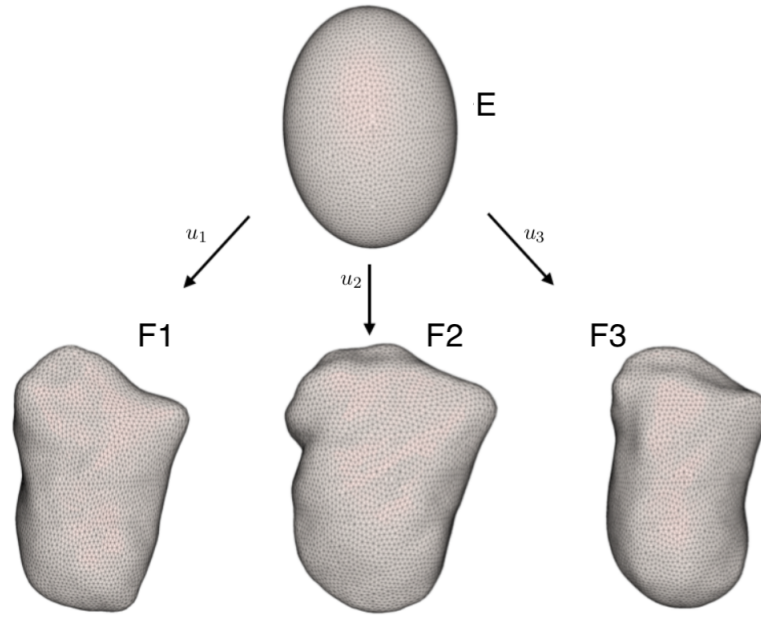


FIGURE 2.10 – Ellipsoid map with elastic morphing to three masseter muscles

At the end of this step, each of the shapes in our database is no longer described by its original mesh obtained by a Marching Cube algorithm, but by the mesh of a reference deformed by elastic morphing. The high density of the template mesh and the prior alignment of the shapes between them allows us to consider each shape in point-to-point correspondence. It is important to note that at this stage, only the surface mesh is retained, the inner tetrahedrons being added only to facilitate the numerical calculation of the elastic morphing.

2.3.3 Parametrization : Dimension Reduction

We can now consider each object of the database as a surfacic displacement u of the reference mesh to each of them. To extract the information of this displacement database, we choose to performe a parametrization. At first with a PCA method, because it is a well known method easy to implement. Then a second time to be more coherent, and keep all the process deterministic, we present a greedy method.

Principal Components Analysis

PCA is a method used to reduce the complexity of the data, if it is in space with a small Kolmogorov dimension. This allows for a large number (in our case we have acquired 126 snapshots) of similar functions u_k to be represented with just a handful of well-chosen linearly combined components.

It involves computing the variance-covariance matrix A with entries $a_{k\ell} = \langle u_k, u_\ell \rangle$ (where $\langle \cdot, \cdot \rangle$ stands for an appropriate scalar product in the space of anatomical displacement items u). Then we extract the eigenvectors and eigenvalues of A sorted in decreasing order, and construct the reduced basis :

$$\varphi_\ell = \sum_{k=1}^{126} v_k^\ell u_k, \quad (2.26)$$

where v_k^ℓ are the components of the ℓ the eigenvectors of A , where we retain only the first few ones : $\ell = 1, \dots, n, n \ll 126$.

These modes allow to approximate, by linear combination, all the other object of the database :

$$\alpha_1^k \varphi_1 + \alpha_2^k \varphi_2 + \dots + \alpha_n^k \varphi_n, \quad (2.27)$$

where $\alpha_\ell^k = \frac{\sum \langle u_k, \varphi_\ell \rangle}{\sum \langle \varphi_\ell, \varphi_\ell \rangle}$ is a good approximation of each u_k with very few modes (n of the order of 5). Thus an approximation of an unknown muscle can be proposed by determining its coefficients α_ℓ , $\ell = 1, \dots, n$.

At first we used the L_2 scalar product to compute the matrix A , and we obtained the presented decrease of eigenvalues, Figure 2.11.

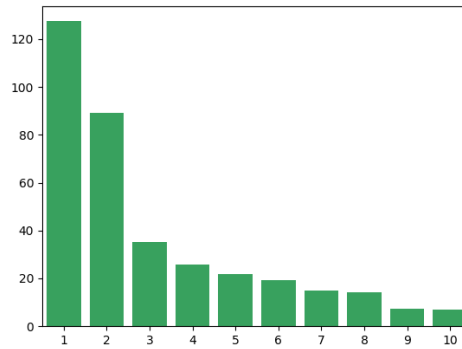


FIGURE 2.11 – Decrease of the 10 first eigenvalues for our masseter muscles example

A possible improvement, to expect a better representation of the eigenvalues, would be to use the H_1 scalar product. Nevertheless it is necessary to compute the gradient in this case, and it needs to be done during the resolution of the elastic morphing.

Once the whole process is performed, from the data acquisition to the PCA, we only need a few coefficients (n between 5 and 15 depending the precision needed and the application) to describe an object like the masseter muscle for exemple, instead of 5000 3D coordinates of the mesh points.

Table 2.1 presents the discrepancies between the different reconstructions and the target morphed masseter, using 5, 10 and 20 coefficients. On the left, we can see the error computed with all the element in the database used for performing the PCA. On the right, the PCA modes were computed without the masseter reconstructed, for which we compute the error.

The visualisation of those errors is shown in the next section called « 3D Visualisation ».

TABLE 2.1 – Discrepancies between reconstructions and target, using PCA algorithme

	Leave-All-in			Leave-One-Out		
	5 coef	10 coef	20 coef	5 coef	10 coef	20 coef
Mean	0.95495	0.50475	0.30059	1.01208	0.55879	0.37108
SD	0.27560	0.10551	0.04472	0.30112	0.13366	0.08206
Min	0.47886	0.31587	0.20424	0.49172	0.34276	0.22627
Max	2.04961	0.86739	0.45761	2.10330	1.04464	0.69908

Greedy Algorithm

From the series of snapshots of masseters M_i , $i = 1, \dots, N$, that we have, we want to extract a different basis, better suited to our futur goal.

We first choose a « representative masseter » as being the first element in the basis, we name this masseter M_1^* . The choice of M_1^* can be random, or it can be the object that best represents all the others (i.e. it minimizes the projection error on each member of the database).

We then approximate each masseter M_i in the vectorial space spanned by M_0

$$M_i \simeq \lambda_1^i M_1^*$$

with a coefficient λ_1^i fitted so that the points that are selected on M_i are best approximated (in a mean square sense) by $\lambda_1^i M_1^*$.

Let us define by M_2^* the masseter that is the worse approximated (everywhere, and not only in the reliability region) by $\lambda_1^i M_1^*$.

We have now a two dimensional approximation by combining M_1^* and M_2^*

We proceed recursively by defining, at step k an approximation

$$M_i \simeq \sum_{j=1}^k \lambda_j^i M_j^*$$

where the coefficients λ_j^i are fitted so that M_i are best approximated (in a mean square sense) by $\sum_{j=1}^k \lambda_j^i M_j^*$.

and M_{k+1}^* is chosen as being the masseter that is the worse approximated by $\sum_{j=1}^k \lambda_j^i M_j^*$.

Table 2.2 presents the discrepancies between the different reconstructions and the target morphed masseter, using 5, 10 and 20 coefficients. On the left, we can see the error computed with all the element in the database used for performing the Greedy algorithm. This explained why the minimum of the error is 0. On the right, the Greedy modes were computed without the masseter reconstructed, for which we compute the error.

TABLE 2.2 – Discrepancies between reconstructions and target, using Greedy algorithme

	Leave-All-in			Leave-One-Out		
	5 coef	10 coef	20 coef	5 coef	10 coef	20 coef
Mean	1.23136	0.66722	0.39767	1.30032	0.75220	0.49460
SD	0.42973	0.24113	0.18634	0.38255	0.19295	0.10824
Min	0.00000	0.00000	0.00000	0.52633	0.33344	0.24367
Max	2.27286	1.15129	0.65106	2.47522	1.44458	0.99699

The visualisation of those errors is shown in the next section called « 3D Visualisation ».

3D Visualisation

We can see on Figures 2.12 and 2.13, the respective reconstructions of two masseters, one being in the database we used for the reconstruction of the modes, the next one not being part of this database. For each of these figures, the top line corresponds to the reconstruction made using the PCA modes and the bottom line is made using the Greedy modes.

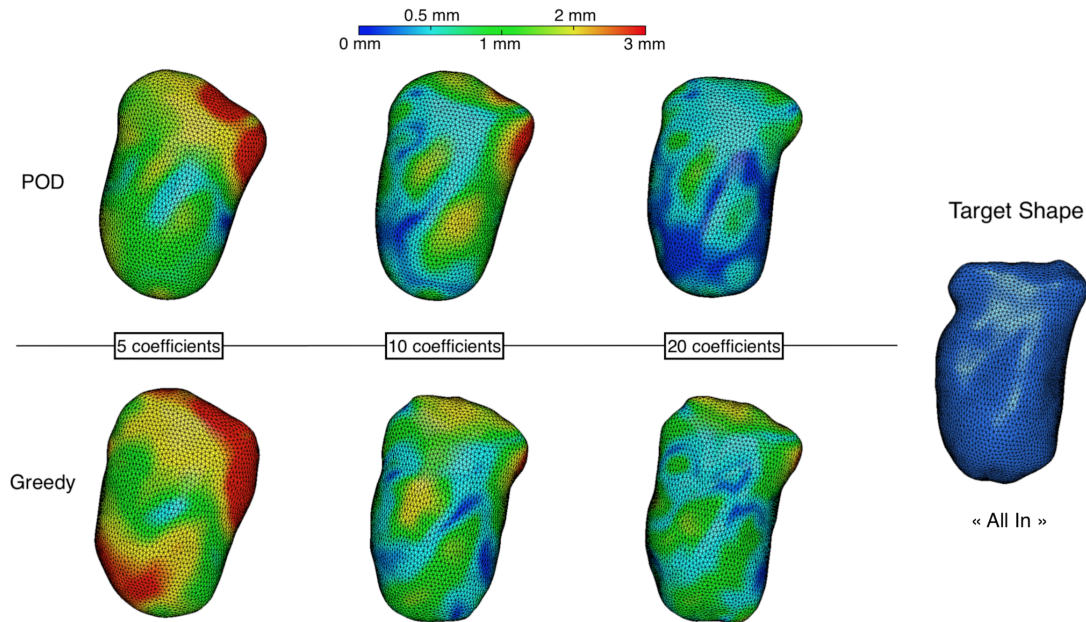


FIGURE 2.12 – One object **in** our reduced basis reconstructed with 5, 10 and 20 coefficients with the POD method on the top and with the Greedy one on the bottom. On the right the control

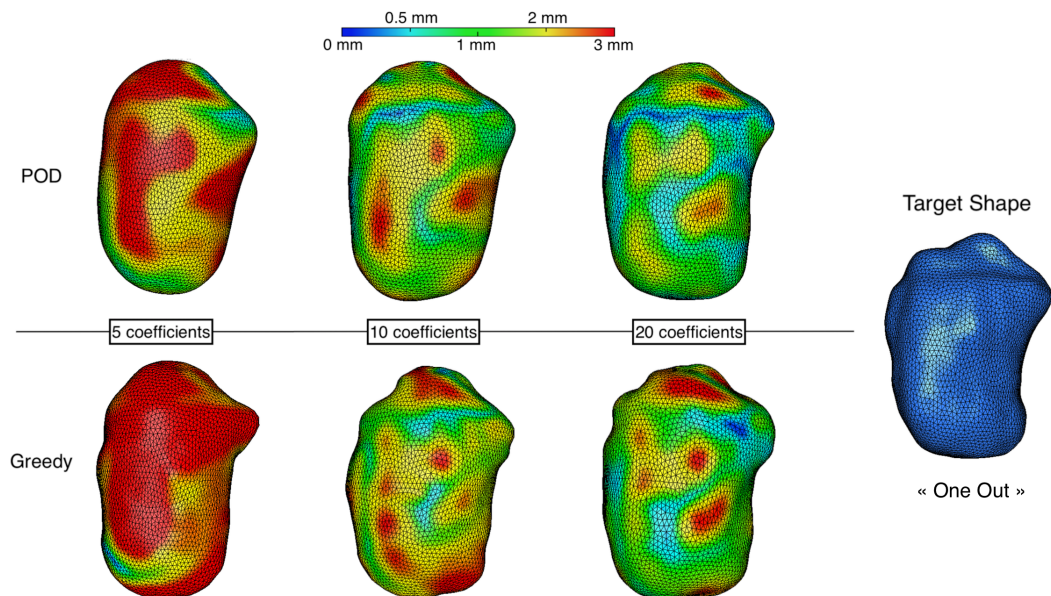


FIGURE 2.13 – A other object **out** of our reduced basis reconstructed with 5, 10 and 20 coefficients with the POD method on the top and with the Greedy one on the bottom. On the right the control

These visual results confirm those shown in the error tables above :

- we can see that the results are better when the object to be reconstructed is itself in the database
- the POD method seem to prove more efficient for the « best reconstruction » possible here,
- using 20 coefficients of 126 element in the database, most of the error is under 0.5 - 1mm in the Figure 2.12, and under 1 mm for the Figure 2.13.

From this easy description of an anatomical object, different applications can be developed, in the next section, we briefly introduce two of them.

2.4 Application of reduces basis of 3D shapes

2.4.1 Shape prediction of anatomical element

It is possible to learn the coefficients α_ℓ , $\ell = 1, \dots, n$, from a training set, which links two objects of the database. In our example of the masseter, we know from the previous chapter, that the shape of this muscle depends a lot of the skull shape. So if we have 2 reduced basis of 3D shapes, one for the muscle and one for the skull, computed from the same CT-scan data set, we can learn the coefficient α of the muscle from the ones of the skull. And so, create muscles from the only knowledge of the skull.

$$m_k \xrightarrow{\mathcal{L}} \alpha_i^k,$$

where m_k are measurments of the known object or their own α coefficients extracted from the previous process, \mathcal{L} a machine learning process (like a neural network), and α_i^k the coefficients we want to obtain by learning.

This application is detailed in a full section of the Chapter 7, for facial reconstruction.

2.4.2 Segmentation and reconstruction

Segmentation of soft tissus

As already mentioned before, segmentation of soft tissues is a difficult process. But the ability of describing an object like a muscle with only few coefficients to identify, can make the whole process easier. Indeed by selecting only a few points on medical images, we can resolve a linear problem which gives us these α coefficients, and let us reconstruct the expected shape on the image.

All this process is described in details in the next part of this thesis.

Facial Reconstruction

The process of facial reconstruction involves giving an approximation of the face of an unknown person from the only knowledge of its skull shape. An adequate database for Facial reconstruction must contain couples of faces and skulls coming from an healthy individual together with anthropological parameters like age, sex, Body Mass Index (BMI). Since computer science emerge in forensic sciences, this imply a database of skulls, faces and even muscles 3D shapes linked to each other.

Our method can be a really good way to treat those datas and can also be useful for the facial reconstruction application itself. Once the database is acquired as described before, it becomes possible with only some mesurements on the skull (or just with the 3D shape of the skull bones) to reconstruct muscles and/or faces.

All this process is described in details in the last part of this thesis, in the Chapter 7.

2.5 Conclusion

This chapter presents a way to describe a 3D shapes database with a reduced basis, after performing some preprocessing step, starting from segmentation. Even if most of the tools presented

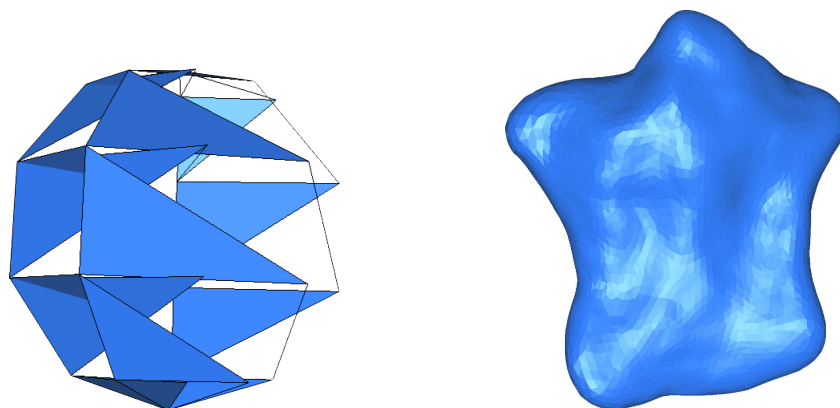
in this chapter are usually used in this kind of process to create anatomical atlas, some points nevertheless deserve a particular interest. First all the method is devoted to be fully automatic, and this without selecting landmarks. In addition, the whole procedure is based on a purely deterministic approach, which allows us to build a database of dense three-dimensional surface meshes. Unlike most of the « statistical atlases » described in the literature, which are based as their name suggests on statistical, and sometimes probabilistic, models. The PCA, proposed in this chapter, being thought of as a reduction of complexity, rather than as a statistical regularization, could also be a greedy algorithm.

To conclude we present two different applications, where this approach is efficient, which are detailed in the two next parts of this thesis.



Second Part : Segmentation

	Introduction	99
3	Proof-of-Concept in 2D	101
3.1	Introduction : State of the art	
3.2	Notation and problem setting.	
3.3	Numerical experiments in 2D	
3.4	First 3D numerical exploration	
3.5	Conclusions and Perspectives.	
4	Semi-automatic segmentation method in 3D	115
4.1	Introduction	
4.2	Modes in the reference configuration	
4.3	Overview of the method for 3D segmentation in a real case	
4.4	Application in a real case : the masseter segmentation	
4.5	Discussion and Conclusion	
5	Pratical Application	127
5.1	Introduction	
5.2	Materiels and Methods	
5.3	Results	
5.4	Discussion	
5.5	Conclusion	



INTRODUCTION PART II

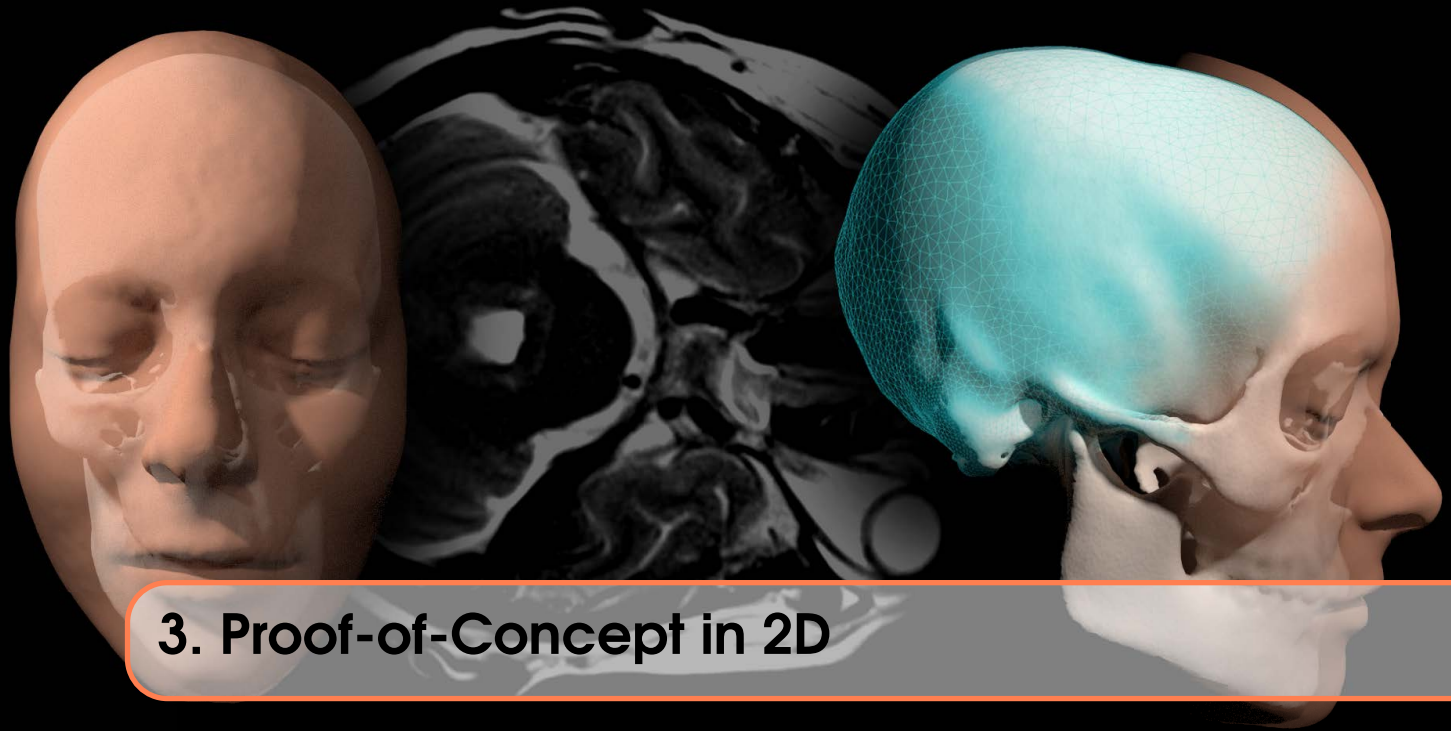
This second part contains three chapters, and constitutes the work done on semi-automatic segmentation, that found its motivation during this thesis. Indeed, the significant lack of data, resulting from the fact that the segmentation involves human treatment during the final learning phase of Chapter 2 obviously penalize the results. It led us to focus on this new subject, for which the availability of the reduced models is a basic ingredient, although it is not the main subject of the thesis.

The first chapter of this part, chapter 3 of the thesis, presents the concept we want to implement, for segmentation. A state of the art and a brief comparison of our results with existing methods is also presented. The short note extracted from this chapter appears in Appendix A. All the details and discussions associated with the method are presented and extended in the following more detailed chapter.

Chapter 4 of this thesis takes up the idea quickly outlined above, and details the method via a numerical analysis and an application on real case of medical image in three dimensions. Our method consists in selecting about fifty reliable and precise points at the edge of the object of interest, for us the muscle masseter, through the CT-scan slides. Then rebuilding the shape of the muscle based on the 3D database of shape already constituted during Chapter 2.

The last chapter of this part, chapter 5 of this thesis, is a practical application of this method, for which we have developed a software that allows physicians to use this tool, while allowing us to evaluate it. Two young medical practitioners, expert in anatomy of the maxillofacial region, but without specific skills in segmentation of medical images, performed with us this validation test. They have carried out manual and semi-automatic segmentations, which allowed us to set up a comparative study in a real situation. The results show a real time saving, and a preservation of the involvement of practitioners in the process without the need for training. This work is still under development, and the subsequent results are therefore to be interpreted with reserve.

**the nice figures presented above are the results of unfortunate numerical simulations carried out during the work on Chapter 4, and they also illustrate some of the difficulties of numerical implementation work.*



3. Proof-of-Concept in 2D

Sommaire

3.1	Introduction : State of the art	101
3.2	Notation and problem setting.	104
3.3	Numerical experiments in 2D	105
3.3.1	Reference configuration	105
3.3.2	Generation of the database set	106
3.3.3	Singular Values Decrease	106
3.3.4	Application and results	107
3.3.5	Reconstruction error	108
3.4	First 3D numerical exploration	108
3.4.1	Spherical harmonics - Definition in 3D	109
3.4.2	Parameterization of shapes	110
3.4.3	Reconstruction of a new shape	112
3.4.4	Analytic error	112
3.5	Conclusions and Perspectives.	113

Fast semi-automatic segmentation based on reduced basis

This work is a collaboration with Damiano Lombardi and Yvon Maday. The version accepted in Comptes Rendus Mathématique de l'Académie des Sciences of this work is presented in the first appendix of this thesis. Indeed the short format of this review did not allow to detail as much as it was necessary here.

3.1 Introduction : State of the art

One of the recurring and time consuming challenges in medical imaging is the segmentation of parts of interest. Segmentation of medical images consists in identifying and labelling the voxels

(3D pixels) of the entire image or object of interest [68]. This has been for years, the effort of specialists and it is quite time consuming. In Figure 3.1, we try to illustrate this both definition : voxel and segmentation.

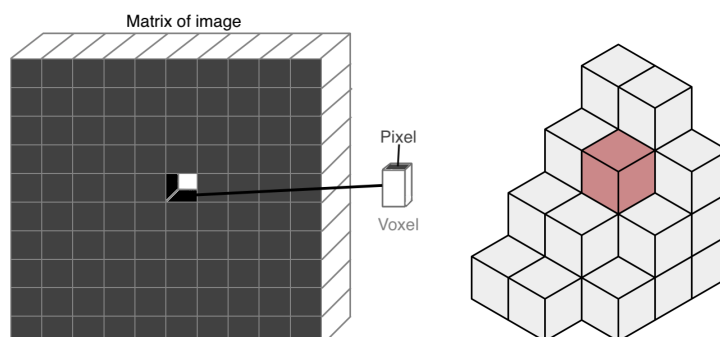


FIGURE 3.1 – On the left, we illustrate the definition of a scanner image as a 3D matrix whose unitary element is the voxel ; and on the right is shown the selection of one of these voxels in red, which corresponds to the segmentation process.

Beyond the specifics task of each particular application, the general issue is to find a way to identify automatically an anatomical region of interest in order to speed up the process. Indeed automatic or semi-automatic segmentation methods have a wider scope of application. For example, they are widely used in « computer-assisted diagnosis », which has become one of the main research topics in medical imaging and radiology [59, 60, 62, 70, 217] in recent decades. In the 1980s, the concept of automatic or computer-assisted diagnosis was already known from studies dating back to the 1960s : [19, 132, 150], but these first attempts were not a real success. Indeed, the automatic detection of organs or lesions has proven extremely difficult.

Nowadays, techniques are more and more numerous, partly thanks to the technological development of computers and acquisition methods. When the contrast is high enough (e.g. for bones, or between bones and tissues) automatic segmentation is quite efficient and various methods are proposed and implemented [115, 175, 262]. One automatic segmentation example is shown in Figure 3.2 (b). Likewise for anatomical major organs like the brain or the heart [16, 33, 196], which have always aroused great interest among carers. On the contrary, when the contrast is not high enough (e.g. segmentation between different soft tissues on CT scans) the most common imaging modalities fail and there are very few approaches available. One manual segmentation exemple of soft tissues is show, Figure 3.2 (c).

The common methods of use for these types of applications are the so-called thresholding or edge detection methods. The first consists in grouping in the same label the pixels which have a close grey level or more exactly contained by one or more threshold values [176]. The second, which also relies on the detection of grey levels, looks for the boundaries of anatomical regions by analyzing the rapid transitions of these levels, and assembles the homogeneous voxels into a single label [133]. These two methods are based on the detection of grey levels, which allows experts to differentiate two anatomical regions and perform manual segmentation [170]. This type of strategy, mimicking the knowledge of experts, is the first to be implemented. They are simple and effective approaches to segment anatomical details featured by high contrast, as, for instance, the bones (that appear as light objects on dark background). However it is more challenging for the detection of objects that do not have a marked gray scale signature, as the muscles. Different classifications of these methods exist, for example, we can quote [94, 131, 258].

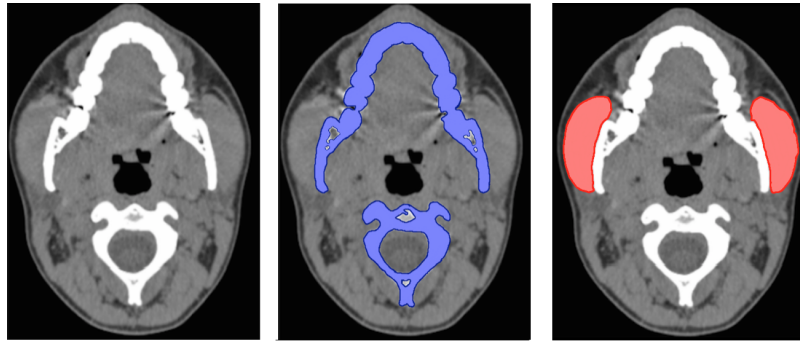


FIGURE 3.2 – Segmentation examples : (a) an axial CT-Scan image of a head, (b) an automatique segmentation of the skull, and (c) a manual segmentation of the masseter muscle.

Therefore, more recently, other types of methods have gradually developed, such as deformable models, guided atlases or the massive use of machine learning. They differ, among other things, by the amount of knowledge *a priori* injected into the method [40].

Statistical atlases use as a reference one or more already segmented structures used as prior knowledge for new segmentations [105, 180]. The segmentation of a new image is then based on a registration and deformation that allows to define an optimal transformation between the atlas and the new image. Different types of algorithms exist to optimize the deformation [6, 173, 223], or the use of the atlas itself [2, 45, 259]. These segmentation methods have proven effective in major segmentation competitions organized by « the American Association of Physicists in Medicine », or « the Medical Image Computing and Computer-Assisted Intervention Society ».

Deformable models require more information *a priori*. When the latter are available, characteristic variations in the interest structure shape can be used to statistical shape models. This limits the results obtained from segmentations to anatomically plausible shapes [94]. However, these methods are also less flexible for the reason mentioned above. In addition, the size and content of the training data also limits the performance of the results. This method is still frequently used for pelvic anatomical structures [72, 127, 187].

Statistical learning, applied to image segmentation, groups together a wide range of methods in full swing, such as machine vector support, decision trees, deep learning or neural networks [110, 218]. These are already found in multiple applications such as tumor segmentation in the brain, or in the liver, etc [126, 143, 151, 183]. The results obtained by these algorithms are promising for the applications for which they are developed. But it is not always obvious to extend them to all types of images and often requires a large dataset in view of the human variability underlying the medical data [110].

It is important to keep in mind that most often segmentation methods are developed for a specific purpose, and it is important to note that there is, at least for the moment, no universal segmentation method. Each algorithm responds to a unique set of constraints and objectives, making the method implemented particularly interesting for a specific application and sometimes less so for others.

We propose here to develop a model based semi-automated method to help segmentation, which have most in common with the three last types of methods cited above. In particular, the shape of the object of interest is represented by an elastic deformation field of a reference configuration. A reduced basis representation of the object of interest is introduced, that exploits an *a posteriori* knowledge of a database of available segmentations. Given an image to be segmented, the elastic deformation field can be approximated as a linear combination of a small number of modes. This

provides, in turn, a powerful regularisation method and a significant speed-up of the procedure since only few appropriate points need to be selected by the user in order to define the field. We can find a similar idea in [25], but with a probabilistic point of view, and where all the modes of the PCA are used as a regularisation and not as a dimensional reduction. Moreover, PCA is here a quick way to make a first test which will be later, in chapter 4, replaced by a greedy algorithm, making the process entirely deterministic.

The proposed method is complementary to the ones exposed before, first because it requires some preliminary segmentations to « build » the reduced basis, and second because it can be used on indifferently on CT and MR image for any type of object, even the ones difficult to identify like soft tissues on a CT. This work remains a preliminary presentation of the concept in 2D and 3D, we wish to develop. Some details will be better explained in the next chapter, with more realistic and complex examples. While improving the points of weakness that could be highlighted from these first very simplified results.

The chapter is structured as follows : in Section 3.2, the problem and the notation are presented, in the next Section 3.3 some 2D numerical experiments are detailed, then Section 3.4 presents first 3D numerical results.

3.2 Notation and problem setting.

Most medical imaging modalities produces a gray-scale image, i.e. a function defined over a subset of \mathbb{R}^2 (or \mathbb{R}^3 for 3D imaging), $f : \mathbb{R}^2 \rightarrow [0, 1]$ associating a scalar value to each point of the space (denoted later on by $x = (x_1, x_2)$ (or by $x = (x_1, x_2, x_3)$ in 3D)). After a manual segmentation of a region of interest is performed, it is possible to model this region by using an elastic morphing that maps a reference object : e.g. an ellipse in \mathbb{R}^2 (or an ellipsoid in \mathbb{R}^3) onto the boundary of the two-dimensional (or three-dimensional) segmented region. In the present work, for the sake of simplicity, we will restrict to two-dimensional configurations. Having a collection of segmented objects (belonging to a coherent family) is equivalent to having a set of 2D elastic displacement fields mapping a same (reference) ellipse into the different segmented objects.

Let us assume that the reference configuration is an ellipse $E \subset \mathbb{R}^2$; a point $\xi \in \partial E$ is mapped through a displacement field into a point $\mathbf{x} \in \partial F \subset \mathbb{R}^2$, where F is the boundary of the segmented object. It holds :

$$\begin{cases} Id + u : E \rightarrow F \\ \xi \mapsto \mathbf{x} = \xi + u(\xi), \end{cases} \quad (3.1)$$

and $u \in H^1(E)$.

From an acquired database ¹ consisting of $N \in \mathbb{N}^*$ such elastic displacements : $\mathcal{D} = \{u^{(1)}, \dots, u^{(N)}\}$, let us assume that a set of $n \in \mathbb{N}^*$ Proper Orthogonal Decomposition (POD) modes is extracted :

$$\varphi_i : E \rightarrow F, \quad i = 1, \dots, n. \quad (3.2)$$

When a new image to be segmented is available, the unknown elastic displacement mapping the reference configuration onto the image can be approximated by using the POD basis as follows :

$$u \approx u_n = \sum_{i=1}^n \alpha_i \varphi_i. \quad (3.3)$$

The goal is to find the coefficients α_i in such a way that the reference ellipse, mapped by the displacement field $Id + u_n$ is as close as possible to the actual image, hence providing an already

1. This database is assumed to be large enough to represent well the full coherent family we are interested in.

good guess for the segmentation. In order to identify the coefficients α_i a semi-automated procedure is devised. The image does not correspond, in general, to the reference configuration (this would be the case in which $\alpha_i = 0, \forall i$). A number of $m \in \mathbb{N}^*$ points $\mathbf{x}^{(j)} \in \partial F$ is selected in which there is a discrepancy between the actual image and the reference configuration. Each of these points corresponds to an equation for the displacement field : there exists a $\xi_*^{(j)} \in \partial E$ such that :

$$\mathbf{x}^{(j)} = \xi_*^{(j)} + \sum_{i=1}^n \alpha_i \varphi_i(\xi_*^{(j)}), \quad j = 1, \dots, m. \quad (3.4)$$

This is a non-linear system of equations in the variables $\alpha_i, \xi_*^{(j)}$; however, if the points $\xi_*^{(j)}$ are known, this system is a linear system of equations for the coefficients α_i . In the present work, the points $\xi_*^{(j)}$ are chosen as the ones minimising the distance to the point $\mathbf{x}^{(j)}$ ² :

$$\xi_*^{(j)} = \arg \min_{\xi \in E} \|\mathbf{x}^{(j)} - \xi\|_{\ell^2}^2, \quad j = 1, \dots, m. \quad (3.5)$$

This corresponds to a regularisation for the solution of the non-linear system Eq.(3.4). The linear system to be solved reads :

$$\Phi \alpha = d, \quad (3.6)$$

$$\Phi_{jik} = \varphi_{i,k}(\xi_*^{(j)}), \quad (3.7)$$

$$d_{j,k} = \mathbf{x}_k^{(j)} - \xi_{*k}^{(j)}, \quad (3.8)$$

where Φ is a tensor, assumed to be of maximal rank (remember that it is constructed from POD vectorial modes). Of course, as soon as $m \geq n$, the system is solved in a least-square sense, and admits a unique solution. When discretizing and solving this system, the following choices are made. The minimisation step described by Eq.(3.5) is solved by using a nearest neighbor algorithm that, among the points of the discretised ∂E selects the one which is closest to a given $\mathbf{x}^{(j)}$. Then, the vector system in Eq.(3.6) is unfolded and solved by using a rank revealing QR decomposition.

3.3 Numerical experiments in 2D

3.3.1 Reference configuration

In this section, some numerical experiments are shown on a simple 2D test case to assess the performances of the proposed semi-automated segmentation approach. The reference configuration, depicted in Figure 3.3, is a unit circle, divided into two semicircles.

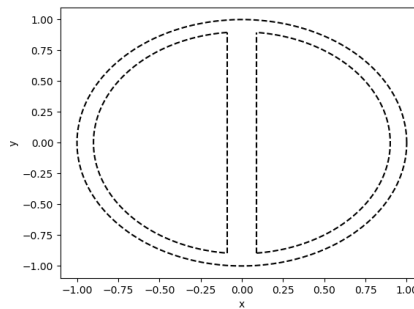


FIGURE 3.3 – Reference configuration

2. Remark that this point might not be unique.

3.3.2 Generation of the database set

The images are defined by deforming the reference configuration by a parameter dependant field, generated as follows. The displacement of each point on the reference circle is normal to the circle and constructed by summing the set of $N_h \in \mathbb{N}^*$ harmonics (eigenfunctions of the Laplace-Beltrami operator), scaled with a parameter dependant coefficient : let the undeformed configuration points be denoted by $\xi \in \mathbb{R}^2$, $r = \|\xi\|_2 \leq 1$, $\vartheta \in [0, 2\pi]$ (i.e. $\xi_1 = r \cos(\vartheta)$, $\xi_2 = r \sin(\vartheta)$), the unit vector in the radial direction be denoted by \hat{e}_r , and the displacement providing the deformed image configuration be $x \in \mathbb{R}^2$:

$$x = X(\xi) = \xi + r \left(\sum_{j=1}^{N_h} \gamma_j (j+1)^{-\beta} \right) \hat{e}_r, \quad (3.9)$$

where $\gamma_j = \gamma_j(\mu)$, have an amplitude which decreases as a power law of the harmonics numbers : $(j+1)^{-\beta}$ with $\beta = 1.5$, and μ is a parameter that identifies each image. The level of different level of regularisation can be illustrated by the Figure 3.4.

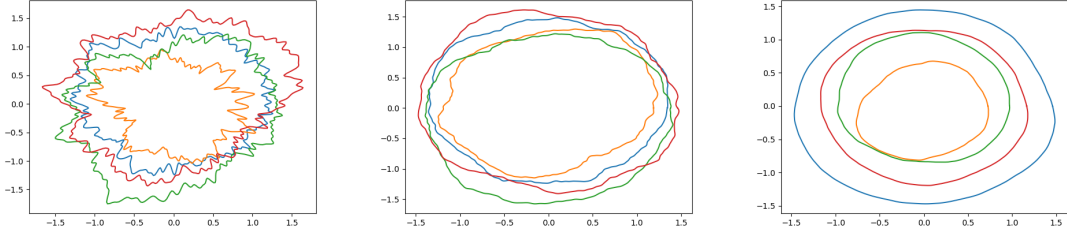


FIGURE 3.4 – Illustration of the regularisation coefficient (a) $\beta = 1$, (b) $\beta = 1.5$, (c) $\beta = 2$.

Consider the following radial displacement, depending upon the parameter $\mu \in [0, 1]^2$. The harmonics coefficients are chosen according to the following expression :

$$\gamma_j = \frac{A}{j^2} [\sin(2\pi j \sqrt{\mu_1}) + \cos(2\pi j \sqrt{\mu_2})],$$

With this process we are able to generate various type of configuration, as shown in the three examples of the Figure 3.5.

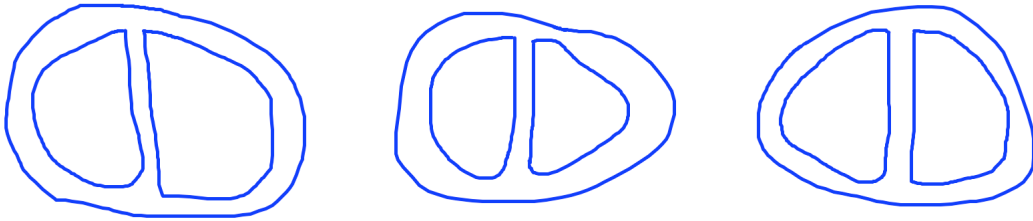


FIGURE 3.5 – Examples of automatically generated shapes in our 2D database

3.3.3 Singular Values Decrease

In the present work $K = 100$ harmonics are used to generate the displacement fields. A set of $N = 100$ uniformly distributed in $[0, 1]^2$ samples of the parameter μ are taken, and, for each,

the radial displacement is constructed. The POD basis was computed. The singular value decay is shown in Figure 3.6, exhibiting a faster decay when compared to the one typical of the spherical harmonics for a given regularity.

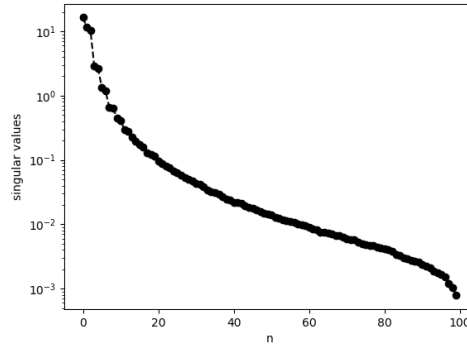


FIGURE 3.6 – Decrease of singular values with POD parametrization

Remark that the displacement is purely radial and that the center of the reference circle $r = 0$ does not move. This corresponds to the case where the various anatomic regions that have been segmented are « aligned » and properly scaled. We are aware that in practice this point is crucial to achieve good outcomes and is not developed in this chapter, but in the next one. Furthermore, given this way of building a database of elastic displacements, the POD modes reduce to a set of vector displacements in the radial direction whose intensity is given by the value of the harmonics. The discretised shape is built by discretising uniformly the interval ϑ using $N_\vartheta = 512$ points.

3.3.4 Application and results

The image (the deformation of the reference shape) is cut by $N_p \in \mathbb{N}^*$ horizontal planes, represented by an green dotted line in Figure 3.7, uniformly distributed on the image, to mimic a medical exam like CT or MRI which are sliced. Each plane intersects the only **outer** boundary of the object in two points ($m = 2N_p$), each of which corresponding to one of the halves of the deformed circle. These points, represented by an orange star in Figure 3.7, provide an equation for the displacement field to be approximated by using the POD modes.

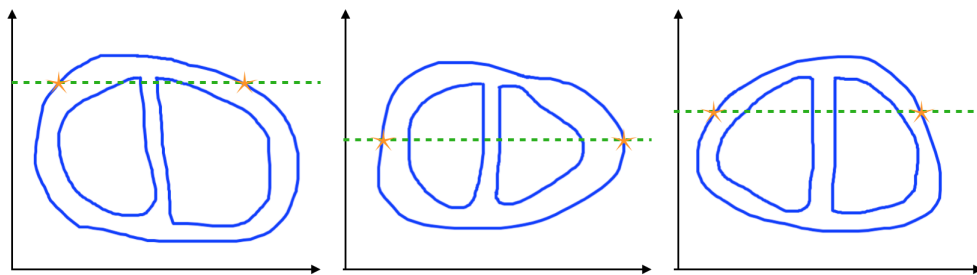


FIGURE 3.7 – Examples of automatically generated shapes in our 2D database

Several numerical experiments are made to assess the performances of the proposed reconstruction method, by varying the number of modes and the number of cutting planes used. In particular, the number of modes used varied from $n = 6$ to $n = 20$ and, for each choice the number of planes was varied from the minimal number of planes needed to have a square system $n \leq m$ to $m = 2n$. In

Figure 3.8 shows two examples of reconstruction proposed, when the images were produced by using $N_h = 100$ harmonics, $n = 20$, $m = 80$. The result is quite precise, all the details of the image are well represented, whether it is the outer edge where points are selected or the edge of the inner hemicycles where no points are selected.

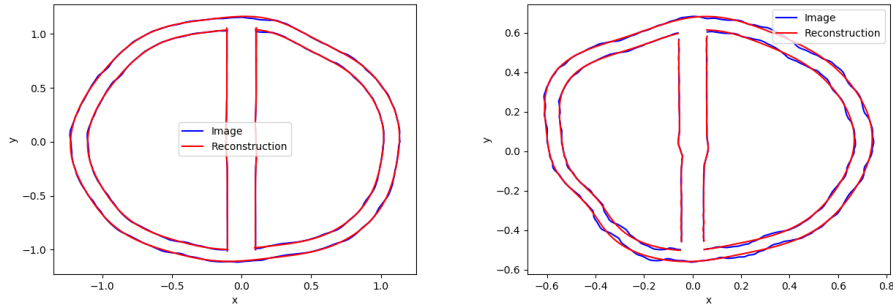


FIGURE 3.8 – Visualisation of two results (a) of a slightly distorted image and (b) of much more distorted image

3.3.5 Reconstruction error

The reconstruction errors are shown in Figure 3.9 for a population of 100 target displacements (that do not belong to the database used to construct the POD modes). The errors are measured in ℓ^2 norm with respect to the discretized images. The average error and standard deviation are shown when the minimal number of planes and the maximum number of planes are used. In general, the errors are compatible with the ones considered as compatible with realistic applications. When the minimum number of planes is used a stability issue can be seen when a large number of modes is used and the standard deviation is quite large. On the contrary, when $N_p = 2n$ (orange), the lack of stability is delayed, the errors decrease and the standard deviation is much smaller, reaching a minimum for $n = 17$.

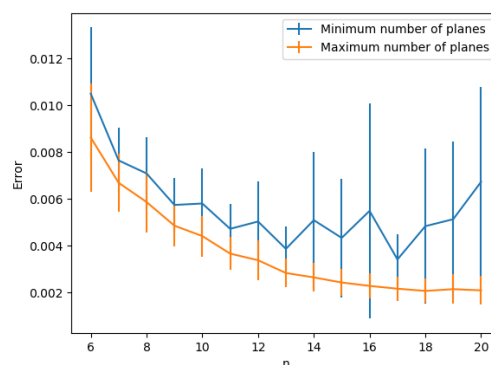


FIGURE 3.9 – Test case presented in Section 3.3 : Error mean and standard deviation

3.4 First 3D numerical exploration

In order to better understand the complexity of the situation in 3D, we chose to also work on a simulated problem. We therefore generated a set of shapes using spherical harmonics to represent

our dataset. Then we extracted the modes with a POD, and reconstructed these shapes according to the basic methods explained in the previous section.

3.4.1 Spherical harmonics - Definition in 3D

Spherical harmonics are special functions defined over the unit sphere. They can be derived as eigenfunctions of the Laplace-Beltrami operator on the sphere. They can be particularly useful to solve rotation invariant problems. They are a complete set of orthonormal functions of $L^2(S^2)$, and thus may be used to represent functions defined on the surface of a sphere, just as circular functions (sinuses and cosines) are used to represent functions on a circle via Fourier series.

The harmonic polynomials $P(x, y, z)$ of degree l form a vector space of dimension $2l + 1$, and can be expressed in spherical coordinates (r, θ, ϕ) :

$$r^l Y_{l,m}(\theta, \phi), \text{ with } -l \leq m \leq +l,$$

where $\theta \in [0, \pi]$ and $\phi \in [0, 2\pi]$.

The cartesian coordinates of a point can be retrieved by the change of coordinates :

$$\begin{cases} x = r \sin \phi \cos \theta \\ y = r \sin \phi \sin \theta \\ z = r \cos \theta \end{cases}$$

In the present work, we will consider the unit sphere and hence $r = 1$.

A real basis of spherical harmonics can be defined in terms of their complex analogues by setting :

$$Y_{l,m} = \begin{cases} \sqrt{2}(-1)^m \text{Im}[Y_l^{|m|}] & \text{if } m < 0, \\ Y_l^0 & \text{if } m = 0, \\ \sqrt{2}(-1)^m \text{Re}[Y_l^{|m|}] & \text{if } m > 0. \end{cases} \quad (3.10)$$

The first real spherical harmonics are shown in Figure 3.10.

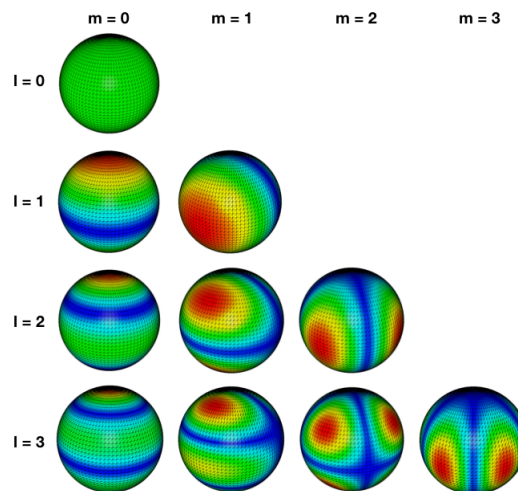


FIGURE 3.10 – Visual representations of the first few real spherical harmonics

3.4.2 Parameterization of shapes

In order to test the proposed method, we define two families of shapes, constructed by using spherical harmonics, in a similar way to the 2D method presented in section 3.3.2.

Let $\xi \in S^2$ be a point of the unit sphere, which is the reference (undeformed) configuration. A shape is defined as the result of a mapping of the unit sphere. Let $\mathbf{x} \in F \subset \mathbb{R}^3$ be a point of the mapped surface. It holds :

$$\begin{cases} Id + u : S^2 \rightarrow F \\ \xi \mapsto \mathbf{x} = \xi + u(\xi), \end{cases} \quad (3.11)$$

where u is the displacement field, defined as follows :

$$u = \sum_{l=1}^L \sum_{m=-l}^l a_{lm}^R Y_{lm}^R + a_{lm}^I Y_{lm}^I$$

Let $L \in \mathbb{N}$. For the first family, the coefficients are defined as follows :

$$\begin{cases} a_{lm}^R = \frac{\gamma_{lm}^R}{(1+l)^\beta} \\ a_{lm}^I = \frac{\gamma_{lm}^I}{(1+l)^\beta} \end{cases} \quad (3.12)$$

with $\gamma_{lm}^{R,I}$ are sample of a uniformly distributed random variable in $[-\frac{1}{2}, \frac{1}{2}]$, and β the regularisation

R The shape family that is constructed here is considered large enough, because all the generated coefficients are independent.

An example of a shape generated by this parametrization with a great regularisation ($\beta = 2$), is shown in 3.11.

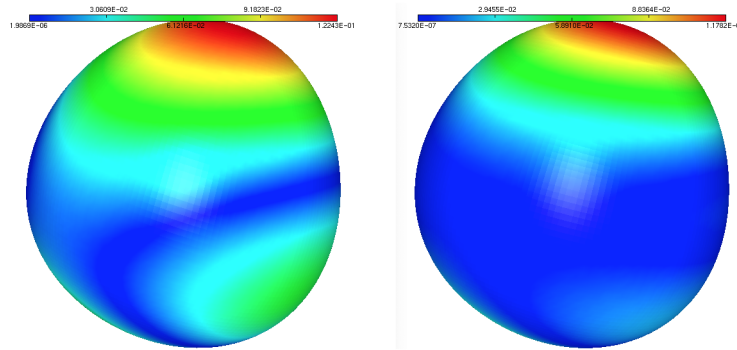


FIGURE 3.11 – Example of shape generated with spherical harmonic functions, from 2 point of view

Aiming at studying shapes featured by common patterns (as one would expect from anatomical parts), we introduce a second family of shapes, in which the coefficients defining the displacement are no longer independent. Instead, they depends upon a small number of parameters. Let $\mu = [\mu_1, \mu_2, \mu_3] \in [0, 1]^3$.

The coefficients of the real part and the imaginary part were chosen as below :

$$\begin{cases} a_{lm}^{Real} = \frac{\sqrt{\mu_3}}{(l+1)^\beta} \cos(2\pi l(m+1)\sqrt{\mu_1}) \cos(2\pi l(m+1)\sqrt{\mu_2}) \\ a_{lm}^{Imag} = \frac{\sqrt{\mu_3}}{(l+1)^\beta} \sin(2\pi l(m+1)\sqrt{\mu_1}) \sin(2\pi l(m+1)\sqrt{\mu_2}) \end{cases} \quad (3.13)$$

An exemple of a shape generated by this second parametrization ($\beta = 1.5$) is shown in Figure 3.12.

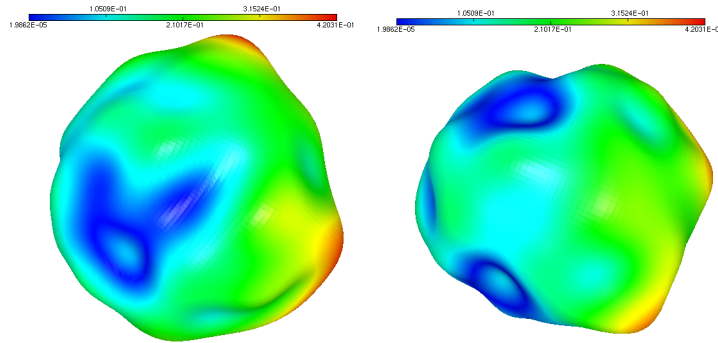


FIGURE 3.12 – Exemple of shape generate with a parametrized spherical harmonic function

Once those two types of shape generated, we perform a Proper Orthogonal Decomposition (POD), by computing the matrix C_{ij} , its eigenvalues λ_i and its eigenvectors $v_j^{(i)}$:

$$C_{ij} = \frac{1}{N} \sum_{k=1}^N \sum_{h=1}^N u_{h,k}^i u_{h,k}^j$$

with $u_{h,k}^i$ being the displacement at point i between the initial sphere and the shape generated by the spherical harmonics.

Thus we compare the decrease of the eigenvalues of the two types of shape in Figure 3.13, in blue the parameterized one and in black the non-parameterized. We can see that the blue curve decreases quicker at first and even during the plate phase, because it represents a parametric family of shapes with a small Kolmogorov dimension (see Chapter 2), just as it is the case of our exemple on masseter muscles.

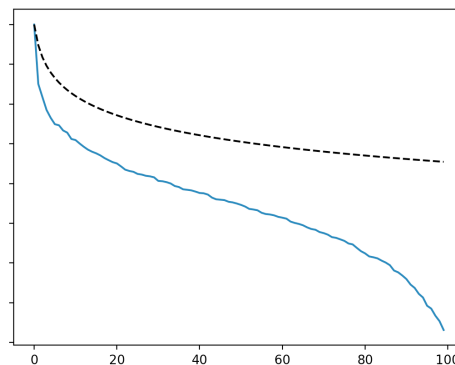


FIGURE 3.13 – Exemple of shape generate with spherical harmonics function

3.4.3 Reconstruction of a new shape

Thus, from the acquired database consisting of $N \in \mathbb{N}^*$ such displacements : $\mathcal{D} = \{u^{(1)}, \dots, u^{(N)}\}$ let us assume that a set of $n \in \mathbb{N}^*$ Proper Orthogonal Decomposition (POD) modes is extracted :

$$\varphi_i = \sum_{j=1}^N v_j^{(i)} u^{(j)}$$

We are now able to approximate, by using the POD basis, the unknown displacement mapping from the sphere reference configuration onto the object F as in the 3.3 equation :

$$u \approx u_n = \sum_{i=1}^n \alpha_i \varphi_i$$

with $n \ll N$, the maximal number of objects consider in the database, here $N = 100$.

The goal is now to find the coefficients α_i , in such a way that the reference sphere, mapped by the displacement field $Id + u_n$ is as close as possible to the actual object. In order to identify the coefficients α_i , we used the method described in the previous section. Where a number of $m \in \mathbb{N}^*$, $m \geq n$ points $\mathbf{x}^{(j)} \in F$ is randomly selected in the actual object F , which allows us to build a linear system that is easy to solve by using a rank revealing QR decomposition.

3.4.4 Analytic error

To simulate the segmentation situation and have a better idea of what can be expected from an error point of view, we performed an analysis of the error of the reconstructed shape, and compared it with the error of projection.

The simulation was performed with these specific parameters :

- for the generation of the hamornic spherical basis, $l = 10$ which means 66 modes were used to construct $N = 100$ random cases with the parametrisation of the section before,
- for the reconstruction of those cases, differents types of reconstructions were tested with $L = 3, 4, 5$ and different regularity $\beta = 0.5, 1, 1.5$,
- we compare the projection error with the reconstruction error with different numbers of selected points : 40, 80, 120, 160, 240, 320, 480,
- the reference sphere had 20002 points.

We obtain the results presented in Table 3.1 for the projection error and in Table 3.2 for the reconstruction error (compute with the $L2$ norm) :

Regularity	Number of modes		
	$L = 3$	$L = 4$	$L = 5$
β			
0.5	0.129079	0.119947	0.108989
1.0	0.046772	0.041385	0.036296
1.5	0.017683	0.014658	0.012290

TABLE 3.1 – Mean projection error

Comparing both these tables, we can conclude that for a regular enough shape ($\beta \geq 1.0$), and mostly thanks to the parameterization introduced in the previous section, our reconstruction error is quite similar to the projection one using 200 randomly selected points, which represent 1% of the data knowledge.

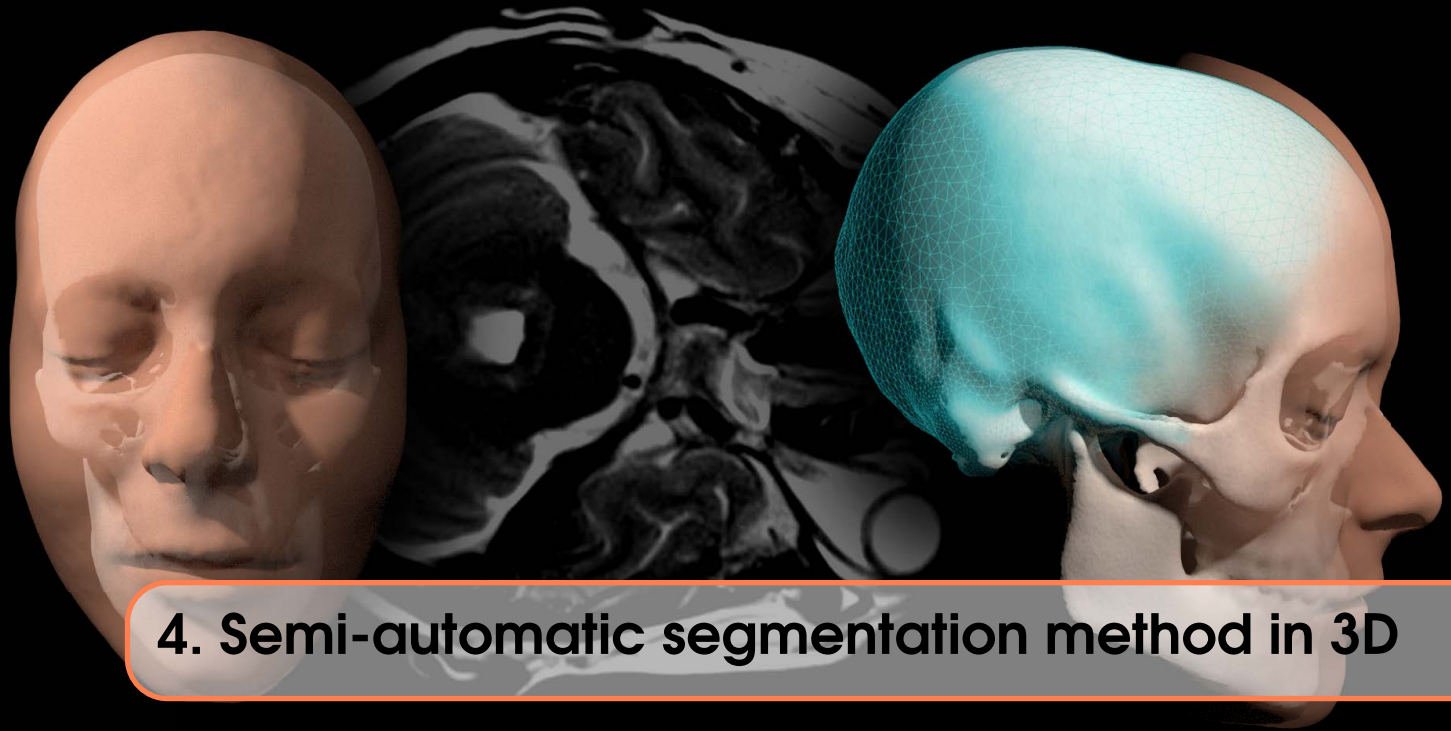
	Number of point						
	40	80	120	160	240	320	480
$\beta = 0.5$							
L = 3	0.182349	0.141464	0.135576	0.132777	0.129772	0.128591	0.127435
L = 4	0.339517	0.151632	0.133166	0.127183	0.122956	0.120914	0.118816
L = 5	2.948415	0.197059	0.138437	0.123788	0.115576	0.112396	0.108925
$\beta = 1.0$							
L = 3	0.067829	0.051235	0.048767	0.047581	0.046769	0.046277	0.045845
L = 4	0.127903	0.051671	0.046598	0.044078	0.042345	0.041570	0.040951
L = 5	0.861894	0.066765	0.046153	0.041285	0.038449	0.037332	0.036283
$\beta = 1.5$							
L = 3	0.024451	0.019803	0.018470	0.018023	0.017598	0.017409	0.017269
L = 4	0.036146	0.019258	0.016425	0.015646	0.015018	0.014741	0.014519
L = 5	0.161430	0.022509	0.015853	0.014126	0.013091	0.012668	0.012321

TABLE 3.2 – Mean reconstruction error

3.5 Conclusions and Perspectives.

In the present work a semi-automated reconstruction method is proposed to help the segmentation of anatomical details in the cases in which the contrast is not enough to use fully automated techniques. The method is based on the use of a reduced basis to approximate an elastic displacement mapping a reference configuration into the actual shapes of the anatomical details of interest. The method uses a nearest neighbors optimisation procedure coupled to a least square approach to solve the problem. A 2D and a 3D test cases are proposed to mimic realistic applications and assess the performances of the method. A set of synthetic generated images was used and the error of the numerical experiments showed that the proposed approach can lead to a viable tool. In this respect, further investigations are mandatory both from the theoretical and applied point of view. In particular a systematic error analysis will be carried out and more realistic tests will be performed, in 3D configuration and by taking the noise and the other experimental error sources into account.

Especially in 3D, several challenges are added to those previously described, especially in the case of a real application. The first one is the constitution of the manual segmentation database : time-consuming and requiring the involvement of an anatomist expert at first. However, the idea is that we will soon be able to propose a first phantom, which will require only a few corrections and will save a lot of time while continuing to feed the database. All these aspects are discussed in detail in the following chapter.



4. Semi-automatic segmentation method in 3D

Sommaire

4.1	Introduction	116
4.2	Modes in the reference configuration	116
4.3	Overview of the method for 3D segmentation in a real case	117
4.3.1	Notation	117
4.3.2	Pipeline	117
4.4	Application in a real case : the masseter segmentation	118
4.4.1	Graphical interface development	118
4.4.2	Coordinates Change	120
4.4.3	Reconstruction	122
4.4.4	Visualisation	124
4.5	Discussion and Conclusion	126

Comparison of two semi-automatic segmentation method : a reduced basis method constructed with a PCA or a greedy algorithm

Work in collaboration of Damiano Lombardi and Yvon Maday, work in progress.

Key Words

Segmentation, Medical Imaging, Spherical Harmonic, POD, Masseter muscle, Greedy algorithm

4.1 Introduction

In medical imaging, segmentation of anatomical parts is still a challenge. Indeed, it is a recurring and time consuming problem, as seen in the previous chapter.

Segmentation is the process of dividing a medical image into distinct anatomical regions [68]. For 3D medical images, this amounts to attribute a label to each voxel (3D pixel) of the image. The gold standards have been, for years, manual segmentations performed by anatomical experts, but on top of the unavoidable errors, it is a time consuming process. The general issue is thus to find a way to identify automatically an anatomical region of interest in order to speed up the process, and eventually standardize as much as possible the generated error. The different existing methods and the associated literature are presented in more detail in the previous chapter.

We propose here to develop a model based semi-automatic method to help segmentation, according to the same general principle as previously exposed in the chapter 3. In particular, the shape of the object of interest is represented by an elastic deformation field of a reference configuration. A reduced basis representation of the object of interest is introduced, that exploits an *a posteriori* knowledge of a database of available segmentations. Given an image to be segmented, the elastic deformation field can be approximated as a linear combination of a small number of modes. This provides, in turn, a powerful regularisation and a significant speed-up of the procedure needs since few appropriate points need to be selected by the user in order to define the field.

This problem and the associated method were first set in last chapter where we proposed a proof of concept. We present here the same problem, extended and adapted in 3D, with a practical application of the masseter muscle segmentation on CT-Scan. However, due to various problems encountered in the 3D generalisation of the techniques, for a realistic application, used for the very simple previous examples, some steps of our segmentation algorithm are significantly modified.

The chapter is structured as follows : a first part about the modes generation according 2 methods (POD and Greedy algorithm). In a second part, we present an overview of the new method adapted for a 3D realistic problem. Finally, a third part which present the application of the latter for the particular case of the masseter muscle on CT-Scan.

4.2 Modes in the reference configuration

The first step of our method involves, as referred on several occasions, computing a reduced basis in which all the elements of our dataset are represented by only a few parameters. All the stages of the constitution of our database are explained in Chapter 2. The construction of the modes can be summarized as follows.

By exploiting the morphing of a reference shape in 3D, the ellipsoid presented in the Chapter 2, it was possible to define the elastic displacements u (Figure 2.10) and from them, the modes.

Two extraction methods of the modes are possible in our application :

1. POD modes, quick to implemented and computed. These are the ones we used for the proof of concept and for the numerical exploration in the previous chapter.
2. Greedy modes, where all masseters are represented by a linear combination of the ones of the database. A specificity is to be noted here : we obtained these modes by taking into account that for our application, the knowledge of the masseters shape is not uniform on the image. The points that will be selected (detail in the step 1 of the methods), due to the nature of the image, won't be uniformly distributed on the image, but restricted to a certain region. Which can present an important advantage for the reconstruction part, even if that kind of algorithm

is slower at first.

A set of $n \in \mathbb{N}^*$ modes is retained. For the present application, we choose to use $n = 20$. And each masseter can now be represented as :

$$\sum_{i=1}^n \alpha_i \varphi_i. \quad (4.1)$$

with α_i the coefficients and φ_i the modes POD or compute with our greedy algorithm.

It is important to specify that due to an artificial translation present for some snapshots in the database, the number of couples (image-segmentation) allowing the implementation of the whole process (including the reconstruction with projection on the image, i.e. the visualisation of the segmentation) is here reduced to 45 masseters (against 126 in our complete database).

In this context, we were all the more confronted with a weakness of this type of model : the need for a consistent database. To overcome this problem, we have implemented an automatic shape generator tool, which from existing shapes and with the help of interpolation and spherical harmonics, allows us to multiply the dataset. We also add in this process small rotation and translation to favour a better registration. Due to the fact that this part of the method is still under development, details of its design and results will not be presented in the following section.

4.3 Overview of the method for 3D segmentation in a real case

As a first step, and in order to clarify the structure of the segmentation algorithm developed here and the modifications made in respect of Chapter 3, we begin in this section by presenting an overview of the different steps and their sequence.

4.3.1 Notation

In what follows :

- $N_p \in \mathbb{N}^*$: number of points selected by the user on the image,
- $N_s \in \mathbb{N}^*$: number of snapshots in the database,
- $\mathcal{N} \in \mathbb{N}^*$: number of points of the reconstructed mesh,
- $n \in \mathbb{N}^*$: number of modes.

4.3.2 Pipeline

The pipeline we have set up is directly linked to the segmentation application : patient-specific geometric transformations must be derived solely from the Dicom image, and geometric transformations that are not linked to the image are common to all patients. This ensures that, for a new patient, we can produce a muscle reconstruction without the need for any additional information (as is the case in realistic applications).

Let the image domain be the subset $\Omega \subset \mathbb{R}^3$. The image is considered as a function \mathcal{F} :

$$\mathcal{F} : \begin{cases} \Omega \rightarrow \mathbb{R} \\ x \mapsto \mathcal{F}(x_1, x_2, x_3). \end{cases} \quad (4.2)$$

We therefore present here the different steps necessary for the semi-automatic segmentation of a new masseter muscle, from the acquisition of the dicom to the projection of the final segmentation

on the dicom images or in 3 dimensions.

- Step 1 - An **interface** that allows the operator to select a set of points describing the muscle and the associated bounding box.

A bounding box $\Omega_m \subset \Omega$ is determined on the image, such that the muscle is contained in it. Moreover, let $N_p \in \mathbb{N}^*$, a set of points $p^{(i)} \in \Omega_m$ are chosen, $i = 1, \dots, N_p$.

The most important thing in this step is to make sure that the whole muscle is contained in the box, or more precisely that all the selected points are contained in the bounding box.

- Step 2 - A **coordinate change** from dicom images to our reduced basis space $[0, 1]^3$.

An affine transformation is built, such that :

$$\mathcal{X} : \begin{cases} \Omega_m \rightarrow [0, 1]^3 \\ x \mapsto \xi. \end{cases} \quad (4.3)$$

We have $\xi = \mathcal{X}(x)$, and, since the transformation is invertible, $x = \mathcal{X}^{-1}(\xi)$.

The points are transported into $[0, 1]^3$, that we call the reference configuration, where the modes are defined and where the reconstruction takes place.

- Step 3 - The **reconstruction** of the 3D masseter from the selected points, i.e. the identification of the best coefficient α to fit those points in our reduced basis.

By exploiting the points, a mesh consisting of $\mathcal{N} \in \mathbb{N}^*$ degrees of freedom is reconstructed : $v^{(i)}, i = 1, \dots, \mathcal{N}$.

These two last step differ significantly from the method described in Chapter 3. All the details and needed examples are given in the next section.

- Step 4 - **Visualisation** and **validation** of our segmentation on the dicom images.

The mesh is transported into the image configuration by using $u^{(i)} = \mathcal{X}^{-1}(v^{(i)})$ and a phantom is computed based on them, which is :

$$\tilde{\mathcal{F}} : \begin{cases} \Omega \rightarrow \mathbb{R} \\ x \mapsto \tilde{\mathcal{F}}(x_1, x_2, x_3). \end{cases} \quad (4.4)$$

This allows the user to check the segmentation and modify it if it is not fitting.

All of these steps, briefly named here, are detailed in the following section.

4.4 Application in a real case : the masseter segmentation

4.4.1 Graphical interface development

All the interface that is presented in this part has been implemented during this thesis, using python language and the package « OpenCv ».

For any manual segmentation, it is necessary to display the slice images of the scanners. We have therefore set up a user interface to read and display the dicoms, allowing users of our semi-automatic application to interact with them by selecting the points and the bounding box. The 3 conventional planes of the space are displayed : axial, coronal and sagittal. This allows the users to orient themselves in 3D. It is also possible to navigate between sections in the same plane using a cursor located below the image, to follow an anatomical structure from top to bottom, from front to back or from right to left, and vice versa. Figure 4.1 is a screenshot of the application display.

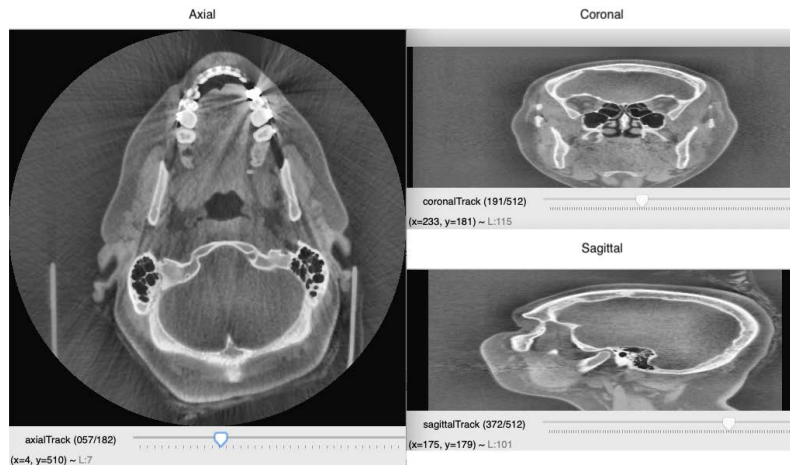


FIGURE 4.1 – Software interface with the 3 views : axial (left), coronal (up), sagittal (bottom)

To this viewer interface, we implemented a function to store the coordinates, in the image coordinate system, of selected points on the images. The aim is to collect these coordinates at the edge of the muscles of the masseter for each patient. Some important modalities are to be specified to the operator :

- select a set of about 50 points per muscle
- on different slices and in different planes of space
- to encourage the selection of points in a region in which the muscle is clearly visible, even if it means favouring specific anatomical zones (we will be able to take this into account thanks to the modes computed using the greedy method).

Figure 4.2 shows the selection of three points on an axial plan.

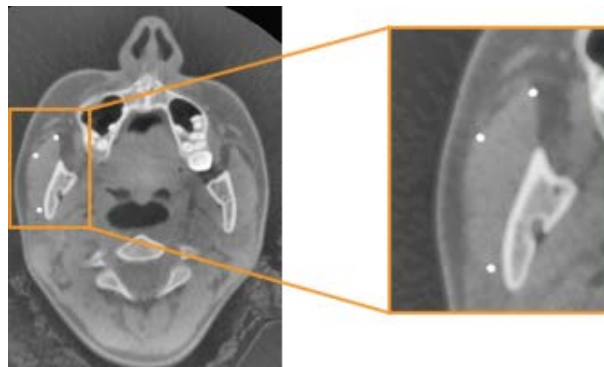


FIGURE 4.2 – An example of points selection on an axial slice

A second essential tool is also implemented in our software. It aims at selecting a box containing

the masseter. The main instruction given to the user is to make sure that the whole muscle is located inside the selected box, even if it seems a little large at first.

In practice it is necessary to select two rectangles : one on the axial section and one on the frontal section, as can be seen in the example in the Figure 4.3.

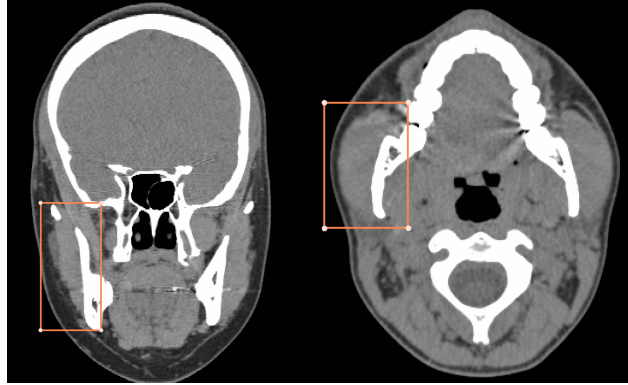


FIGURE 4.3 – An example of a bounding box selection on a frontal (left) and an axial slice (right)

Collecting this data for all 45 Dicom- Segmentation couples in our database was the first step in setting up our reconstruction method.

4.4.2 Coordinates Change

Once the points collected, we need to send them to our reference configuration thanks to the bounding box selected at the same time, and the reversible application \mathcal{X} .

In Figure 4.4, we can visualize the point cloud selected in the image reference, on the left, and the masseter we want to reconstruct in the unit box, reference configuration, where the modes was computed, on the right.

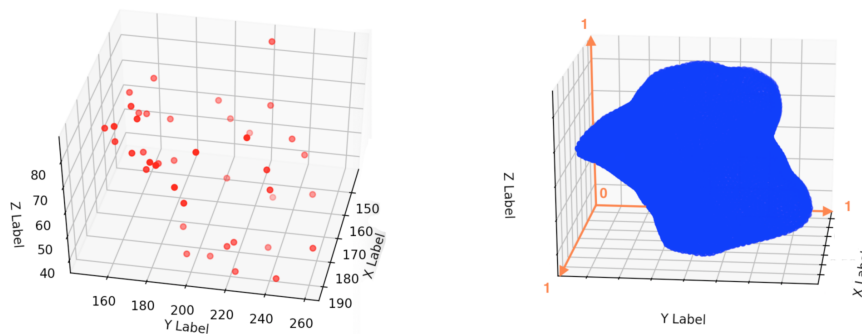


FIGURE 4.4 – (a) Points cloud selected in the image coordinates system, (b) the masseter mesh associated in the unit box

When a point is selected on a dicom image, a local value (i, j, k) based on the pixel numbering is attributed to it. We need to change this coordinates to the cartesian system x, y, z , to be able to perform our analysis. This is made possible because the slice thickness information, voxel spacing, and number of slices s are recorded in the dicom files.

In Figure 4.5, we can visualize a schema of a head that summarizes the orientation of the axes x, y, z according to the image coordinates system. The Cartesian coordinates of the points are

deduced from this, according to the section plane (axial, coronal or sagittal) in which they have been selected.

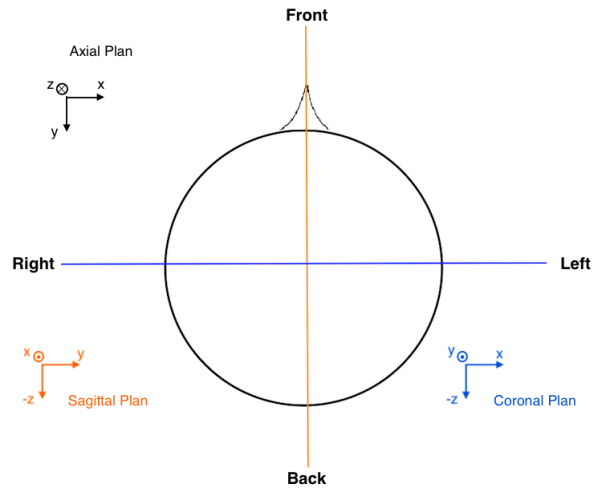


FIGURE 4.5 – Schema of the head of our 3D image data

For the axial plane we got :

$$\begin{cases} i = x \\ j = y \\ k = z \end{cases} \text{ and so } \begin{cases} x = i \\ y = j \\ z = k \end{cases}$$

For the coronal plane (on left) and the sagittal plane (on right) we got :

$$\begin{cases} i = x \\ j = s - z \\ k = y \end{cases} \text{ and so } \begin{cases} x = i \\ y = k \\ z = s - j \end{cases}, \quad \begin{cases} i = y \\ j = s - z \\ k = x \end{cases} \text{ and so } \begin{cases} x = k \\ y = i \\ z = s - j \end{cases},$$

with s the number of slices contained in one CT-Scan. It only affects z coordinates since CT-scan images are acquired in the axial plan. The two other one are being informatically reconstructed according to slice thickness and voxel spacing.

Once the Cartesian coordinates have been computed, we must align the acquired data with those in our database, i.e. the space where the POD was performed. This registration step has a significant impact on the results, and should not be underestimated.

As the reference point of the initial bounding box, the point $G(x_{min}, y_{min}, z_{min})$ is chosen, where x_{min} is the minimum x -coordinate of the selected points in the different sections, projected into the Cartesian coordinate system. It is from this point G that the box is centred in zero :

$$\begin{cases} x_t = x - x_G \\ y_t = y - y_G \\ z_t = z - z_G \end{cases} \quad (4.5)$$

with (x_t, y_t, z_t) the points coordinates in the translated bounding box.

We then build the change of orientation matrix C :

$$C = \begin{bmatrix} \frac{1}{x_{max}-x_{min}} & 0 & 0 \\ 0 & \frac{1}{y_{max}-y_{min}} & 0 \\ 0 & 0 & \frac{1}{z_{max}-z_{min}} \end{bmatrix} \quad (4.6)$$

that we apply to all the points of the box, such as :

$$X_a = \langle C, X_t \rangle_{L_2}, \quad (4.7)$$

with X_t vector (x_t, y_t, z_t) and X_c vector (x, y, z) .

To ensure that all the transported masseters of our database are in our reference space, the unit box, $[0,1]^3$, we applied a discount factor λ identical to all the masseters, when we construct modes (Section 4.3). We therefore apply the same reduction coefficient to the selected points on the image :

$$X = \lambda X_c + \frac{1-\lambda}{2}, \quad (4.8)$$

with in our case $\lambda = 0.7$, the highest coefficient for which the 45 masseters in our database are contained in the unit box.

The result of this registration procedure can be observe in the Figure 4.6, where the points cloud is now almost superimposed on the masseter mesh. This simple 2D illustration does not allow for easy visualization of the distance of the points (in red) to the masseter (in blue) in 3D. However, if we display the rotation of this figure in space (on a computer screen), we can see that all the points are close to the original object.

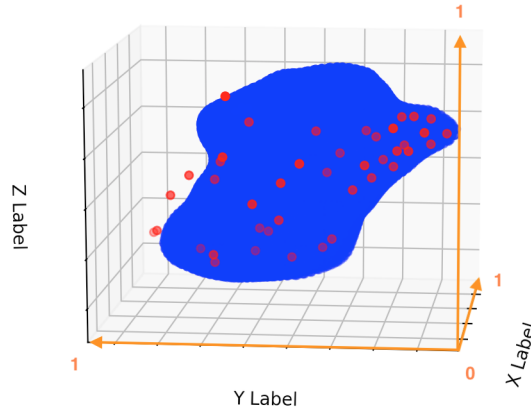


FIGURE 4.6 – Cloud points superimposed on the masseter mesh associated in the unit box

4.4.3 Reconstruction

To be able to perform our reconstruction and as suggested in a previous section, we need to identified the points $\xi_*^{(j)}$ of our reference ellipsoid E by minimizing the distance to the selected

point. Here we presented a potential solution to this problem.

The novelty comes in this reconstruction phase. In the previous chapter, given a point $q^{(i)} = \mathcal{X}(p^{(i)})$, the first step consisted in assessing which was the degree of freedom of the ellipsoid that was more likely to be the one we need to deform to get close to the point. After having performed this task, the problem becomes linear. The problem is that the result could be strongly affected by the correspondence point-dof (that takes care of the non-linearity).

In the present approach, we try to perform the reconstruction by solving the non-linear problem. To this end, a functional is introduced to measure the discrepancy between the points to be matched and the reconstructed mesh.

Let $v^j \in [0, 1]^3$, $j = 1, \dots, \mathcal{N}$, and $v^{(j)} = \xi_\ell^{(j)} + \sum_{i=1}^n \phi_i \alpha_i$ be the j -th reconstructed mesh point.

Let $Q = \{q^{(1)}, \dots, q^{(N_p)}\}$ be the selected points cloud and the reconstructed mesh be $V = \{v^{(1)}, \dots, v^{(N)}\}$.

Then :

$$\mathcal{J} : Q \times V \rightarrow \mathbb{R}^+, \quad (4.9)$$

$$\mathcal{J} = \frac{1}{2} \sum_{i=1}^{N_p} \min_{j \in \{1, \dots, \mathcal{N}\}} |q^{(i)} - v^{(j)}|^2. \quad (4.10)$$

The meaning is : when we have to evaluate the distance from the point $q^{(i)}$ we consider the mesh point which is the closest to it, we compute the Euclidean distance squared, and then we sum over all the contributions.

The points $v^{(j)}$ are function of the coefficients $\alpha \in \mathbb{R}^n$. The reconstruction amounts to solve :

$$\alpha_* = \arg \inf_{\alpha \in \mathbb{R}^n} \mathcal{J}(\alpha). \quad (4.11)$$

This problem is known in the literature as *min-sum-min* because of the structure of the cost functional. To solve this problem we have been inspired by the method developed by A. Demianov in [54]. However, it was necessary to adapt this algorithm to our specific case. Indeed, the examples presented in the article remain quite simple and in 2D, therefore less difficult and expensive to implement. We have thus initially chosen to leave aside the combinatorial part which is exposed in this paper. The present approach to solve our min-sum-min problem reads as follows :

1. The **initial guess** is found by looking, among the elements in the database, to the one which is the closest to the points cloud. Let $A = \{\alpha^{(1)}, \dots, \alpha^{(N_s)}\}$ be the set of the coefficients resulting from the best reconstruction of the database snapshots, in the above introduced sense (minimising \mathcal{J}).

$$\alpha_*^{(0)} = \arg \inf_{\alpha \in \mathcal{A}} \mathcal{J}(\alpha). \quad (4.12)$$

2. When solving for it, a **correspondence « point-dof »** is found, namely :

$$j_*^{(i)} = \arg \inf_{j \in \{\mathcal{N}\}} |q^{(i)} - v^{(j)}|^2. \quad (4.13)$$

That makes it possible to define the set $J = \{j(i), i = 1, \dots, N\}$. The set $V|_J$, whose cardinality is $V|_J = N_p$ is the restriction of the mesh to the points closest to Q .

3. Then we use the set $V|_J$ to get rid of spurious **translations** and linear transformations (intermediate registration step). Update the sets J and V_J .
4. A **least square problem** is solved :

$$\alpha_* = \arg \inf_{\alpha} \|q - \xi_\ell - \Phi|_J \alpha\|_{L^2, N_p}^2. \quad (4.14)$$

5. And finally recompute J , update V_J and **repeat** from step 4 of this procedure.

In step 5, the demonstration of convergence in this type of min-sum-min problem is not trivial at this stage of the method's development. It would therefore be necessary to define more precisely a stop criterion.

Furthermore, it is also possible to add a translation/rotation stage between these different steps to optimise alignment. However, it is also necessary to determine when this stage would be the most judicious and whether it is more interesting to repeat it several times or not.

4.4.4 Visualisation

Once all these steps have been completed, the central operations of the algorithm are carried out. What we want to do now is to show to the user the result of its semi-automatic segmentation. In order to visualise our reconstructions in 3D or to project on the dicom images, we need to reverse the registration process that sent them to the reference configuration. This is easily achieved by reversing the transformation used in section 4.5.2.

The first results obtained, based on a dataset of 45 masseters to build the modes, are visualised on the Figure 4.7. In this figure we see the segmented (left) and reconstructed (right) 3D masseter, placed on the corresponding skull face couple. As well as their superimposition, for better comparison, in the middle of the figure.

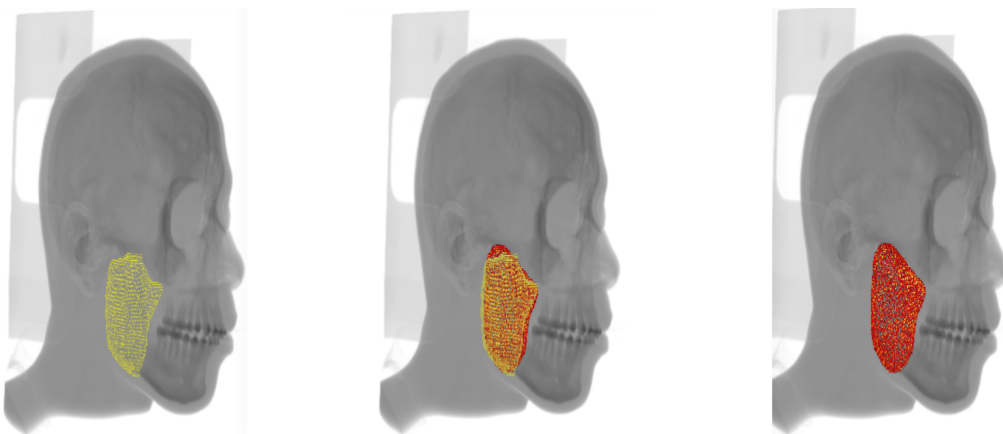


FIGURE 4.7 – Reconstruction in 3D of a masseter projected in its initial space : on the left the manually segmented one, on the right our reconstruction, on the middle a comparison of them both.

It is important to keep in mind that the manual segmentation obtained here (in yellow, on the left of Figure 4.7), is possibly not perfect, as it was performed by a single operator with a developed

knowledge of mandibular anatomy but not of segmentation. The differences observed are therefore difficult to interpret with this 3D representation. Indeed, this 3D visualization does not allow us to judge the quality of the underlying segmentation. This is why we present in Figure 4.8, the projection of this reconstruction directly on the image. Here we can visualise the boundary of the edge of the masseter segmentation on an axial section, by the manual method (in red), our reconstruction using the POD modes (in green), and the one with the greedy algorithm modes (in blue).

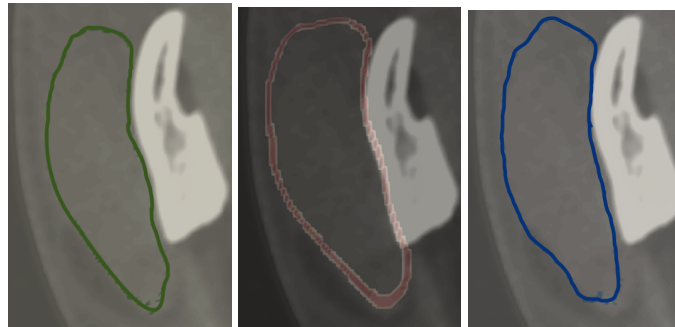


FIGURE 4.8 – Projection of the reconstruction on the original dicom images : on the left our reconstruction with the POD modes, on the middle the manual segmentation, on the right our reconstruction with the greedy modes. (Please note that the quality of the images presented above is not optimal, this is not related to the results themselves, but more to a lack of control of the viewing software. However, they do allow us to observe a first result which is a good basis for discussing the method).

One of the main comments that can be made from these first results is that our method, whether it is carried out with the POD or Greedy method, achieves one of our main objectives : to unravel a first segmentation from little information ask the operator (50 points and a bounding box).

Moreover, the Figure 4.8 shows that the manual segmentation extends slightly over the bone, which is not the case for our reconstructions. This can be explained by different reasons.

First of all, this is a very specific example : a single axial section for a single masseter in our database. We therefore cannot generalize to all cases, but this allows us all the same to make some hypotheses to understand how this could have happened even occasionally.

The operator who performed this manual segmentation probably did not make such a mistake when selecting regions of interest in the slices, but more likely later when using 3D regularization tools that allow to obtain a more coherent 3D shape from an anatomical point of view. This therefore amounts to saying that these are the stages of post-processing of the 3D object which would induce an error in this tedious and time-consuming segmentation.

In the case of our reconstructions, the method we have developed forces the final shape to stay close to the selected points. However, as explained previously, the user who selected the point cloud given as input to our algorithm, clearly visualizes the change in density between the muscle and the bone, and has very probably selected points quite precisely at this level. This therefore allows us not to make any mistakes at this level.

Anyway and in order to be able to discuss this point in more detail, it is important in the rest of this work to do a more in-depth analysis of the error that was made during our reconstruction. For this, additional work to obtain the gold standard of segmentation at the present time : manual segmentations of different experienced operators for the same masseter, is necessary. This will

allow us a more objective comparison using methods currently available in the literature, such as the « dice coefficient », in order to further improve our method still under development.

4.5 Discussion and Conclusion

This method, which is still under development, meets several of our initial criteria, better than the method initially proposed in Chapter 3. However, it is still under development and there is still much that needs to be improved. These include the following :

1. **Regularisation of least squares** : The coefficients $a \in \mathbb{R}^n$ are known for all the elements of the database. A possibility would be to constrain a to belong to a certain sub-set $[a_1^{(min)}, a_1^{(max)}]$ x ... x $[a_n^{(min)}, a_n^{(max)}]$ for a new reconstruction.
2. The **discrepancy measure** for the min-sum-min problem seems to be reasonable. Are there other ways, with easier functionals to be minimised? A test was done by using exponential kernels adopted in computational geometry, but the result was depending from the kernel length (free parameter) in a strong way. A more detailed study of the literature or the use of this parameter could improve this point.
3. **Enrich the database** by considering random expansions based on Laplace harmonics to perturb the reference ellipsoid (we can ensure the fields to be still in $H^{1/2}(\delta|\Omega_\ell)$), as suggested in the section 4.2. This would add a bit of noise to the basis but would also allow it to be increased considerably, which would be particularly useful when the base is really small. It is also possible to account for rigid displacements using this method by adding a small random translation and/or rotation to the deformation. This would improve the alignment and correspondence of the points, between those selected on the images and those of the mesh of the reconstructed masseter.
4. Can we devise a procedure to work **directly with the phantom** ? This would make it possible to show the overall improvement of the reconstruction in real time at each selected point, and would also potentially save computing time.
5. The ultimate goal of this work is to be able to **completely automate** the process. This saves time and hopefully reduces human error. Some ideas are being considered to get rid of the manual selection of points.



5. Pratical Application

Sommaire

5.1	Introduction	128
5.2	Materiels and Methods	128
5.2.1	Medical Image Data	128
5.2.2	Segmentation process	129
5.3	Results	130
5.4	Discussion	131
5.5	Conclusion	133

A comparative study between manual and semi-automatic segmentation of the masseter muscle from CT-scans

Work in collaboration of Camille Cardot, Wided Siai, Patrick Goudot and Thomas Schouman, work in progress.

Foreword

This chapter presents an application of the method described above (Chapters 3 and 4). It is a preliminary work, still in progress, which has enabled us to obtain feedback on the elements of our method that need to be improved. It is not yet possible to use the results presented here to fully evaluate the effectiveness of our software. Some criticisms, put forward in the discussion and conclusions sections, still need to be taken into account in order to obtain lower errors. Once all these have been taken into account, the more detailed comparison with existing methods will be all the more relevant.

Key Words

Manual segmentation, semi-automatic segmentation, Masseter muscle.

5.1 Introduction

3D reconstructions of the facial skeleton obtained from a CT-scan are widely used in clinical practice to analyze facial morphology disorders or lesions of the facial skeleton. More recently, specific digital tools were developed to perform surgical planning and simulation of the morphological result. Any surgical treatment can be planned based on available preoperative diagnostic data [141, 142]. To obtain such virtual model, the hard tissue - bone tissue - represented in the CT scan must be identified to generate the corresponding 3D object through a segmentation process. Bone segmentation is quite easy to perform because its density is radically different from that of adjacent tissues.

However, when a more comprehensive model is needed, soft tissues should also be segmented, such as for a dimensional study of a muscle (cf. Chapter 1) or a facial reconstruction methods (cf. Chapter 7). This implies the skin surface and some of the facial muscles that can impact facial morphology outcome. The masseters are the muscles contributing the most to facial morphology at rest (cf. Chapter 1). Other facial muscles mostly determine facial movements but have no significant contribution to facial volumes. The segmentation of the skin surface is also easy to obtain. However, the segmentation of the muscles from CT-scan images is more challenging as the surrounding tissues have similar density with blurred margins between them. The task is even more arduous when the CT-scan contains artifacts, noise or inhomogeneities. This prevents the automatization of segmentation. Yet the current clinical practice – manual segmentation [141] requires tedious visual identification and manual highlighting of muscles. The process is very time-consuming and subject to operator variability. Accuracy is limited, and it currently requires the input of expert operators [141]. A possible improvement can involve automatization of this process for segmenting target tissues [178].

The purpose of this study is to validate the semi-automatic segmentation method, introduced in the two previous chapters, by comparing it to manual segmentation, for clinicien uses.

5.2 Materiels and Methods**5.2.1 Medical Image Data**

CT-scan data were collected from a Maxillo-facial surgery Department database. All included patients were informed their data would be collected anonymously for scientific purpose and that they could refuse the scientific use of their data. 26 patients (19 female patients/7 male patients) aging from 16 to 47 years were included.

The selection criteria we considered were :

- Preoperative scans exhibiting no bone implants to avoid artifacts.
- No edentulous patients.
- A field of acquisition including the whole masseter muscles.

All CT-scans were obtained using a Discovery CT750HD system (GE Healthcare, Chicago, Illinois, United-States). Slice thickness was 1.25 mm and the pixel spacing was (0.46 mm, 0.46 mm).

5.2.2 Segmentation process

We call here segmentation the process of attributing a label to each voxel (3D pixel) of an image to generate a corresponding 3D object.

A first case was used as training by the two operators with the two methods, to get used to the softwares. After this first training, the segmentation of 40 masseters from 26 CT-scans, was performed. Each operator processed 20 masseters segmentation in a separate database. We needed to limit ourself to this number of segmentation due to the time required for the manual segmentation. First, manual segmentations were done, then the semi-automatic one was performed by the same operator on the same data. The time required for the two segmentations was recorded for comparison.

Manual segmentation

The manual segmentation was performed using Amira® [197] (developed at the ZIB, Berlin, version 2019.05) as shown in Figure 5.1. Each CT-scan was reconstructed in coronal, sagittal and axial planes. Manual segmentation was obtained by delineating the contours of the masseter muscle in axial and coronal views, on every slices. Various selection tools offered by the software have been used for this purpose, such as « region growing », or « selective brushing ». In a final step, the continuity and relevance of the traces were re-verified.

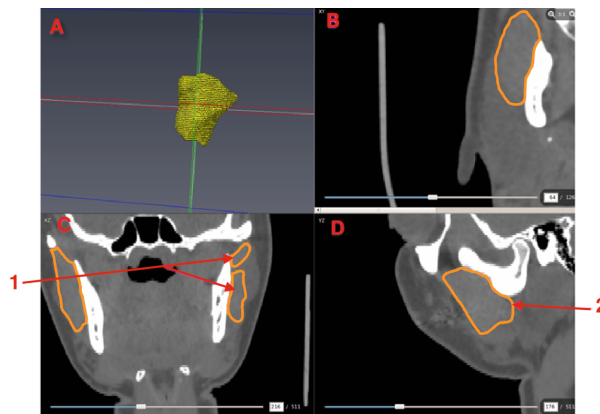


FIGURE 5.1 – Segmentation of the masseter from the 3 scanner cross-sectional planes : A : The final 3D form, B : The axial plane, C : The coronal plane, D : The sagittal plane. 1 : The separation of the two traces shows a segmentation of two different beams of the masseter. 2 : the segmentation of the sagittal plane deduced from the other two planes.

To identification of the cranial and caudal limits of the masseter muscle, and so to define the upper and lower limits, we used the coronal slices. The cranial limit of the masseter was marked at contact with the zygomatic arch. Then double checking was made between the coronal and axial sections in order to check the coherence of the segmentation.

After this first step of segmentation, a specific protocol was used in Amira ® to exclude irregularities and inconsistencies in the 3D objects.

The protocol included the following actions :

- « Remove Island » : to delete isolated parts of less than 15 voxels.
- « Fill Holes » : this function allows to automatically incorporate all the voxels situated in the muscle body and which have not been selected by the operator.
- « Smooth Label » : smooth the 3D general contour, with a tolerance set to 3.

At last, the segmentation was double-checked by a third expert.

Between the two segmentations protocols, a delay of 6 weeks at least was respected.

Semi-automatic segmentation

In a second step, the same two operators performed the semi automatic segmentation for the same sample of patients. The semi-automatic technique uses a 3D muscle database and a model-based computer process with the goal to decrease the time of segmentation and with similar precision, as well as making segmentation accessible to non-expert physicians (cf. Chapter 2, for the 3D muscle database, and Chapter 3 and 4, for the semi-automatic segmentation process). Semi-automatic segmentation is carried out in one step : it consists in selecting 50 points randomly distributed over the masseter's surface in the different sections of the scanner in the axial, sagittal and coronal planes (Figure 5.2). In order to have the most representative selection of points possible, we did not select more than 3 points per slice. The points were all selected in locations where the masseter limits were clearly visible, whether the points are located on the limit between the muscle and the bone or between the muscle and the other soft tissues.

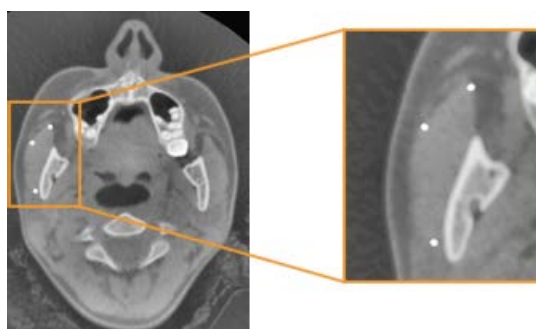


FIGURE 5.2 – Example of a point selection located on the masseter's periphery

Statistical Analysis

Each segmentation has been timed for the 2 operators, to allow for comparison between the 2 segmentation methods. We also computed the mean discrepancy between the two segmentations of the same masseter to complete this comparison, using the L_2 error.

All statistical analyses were performed in R. We performed a t-test [99, 214] for appariate data to compare the time difference between the two methods, and a t-test for non appariate data to compare the global time inter-operator « reproductibility » of the two methods. Since the segmentation was performed on more than 20 slices per indivudal (a segmentation equivalent to about 100 slices) considered as representative sample of all slices, we also performed a t-test between the two operators segmentation to eliminate potential inter-operator measurement bias of the time of segmentation and the errors. The threshold of significance we choose to respect for those test was $p=0.05$.

5.3 Results

The total manual segmentation time for operator 1 was 29 hours and 09 minutes with an average and a standard deviation of (1h27, 20min). For operator 2, the total segmentation time was 39 hours and 57 minutes with an average and a standard deviation of (1h59, 26min). The total semi-automatic segmentation time for operator 1 was 2 hours and 51 minutes, with an average and standard deviation of (8min 30sec, 2min 50sec). For operator 2, the total semi-automatic segmentation time was 3 hours and 36 minutes with an average and a standard deviation of (10min 30sec, 4min 28sec).

In Table 5.1, we show the time of segmentation by operator for the two methods.

	Operator 1		Operator 2	
	MS	SAS	MS	SAS
Mean	1h27m	8m30s	1h59m	10m30s
Max	2h10m	13m	2h40m	20m
min	58m	5m30s	1h10	4m
SD	20m	2m50s	26m	4m28s

TABLE 5.1 – Segmentation time for the two methods with both operators. MS : Manual Segmentation, SAS : Semi-automatic segmentation.

Semi-automatic segmentation was very significantly faster than manual, ($p=5.61e-23$). The inter-operator time was significantly different with the manual method $p = 6.67e-5$, whereas with the semi-automatic one no difference were found $p = 0.07$.

The descriptives statistics of the error between the manual and semi-automatic methods are presented for each operator in the Table 5.2.

	Operator 1	Operator 2
Mean	2.8 mm	2.9 mm
Max	4.4 mm	3.9 mm
min	0.8 mm	0.7 mm
SD	1.0 mm	0.8 mm

TABLE 5.2 – Descriptive statistic of the error performed with the semi automatic segmentation

The inter-operator error (computed for the semi-automatic segmentation) were found not significantly different between the two operators, with $p = 0.79$.

5.4 Discussion

We have presented in this paper a proof-of-concept study focused on the masseter muscle from CT-scan images. The masseter is one example among many structures that can be segmented using a semi-automatic process and the type of image can vary also. Semi-automatic segmentation can be of use in highly diverse clinical applications/settings.

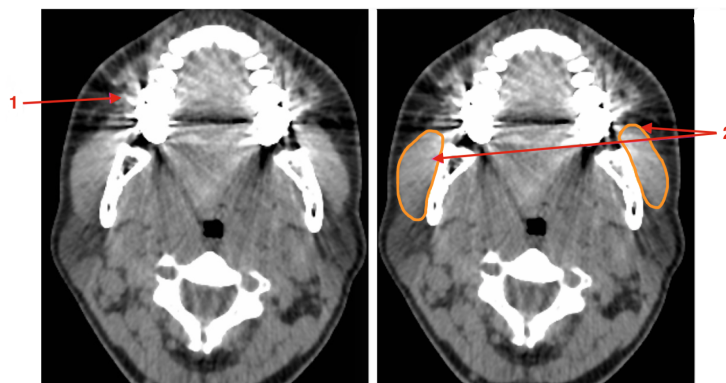


FIGURE 5.3 – 1-Artifacts, 2-Masseter layout hardly discernible due to artifacts

The general process of the segmentation reveals some major difficulties :

First, images may contain artifacts (Figure 5.3), often caused by implants or dental crowns and fillings, which can change the intensity of a voxel so that its classification becomes uncertain [227].

Secondly, because of the blurred boundaries between the masseter and its adjacent anatomical structures, it was sometimes difficult, even for experts, to determine with precision where the muscle boundaries are.

Consequently, it is difficult to achieve a perfect segmentation, due to the occurrence of under-segmentation or over-segmentation. This means, in the first case, pixels belonging to different objects are classified as belonging to the same object; and on the contrary, in the second case, voxels belonging to the same object are classified as being of different objects [39, 141, 142, 227].

We encountered several difficulties in manual segmentation, among which :

- Lateral and medial limits were very difficult to identify on the coronal and sagittal slices, as such we mostly used the axial slice (Figure 5.4).

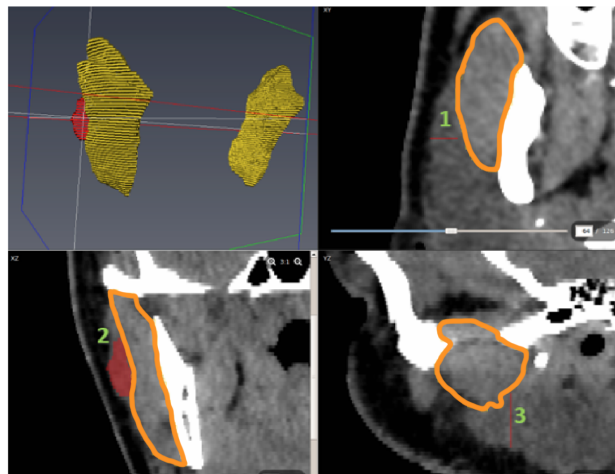


FIGURE 5.4 – The posterolateral contour of the masseter is traced first on the axial (1) and then coronal section (2), followed by a check on the sagittal section(3)

- The masseter can separate into several layers. It is difficult to identify them and to determine the limits of the beams (Figure 5.5) :

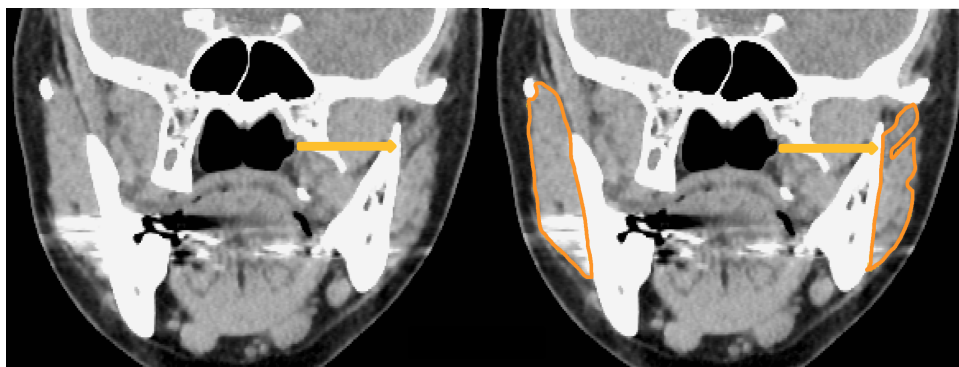


FIGURE 5.5 – The radiolucency shows the separation of the beams

Many techniques proposed in the literature are semi-automated or even fully automated, leading to highly consistent segmentations across multiple users [17], but not on every type of anatomical objects or medical images. In terms of medical ethics and law, the responsibility for errors of diagnosis may lie with the medical practitioner and, therefore, the correction of the automatic

segmentation errors is required to avoid negligence [139], hence the interest of semi-automatic segmentation.

The impossibility to visualize in real time the 3D shape of the masseters as in manual segmentation has been the main difficulty encountered during the semi-automatic segmentation. Indeed the operator often verify their slice segmentation by checking the 3D anatomy. This can also be considered as an improvement as it decreases the operator subjectivity in the segmentation process. The anatomy information being provided by the database with the semi-automatic method and not by the operator anymore.

It has to be noticed, however, that the 2 operators had segmented the masseters manually at first. It made the semi-automatic technique, on the same muscle, easier even if a delay was respected between the 2 segmentations. Nevertheless, as mentioned in the methods section, this method requires a first database of the muscle of interest to be able to work, and this database is mostly done manually.

This study shows a significant gain of time when using the semi-automatic method. We also evidenced that the semi-automatic technique leads to better inter-operator « reproducibility ». The errors made by the semi-automatic segmentation tools developed is in average 2.85 mm (standard deviation 0.9 mm). It is important to keep in mind that, this method is still under development and some improvement can be expected, for the registration time, the error and the reproductibility study, which is really important in our case since the shape approximation depends on the amount and location of the points selected.

The semi-automatic technique uses a 3D muscle database and a model-based computer process with the goal to decrease the time of segmentation, with similar precision, as well as making segmentation more accessible.

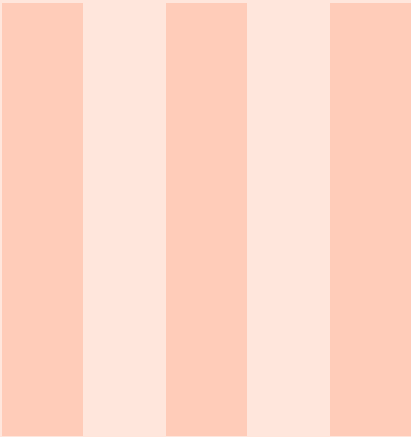
Finally, it must be kept in mind that the segmentation times are relative to the operator's level of experience. A well-trained operator, with a better knowledge of segmentation processes, would probably have reduced segmentation times. However, it can be reasonably assumed that this would probably be the case for both methods presented. The semi-automatic method would then keep its advantage.

5.5 Conclusion

This chapter presents a new, simpler and less time-consuming technique for segmenting soft tissue from CT data sets, than the usual manual segmentation. Muscle segmentation is a difficult task due to its resemblance to surrounding soft tissue. However, this new method shows that by incorporating prior knowledge of the shape (with a database and a compute model method), clinically acceptable results can be obtained through a semi-automatic segmentation software.

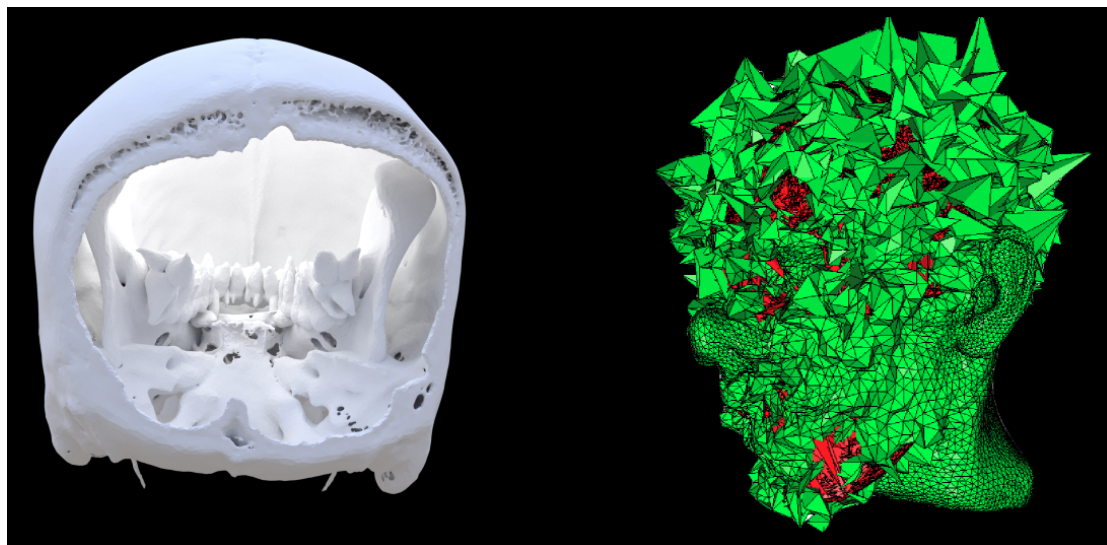
Since this method is still under development, it would be interesting to test a number of additional tools to determine how the result would be affected. We can cite :

- a complete inter- and intra-operator reproducibility study,
- a guest phantom, on 2D images of the anatomic object, as the points selection is made for the semi-automatic method,
- a 3D visualization, of the anatomic object, as the points are selected for the semi-automatic method,
- the option of manually editing the anatomical object obtained semi-automatically, to allow the enrichment of a database under construction. This would speed up the initial process, while allowing to continue acquiring new shapes for the dataset.



Third Part : Application to facial reconstruction

	Introduction	137
6	Shape matching	139
6.1	Introduction	
6.2	A shape optimization framework	
6.3	Two functionals for shape matching	
6.4	Numerical issues and examples	
7	Facial Reconstruction	155
7.1	Introduction	
7.2	Anatomy	
7.3	Facial reconstruction process	
7.4	Validation	
7.5	Discussion and Conclusion	
	Conclusion and perspectives	173



INTRODUCTION PART III

This last part contains two chapters, about the primary objective of this thesis work : facial reconstruction and the morphing method used to obtain it.

In chapter 6, the morphing method is detailed, which constitutes one of the main elements of the facial reconstruction method detailed later on. This work is a follow-up to the one presented by Maya de Buhan and Chiara Nardoni in [36], and was carried out jointly with both of them. Chiara Nardoni has already presented it in her own thesis [158]. In particular, my contribution to the development of the boundary method, its comparison with the volumic method, and 2D and 3D numerical simulations.

This last chapter (chapter 7 of the thesis) is the outcome for the FaciLe project, dedicated to facial reconstruction for forensic medicine, and presents an improvement of the method proposed by Maya de Buhan and Chiara Nardoni in [35], taking into account the underlying anatomy of the face. All the process is fully automatic, which allowed us to propose an application to validate our method compared to the one mentioned above via the recognition from a picture of different reconstructions by a population of more than 100 people.

**the nice figures presented above are the results of unfortunate numerical simulations carried out during the work on Chapter 6 and 7, and they also illustrate some of the difficulties of numerical implementation work.*



6. Shape matching

Sommaire

6.1	Introduction	140
6.2	A shape optimization framework	141
6.2.1	Shape sensitivity analysis : Hadamard's shape derivative	141
6.2.2	General procedure for the minimization of a shape functional	143
6.3	Two functionals for shape matching	144
6.3.1	Shape matching without constraint on the displacement	144
6.3.2	Shape matching with extension and regularization of the descent direction	145
6.4	Numerical issues and examples	146
6.4.1	Boundary functional P	146
6.4.2	Volume functional J	148
6.4.3	Comparison of the proposed methods	149

Volumic and Boundary shape matching : comparison of two optimization methods

Work in collaboration with Maya de Buhan and Chiara Nardoni, submitted in ESAIM :M2AN.

Abstract

In shape matching, the general issue is to find a transformation from a given 'template' shape into a 'target' shape. In this article, we propose to define this transformation as an elastic deformation obtained by minimizing a functional based on the distance between the two shapes. To achieve our goal, we rely on techniques from shape optimization. We introduce and compare two cost functionals devoted to measure the discrepancy between shapes. At first, we introduce a boundary

criterion depending on the squared Euclidean distance to the boundary of the target shape. Then, a novel volume criterion depending on the signed distance function to the target shape is used. Both deformation models are driven by a computational mesh and have been implemented in a finite elements setting. We present numerical examples in two and three dimensions to compare their efficiency as well as their drawbacks.

Key Words

Shape optimization, Shape matching, Level-set function, Finite elements, Mesh deformation.

6.1 Introduction

This article is devoted to the problem of $2d$ and $3d$ shape matching (or shape morphing). The main issue is to find a transformation from a given 'template' shape Ω_0 into a 'target' shape Ω_T . Such a transformation may be used to compare the two shapes Ω_0 and Ω_T and find their similarities which is a key ingredient in shape retrieval, classification, recognition or shape tracking. One can also be interested in computing the physical deformation of Ω_0 into Ω_T to reconstruct or simplify the target shape, or simply in transporting quantities of interest as textures from Ω_0 to Ω_T .

In our approach, the desired transformation is realized as a sequence of elastic displacements, which are obtained by minimizing an energy functional based on the distance between Ω_0 and Ω_T . Indeed, we introduce two functionals devoted to measure the discrepancy between shapes : the first one uses a boundary criterion that depends on the square of the Euclidean distance between the boundaries of the two shapes, whereas the second one is based on a volume criterion depending on the signed distance function (that will be defined in (6.8)) computed on the target shape. The latter has been already briefly presented in [36]. In the current article, we complete the theoretical framework, give more details about the numerical implementation, show new 2d and 3d examples and, above all, propose a comparison of the original volume criterion with the more intuitive boundary one to prove its superiority.

Our method has much in common with [192, 193] as it proposes a physically inspired deformation model and also with [14], borrowing techniques from optimal control and shape optimization. For a general overview on shape matching methods, we refer to the survey [244]. Let us only mention here a few techniques.

In the field of computational anatomy, a series of articles (see e.g. [21, 67, 85]) have suggested to describe the deformation of Ω_0 onto Ω_T via a diffeomorphic map. The restraint to diffeomorphisms prevents discontinuous or self intersecting deformations. This approach leads to the so-called Large deformation Diffeomorphic Metric Mapping (LDDMM) method which has received a lot of interest in the last years, especially for dealing with medical data. The LDDMM approach considers shapes embedded in a metric space and describes the diffeomorphism between two items Ω_0 and Ω_T as the dynamic flow of a velocity field v . The search for v is then casted as an optimal control problem. The criterion to be minimized is the sum of a matching functional - representing the cost of the flow which transports Ω_0 onto Ω_T - and a regularization term, guaranteeing the smoothness of the deformation. The structure of metric space allows the definition of similarity measures between shapes, in terms of geodesics in the shape space. The LDDMM formulation produces a global deformation of the ambient space, which in particular matches the shapes of interest into each other. In [159] the energy functional associated to a LDDMM problem is used for defining a measure of similarity between two shapes, defined as the geodesic path in the space of diffeomorphism by minimizing an energy functional. The LDDMM framework has been used for landmarks-based matching using the spline interpolation theory [113], unlabelled point-sets [81], $3d$ stacks of density images [20, 21], curves [82, 83] or surfaces [80, 235]. In [235] a theoretical framework is provided for encoding surfaces embedded in \mathbb{R}^3 as currents; the optimal control problem is defined consequently as matching of currents. The resulting mapping is used to study

features of organs, detect anomalies, etc.

Conformal geometry theory has been used for translating a 3d shape matching problem into a 2d one by conformal parametrization of the boundary, via harmonic maps, conformal maps, least square conformal maps [86, 136, 245]. In a series of articles devoted to shape matching and retrieval, 3d shape matching is achieved by extraction and comparison of topological features, namely Reeb graphs [97], or others topological indicators. However, a Reeb graph is computed from the analysis of the isosurfaces of a real-valued function defined in a manifold; for many shapes the extraction of such a function is not a trivial task.

More recently, in the field of Computer Graphics, the optimal transport point of view has been used to displace an input tetrahedral mesh onto a given object [130, 215] and to register 2d images [92]. In the optimal transport point of view a measure (derived on a density function supported by a computational mesh or defined as a sum of Dirac masses) is displaced into another by minimizing the celebrated Monge-Kantorovitch optimal mass transportation cost. Methods from optimal transport have the merit to be insensitive to a rigid-body motion of the target shape, which is of tremendous importance for searching shape similarity, and to allow topology changes.

Several shape matching methods use landmarks or anchor points for which the correspondence is supposed known and the deformation is guided by this information. Depending on the application, these feature points are defined manually (for example in the case of anatomical landmarks) or by automatic extraction, for instance as critical points of a well-suited scalar function defined on the shape. In [22] for example, the authors start by distributing sample points on the contour of both shapes, that will be matched according to their 'shape context', namely a shape descriptor defined as an histogram of the relative position of the sampled points with respect to a given point on the shape. Our method does not make use of any preprocessing feature extraction. In the proposed problem the 'template' shape Ω_0 is numerically described by means of a computational mesh whereas the 'target' shape Ω_T is known only via its boundary. The sole restrictive assumption is that both shapes share the same topology.

The paper is organized as follows. We first introduce the shape optimization framework in 6.2. Both methods, boundary and volumic, are presented in 6.3. Eventually, in 6.4, we compare the results obtained with the two functionals thanks to several numerical examples.

6.2 A shape optimization framework

Generally speaking, shape optimization is about optimizing a cost functional $F(\Omega)$ - or objective functional - over a set of admissible shapes \mathcal{O}_{ad} . A generic shape optimization problem reads as :

$$\min_{\Omega \in \mathcal{O}_{ad}} F(\Omega), \text{ or } \max_{\Omega \in \mathcal{O}_{ad}} F(\Omega).$$

When the optimization problem is cast over a set \mathcal{O}_{ad} of shapes, some additional difficulties come into play, from both theoretical and numerical points of view. First, one needs a way for describing admissible variations over the space \mathcal{O}_{ad} and a notion of differentiation over the space \mathcal{O}_{ad} , which is needed for inferring optimality conditions. Moreover, in most problems the dependency of the objective functional on the domain is highly non-trivial; the functional F may depend on geometric properties of the domain (i.e. curvature, normals, thickness) but also on a state u_Ω - achieved as the solution of a PDE posed on Ω - and its derivatives. In this case we have to deal with the derivation of the state u_Ω under consideration with respect to the domain.

6.2.1 Shape sensitivity analysis : Hadamard's shape derivative

Several notions of differentiation with respect to the domain are available in the literature. Here we refer to the Hadamard's boundary variation method (see e.g. [3, 96, 157]). The general idea is to

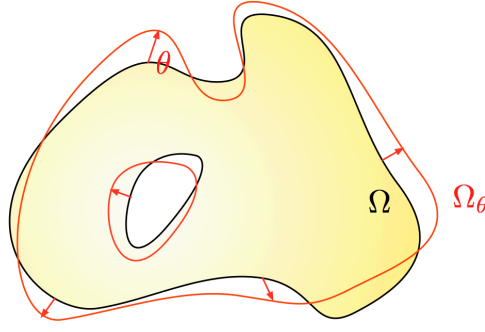


FIGURE 6.1 – Variation Ω_θ of a shape Ω according to Hadamard's method.

establish a correspondence between variations of the domain and diffeomorphisms of \mathbb{R}^d ($d = 2, 3$). Thus, variations of a given shape Ω are considered under the form :

$$\Omega_\theta = (I + \theta)(\Omega),$$

where $\theta : \mathbb{R}^d \mapsto \mathbb{R}^d$ is a 'small' vector field. Indeed, each admissible variation Ω_θ of Ω is parametrized in terms of a transformation of the form $I + \theta$, which remains 'close' to the identity. The admissible vector field θ is sought among the Banach space $W^{1,\infty}(\mathbb{R}^d, \mathbb{R}^d)$ of bounded and Lipschitz functions $\theta : \mathbb{R}^d \mapsto \mathbb{R}^d$ endowed with the norm :

$$\|\theta\|_{W^{1,\infty}(\mathbb{R}^d, \mathbb{R}^d)} := \|\theta\|_{L^\infty(\mathbb{R}^d)^d} + \|\nabla\theta\|_{L^\infty(\mathbb{R}^d)^{d \times d}}, \quad \forall \theta \in W^{1,\infty}(\mathbb{R}^d, \mathbb{R}^d).$$

The convenience of the choice of this space follows from the following result (from [3]).

Lemma 6.2.1 For any $\theta \in W^{1,\infty}(\mathbb{R}^d, \mathbb{R}^d)$ such that $\|\theta\|_{W^{1,\infty}(\mathbb{R}^d, \mathbb{R}^d)} \leq 1$, the application $I + \theta$ is a Lipschitz homeomorphism with Lipschitz inverse.

Using the correspondence between vector fields and domains, the Hadamard shape derivative is defined in terms of the classical derivative over a functional space.

Definition 6.2.1 A function $F(\Omega)$ of the domain is said to be *shape differentiable* at Ω if the mapping $\theta \mapsto F(\Omega_\theta)$, from $W^{1,\infty}(\mathbb{R}^d, \mathbb{R}^d)$ into \mathbb{R} , is Fréchet differentiable at $\theta = 0$. The associated Fréchet differential is denoted as $\theta \mapsto F'(\Omega)(\theta)$ and called the shape derivative of F . The following expansion then holds :

$$F(\Omega_\theta) = F(\Omega) + F'(\Omega)(\theta) + o(\theta), \quad \text{where } \frac{|o(\theta)|}{\|\theta\|_{W^{1,\infty}(\mathbb{R}^d, \mathbb{R}^d)}} \xrightarrow{\theta \rightarrow 0} 0.$$

The form $\theta \mapsto F'(\Omega)(\theta)$ (at least at first order) does not depend on the tangential component of θ on $\partial\Omega$. More precisely we have the following statement (see [3]).

Proposition 6.2.2 Let Ω be bounded, Lipschitz domain in \mathbb{R}^d . Let F be a functional differentiable at Ω . If $\theta \cdot n = 0$, n standing for the outer normal to $\partial\Omega$, then we have :

$$\forall \theta \in W^{1,\infty}(\mathbb{R}^d, \mathbb{R}^d), \quad F'(\Omega)(\theta) = 0.$$

Moreover, for a large class of functionals F , the shape derivative F' takes the following form

$$\forall \theta \in W^{1,\infty}(\mathbb{R}^d, \mathbb{R}^d), \quad F'(\Omega)(\theta) = \int_{\partial\Omega} f \theta \cdot n \, ds, \quad (6.1)$$

where f is a scalar field defined on $\partial\Omega$, depending on the problem at stake. The choice of $W^{1,\infty}(\mathbb{R}^d, \mathbb{R}^d)$ as underlying Banach space guarantees that the application $I + \theta$ is a Lipschitz homeomorphism with Lipschitz inverse. However, in order to compute the shape derivative of a surface functional, we will sometimes require the vector field θ to enjoy more regularity than the one inherited from the space $W^{1,\infty}(\mathbb{R}^d, \mathbb{R}^d)$. In such a case we will consider the space $\mathcal{C}^{1,\infty}(\mathbb{R}^d, \mathbb{R}^d) := W^{1,\infty}(\mathbb{R}^d, \mathbb{R}^d) \cap \mathcal{C}^1(\mathbb{R}^d, \mathbb{R}^d)$ endowed with the norm :

$$\forall \theta \in \mathcal{C}^{1,\infty}(\mathbb{R}^d, \mathbb{R}^d), \quad \|\theta\|_{\mathcal{C}^{1,\infty}(\mathbb{R}^d, \mathbb{R}^d)} := \sum_{l=0}^k \sup_{\alpha \in \mathbb{N}^d, |\alpha|=l} \left\| \frac{\partial \theta}{\partial x^\alpha} \right\|_{L^\infty(\mathbb{R}^d)^d}.$$

Note that an equivalent definition of shape derivative holds over the space $\mathcal{C}^{1,\infty}(\mathbb{R}^d, \mathbb{R}^d)$.

6.2.2 General procedure for the minimization of a shape functional

From the expression of the shape derivative (6.1), we deduce that the vector field

$$-fn, \tag{6.2}$$

is a natural descent direction for F . Indeed, if $\theta = -tfn$ with $t > 0$ small enough, it guaranties that :

$$F(\Omega_\theta) = F(\Omega) - t \int_{\partial\Omega} f^2 ds + o(t^2) < F(\Omega).$$

This paves the way for an iterative algorithm, producing a sequence $(\Omega_k)_{k=0,\dots}$ of shapes, with decreasing values of $F(\Omega_k)$: at each step, Ω_k is updated according to

$$\Omega_{k+1} = (I + \theta_k)(\Omega_k), \text{ where } \theta_k \text{ is (an extension to } \Omega_k \text{ of) } -tfn. \tag{6.3}$$

From the discrete point of view, the procedure generates a sequence of meshes $(\mathcal{T}_k)_{k=0,\dots}$. At each iteration the mesh \mathcal{T}_k is updated by pushing its vertices according to the descent direction :

$$\forall x \text{ vertex of } \mathcal{T}_k, x \mapsto x + \theta_k(x). \tag{6.4}$$

The formal procedure described above boils down to deforming a shape Ω in the negative direction of the $L^2(\partial\Omega)^d$ gradient of the differential $\theta \mapsto F'(\Omega)(\theta)$:

$$F'(\Omega)(\theta) = \langle f, \theta \cdot n \rangle_{L^2(\partial\Omega)^d}. \tag{6.5}$$

Unfortunately, the descent direction associated to the vector field (6.2) reveals unsuited for at least two reasons :

- the vector field featured in (6.2) is defined only on the boundary of Ω ; it has therefore to be extended to Ω as a whole so that it can be a guide for displacing the vertices of \mathcal{T} ;
- if no particular attention is paid to this extension, the extended displacement field may impose an important stretching in Ω , making the motion of the vertices of \mathcal{T} via (6.4) impossible to achieve without invalidating the mesh.

To overcome both these difficulties we rely on a procedure of extension and regularization of the descent direction (6.2) by using the gradient of $\theta \mapsto F'(\Omega)(\theta)$ associated to another inner product. This *velocity extension - regularization* issue is quite classical in shape optimization (see [37, 84] and references therein), and can be thought of as an efficient preconditioning of the naive procedure (6.3). The general strategy is described in the following. Suppose that the space of admissible deformations is endowed with a structure of Hilbert space V . Let $\langle \cdot, \cdot \rangle_V$ be the inner scalar product in V . Therefore, we can consider the following linear form $l(\cdot)$ acting on elements of V :

$$\forall v \in V, l(v) = F'(\Omega)(v).$$

Now let $a_V(\cdot, \cdot)$ be a suitable symmetric, V -elliptic bilinear form acting on elements of V . The Lax-Milgram theorem ensures the existence of a unique $u_\Omega \in V$ solution of the variational problem :

$$\forall v \in V, a_V(u_\Omega, v) = l(v).$$

The vector field $-u_\Omega$ is a descent direction for F since :

$$F'(\Omega)(-u_\Omega) = -a_V(u_\Omega, u_\Omega) < 0.$$

A suitable choice in our context is to use the extension inherited from a particular mechanical system, that of linear elasticity. See 6.3.2 for an example of such a procedure.

6.3 Two functionals for shape matching

6.3.1 Shape matching without constraint on the displacement

Let Ω_0 and $\Omega_T \subset \mathbb{R}^d$ be respectively ‘template’ and ‘target’ shapes. Under the assumption that they share the same topology, our purpose is to map Ω_0 onto Ω_T by minimizing an energy functional which measure the discrepancy between the shapes. In order to achieve our goal, we introduce two shape functionals. At first, consider the following boundary functional $P(\Omega)$:

$$P(\Omega) = \int_{\partial\Omega} d^2(s, \partial\Omega_T) ds, \quad (6.6)$$

where $d(\cdot, \partial\Omega_T)$ denotes the usual Euclidean distance function to $\partial\Omega_T$. This functional is based on a classical paradigm - aligning two shapes by aligning their boundaries - and is used in a wide variety of situations in the context of non rigid registration (see [263] for example).

Then, consider the following functional $J(\Omega)$ of the domain :

$$J(\Omega) = \int_{\Omega} d_{\Omega_T} dx, \quad (6.7)$$

which involves the signed distance function d_{Ω_T} to Ω_T , defined by :

$$\forall x \in \mathbb{R}^d, d_{\Omega_T}(x) = \begin{cases} -d(x, \partial\Omega_T) & \text{if } x \in \Omega_T, \\ 0 & \text{if } x \in \partial\Omega_T, \\ d(x, \partial\Omega_T) & \text{if } x \in {}^c\overline{\Omega_T}. \end{cases} \quad (6.8)$$

Note that the functional J is defined on the whole domain of interest Ω . In order to decrease the value of $J(\Omega)$, the domain Ω must expand in the regions of the ambient space \mathbb{R}^d where d_{Ω_T} is negative (that is, in the regions comprised in Ω_T), and to retract in those where it is positive (see 6.2). By deforming the template shape as above we can always obtain better values for J until the deformed template shape reaches the target shape Ω_T . Therefore, $J(\Omega)$ has a unique, global minimizer $\Omega = \Omega_T$ if we assumed that $\Omega_T \in \mathcal{O}_{ad}$. A functional similar to (6.7) has also been used in [52] for shape optimization purposes.

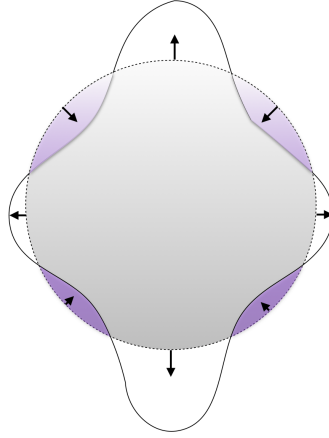
By a classical calculation (see [3, 96]), the functionals (6.6) and (6.7) are shape differentiable at any (enough) regular shape Ω , and the associated shape derivatives reads respectively :

$$\forall \theta \in C^{1,\infty}(\mathbb{R}^d, \mathbb{R}^d), P'(\Omega)(\theta) = \int_{\partial\Omega} \left(\frac{\partial d^2}{\partial n} + \kappa d^2 \right) \theta \cdot n ds, \quad (6.9)$$

where κ is the mean curvature of $\partial\Omega$, and

$$\forall \theta \in W^{1,\infty}(\mathbb{R}^d, \mathbb{R}^d), J'(\Omega)(\theta) = \int_{\partial\Omega} d_{\Omega_T} \theta \cdot n ds. \quad (6.10)$$

Following 6.2.1, a descent direction is inferred from formulas (6.9) and (6.10). An iterative algorithm devoted to the minimization of P (or J) will produce a sequence of shapes which are ‘closer and closer’ to Ω_T .

FIGURE 6.2 – Deformation of the template shape decreasing the value of J .

6.3.2 Shape matching with extension and regularization of the descent direction

As recalled in 6.2.1, it is crucial for numerical purposes to use the gradient of the mapping $\theta \mapsto P'(\Omega)(\theta)$ associated to another inner product instead of the one featured in (6.5). Therefore, assume that all the considered shapes Ω are filled with a linear elastic material. Also, imagine that any such shape Ω contains a given subset $\omega \Subset \Omega$ on which it is clamped. We now obtain a descent direction for $P(\Omega)$ as the unique solution u_Ω belonging to $H_\omega^1(\Omega)^d := \{v \in H^1(\Omega)^d, v = 0 \text{ in } \omega\}$ of the linearized elasticity system :

$$\forall v \in H_\omega^1(\Omega)^d, \int_\Omega \sigma(u_\Omega) : \varepsilon(v) dx = -P'(\Omega)(v) = - \int_{\partial\Omega} \left(\frac{\partial d^2}{\partial n} + \kappa d^2 \right) v \cdot n ds, \quad (6.11)$$

where $\varepsilon(v) = \frac{1}{2}(\nabla v + \nabla v^T)$ is the linearized strain tensor and σ is the associated stress tensor via the Hooke's law with Lamé coefficients λ, μ :

$$\sigma(u) = 2\mu\varepsilon(u) + \lambda \operatorname{tr}(\varepsilon(u))I.$$

This vector field u_Ω is a descent direction for $P(\Omega)$ since $P'(\Omega)(u_\Omega) \leq 0$ thanks to (6.11), and its advantages over the 'natural' deformation field $-\left(\frac{\partial d^2}{\partial n} + \kappa d^2\right)n$ are twofold :

1. u_Ω is defined on the whole shape Ω ; owing to the regularizing effect of elliptic equations, it is intrinsically smoother (see for instance [42]);
2. Owing to the mechanical features of elastic displacements (notably their 'rigidity'), it is expected that u_Ω will be more amenable to the displacement of the mesh \mathcal{T} into a valid mesh via (6.4); see e.g. [15] for an example of use of elastic displacements in the context of mesh displacement.

Furthermore, we can infer a descent direction for $J(\Omega)$ as the unique solution u_Ω belonging to $H_\omega^1(\Omega)^d$ of the variational problem :

$$\forall v \in H_\omega^1(\Omega)^d, \int_\Omega \sigma(u_\Omega) : \varepsilon(v) dx = -J'(\Omega)(v) = - \int_{\partial\Omega} d_{\Omega_T} v \cdot n ds. \quad (6.12)$$

R From the numerical point of view, the choice of a subset ω corresponds to a global alignment of shapes (cf. 6.3). This restriction we used to guarantee the well-posedness of Problems (6.11) and (6.12) could be replaced by adding a 0th-order term. Note also that by construction the boundaries $\partial\omega$ and $\partial\Omega$ do not intersect, preventing the loss of regularity at the interface between boundary conditions of different natures.

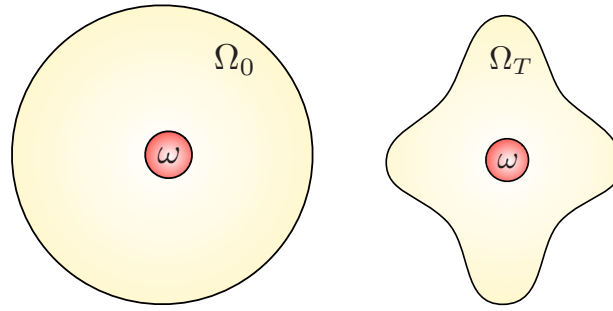


FIGURE 6.3 – Target and template shapes sharing a common fixed subset ω .

6.4 Numerical issues and examples

As far as the numerical setting is concerned, the template shape Ω_0 is discretized as a simplicial mesh (filled with triangles in 2d and tetrahedra in 3d). The computational mesh is non uniform : it is refined in the vicinity of the boundaries according to a curvature based sizing function and coarsened in the interior of the domain. This has proven to prevent severe distorsion/tangling of the elements avoiding the need to remesh the domain. In all the 2d examples, the chosen template mesh \mathcal{T}_0 is a disk that has about 18000 triangles. The set ω chosen for aligning Ω_0 and Ω_T is a small disk located in the interior of both shapes. Starting from the template shape Ω_0 we perform a standard gradient descent algorithm with adaptive step size in order to get a sequence of pairs $(\Omega_k, \mathcal{T}_k)$ of domains and their corresponding meshes with decreasing values of the functional. The general algorithm is the following :

Algorithm 6.1 Start from an initial shape Ω_0 ,
for $k = 0, \dots$, **convergence**

1. compute the value of the shape functional ;
2. compute the state u_{Ω_k} of the considered elasticity system on Ω_k by a \mathbb{P}^1 finite elements discretization ;
3. perform a line search for getting the optimal step size τ_k so as to guarantee the decrease of the shape functional ;
4. advect the shape Ω_k according to this displacement field, so as to get

$$\Omega_{k+1} = (I + \tau_k u_{\Omega_k})(\Omega_k).$$

The algorithm stops when the step size is smaller than a fixed tolerance ε . The global mapping from Ω_0 to Ω_T is easily recovered by the composition of the different displacements obtained at each iteration. Note that by moving the mesh at each iteration we are able to devise a deformation between two shapes which are not close from one another by using a linear elastic model, which accounts in principle for 'small' displacements. Note that that we can compose the deformations from the template Ω_0 onto two targets Ω_T, Ω'_T in order to obtain the mapping from Ω_T to Ω'_T and conversely.

6.4.1 Boundary functional P

In the boundary case, the computation of the shape gradient $P'(\Omega_k)$ requires at each iteration k the computation of :

- the normal derivative of the distance function d at each vertex x_i of the boundary $\partial\Omega_k$ by the

formula :

$$\frac{\partial d^2}{\partial n} = \nabla(d^2) \cdot n(x_i) = 2(x_i - p_{\Omega_T}(x_i)) \cdot n(x_i),$$

where $p_{\Omega_T}(x_i)$ stands for the projection of x_i on $\partial\Omega_T$;

- the discrete mean curvature κ of the boundary $\partial\Omega_k$. In $2d$ we follow the approach described in [52]. Let $\{x_i\}_{i=0,\dots,n}$ be the list of points lying on $\partial\Omega_k$. Let us suppose that the edges of the boundary have been sorted in such a way that for each vertex x_i the vertex x_{i-1} (resp. x_{i+1}) denotes the vertex placed before (resp. after) x_i , according to a counterclockwise orientation. In such a situation the normal vector at point x_i is estimated as the orthogonal of the (normalized) vector $\overrightarrow{x_i x_{i-1}}$. Then the discrete radius of curvature at vertex x_i is given by the formula :

$$r_i = \frac{1}{4} \left(\frac{\overrightarrow{x_i x_{i-1}} \cdot \overrightarrow{x_i x_{i-1}}}{-n(x_i) \cdot \overrightarrow{x_i x_{i-1}}} + \frac{\overrightarrow{x_i x_{i+1}} \cdot \overrightarrow{x_i x_{i+1}}}{-n(x_i) \cdot \overrightarrow{x_i x_{i+1}}} \right).$$

The discrete curvature κ_i at x_i is taken as the inverse of the radius of curvature when the latter is not vanishing, and is set to zero otherwise.

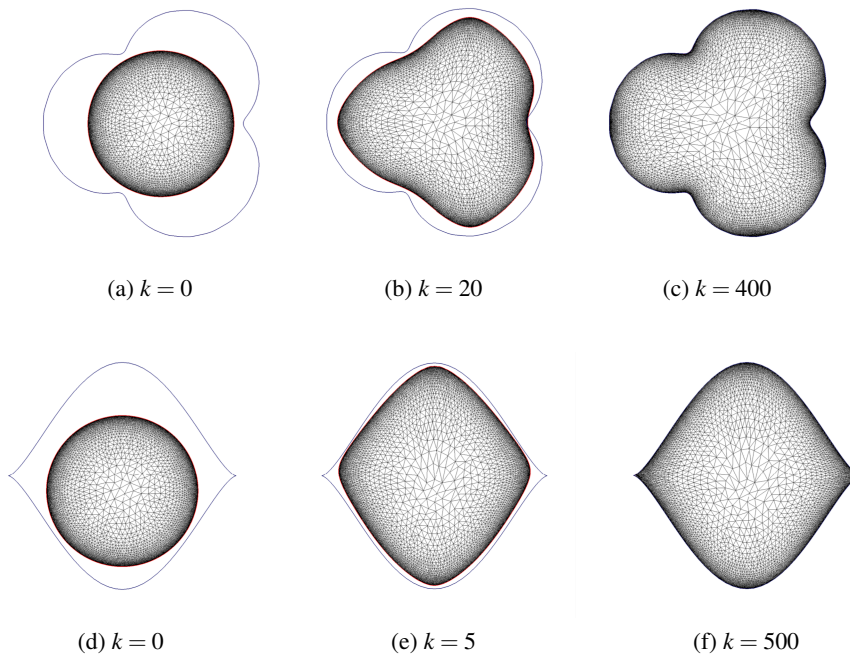


FIGURE 6.4 – Simple 2d examples for the boundary functional. Boundary of the target shape (blue contour) and computational mesh of the template shape Ω_k at iteration k .

Let us now present several examples of $2d$ shape matching using the boundary functional. First, consider the test cases of 6.4. The algorithm converges in few iterations and is able to perfectly recover the target shape, even in regions of high curvature. Then, the same template is deformed onto the targets represented in 6.7. In these cases, the algorithm fails to converge, invalidating the mesh after few iterations. The occurrence of singularities is due to a lack of differentiability of the distance function when the set of projections of a point over the boundary of the target shape is not a singleton. In such case the shape derivative is not well defined since we have as many descent directions as projection points. This is an important drawback of the proposed functional.

6.4.2 Volume functional J

For the volume functional, the computation of the shape gradient $J'(\Omega_k)$ does not demand the evaluation of the discrete curvature or the normal derivative of the distance function. The only information required about the target shape Ω_T is the datum of its signed distance function e.g. a \mathbb{P}^1 piecewise affine function on the fixed mesh of a large computational domain \mathcal{D} , which can be defined on a possibly non-conforming mesh (e.g. showing small gaps, overlapping entities, etc.). The calculation of the signed distance function to Ω_T is performed using the algorithm [51]. An example of signed distance function to a target shape is shown in 6.6-(a).

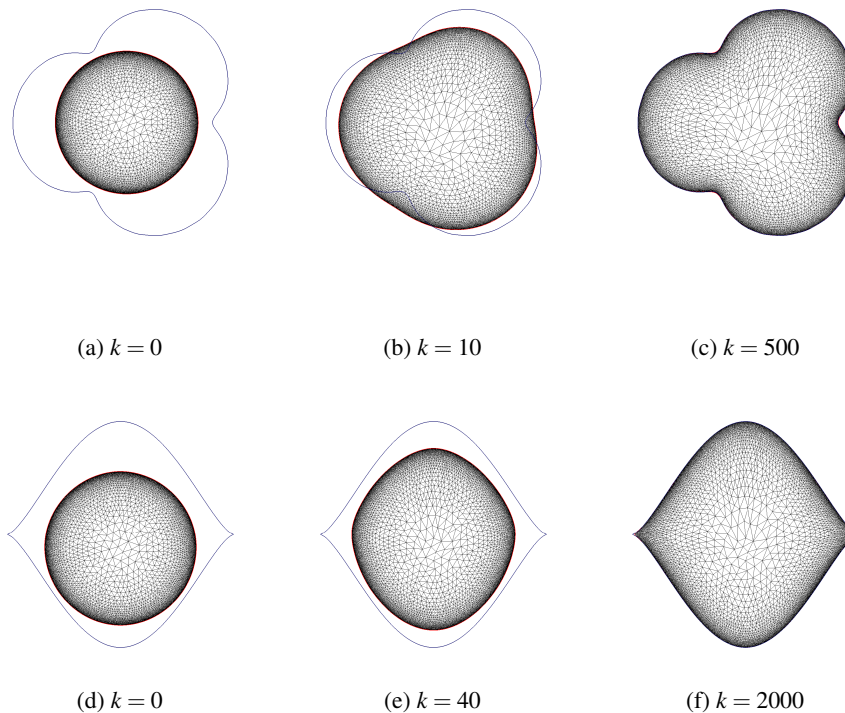


FIGURE 6.5 – Simple 2d examples for the volume functional. Boundary of the target shape (blue contour) and computational mesh of the template shape Ω_k at iteration k .

Let us present several 2d numerical examples to show the performances of the method. Both target and template meshes are embedded in a unit computational box with dimensions $[0, 1]^2$. At first, we consider the test cases depicted in 6.5 that result in an excellent recovery of Ω_T . In 6.8, note that the algorithm is also able to recover isolines of high curvature resulting in an excellent matching, even for template and target shapes very far from one another. Also notice that the use of linear elasticity equations makes the deformation smooth preserving the quality of the mesh under deformation. 6.6 shows the contour superposition between the deformed template mesh and the contour of the target shape model under consideration. Note that the template shape is never remeshed during the process. This allows to keep a point-to-point correspondence between the template mesh and the final mesh of the target, which may be useful in applications. However, in the example depicted in 6.8-(g)-(i), the matching in the extremity of the tail could be improved by adding new boundary points in this area.

Next, we consider a 3d example; see 6.9. Both the target and the template meshes are embedded

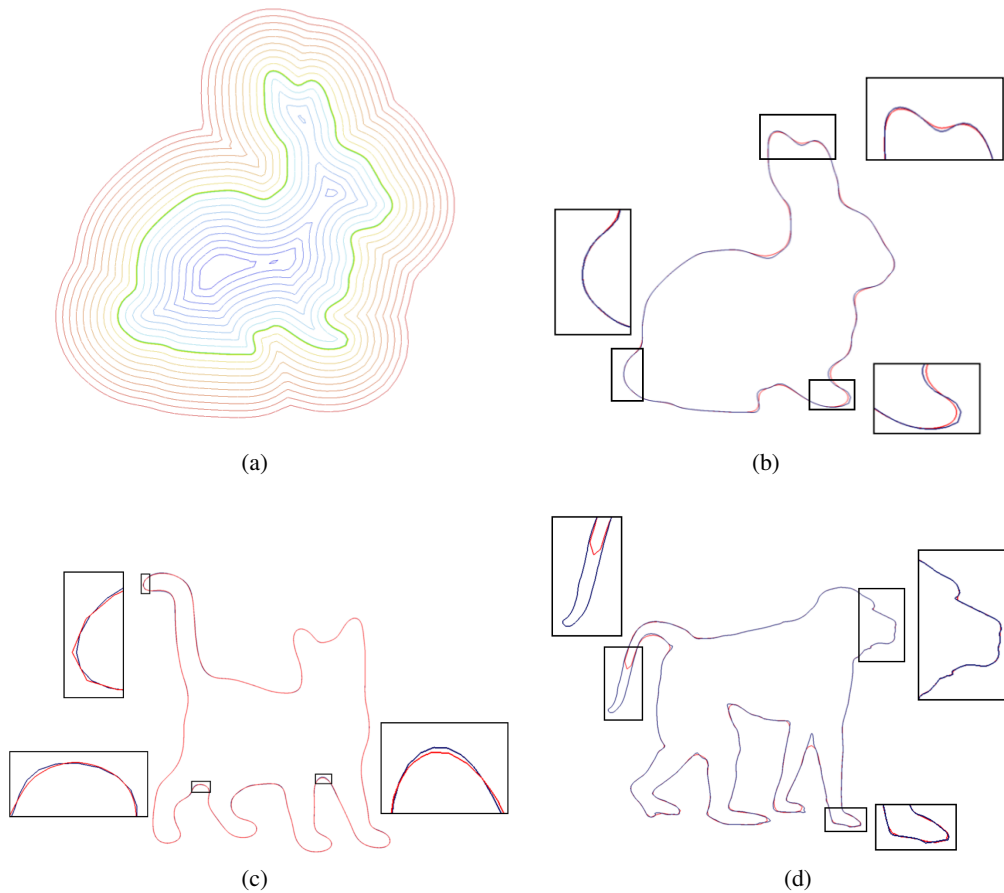


FIGURE 6.6 – (a) Isolines of the signed distance function. (b)-(c)-(d) Discrepancy between Ω_T and the deformed template shape for the test cases of 6.8.

in a unit computational box $D = [0, 1]^3$. The shapes Ω_0 and Ω_T are aligned by choosing a small ball ω in $\Omega_0 \cap \Omega_T$. The template mesh \mathcal{T}_0 has about 9000 triangles, and 1300 iterations of the gradient descent algorithm have been performed to achieve convergence for a tolerance $\varepsilon = 10^{-6}$, running in a few minutes on a standard laptop computer. The L^2 norm of the distance between the boundaries of the final shape Ω_{1300} and the target shape Ω_T is 5.04×10^{-4} (much smaller than the minimal mesh size). Eventually, in 6.10 an ellipsoid template mesh is mapped onto a shape of hippocampus that was obtained from segmentation of medical images.

6.4.3 Comparison of the proposed methods

The meshes obtained with both functionals are valid, and as we never remesh the template during the process, it is easy to compare the results and the associated errors. The convergence analysis relative to all the considered 2d examples is detailed in Table 6.1. The quantitative analysis of the error is performed by computing the discrepancy between the boundaries of the last deformed template Ω_k and the target shape Ω_T .

For the 2d examples depicted on 6.4 and 6.5, we obtain similar results using the two proposed functionals. The main advantage of the volume functional is the ability to converge in all the proposed examples, with a little number of iterations. The boundary functional has shown good performances and even more accuracy in few examples (see 6.4 for instance) but it is very sensitive to the initial alignment of both target and template shapes, failing to converge in most cases and

	Boundary functional		Volume functional	
Test case ...	L^2 mean	Iterations	L^2 mean	Iterations
1. Flower	4.8×10^{-4}	400	6.4×10^{-4}	500
2. Lip	2.9×10^{-5}	500	1.9×10^{-4}	2000
3. Rabbit	Do not converge	1000	1.0×10^{-3}	500
4. Cat	Do not converge	680	5.7×10^{-4}	1500
5. Monkey	Do not converge	300	1.2×10^{-3}	2300

TABLE 6.1 – Comparison between the boundary and volume functionals. Computation error and number of iterations needed to reach convergence for the 2d cases.

generating singularities. Note that the signed distance function to Ω_T is not differentiable at points of the space having multiple projections over $\partial\Omega_T$. However this lack of differentiability does not create ambiguities in the volume case because the expression of the shape derivative depends only on the value of the signed distance function and not on the projection points. Hence, the volume functional based on the paradigm 'ask to Ω_0 to fill all the space occupied by Ω_T ' has proven to be more efficient in most situations with respect the one based on the alignment of boundaries. In [35] where the volumic method is used to efficiently infer correspondences in a database of 3d shapes coming from segmentation of medical images. The inferred correspondence is used to drive a new numerical method for facial reconstruction, which is a challenging problem in forensic science. Note also that the volume functional, although much lesser sensitive that its boundary counterpart, is not independent to the initial alignment of both shapes : a rigid body motion applied to the initial shape could lead to a very different mapping between template and target. Future works could compare combine the proposed method with techniques which are unsensitives to the initial alignment, notably the ones based on optimal transport theory. Indeed, the discrepancy between shapes could be measured by means of the Wasserstein distance (that, precisely, involved in optimal transport).

Acknowledgments

The authors would like to kindly thank P. Frey, Y. Maday, C. Dapogny and the partners of project FaciLe for fruitful discussions.

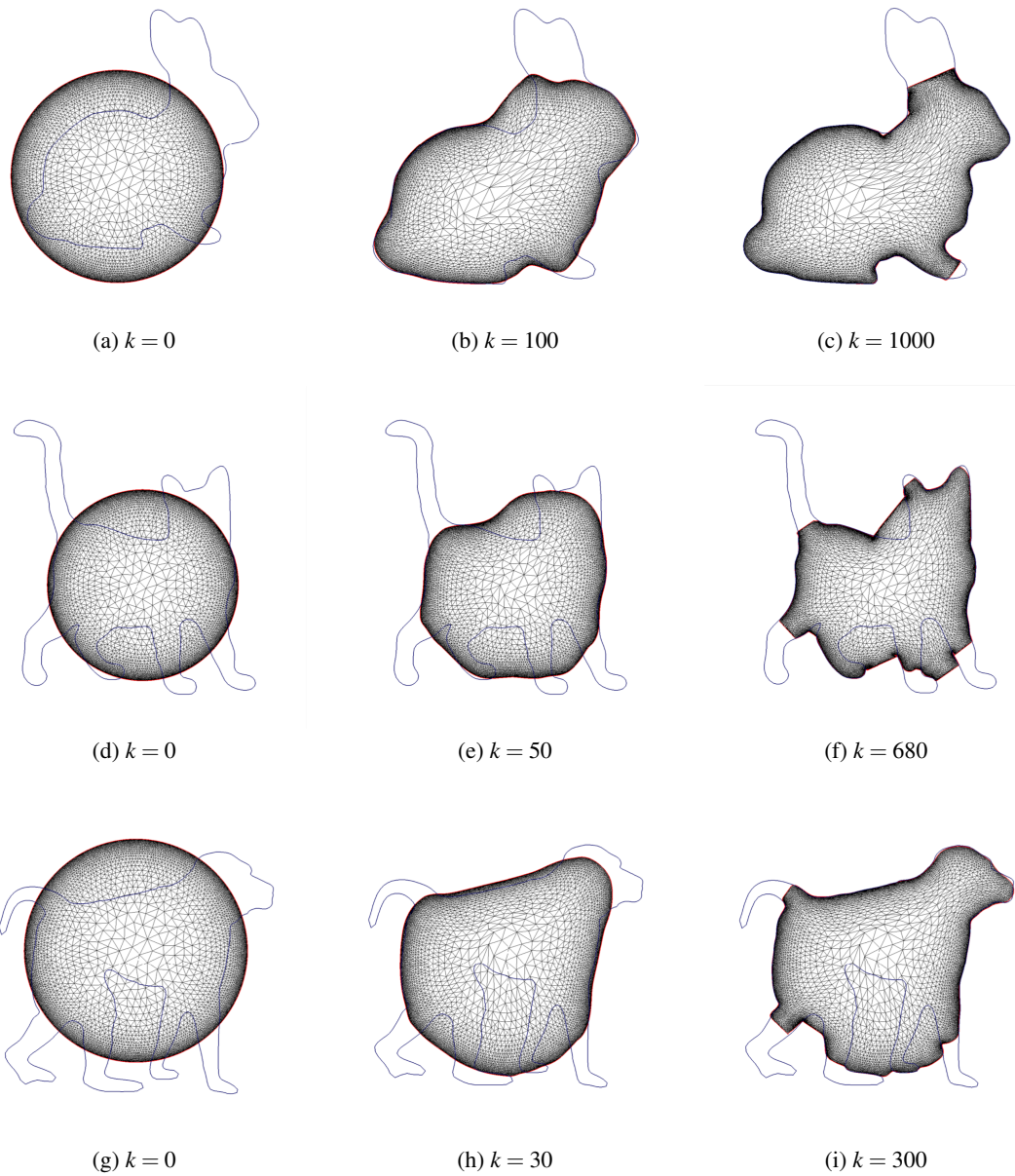


FIGURE 6.7 – Three 2d examples for the boundary functional. Boundary of the target shape (blue contour) and computational mesh of the template shape Ω_k at iteration k . The use of the surface functional (6.6) generates singularities.

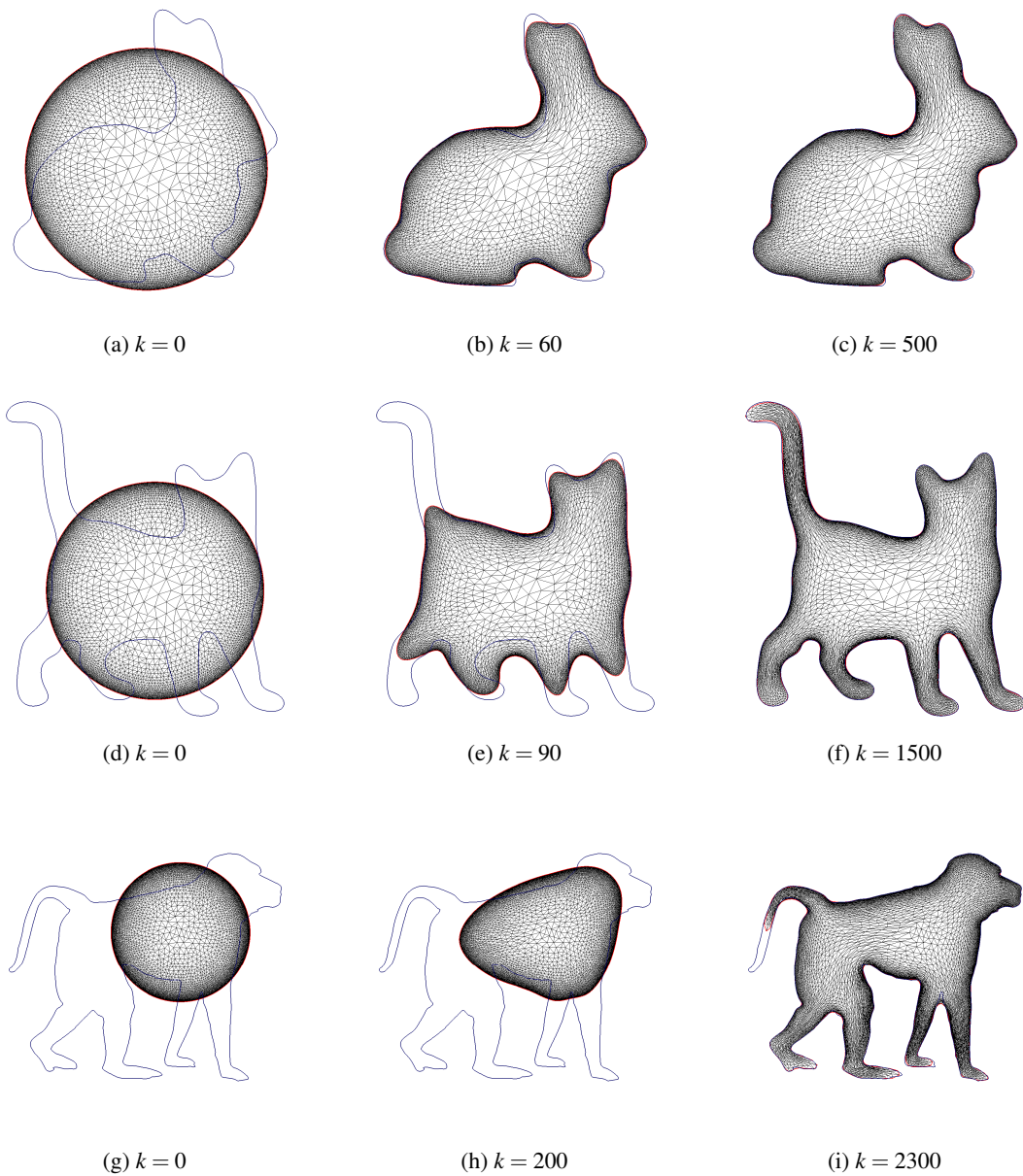


FIGURE 6.8 – Three 2d examples for the volume functional. Boundary of the target shape (blue contour) and computational mesh of the template shape Ω_k at iteration k .

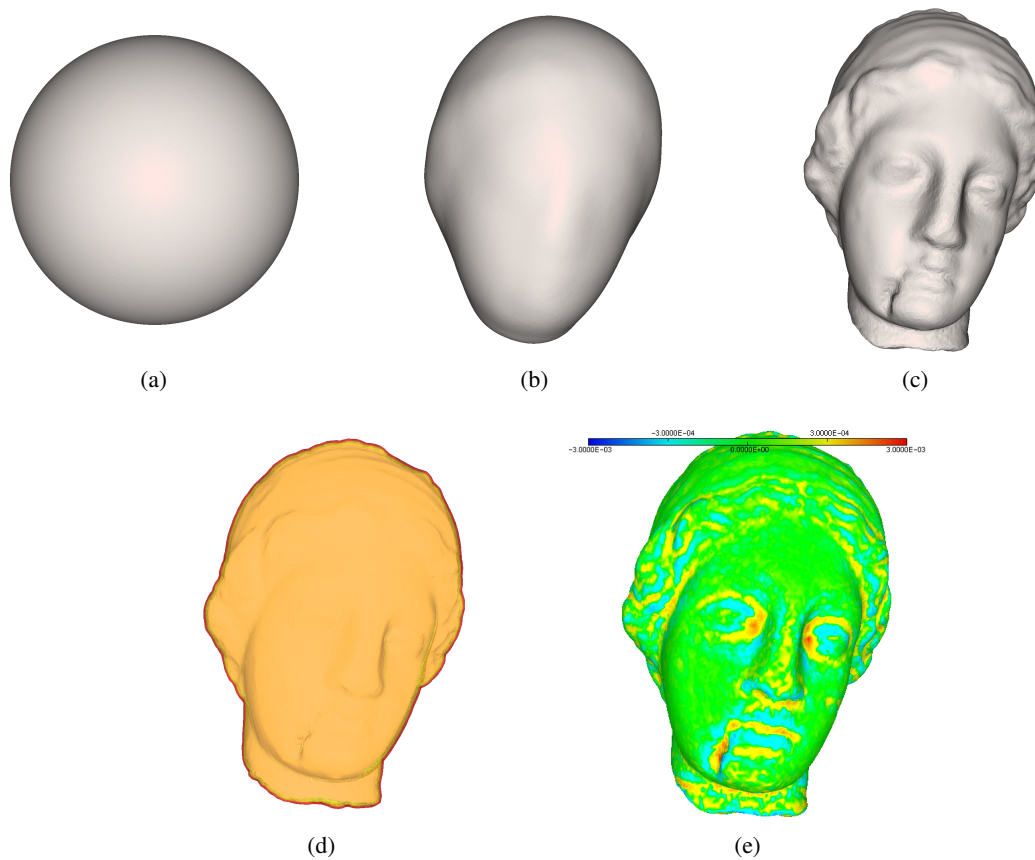


FIGURE 6.9 – An example in 3d with the volume functional : the mapping on the *Igea* model. (a) Template shape Ω_0 . (b) Deformed shape Ω_k for $k = 20$. (c) Deformed shape Ω_k for $k = 1500$. (d) Isovalues of the signed distance function to the target shape Ω_T . (e) Discrepancy between Ω_T and Ω_{1500} .

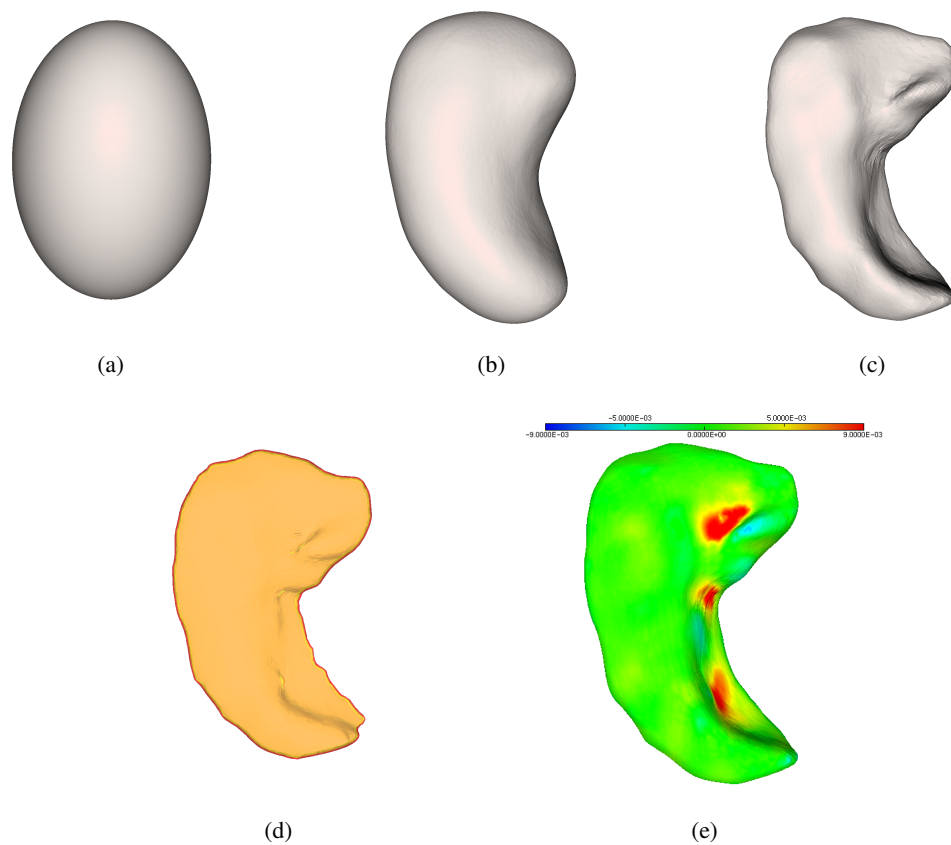
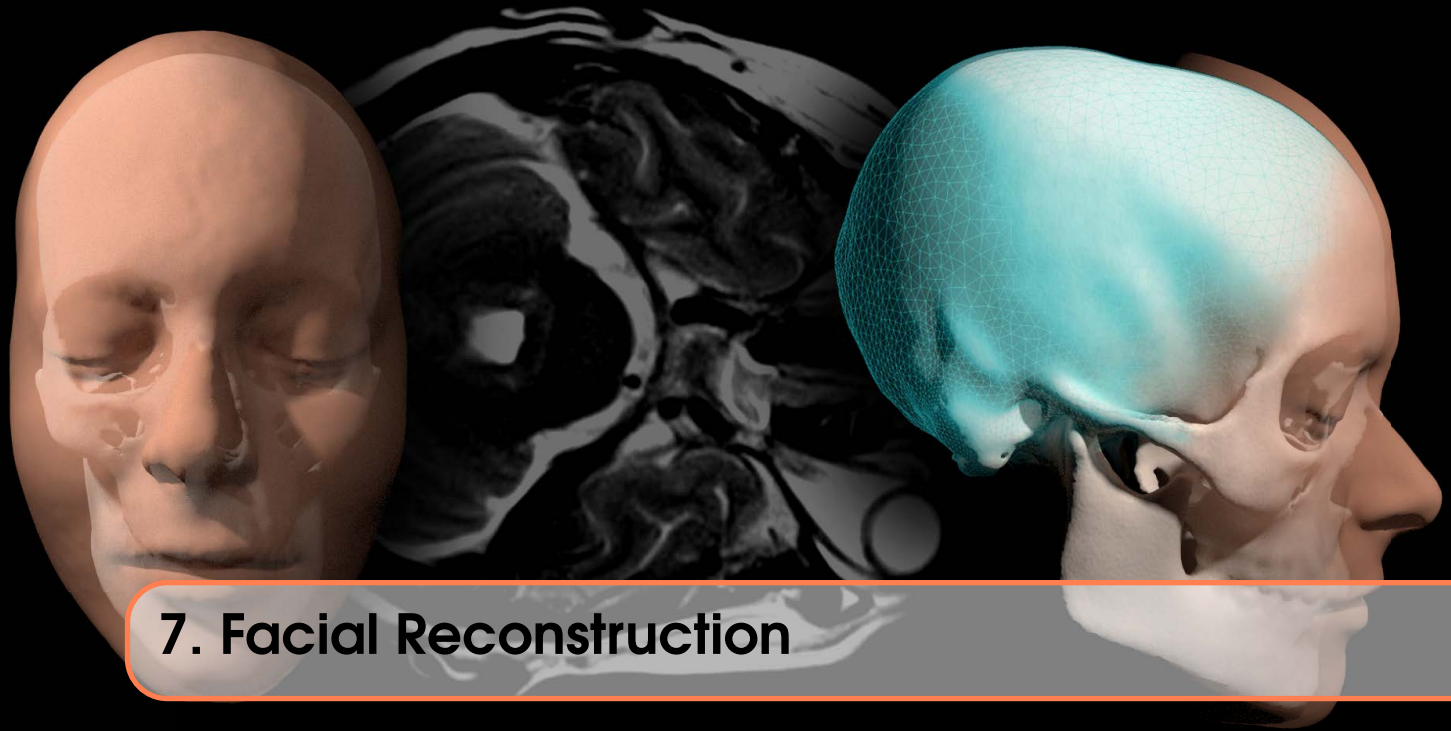


FIGURE 6.10 – An example in 3d with the volume functional : the mapping on a human hippocampus. (a) Template shape Ω_0 . (b) Deformed shape Ω_k for $k = 50$. (c) Deformed shape Ω_k for $k = 1500$. (d) Isovalues of the signed distance function to the target shape Ω_T . (e) Discrepancy between Ω_T and Ω_{1500} .



7. Facial Reconstruction

Sommaire

7.1	Introduction	156
7.2	Anatomy	157
7.2.1	Link between the skull and the face	157
7.2.2	The masseter muscle	158
7.3	Facial reconstruction process	158
7.3.1	The Database : from CT-scan to 3D shape	159
7.3.2	Reconstruction of the masseter muscle	160
7.3.3	Results presentation : combinaison with a general method of facial reconstruction	165
7.4	Validation	168
7.4.1	Protocol description of the survey	169
7.4.2	Results	170
7.5	Discussion and Conclusion	170

A new anatomic facial reconstruction methods and validation

Work in collaboration with Yvon Maday, Patrick Goudot and Thomas Schouman, to be submitted in Forensic Sciences Research.

Key Words

Facial reconstruction, Shape matching, Principal components analysis, Validation

7.1 Introduction

Facial reconstruction (FR) is the process of deducing, from the sole knowledge of a dry skull, the shape of a deceased person's face [111]. It is still a challenge today with many different applications that can be medical, legal, or even historical.

The work on this paper began with a forensic science goal to identify bodies that could not otherwise be recognized. An essential part of this process is therefore the identification of the deceased's face. This provides a means of police investigation in some cases [146, 236] and valuable evidence in otherwise unsolvable cases [108, 109, 221]. Often the good results obtained draw the attention of the media and the public to the reconstructed image of a face [237, 255]. However, the recognition of other elements such as personal clothing or accessories (glasses, hats, necklaces) displayed with facial recognition triggers recognition rather than the estimated facial morphology itself [76, 91, 204]. Subsequently, the usefulness of these methods was verified in practice and often used in high-profile cases [91, 108, 109, 204, 221, 236]. However, it is beneficial to maximize their abilities to generate recognition from facial morphology. It is useful to use science to improve or test methods in the laboratory and in the field [212].

The FR problem is thorny because it is really ill-posed. Indeed, the solution is not unique : a skull does not correspond to a unique face [138]. Some parameters such as ageing or corpulence are respectively difficult or impossible to extrapolate from the knowledge of a dry skull alone [42, 138, 153]. These difficulties make the FR a research subject that is still active today.

However, many methods have already been developed to try to solve the FR problem. The first use of facial approximation in a forensic case was reported in 1916 [8, 9], but the method had been studied in the context of anthropological and anatomical research since 1898 [69, 123]. Traditional methods are most often carried out manually in 2D [71, 208, 219, 222, 232] or 3D [74, 111, 208, 251] (portraits or sculptures). These methods essentially consist of three common steps [252] :

1. equip the raw skull with a series of sparse anatomical landmarks,
2. apply an average thickness of soft tissue to each skull mark to estimate a corresponding mark on the face,
3. draw (2D) or sculpt (3D) a face corresponding to the estimated landmarks.

Most of the time these traditional methods are performed by an artist who is an expert in facial anatomy. Although the results are often very plausible, the subjectivity of practitioners is inevitable [199]. These methods are also time-consuming and can take from a few days to a week to complete a reconstruction. These are two criteria, subjectivity and long implementation time, that we are trying to get rid of.

In addition, the blooming up of numerical methods over the past few decades has greatly affected many disciplines. Numerical simulations for FR have therefore also been developed since early 1990s [71, 232, 242, 243], and through automatisisation processes, have made it possible to overcome subjectivity and really accelerate the whole process.

At this stage, numerical reconstructions are most often carried out with a statistical model and a database. The database can be either a 3D shaped database that associates a face with a skull, or a soft tissue thickness database with a given landmark, or a combination of the two. Here two types of approaches can be described : 1- computerized facial modelling using retroactive devices and 3D scanning of the skull [129, 252, 255, 257], and 2- computerized facial reconstruction using more complex and computerized 3D routines [35, 43, 44, 90, 168, 174, 216, 229, 230, 231, 240, 241]. Several recent examples of these methods, which have been made and tested in the last 20 years, can be given [204].

In all of these approaches, there is near-universal reliance on measurements of the thickness of the soft tissue of the face [43, 111, 129, 202, 204, 233], which renders the Russian–American

classification entirely obsolete [202, 204, 233].

Starting with the simple methodology of placing soft tissue layers on the dry skull before deforming a facial mesh towards these estimated facial landmarks [44]. An other possibility, explored in [78], consists in using, in addition to these measurements, a face statistical shape model, allowing to obtain a global estimation, taking more into account the possible variations. However [211] shows that, whatever the methods used, soft tissue thickness measurements are linked to a significant error (of about 10%).

Using this idea of local approximation initially, via statistical shape models, some studies uses a least square regression to obtain a smooth face [55, 101]. This idea of local approximation also includes an analysis of regional facial features, such as the position of eyeballs in orbits [49, 65, 89, 118, 165, 201, 206, 210, 254], the shape of the nose [4, 74, 144, 179, 182, 209, 213, 233, 234], the width of the mouth [198, 256], the shape and size of the lips [145, 256], the morphology of the ears [1, 88], the morphology and thickness of the mastication muscles [203].

We can also mention the methods used to identify the parameters that characterize the mapping between a skull and its face via a database correlating several pairs of skull and associated face. First [191], which uses a statistical form model applied to a large CT-scan database. Others, such as [66, 169, 190], suggest a last step that take into account corpulence.

Finally, a last type of approach consists in statistically simulating the database [138], also allowing to present not a unique face but a set of possibilities. A large majority of these methods are based on statistical or probabilistic models.

The method presented in this article takes advantage of these recent contributions, as well as the history of the FR, but attempts to distinguish itself by a deterministic approach to the problem. Our method consists of adding the facial muscles one by one, then the fat and skin, as the artists did but using mathematical modelling. This requires building parametric models of facial muscles to be able to adapt them to the underlying facial skeleton. For the moment, we have focused on the masseter muscle, which is the largest muscle of the face and influences its shape in a prominent way [260]. Then we applied the elastic deformation method of [35]. We also propose here, an application to validate the process from the point of view of recognition, which also allows us to compare our methods with others.

7.2 Anatomy

The starting points of our approach are anatomical and medical. The main idea is to integrate this knowledge into the mathematical model. Indeed, the article by Stephan et al. [203] shows us that although the anatomy of the muscle of the face, is well defined in the literature, few recently published FR methods take this information into account.

In this first part we are therefore interested in the anatomy of the masseter muscle, and the possible repercussions of its shape on that of the face.

7.2.1 Link between the skull and the face

The anatomy of the skull largely determines the shape of the face. Different studies show, for example, the link between long face and short face and mandibular angle [163, 184]. Others have a link between the angular measurements of the skull and masticatory muscles such as the masseter [10, 12, 31, 56]. This is also what we contributed to in the first chapter of this thesis, by including new features.

The important link between bone morphology and muscles morphology described in the literature was the first step in the development of this FR method. The originality is to do this anatomical reconstruction numerically and not manually, as [76, 77].

7.2.2 The masseter muscle

The human head has nearly a hundred muscles. A large majority of them are so-called mimic muscles. However, the most voluminous muscles are those of the masticatory system, which is composed of four main muscles : the masseter, the temporal, the internal pterygoid and the lateral pterygoid.

The masseter muscle is one of the most important muscles of the face, as much by its size, its location as its function. Indeed, it has the largest volume of muscle of the face, and therefore it participates to the actual shape of the face [260]. The masseter is an elevator muscle of the mandible, thus its role in mastication is also very important : it is one of the most powerful muscles in the mandible. Another pertinent muscle candidate, superficial and quite large, would have been the temporal muscle, but because of its location, it is often hidden by the hair, and in this area of the face it does not seem to exceed half of the soft tissue thickness [207]. This is why we chose to study first the influence of the masseter muscle on the morphology of the face. Keeping in mind to add other muscles to our facial reconstructions afterwards, such as the temporal muscle.

Many anatomical studies describe masseter muscles such as [29]. Stratified dissections and anatomical sections in different spatial planes showed that the muscle masseter had a typically pennate structure consisting of a succession of alternating musculoaponeurotic layers. The muscle has three clearly differentiated parts : the superficial, intermediate and deep beams. The masseter insertions are on the gonion and zygomatic bone [38].

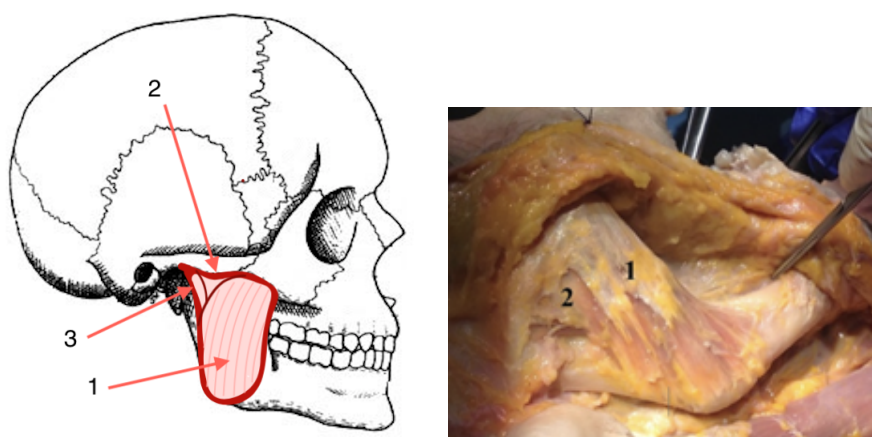


FIGURE 7.1 – Anatomical location of the masseter muscle and its three layers : (a) a schema, (b) a picture of a dissection we performed (1- the superficial layer, 2- the vertical medium layer 3- the deep layer of the masseter)

7.3 Facial reconstruction process

We call here « reconstruction », the process of giving a face to a skull, for forensic investigation [109]. We have to keep in mind that it is an approximation process, which will give us a guess of the face associated to the unknown skull : one will not be able to recover a large amount of face features (eyes, hair, lips and ears). The main parameters of interest for us is therefore the shape of the face.

The first step of our methods is to reconstruct from measurements on the skull the muscles like the masseter. And in a second step we add a mask of the remaining soft tissue with a general reconstruction process, based on elastic deformation process [35].

But even before the reconstruction part, we need to constitute a database of 3D skull, face and masseters muscles, associated for a unique personne.

7.3.1 The Database : from CT-scan to 3D shape

This process is the one described in the second chapter of this thesis.

All the 3D data used in the reconstruction process, are extracted of CT-Scan of patients of the maxilo-facial surgery departement of La Pitié Salpêtrière Hospital, Paris, France, that we acquired during this thesis.

We collected 24 CT-scan of patients with no major dysmophy, with all their teeth and with a complete head scan. All the CT-scan were performed using a Discovery CT750HD system (GE Healthcare, Chicago, Illinois, United-States), the slice thickness for bones acquisition was 0.62 mm and for soft tissus 1.25 mm. We chose to use CT-scans because they are an excellent 3D imaging tool to visualize bones, and they also allow a very accurate visualization of soft tissues [116]. Our goal is to infer soft tissue information from bone information (in order to reconstruct the face), so we need to ensure the best possible information on the skull and correct information for soft tissue.

The first step of acquisition of the database is the segmentation of medical image. The segmentation process is the identification of each anatomic structure and the attribution of a label to each voxel (3D pixel) on the image. For the masseter muscle the segmentation was performed manually, with Amira Software (version 2019.05) [197]. For the skull and the face the CT slices are automatically pre-segmented using a multi-thresholding technique. This step consists in partitioning the original images into subdomains whose boundaries are identified by given intensity values. Nevertheless in most of the subjects, large artefacts due to dental filling are observed on the images. These defects need to be manually removed on each affected slice, even for the bones and the face segmentation.

From the 2D slices segmentation, we generated with the marching cube algorithm of Amira Software [197], a first 3D mesh. These initial meshes contain, in general, a large number of elements that are redundant and oversampled to correctly describe the geometry of the model. These dense meshes are remeshed with mmg [50, 57] to obtain a valid computational mesh (Figure 7.2).

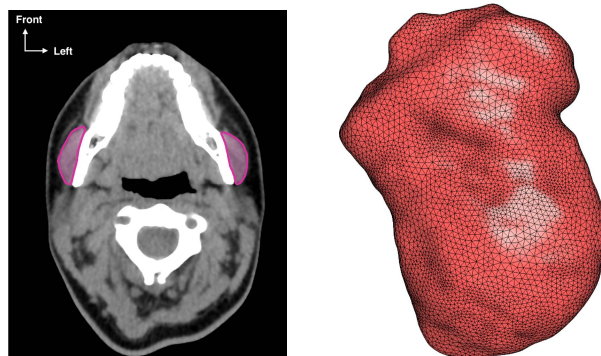


FIGURE 7.2 – CT-Scan segmented and the 3D surfacic mesh of one of the masseter muscles associated

The human skull is characterized by a complex structure, that is difficult to both acquire and handle numerically. Due to these difficulties, several authors opt for describing the skull through underlying anatomical or geometrical substructures. The most popular choice leads to the definition of a sparse set of anatomical landmarks, possibly coupled with a dense representation of the skull [43, 121, 240]. Some authors use automatically detected continuous crest-lines [174].

Here we choose, in order to keep the more possible information of the skull and to keep the whole process fully automatized, to perform the same process for the skull and the face as for the

masseter muscle, explained above (Figure 7.3). And thus to represent the skull by a 3D surface mesh.

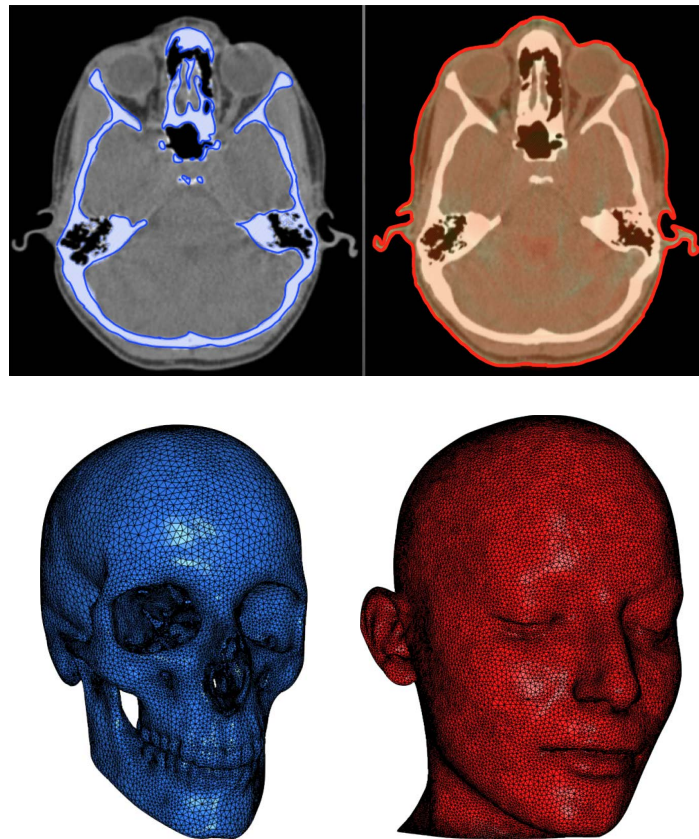


FIGURE 7.3 – CT-Scan segmented and the 3D surfacic mesh of the couple skull/face associated

So we get in our database 24 couples meshes of skull and face associated, and their two masseter muscles so 48 in total. To improved our results for the masseter reconstruction, we decided to add more segmentation of this muscle, using CT-scan from the same surgery departement, to reach the number of 126 masseter muscles segmented in 3D. It is important to keep in mind that increasing the number of skull/face mesh pairs, particularly by paying attention to diversifying as much as possible the morphologies (long face/short face, dental class, etc.) but also the ethnic groups represented, would further improve the results of the overall reconstruction process.

7.3.2 Reconstruction of the masseter muscle

As mentioned above, the shape of the bones and muscles above are highly correlated. In this section we put this principle into practice, by trying to learn from the shape of the bone that of the muscle, through measurements made on the skull or directly with the mesh of its 3D shape. In our case, it is a question of reconstructing the shape of the masseter muscle, according to that of the mandible.

A parametric model of the masseter muscle

To do this, we need a parametric model to represent the masseter muscles and the mandible associated with them. We use here the notion of manifold of shapes and remark it has a small complexity, mathematically stated as having a small Kolmogrov n -width. We thus obtain a model, which allows us to represent a shape no longer as a 3D mesh of 5000 points (Figure 7.2), but as a linear combination of simpler shape defined by some coefficients only.

From the 3D meshes obtained after segmentation we therefore apply the method developed in chapter 2 of this thesis, and the following steps are implemented :

1. elastic deformation of an ellipsoid of reference to each muscle, in order to obtain a mesh having the same characteristics (number of points, triangles, etc.) whatever the masseter muscle considered (this elastic deformation is obtained using the volumis morphing algorithm, described in the Chapter 6),
2. Principal Component Analysis of all the displacements of the reference ellipsoid mesh to all the masseter muscles of our database (in the way described in the Chapter 2) to get the basic shapes,
3. reconstruction of a masseter muscle from only some measurements made on the skull with a linear combinaison fo the basic shapes.

First of all, we can present the case of Figure 7.4, where we use Reduced Basis (RB) to reconstruct a muscle whose true shape is known but which was not used to compute the principal components. The three muscles on the left are represented using respectively 5, 10 and 20 coefficients, while the muscle on the right is our target.

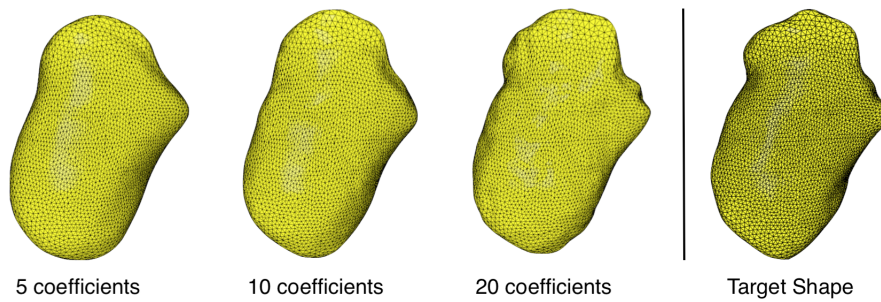


FIGURE 7.4 – RB reconstruction of a masseter muscle : from (a) 5 coefficients, (b) 10 coefficients, (c) 20 coefficients and (d) the real muscle

With 5 coefficients, we can see that the overall shape of the muscle is already captured. However, it takes between 10 and 20 coefficients to obtain a more accurate result. In consideration of our purpose in this chapter (and as opposed to those required in Part II of this thesis), we have subsequently decided to consider a masseter by its approximation to the first 5 coefficients, the main information being contained within.

The next step is to link the first five RB coefficients of the masseters muscles with the shape of their associated skull. Here we propose and compare two approaches to represent the skull :

A - anthropological measurements on the skull, a method that is similar to what can be found in existing methods, or

B - to use a parametric model to describe the mandible (bone underlying the masseter), allowing a global automatization of the process.

A - Measurements on the skull

We first made various measurements on the skull, nine in total, between anatomical landmarks. In Figure 7.5 we can visualize these different landmarks :

1. Glabella : most prominent point in the median sagittal plane between the supraorbital ridges,
2. Orbital : most inferior point on margin of orbit,
3. Gnathion : point located perpendicular on mandibular symphysis midway between pogonion and menton,
4. Point F : intersection between the dental plane and most anterior part of the mandible branch,

5. Point H : intersection between the dental plane and most posterior part of the mandible branch,
6. Gonion : most posterior inferior point on angle of mandible,
7. Coronion : tip of the coronoid process of the mandible,
8. Condylion Superior of the Temporo-mandibular articulation : most superior point on the condyle of mandible,
9. Porion : most superior point of outline of external auditory meatus,
10. Point E : intersection between the dental plane and the middle of most exterior part of the mandible branch,
11. Point G : intersection between the dental plane and the middle of most interior part of the mandible branch.

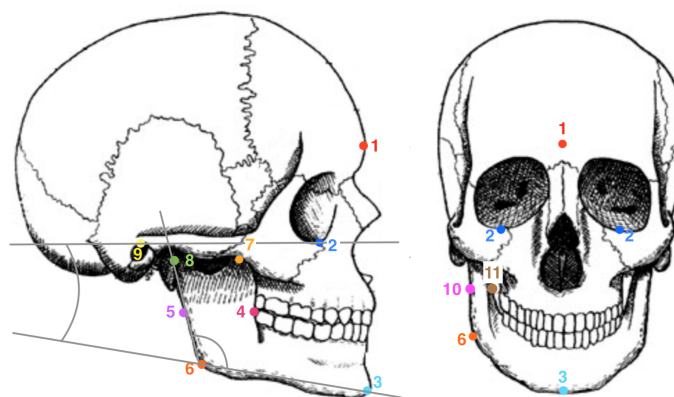


FIGURE 7.5 – Landmarks use for the measurments made on the skull

Between these points we measured seven distances and two angles, used to learn the first five RB coefficients of the masseter muscle. All measurements were made in 3D with Osirix® (Pixmeo, Geneva, Swiss), as shown in the Figure 7.6. They are all described below :

- Gognion to Gnathion distance (Go-Gn),
- Gognion to Condylion Superior distance (Go-Cs),
- Gognion to Coronion distance (Go-Co),
- Right Gognion to Left Gognion distance (GoR-GoL),
- Glabella to Gnathion distance (Gl-Gn),
- Point H to Point F distance = Mandibular branch width (H-F),
- Point E to G Point distance = Mandibular branch thickness (E-G),
- Mandibular plane angle : angle between Frankfort horizontal line and the line intersecting Gonion-Menton (FMA),
- Gonial angle : angle between the mandibular line (Gonion to Gnathion) and le posterior line of the mandibular branch (GoAngle).

The descriptive statistics of these measurements are given in the following Table 7.1 :

	Go-Gn	Go-Cs	Go-Co	H-F	E-G	GoR-GoL	Gl-Gn	FMA	GoAngle
Mean	7.37	5.43	5.86	2.91	0.74	9.04	12.43	118.99	27.09
Sd	0.48	0.53	0.56	0.29	0.15	0.63	0.91	6.30	5.89
Min	6.62	4.40	4.71	2.28	0.44	7.4	10.75	108.55	11.82
Max	8.95	6.72	6.95	3.5	1.17	10.68	15.31	136.7	46.54

TABLE 7.1 – Description of the measurements made on the skull

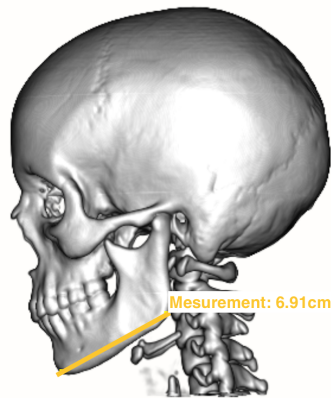


FIGURE 7.6 – Example of measurements made in 3D

B - A parametric model of the mandible

In a second step, in order to avoid having to perform these various tedious measures, we took a direct interest in the shape of the mandible. We used the same process, described in Chapter 2 of this thesis, for mandibles as for masseters, in order to describe them using only a few coefficients, extracted from the RB. To best match the shapes, it was necessary to « cut » the mandibles in half, each half referring to the masseter muscles on the corresponding side. The warping step, described as optional for masseters, proved to be necessary and very practical here. This allowed to consider a mandible as a closed 3D surface, see Figure 7.7.

After the implementation of this whole process, we also obtained a parametric model for the mandibles, each described by the first ten RB coefficients of all the mandibles in the database.

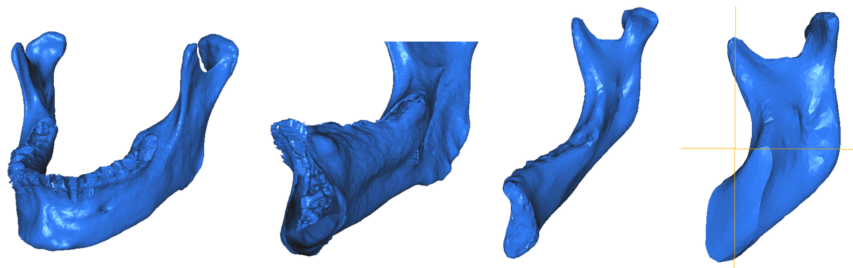


FIGURE 7.7 – (a and b) Mandible mesh model issued from segmentation of medical images, (d and c) Closed surface model of a half mandible generated with our warping algorithm

We now have two ways to describe the shape of the skull, and more specifically that of the mandible : 9 anthropological measurements or the ten first RB coefficients of the mandibles. The first method consisting in linking measurements on the skull and the shape of the masseter muscle has been largely legitimized by the literature but also by the first chapter of this thesis. However which is not the case with the second approach, where we want to link the coefficients of the mandibular RB with those of the masseter. Table 7.2 summarizes the excellent correlations, 0.8986 on average (p -value < 0.05 , with a Pearson correlation test), found between the first five coefficients of the two RBs. This allows us to validate our approach conceptually, before moving on to the next step.

	cMass5	cMass4	cMass3	cMass2	cMass1
cMand5	0.9844	0.9923	0.8725	0.9075	0.9444
cMand4	0.9802	0.9956	0.8855	0.9178	0.9342
cMand3	0.9723	0.9930	0.8791	0.9068	0.9209
cMand2	0.9749	0.9929	0.8763	0.9066	0.9266
cMand1	0.9801	0.9894	0.8613	0.8974	0.9404

TABLE 7.2 – Correlation between the 5 coefficients of the mandible and the masseter RB, with cMass the masseter coefficients and cMand the mandibule coefficients, both in descending order

Machine learning results

With the two sets of information characterizing the shape of the skull and more particularly the mandible, it is then possible, using a machine learning algorithm, such as neural networks, to deduce the first 5 RB coefficients of the masseters. This allows us to find the shape of a muscle on a dry skull to identify.

In Figure 7.8, we present the reconstructions of masseter muscles after learning, on two examples. The two masseters on the left are represented after deduction of the learning algorithm of the first 5 RB coefficients, the first according to the 9 cephalometric measurements described above, the second, on the left, according to the mandibular RB coefficients. The middle masseter, in blue, is our target.

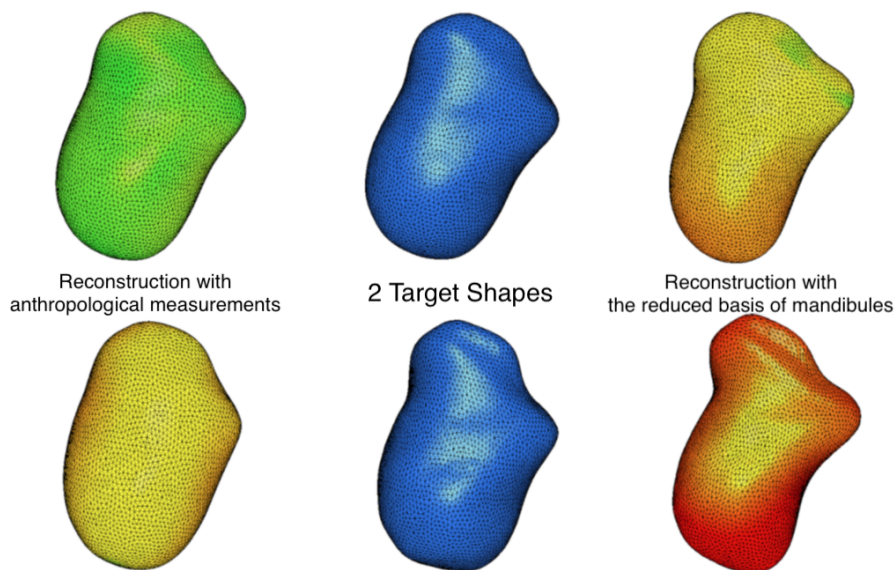


FIGURE 7.8 – Two examples of reconstructed masseter via machine learning, on the left with the measurements, on the right with the RB of the mandibule, and on the middle the target shape.

After examining some examples, it seems quite clear that learning through cephalometric measurements is more effective. Indeed, in Figure X, the color maps show a lower error for reconstruction via measurements (left) compared to that via mandibular RB (middle). However, this remains only a first observation because when we made this first analysis we had only 68 masseter couples and measurements at our disposal, and 30 masseter couples and mandibles segmented

separately (and thus allowing us to make a RB). So very little data for effective learning. It is in response to this problem of lack of data that we have begun work on semi-automatic segmentation presented in Part II.

In the context of facial reconstruction and in view of the correct results found by learning through measurements made on the skull, we first used this reconstruction of the masseters. We keep in mind that the second method (mandibular RB), in the light of the significant correlation found, may be more efficient, or at least as effective, with more data in the long term. This would allow full automation of the process.

7.3.3 Results presentation : combinaison with a general method of facial reconstruction

Our method has mostly two steps. The first one is to add to the dry skull, the muscles we reconstruct from knowledge of the skull, measurements or 3D shape (Figure 7.9). This is what we presented in the section above and in more details described in the second chapter of this thesis. This allows local anatomical knowledge to be integrated into the complete facial reconstruction process, this is what is new in comparison to [158] and which is original because it has not yet been developed, numerically and automatically, to our knowledge.

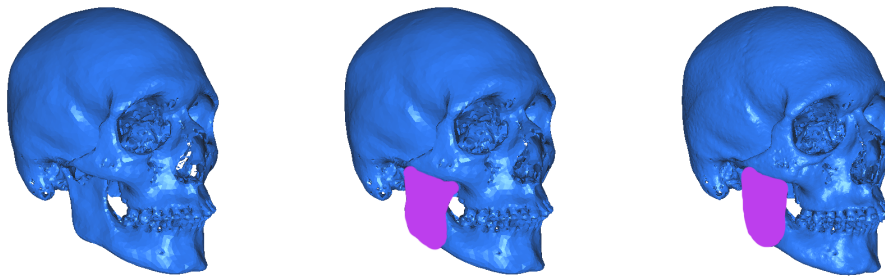


FIGURE 7.9 – Example of a skull of our database with (a) no muscle, (b) the real segmented masseter muscle, and (c) our masseter muscle reconstruction

The second step is to deform a mask of the other soft tissues (Figure 7.10) with the methods of [34, 35], but instead to consider as input the dry skull, we consider the skull augmented with the masseter muscles reconstruction.

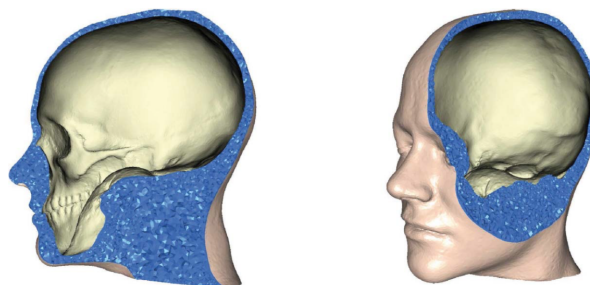


FIGURE 7.10 – An example of a mask which include the knowledge of the masseter muscle

To be able to carry out this second step, it is necessary to go through a « warping » step described in chapter 2, which allows us to describe our skull + masseter group as a 3D surface mesh. We

can visualize on Figure 7.11, the same skull and its masseter as that of Figure 7.9, but after the « warping » process.

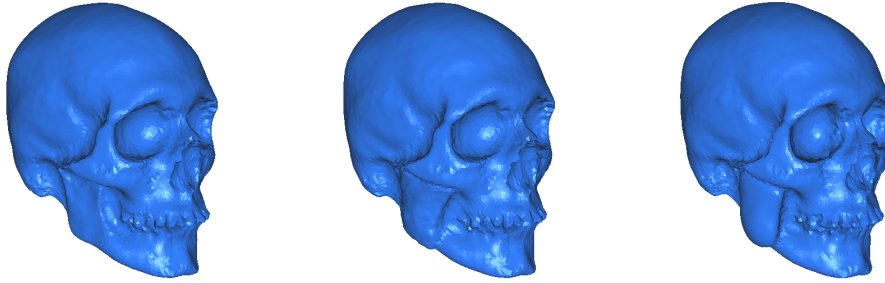


FIGURE 7.11 – The same example skull as in Figure 7.9, but after using the warping algorithm to close it

Once all the skulls in the database have been closed, with the masseter muscle, segmented or reconstructed, it is possible to map each skull/face pair of the database, via a deformed skull/face reference pair, using an elastic morphing described in the previous chapter, to each of these so-called pairs. Thus, when identifying a new skull, it is sufficient to match it with the reference skull/face pair, to be able to deform any face from the database to this new skull.

In view of the limited data, all the reconstructions were carried out via a "Leave-One-Out" process. This allowed us to perform 24 face reconstructions in a simulated « real situation », since during the reconstruction of an individual A, the skull/face pair of this individual was removed from the database, before performing the reconstruction.

However, there is one last point to be clarified : when an unknown skull must be identified, which skull from the database is chosen to reconstruct its face, via elastic deformation of the skull/associated face mask ? In our case we decided to select the 3 skulls from the database, the closest to the unknown skull (according to their L^2 scalar product) , then to average the three faces obtained. On this point, different methods could be proposed and compared in order to obtain better results.

We can present one exemple of facial reconstruction performed by this new method in the Figure 7.12 :

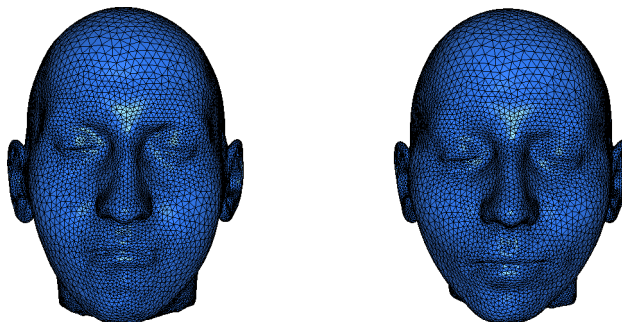


FIGURE 7.12 – One exemple of reconstruction with our method on the left versus the 3D segmented face on the right

With this only Figure 7.12, it is really difficult to appraise the accuracy of the method, with

the naked eye. In Figure 7.13, we can more easily compare the discrepancy of those reconstructions with the real face by adding a color map, which express the error made between the surface reconstruction and the 3D segmented surface of the face. The Figure 7.13 presents, on the left, the reconstruction of an individu of our dataset made with the methode of [35] without the masseter muscle (front and side); on the middle, the reconstruction performed with the segmented masseter muscle; and on the right, the reconstruction performed with the reconstructed masseter muscle (using the Chapter 2 method). After comparison a similar result is obtain, exepcted in the region of the anatomical details ad-up of the masseter, where a better accuracy can be shown for both of the reconstruction including a masseter muscle. Moreover, these two reconstructions performed with the masseter muscle differ little from each other. This leads us to believe that our muscle reconstruction is precise enough for this application.

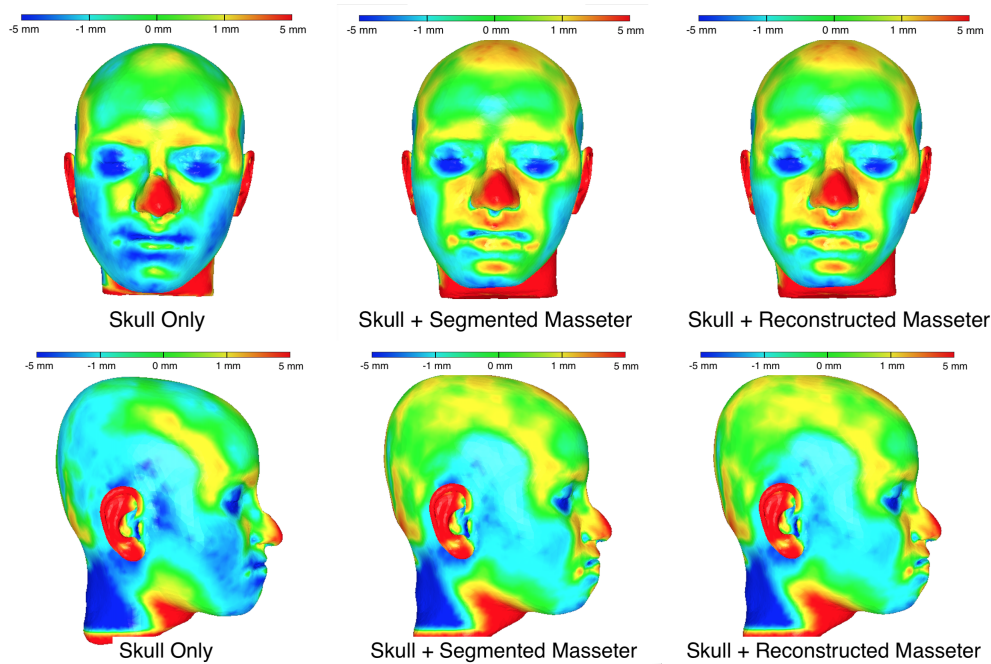


FIGURE 7.13 – Color map of the errors made on an example of reconstruction without (on the left), with the segmented masseter muscle (on the middle), and with the reconstructed masseter muscle (on the right).

The Figure 7.13 is only an example of reconstruction. We used these three methods on a set of 24 skulls, to reconstruct their associated faces, with a leave-one-out method. The descriptive statistics of the errors found for these different applications are expressed in the Table 7.3. The signification of each columns is detailed above :

- SkullOnly = the reconstruction 3D face without the masseter muscle
- RealMass = the reconstruction 3D face with the 3D segmented masseter muscle
- RBMass = the reconstruction 3D face with the masseter muscle reconstructed

	Skull Only	RealMass	RBMass
Mean	11.74 mm	11.85 mm	11.77 mm
Sd	14.09 mm	14.09 mm	13.97 mm
Min	72.66 mm	72.63 mm	72.49 mm
Max	0.086 mm	0.086 mm	3.37 mm

TABLE 7.3 – Description of reconstruction errors

These results seem completely disproportionate compared to the visualization of Figure 7.13, where the error is less than 5mm on the majority of the face. Several remarks expressed below may be the cause of this.



- The ears are not included in the face-matching process, since these structures are not linked with the underlying skull morphology. So the errors made on them has to not be take into account.
- The neck is taken into account in the shape-matching process but it is not a good indicator of the mistake made. Indeed, depending on the acquisition modalities of each scanner, the images do not all stop at the same level, leading to a large variability that is not representative of the face.

To illustrate this, we present below, in Figure 7.14, a second visualization with a wider color scale between 0, 2 and 10mm against 0, 1 and 5mm. This allows us to confirm that the majority of the error on the face is between 0 and 2mm.

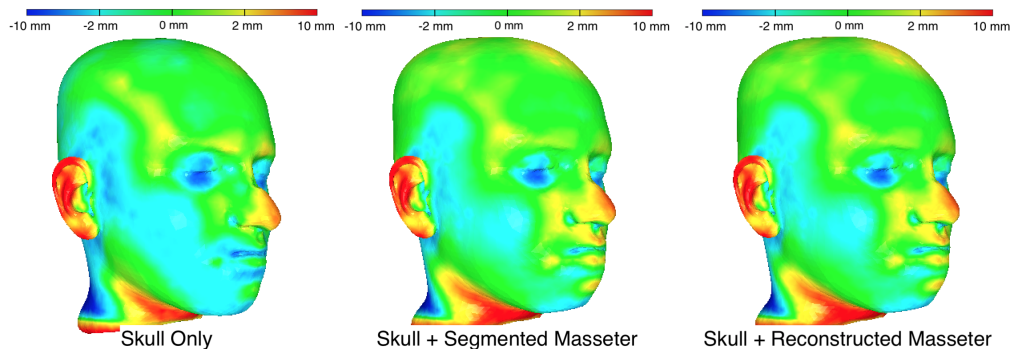


FIGURE 7.14 – Color map of the errors made on an example of reconstruction, different color scale, without (on the left), with the segmented masseter muscle (on the middle), and with the reconstructed masseter muscle (on the right).

To test these hypotheses in more detail, and to be able to make a more interesting and accurate comparison between the three methods, one idea would be to select an area of interest and calculate the associated errors.

This procedure is often used in facial reconstruction and would allow us to set aside areas we know we are not able to reconstruct with the methods used (ears and neck), and compare these results with the existing published literature. It could also allow us to study in detail a particular anatomical area such as the area where the masseter is located.

These first results, which are still encouraging, show the interest of using anatomical knowledge for the facial reconstruction process, even with numerical tools. But this kind of validation, often carried out in the field of facial reconstruction, is purely theoretical. Thus, we also develop in the following section a more realistic method of facial reconstruction recognition.

7.4 Validation

In order to show that those methods of reconstruction can be useful in forensic science, we have built a validation test, which compares the ability of a large population to identify, from a picture, a 3D volume of the face of the same individual and their reconstructions with and without the muscles. On the Figure 7.15, we show an example of reconstruction, from our database, performed in three different ways : without any muscles, with the real 3D segmented masseter and with the

reconstructed masseter. This is the recognition of those four different faces, from a picture of the same individual, that we want to evaluate.

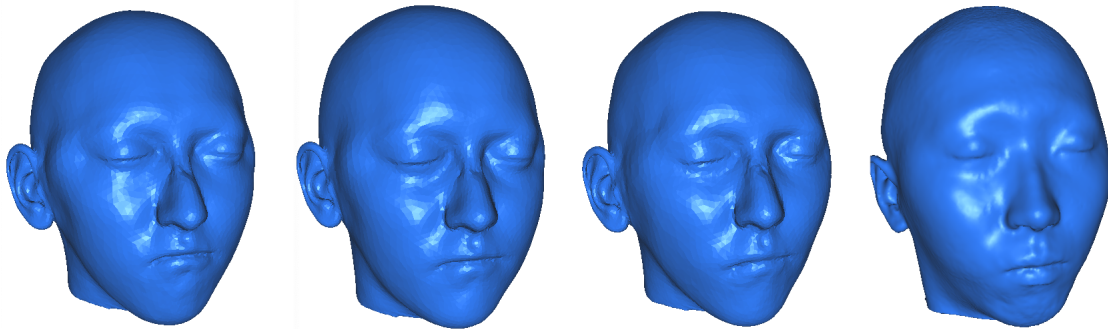


FIGURE 7.15 – One example reconstruction with the three tested cases with (a) only the skull, (b) the real segmented masseter, (c) the reconstructed masseter, and (d) the 3D segmented face

7.4.1 Protocol description of the survey

To be able to determine if our methods can improve the recognition of someone's face in comparison of other methods, we also need to show that people are able to identify a reconstruction face as well as with the segmented 3D representation, and later on better with the masseter muscle than without. After research in the literature, there is to our knowledge only few practical validation method tested for the recognition of facial reconstructions in forensic sciences. Most of the time on a small reconstruction sample (about ten), with few test participants (less than 100) and in 2D. The results are mixed and tend to show little interest in facial reconstruction for forensic identification [200, 208].

We have thus conceived and realized a survey. The survey is constructed as follow : a front and side view of an individual is presented to the user, who must choose one among five 3D face representations, one of which is the one he recognizes as the individual of the pictures. Every participants who answers to the survey have 10 questions to validate.

For each of these 10 questions, the five 3D faces are selected from one of these four categories (hidden from the participant) :

- the real 3D segmented face
- the reconstruction 3D face without the masseter muscle
- the reconstruction 3D face with the 3D segmented masseter muscle
- the reconstruction 3D face with the masseter muscle reconstructed

The selection of the categories, chosen for a question, is made randomly.

For now, 122 persons use this test application, and they all performed the test on 10 cases, randomly chosen from the 24 individuals of our database. We are aware of the too few participants who answered the survey for now, but those results are a really interesting first attempt to perform a validation of the recognition process and a good way to compare different methods[205].

On the Figure 7.16 and 7.17, the application and how to use it on a example case are shown (at the end of the chapter).

7.4.2 Results

In this section we first present the Table 7.4 of the normalized descriptive statistics of our survey. The signification of each columns is detailed above :

- RealSkin = the real 3D segmented face
- SkullOnly = the reconstruction 3D face without the masseter muscle
- RealMass = the reconstruction 3D face with the 3D segmented masseter muscle
- RBMass = the reconstruction 3D face with the masseter muscle reconstructed

	RealSkin	SkullOnly	RealMass	RBMass
Mean	0.796	0.439	0.448	0.454
Sd	0.192	0.171	0.193	0.215
Min	0.273	0.063	0.167	0
Max	1	0.760	0.833	0.867

TABLE 7.4 – Description of survey results

In average a 3D real face is recognized in 79.6% of cases, a 3D reconstruction 45.4% of cases, while chance would be one among five (20%).

With a basic t-test we can show that the real face is with any doubt best regonized with respect to the reconstruction from pictures, but not perfectly either. And we found no significantly differences between the three reconstructions preposed, even if the RBMass is slightly larger. This can be attributed to different interpretations :

1. the accuracy of the method and the recognition process are two differents things, and people do not seem to look at the masseter region to recognize someone,
2. the only few people we tested is not enough to demonstrat a real difference.

7.5 Discussion and Conclusion

This article show a complementary method to [35], with more accuracy in terms of distance to the real face, with slight improvement in terms of recognition. A way to even improve our results would be to

- add the reconstruction of other muscles than the only masseter,
- add a parametric way to control the fat tissue, in order to better represent the corpulence,
- increase the number of individuals in the database, particularly to diversify morphologies as much as possible,
- look for a more subtle way to define the skulls closest to the unknown skulls, or to combine the faces obtained.

It also propose a way to compare the results of differents facial reconstruction studies, with a protocol validation easy to implement. This has not been done extensively in the field of facial reconstruction before. To complete this first approach, we could consider completing this test with two other tests :

- submit 5 pictures of individuals in order to identify a face reconstructed in 3D, this would allow a more realistic situation to be simulated,
- compare for a selected picture, which of the two reconstructions, with or without muscle masseter, is identified as the best.

In addition to that an interesting study would also be to compare our validation method with the result obtained by automatic face recognition by computer, a currently prolific field of research, and also with the more classical statistic facial reconstruction [166, 167].

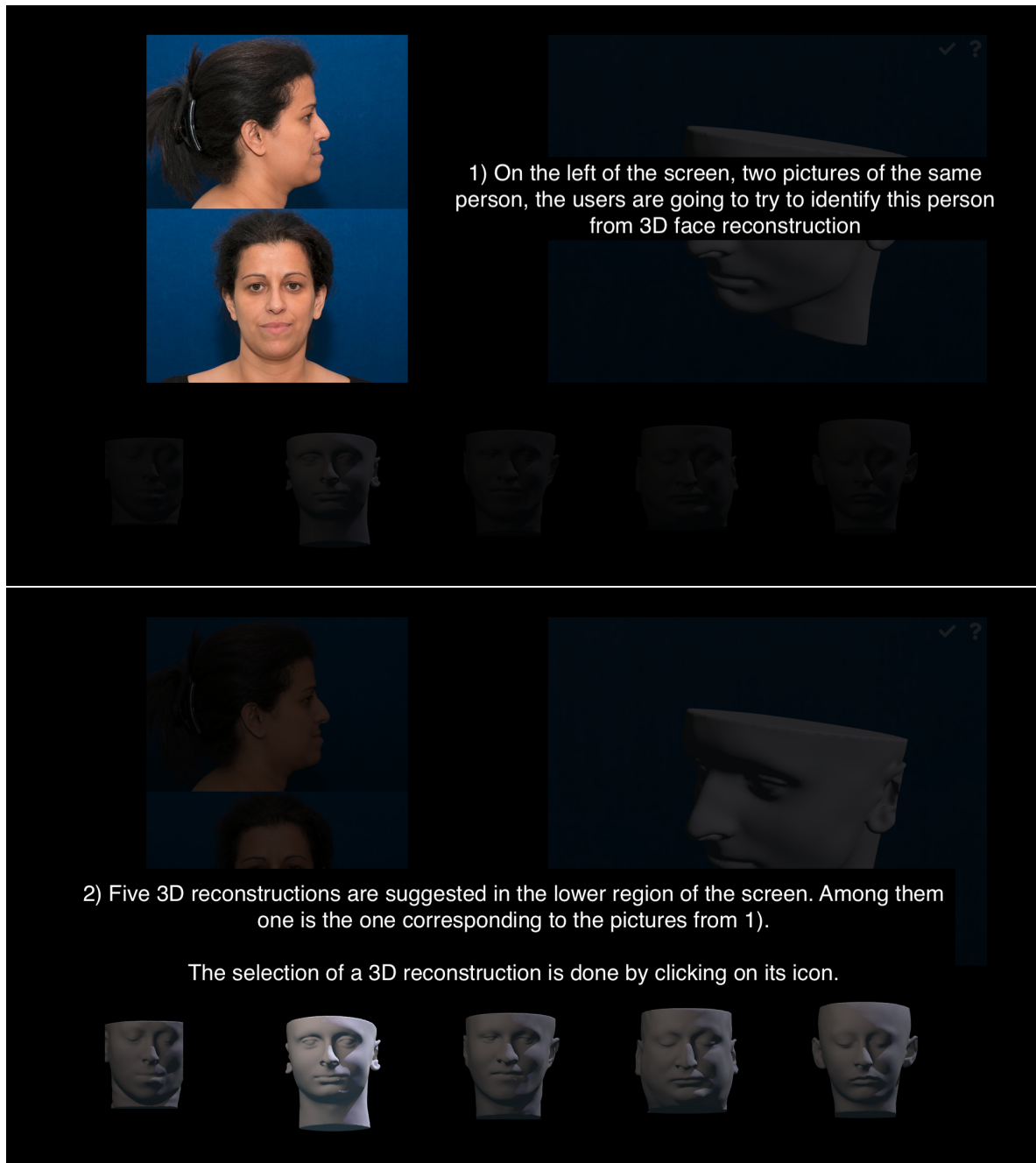


FIGURE 7.16 – Application of validation - 1

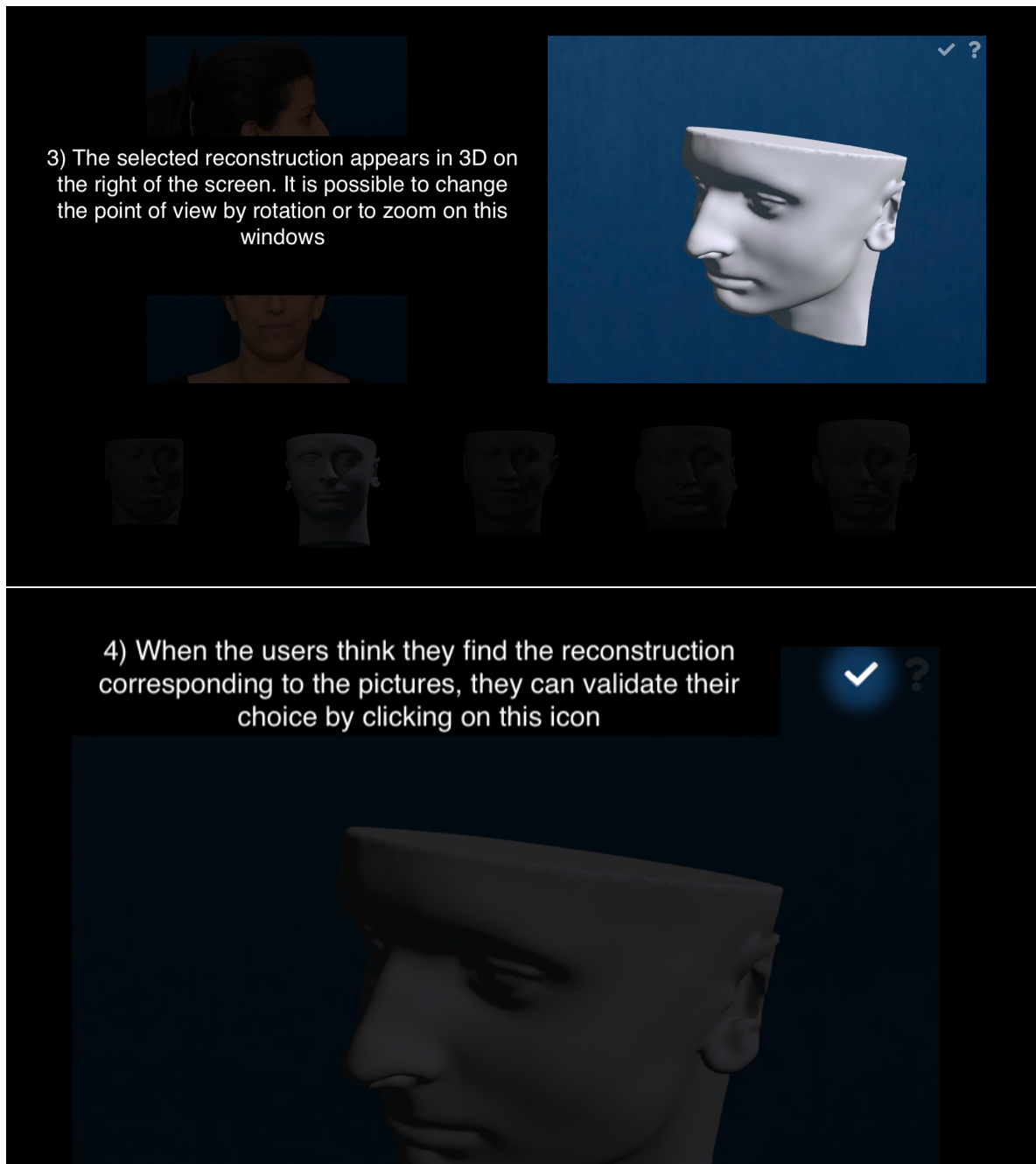


FIGURE 7.17 – Application of validation - 2



Conclusion and perspectives

This multidisciplinary thesis presents a compilation of mathematical tools, sometimes previously described in the literature, develops and combines them in an original way, to propose new methods, with a precise application objective. It is indeed a global view of the aspects and fields covered by a carried out multidisciplinary project : from abstract reasoning to practical application.

The main objective of this thesis was, in connection with the FaciLe project, facial reconstruction for forensic medicine. In addition, another secondary application, which emerged in the context of the work on reconstruction, was developed in this thesis, namely the semi-automatic segmentation of soft tissues on CT-Scan.

The main developed tools and their applications presented in the different chapters of this manuscript are listed below :

1. the creation of a reduced basis of 3D shapes, and its use for reconstruction in forensic or imagery ;
2. the design of a semi-automatic segmentation method, and its application in 3D imaging ;
3. the comparison of two elastic morphing methods, in order to find the most suitable one, to be used for different applications during this thesis work.

Below iare presented limits and possible improvements of these three methods.

First there are several possible perspectives on the creation of the database :

- a more detailed analysis of the eigenvalues decrease according to the type of scalar product used, in the Chapter 2 we present the work for the L2 scalar product only, it would be interesting to compare to the H1 scalar product ;
- although this step is not always necessary, a more stable and faster warping algorithm, exploring for example another type of distance computation, could improve the support of some complex objects as skull in the database ;
- better define templates with finer meshes, which can be use for any kind of 3D objects.

Secondly for semi-automatic segmentation, there are still many ways to explore :

- enlarging the database is the first thing we need to do to improve our results, which are produced on a small database. Two possibilities are then possible : to acquire new "real" data manually segmented (at least partially), which would allow a better consideration of the different existing morphologies ; but also a diversification of the shapes already present in the database, generated with the help of perturbation of these shapes by spherical harmonics ;
- the whole part dedicated to the data alignment between them is central in the 3D objects management procedures, as discussed in this thesis. It is therefore quite possible to imagine different methods improving this aspect in the work presented in chapters 3 and 4, as the impact on the results could be significant. One proposal would be to integrate rigid movements to the variations added by the spherical harmonics used to enlarge the database, as suggested above ;
- in order to be as systematic as possible a more detailed comparison of the 3D results presented in Chapter 4 with the pre-existing literature results, either from a numerical error point of view or from a 3D visualization point of view.

Finally as far as morphing is concerned, as presented in the Chapter 6, other aspects can still be explored :

- the use of a faster method than the gradient descent used, in order to accelerate the process ;
- the combination of the two functionalities presented : the volume one, fast and efficient in many situations, and the surface one, less robust but more accurate when the target shape has singularities. This would allow to better take advantage of the advantages of each of the two methods ;
- improve the so-called surface method, which does not succeed systematically, by including a remeshing step in some iterations, thus avoiding the algorithm to get stuck due to a lack of points.

Although there are still several possible improvements for each of these methods, as detailed above for example, they have all already been implemented on different applications and real cases, detailed below. This allows feedback on the potential and effectiveness of each, as well as the possibility of critical thinking to further improve them.

1. the semi-automatic segmentation, which uses the 3D shape database of the masseter muscle to model the object to be segmented. This method under development can still be improved, but it already speeds up the first part of the process.
2. facial reconstruction with anatomical precision on the masseter muscle, a tool we used to reconstruct the face of the New Caledonian warlord Atai, presented in the introduction (Figure 7.18). In this method it would be possible to add other muscles, to integrate a nose reconstruction method to obtain more details, or to allow reconstruction on altered skulls (without teeth or with a damaged mandible, cf. Appendice B).

As regards to facial reconstruction, one aspect that was left out during this thesis is the reconstruction of secondary characters. In the Figure 7.18, a possible interpretation, designed by Sebastien Le Gall (ISCD, Sorbonne Université, Paris), of Atai's face is presented, based on known historical information about him. However, it would be interesting to try to systematize this approach using work on the genetic determination of secondary traits (skin, eyes and hair colours, hair type, etc.) for example.

The clinical context has also not been put aside, since on the one hand, thanks to an analysis between cephalometry and the masseter muscle size, we were able to establish and confirm the anatomical hypotheses on which all the tools and applications developed are based (Chapter 1). On

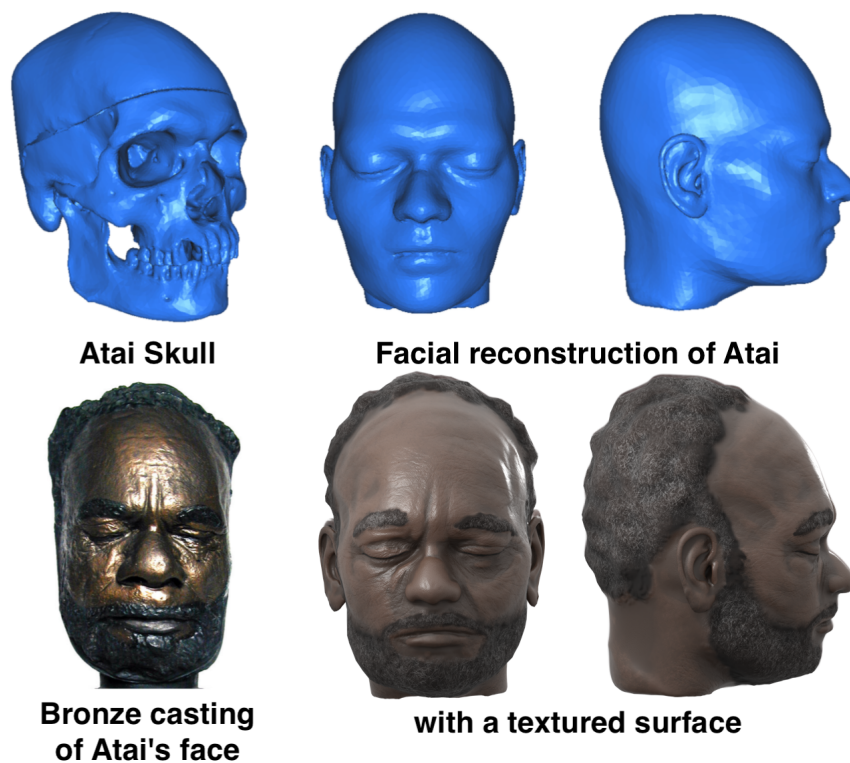


FIGURE 7.18 – (Top) 3D Skull then facial reconstruction of Atai from the front and profile, (Bottom) on the left a bronze mortuary casting of the face of Atai, and on the middle and the right a suggested face with secondary features, for the reconstruction of Atai, by Sebastien Le Gall

the other hand, a validation carried out by clinicians for segmentation, or more varied users for facial reconstruction, allowed hands-on analyses of these tools.

These validation methods are still under development and can be further improved, especially with regard to face recognition (Chapter 7). Indeed, they are for the moment dependent only on visual recognition by subjects participating in the study, whereas many facial recognition software already exist. It would therefore be interesting to validate these recognition applications and compare the results.

IV

Appendices

A	Annexe Proof-of-Concept in 2D	179
A.1	Introduction	
A.2	Notation and problem setting.	
A.3	Numerical Experiments	
A.4	Conclusions and Perspectives.	

B	Annexe Facial Reconstruction Software	185
B.1	Installation	
B.2	Creation of the database	
B.3	Facial reconstruction from a new skull	
B.4	How to add step?	
B.5	Independent use of the scripts	

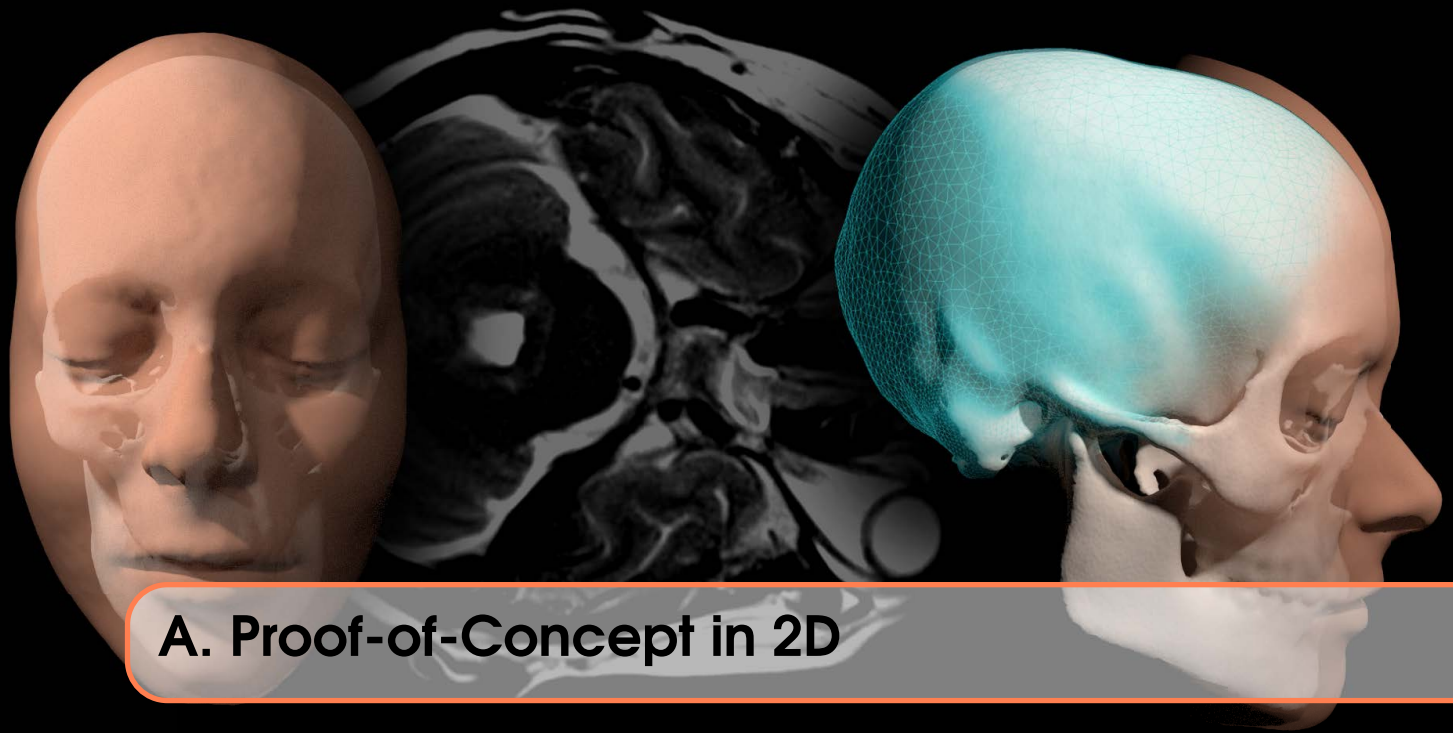
C	Annexe Anthropological Application	193
C.1	Context	
C.2	The test case	
C.3	Numerical results	
C.4	Conclusion	

List of Tables	199
-----------------------	------------

List of Figures	205
------------------------	------------

Bibliography	207
---------------------	------------

Books
Articles
Phd Thesis
Misc



A. Proof-of-Concept in 2D

Sommaire

A.1	Introduction	180
A.2	Notation and problem setting.	180
A.3	Numerical Experiments	182
A.4	Conclusions and Perspectives.	183

Fast semi-automatic segmentation based on reduced basis

In this appendix, I present the submitted version of the work presented in Chapter 3. The main constraint, to present the work in 6 pages, did not allow to give as many details as it is the case in this thesis.

Work in collaboration with Damiano Lombardi and Yvon Maday, submitted in *Compte Rendu Mathematique de l'Academie des Sciences*.

Abstract

This note addresses the following segmentation problem in medical imaging : minimize expert intervention for semi-automatic segmentation process. Using a reduced basis, we have an a priori knowledge of the objet we want to identify on the images, like a muscle on a CT-Scan. We just have to identify the coefficients associate to the object of interest, by solving a linear system taking as input the coordinates of some selected points on the image. An example implemented in 2D is shown. This method is independent of the grayscale of the image, and can therefore be applied to all objects and images.

Key Words

Segmentation, Medical Imaging, POD

A.1 Introduction

One of the recurring and time consuming challenges in medical imaging is the segmentation of parts of interest. Segmentation is the process of dividing a medical image into distinct anatomical regions [68]. This has been for years the effort of specialists and it is quite time consuming. Beyond the specifics takes to each particular application, the general issue is to find a way to identify automatically an anatomical region of interest in order to speed up the process. When the contrast is high enough (e.g. for bones, or between bones and tissues) automatic segmentation is quite efficient now and various methods are proposed and implemented [115, 175, 262]. Likewise for anatomical major organs like the brain or the heart [16, 33, 196]. On the contrary, when the contrast is not high enough (e.g. segmentation between different soft tissues on CT scans) the most common imaging modalities fail and there are very few approaches available.

Understandably enough, most of the current segmentation methods are based on the gray scale which can let experts easily differentiate 2 objects [170]. Several classifications of those methods exists, we can cite [258] for an overview. We limit ourselves to mentioning here a few approaches, for some more detail surveys we can look at [94, 131], for example.

Thresholding and edge detection are two very common approach used for image segmentation [133, 176]. They are simple and effective approaches to segment anatomical details featured by high contrast, as, for instance, the bones (that appear as light objects on dark background). However it is more challenging for the detection of objects that do not have a marked gray scale signature, as the muscles. We can also cite the region based method. Three other types of process can be exposed here : the deformable models [94], the atlas guided [105] and all the approaches dealing with artificial intelligence, which has recently blooming up in the field of medical image segmentation [189, 258].

We propose here to develop a model based semi-automated method to help segmentation, which have most in common with the three last types of methods cited above. In particular, the shape of the object of interest is represented by an elastic deformation field of a reference configuration. A reduced basis representation of the object of interest is introduced, that exploits an *a posteriori* knowledge of a database of available segmentations. Given an image to be segmented, the elastic deformation field can be approximated as a linear combination of a small number of modes. This provides, in turn, a powerful regularisation and a significant speed-up of the procedure needs since few appropriate points need to be selected by the user in order to define the field. We can find a similar idea in [25], but with a probabilistic point of view, and where all the modes of the PCA are used as a regularisation and not as a dimensional reduction.

The proposed method is complementary of the ones exposed before, first because it requires some preliminary segmentations to "build" the reduced basis, and second because it can be used on indifferently on CT and MR image for any type of object, even the difficult one to identify like soft tissues on a CT.

The paper is structured as follows : in Section A.2 the problem and the notation are presented. Then, in Section A.3 some numerical experiments are detailed.

A.2 Notation and problem setting.

Most medical imaging produces a gray-scale image, i.e. a function defined over a subset of \mathbb{R}^2 (or \mathbb{R}^3 for 3D imaging), $f : \mathbb{R}^2 \rightarrow [0, 1]$ associating a scalar value to each point of the space (denoted later on by $x = (x_1, x_2)$ (or by $x = (x_1, x_2, x_3)$ in 3D)). After a manual segmentation of a region of interest is performed, it is possible to model this region by using an elastic morphing that maps a reference object : e.g. an ellipse in \mathbb{R}^2 (or an ellipsoid in \mathbb{R}^3) onto the boundary of the two-dimensional (or three-dimensional) segmented region. In the present work, for the sake of simplicity, we will restrict to two-dimensional configurations. Having a collection of segmented

objects (belonging to a coherent family) is equivalent to having a set of 2D elastic displacement fields mapping a same (reference) ellipse into the different segmented objects.

Let us assume that the reference configuration is an ellipse $E \subset \mathbb{R}^2$; a point $\xi \in \partial E$ is mapped through a displacement field into a point $\mathbf{x} \in \partial F \subset \mathbb{R}^2$, where F is the boundary of the segmented object. It holds :

$$\begin{cases} Id + u : E \rightarrow F \\ \xi \mapsto \mathbf{x} = \xi + u(\xi), \end{cases} \quad (\text{A.1})$$

and $u \in H^1(E)$.

From an acquired database consisting of $N \in \mathbb{N}^*$ such elastic displacements : $\mathcal{D} = \{u^{(1)}, \dots, u^{(N)}\}$ ¹ let us assume that a set of $n \in \mathbb{N}^*$ Proper Orthogonal Decomposition (POD) modes is extracted :

$$\varphi_i : E \rightarrow F, \quad i = 1, \dots, n. \quad (\text{A.2})$$

When a new image to be segmented is available, the unknown elastic displacement mapping the reference configuration onto the image can be approximated by using the POD basis as follows :

$$u \approx u_n = \sum_{i=1}^n \alpha_i \varphi_i. \quad (\text{A.3})$$

The goal is to find the coefficients α_i in such a way that the reference ellipse, mapped by the displacement field $Id + u_n$ is as close as possible to the actual image, hence providing an already good guess for the segmentation. In order to identify the coefficients α_i a semi-automated procedure is devised. The image does not correspond, in general, to the reference configuration (this would be the case in which $\alpha_i = 0, \forall i$). A number of $m \in \mathbb{N}^*$ points $\mathbf{x}^{(j)} \in \partial F$ is selected in which there is a discrepancy between the actual image and the reference configuration. Each of these points correspond to an equation for the displacement field : there exists a $\xi_*^{(j)} \in \partial E$ such that :

$$\mathbf{x}^{(j)} = \xi_*^{(j)} + \sum_{i=1}^n \alpha_i \varphi_i(\xi_*^{(j)}), \quad j = 1, \dots, m. \quad (\text{A.4})$$

This is a non-linear system of equations in the variables $\alpha_i, \xi_*^{(j)}$; however, if the points $\xi_*^{(j)}$ are known, this system is a linear system of equations for the coefficients α_i . In the present work, the points $\xi_*^{(j)}$ are chosen as the ones minimising the distance to the point $x^{(j)}$ ² :

$$\xi_*^{(j)} = \arg \min_{\xi \in E} \|\mathbf{x}^{(j)} - \xi\|_{\ell^2}^2, \quad j = 1, \dots, m. \quad (\text{A.5})$$

This corresponds to a regularisation for the solution of the non-linear system Eq.(A.4). The linear system to be solved reads :

$$\Phi \alpha = d, \quad (\text{A.6})$$

$$\Phi_{jik} = \varphi_{i,k}(\xi_*^{(j)}), \quad (\text{A.7})$$

$$d_{j,k} = \mathbf{x}_k^{(j)} - \xi_{*k}^{(j)}, \quad (\text{A.8})$$

where Φ is a tensor, assumed to be of maximal rank (remember that it is constructed from POD vectorial modes). Of course, as soon as $m \geq n$, the system is solved in a least-square sense, and admits a unique solution. When discretising and solving this system, the following choices are made. The minimisation step described by Eq.(A.5) is solved by using a nearest neighbor algorithm that, among the points of the discretised ∂E selects the one which is closest to a given $\mathbf{x}^{(j)}$. Then, the vector system in Eq.(A.6) is unfolded and then solved by using a rank revealing QR decomposition.

1. This database is assumed to be large enough to represent well the full coherent family we are interested in
2. Remark that this point might not be unique.

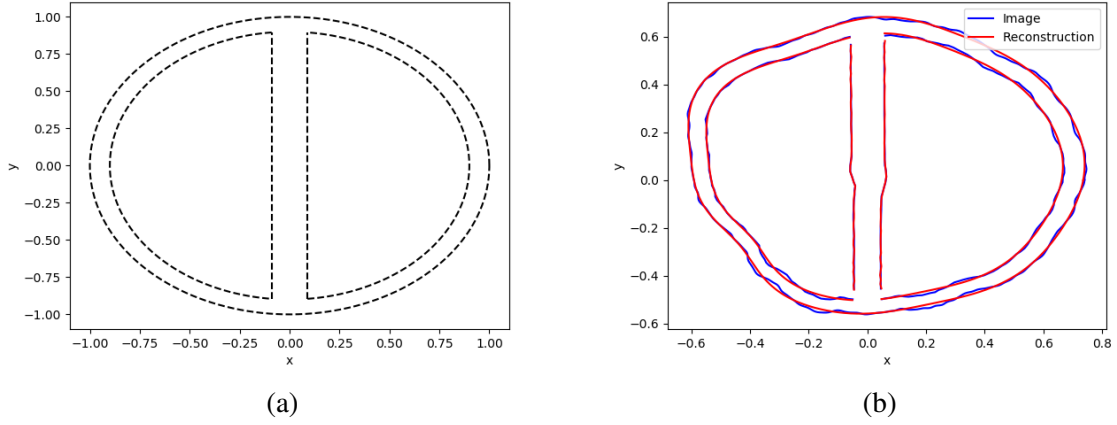


FIGURE A.1 – Test case presented in Section A.3 : (a) Reference configuration (b) an image and its reconstruction.

A.3 Numerical Experiments

In this section, some numerical experiments are shown on a simple 2D test case to assess the performances of the proposed semi-automated segmentation approach. The reference configuration, depicted in Figure 1.a), is a unit circle, divided into two semicircles. The images are defined by deforming this configuration by a parameter dependant field, generated as follows :

the displacement of each point on the reference circle is normal to the circle and constructed by summing the set of $N_h \in \mathbb{N}^*$ harmonics (eigenfunctions of the Laplace-Beltrami operator), scaled with a parameter dependant coefficient : let the undeformed configuration points be denoted by $\xi \in \mathbb{R}^2$, $r = \|\xi\|_2 \leq 1$, $\vartheta \in [0, 2\pi]$ (i.e. $\xi_1 = r \cos(\vartheta)$, $\xi_2 = r \sin(\vartheta)$), the unit vector in the radial direction be denoted by \hat{e}_r and the displacement providing the deformed image configuration be $x \in \mathbb{R}^2$:

$$x = X(\xi) = \xi + r \left(\sum_{j=1}^{N_h} \alpha_j (j+1)^{-\beta} \right) \hat{e}_r, \quad (\text{A.9})$$

where $\alpha_j = \alpha_j(\mu)$, have an amplitude which decreases as a power law of the harmonics numbers : $(j+1)^{-\beta}$ with $\beta = 1.5$, and μ is a parameter that identifies each image.

Consider the following radial displacement, depending upon the parameter $\mu \in [0, 1]^2$. The harmonics coefficients are chosen according to the following expression :

$$\alpha_j = \frac{A}{j^2} [\sin(2\pi j \sqrt{\mu_1}) + \cos(2\pi j \sqrt{\mu_2})],$$

In the present work $K = 100$ harmonics was used to generate the displacement fields. A set of $N = 100$ uniformly distributed in $[0, 1]^2$ samples of the parameter μ are taken, and, for each, the radial displacement is constructed. The POD basis was computed. The singular value decay is shown in Figure A.2.a, exhibiting a faster decay if compared to the one typical of the spherical harmonics for a given regularity.

Remark that the displacement is purely radial and that the center of the reference circle $r = 0$ does not move. This corresponds to the case where the various anatomic regions that have been segmented are “aligned” and properly scaled. Furthermore, given this way of building a database of elastic displacements, the POD modes reduce to a set of vector displacements in radial direction whose intensity is given by the value of the harmonics. The discretised shape is built by discretising uniformly the interval ϑ using $N_\vartheta = 512$ points.

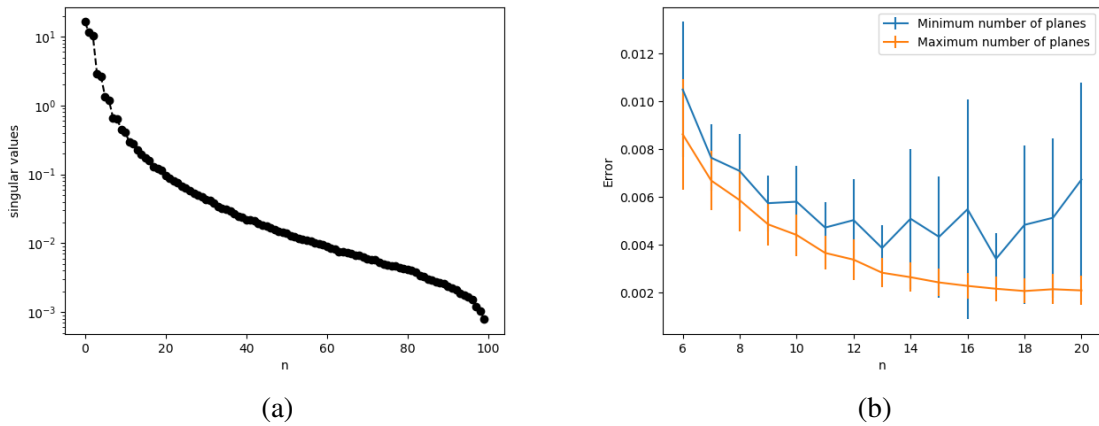


FIGURE A.2 – Test case presented in Section A.3 : (a) Decreasing of singular values with parametrisation (b) Error mean and standard deviation.

The image (the deformation of the reference shape) is cut by $N_p \in \mathbb{N}^*$ horizontal planes, uniformly distributed on the image, to mimic a medical exam like CT or RMI which are sliced. Each plane intersects the outer boundary of the object in two points ($m = 2N_p$), each of which corresponding to one of the halves of the deformed circle. These points provide an equation for the displacement field to be approximated by using the POD modes.

Several numerical experiments are made to assess the performances of the proposed reconstruction method, by varying the number of modes and the number of cutting planes used. In particular, the number of modes used varied from $n = 6$ to $n = 20$ and, for each choice the number of planes was varied from the minimal number of planes needed to have a square system $n \leq m$ to $m = 2n$. In Figure A.1.b) an example of reconstruction is proposed, when the image was produced by using $N_h = 100$ harmonics, $n = 20$, $m = 80$. The result is quite precise, all the details of the image are well represented, whether it is the outer edge where points are selected or the edge of the inner hemicycles where no points are selected.

The reconstruction error are shown in Figure A.2.b for a population of 100 target displacements (that do not belong to the database used to construct the POD modes). The errors are measured in ℓ^2 norm with respect to the discretised images. The average error and the standard deviation are shown when the minimal number of planes and the maximum number of planes are used. In general, the errors are compatible with the ones considered as compatible with realistic applications. When the minimum number of planes is used a stability issue can be seen when a large number of modes is used and the standard deviation is quite large. On the contrary, when $N_p = 2n$ (orange), the lack of stability is delayed, the errors decrease and the standard deviation is much smaller, reaching a minimum for $n = 17$.

A.4 Conclusions and Perspectives.

In the present work a semi-automated reconstruction method is proposed to help the segmentation of anatomical details in the cases in which the contrast is not enough to use fully automated techniques. The method is based on the use of a reduced basis to approximate an elastic displacement mapping a reference configuration into the actual shapes of the anatomical details of interest. The method uses a nearest neighbors optimisation procedure coupled to a least square approach to solve the problem. A 2D test case is proposed to mimic realistic applications and assess

the performances of the method. A set of synthetic generated images was used and the error of the numerical experiments showed that the proposed approach can lead to a viable tool. In this respect, further investigations are mandatory both from the theoretical and applied point of view. In particular a systematic error analysis will be carried out and more realistic tests will be performed, in 3D configuration and by taking the noise and the other experimental error sources into account.

Especially in 3D, several challenges are added to those previously described, especially in the case of a real application. The first one is the constitution of the manual segmentation database : time-consuming and requiring the involvement of an anatomist expert at first. However, the idea is that we will soon be able to propose a first phantom, which will require only a few corrections and will save a lot of time while continuing to feed the database. Moreover, the mapping of the points would remain assured by the same idea as in 2D from a deformed reference configuration. However, instead of using a nearest neighbor algorithm, we would opt to define a probability density of each point in the point cloud of the corresponding dataset. In a second step, it is envisaged to replace the POD by a glutton algorithm, to increase robustness.



B. Facial Reconstruction Software

Sommaire

B.1	Installation	185
B.1.1	Github	186
B.1.2	Python Librairies	186
B.1.3	Executables	186
B.1.4	Installation testing	186
B.2	Creation of the database	187
B.3	Facial reconstruction from a new skull	187
B.4	How to add step ?	187
B.4.1	Script python stand-alone	187
B.4.2	Incorporate an external program	187
B.4.3	Run several functions or scripts in parallel	188
B.4.4	Handle and edit a step	188
B.5	Independent use of the scripts	188

How to construct the database for facial reconstruction and performe a new one ?

Work in collaboration with Sarah Julisson and Loic Norgeot.

B.1 Installation

To be able to use the facial reconstruction software we developed, it is necessary to install a number of tools.

B.1.1 Github

All the code developed during my PhD and needed for the process are available on the github of the ISCD Tools Box. It is necessary to install the whole « Commons » library and « facile-python ». To understand in detail the installation of these libraries, it is possible to refer to the « Read Me » that corresponds to them on github. The one concerning « facile-python » is also detailed below.

B.1.2 Python Librairies

The scripts are written in python 3, of which you must have an installed version. Anaconda is the most convenient to install and avoids having to re-download libraries, but classic python 3 can be perfectly sufficient and takes up less disk space.

The additional python libraries to install are :

- scipy
- numpy
- scikit-image

They can be installed with :

```
pip3 install scikit-image numpy scipy
ou
conda3 install scikit-image numpy scipy
```

B.1.3 Executables

You must also have access to the following executables (their path must be specified correctly in the lib-exe.py file, so that they can be invoked as they are on the command line) :

- tetgen
- mmg3D
- mmgs
- blender
- warping
- morphing
- medit

All of those are in open access on the web, either on the ISCD GitHub or on the website of the official developer.

B.1.4 Installation testing

In the scripts folder, from « facile-python », are present all the necessary python files, which can be used as independent executables (see the Section A.5).

« tests.py » is the file that allows you to run the code on test data. This allows you to test that everything is installed and that the different sripts used during the reconstruction are working.

Il se lance ainsi :

```
python3 scripts/tests.py -d tests/ [-m]
```

Note that the -m option will open each result with medit, useful to check that the signed distances are correctly calculated, that the references for the masks are the right ones, or that the meshes are not degenerated.

B.2 Creation of the database

All the tested scripts, mentioned above, are in fact called in a « global » file allowing to create a reduced 3D database, named « database.py », which manages the different steps described in chapter 2 (data download, scaling, alignment, warping, morphing, etc).

This script recovers the initial files present in the « mesh » folder, then performs the required transformations one after the other, writing each result in a folder corresponding to the step performed.

The script is executed as follows :

```
python3 scripts/database.py -d DATA-DIRECTORY -t TEMPLATES-DIRECTORY
```

with :

- DATA-DIRECTORY : folder in which all the files will be processed, and where the different step results will be stored in separate folders created by this script. Note that the root folder « DATA-DIRECTORY » must be created beforehand.
- TEMPLATES-DIRECTORY : folder containing the .mesh files used as templates for the different steps of the algorithm (sphere used for skull warping, reference ellipsoid for masseter alignment and morphing, etc.).

B.3 Facial reconstruction from a new skull

Once the reduced database of 3D shapes generated by the script presented above, there is only one quick step left to rebuild a new face.

You have to run the script « reconstruct.py », this way :

```
python3 scripts/reconstruct.py -i UNKNOWN-SKULL -d DATA-DIRECTORY
-t TEMPLATES-DIRECTORY
```

with : UNKNOWN-SKULL the mesh of the skull whose face we want to reconstruct.

B.4 How to add step ?

B.4.1 Script python stand-alone

To create a new step, the idea is to create, as much as possible, a new python script that can be executed in "stand-alone" mode with a few arguments on the command line.

Some guidelines for a new script :

- manage arguments on the command line with « argparse »,
- check that the arguments are correct (that the files exist for example),
- use `mesh = lib-msh.Mesh("fichier.mesh")` to open a new file .mesh
- edit « mesh.verts », « mesh.tris », « mesh.scalars », « mesh.tets » which correspond to the mesh elements,
- use `mesh.write("sortie.mesh")` to write a file .mesh
- incorporate an external program (such as warping or morphing, code in C and previously compile).

B.4.2 Incorporate an external program

To incorporate an external program into a python script, the most convenient way is to use the « lib-exe.execute() » function of the « lib-exe.py » file. For example :

```
lib-exe.execute("mmgs-03 maillage.mesh -o output.mesh -hausd 0.01 -hgrad 1.23")
```

or, in a more practical form to use variables as program arguments :

```
lib-exe.execute("mmsg-03 %s -o %s -hausd %f -hgrad %d" %
(maillage.mesh, sortie.mesh, 0.01, 1.23))
```

B.4.3 Run several functions or scripts in parallel

When it is necessary to handle many cases, and therefore try to benefit from parallelization, it is best to encapsulate the actions to be performed in parallel in a function taking a single argument (this is what is done in the « database.py » file), and to use the « parallel » function of the lib-exe file: `lib-exe.parallel(myFunction, myArguments)`

This function will loop through "myArguments" (which must therefore be a list), and will launch the "myFunction" function on each of the elements of "myArguments", in parallel.

Note that the function used may contain calls to programs executed on command lines.

B.4.4 Handle and edit a step

The « database.py » script performs a set of function calls on files contained in folders.

To add a new step (or modify an existing one) :

- we create a function that takes as argument the name of the file to convert,
- in this function, we run the corresponding script with the arguments created from the file name, to which we have added the path of the relevant folders,
- we create a list of all the files that we want to process in the corresponding folder,
- only files whose names are not already in the file output folder after processing are kept in this list,
- to test or perform only a few steps, it is best, for example, to use the `test()` function of the database.py file by following the example presented.

B.5 Independent use of the scripts

Below is a list of the different individual python scripts needed to run global scripts, then a detailed description of how to use them.

1. `carve.py` : rebuilds a rough voxelized shell from a .mesh file,
2. `convert.py` : transforms a.stl or.obj file into .mesh,
3. `distance.py` : creates a .sol containing the Euclidean distance between two .mesh files,
4. `download.py` : downloads files from an FTP server,
5. `fill.py` : fills a surface mesh with a volumetric mesh and an optional icosphere in the center (for morphing algorithm),
6. `icp.py` : calculates the transformation matrix of an ICP between two meshes,
7. `levelset.py` : extracts the surface levelset from a result of `mshdist`,
8. `mask.py` : generates a volume mask between two surfaces,
9. `merge.py` : merges several meshes into one,
10. `morph.py` : morphs between a template and a signed distance,
11. `pca.py` : calculates the coefficients of a PCA and reconstructs an object with a PCA on a set of .mesh,
12. `shell.py` : creates a volumic envelope around a surface mesh, useful for warping,
13. `signed.py` : calculates a signed distance, possibly by adapting a 3D mesh beforehand,
14. `split.py` : cleanly cuts a .mesh file in half on the X axis,
15. `transform.py` : scales, moves, and applies a transformation matrix to an.mesh file,
16. `warp.py` : warping from a 3D reference mesh to a surface mesh.

In all the commands below, the arguments in square brackets are optional.

carve.py

Creates a rough shell of a .mesh file with a « Space Carving » technique, which has the effect of voxelizing the object. May be more appropriate than a convex envelope to prepare the warping and obtain a manifold surface after remeshing for example.

```
python3 carve.py -i INPUT -o OUTPUT [-r RESOLUTION]
```

INPUT : .mesh file to carve

OUTPUT : output .mesh file

RESOLUTION : resolution of the voxel lattice to consider, default at 51. Set a smaller value if the points are scattered, you can set a larger value for a very dense mesh size.

convert.py

Converts a .obj or .stl file to .mesh using meshlabserver to avoid binary file problems.

```
python3 convert.py -i INPUT -o OUTPUT
```

INPUT : .obj or .stl file

OUTPUT : output .mesh file

distance.py

Computes the Euclidean distance between two .mesh files as a .sol. Note that both meshes must have the same number of points.

```
python3 distance.py -i1 INPUT1 -i2 INPUT2 -o OUTPUT
```

INPUT1 : first .mesh file

INPUT2 : second .mesh file

OUTPUT : .mesh or .sol file to write, If the format is .mesh, the file and its associated .sol will be created, if .sol, only the solution.

download.py

Downloads all .stl and .mesh files from a folder on an FTP server, and renames them according to their original name ("003-OsB.obj" will be downloaded as "003-bone.obj").

```
python3 download.py -a IP -u USER -p PWD -i FTPFOLDER -o LOCALFOLDER
```

IP : IP address of the FTP server

USER : username on the server

PWD : associated password

FTPFOLDER : path of the folder on the FTP server from which to download the files

LOCALFOLDER : local folder where to download the files

fill.py

Fills a surface with a volumetric mesh and an icosphere in the center. This step is necessary to be able to perform the morphing.

```
python3 fill.py -i INPUT -o OUTPUT [-c cx cy cz] [-r RADIUS]
```

INPUT : .mesh file for the surface to be filled

OUTPUT : .mesh output file

cx, cy, cz : coordinates of the center of the icosphere to be included in the surface (default 0,0,0)

RADIUS : radius of the icosphere (default 0.1)

icp.py

Computes the result of the transformation by ICP of a source mesh to a target mesh. The two meshes must already be « relatively » close to each other to obtain good results.

```
python3 icp.py -s SOURCE -t TARGET -m MATRIX[-mIts ITERATIONS] [-mPts MAXPTS] [-tol TOLERANCE]
```

SOURCE : .mesh file of the source (object to be transformed)

TARGET : target .mesh file (file to transform to)

MATRIX : .txt file in which to write the obtained transformation matrix

ITERATIONS : maximum number of iterations, default 200

MAXPTS : maximum number of points on which to calculate the PCI (practice for large mesh sizes), default 5000

TOLERANCE : Convergence tolerance, default 1e-4

levelset.py

Extract the surface corresponding to a specified value from levelset (i.e. the reference surface 10 following extraction with mmg3d) for a tetrahedral .mesh file containing signed distance information.

```
python3 levelset.py -i INPUT -o OUTPUT[-d HAUSDORFF] [-l LEVELSET]
```

INPUT : input .mesh file, must match with a mshdist output

OUTPUT : .output mesh, will only contain the surface

HAUSDORFF : Hausdorff distance, default at 0.01

LEVELSET : value for the levelset, default at 0

mask.py

Generates a volumetric mask from an inner and outer surface.

```
python3 mask.py -i INTERIOR -e EXTERIOR -o OUTPUT [-t TEMPLATE]
```

INTERIOR : inner surface

EXTERIOR : outer surface

OUTPUT : output file

TEMPLATE : .mesh file which will allow to write an assigned .sol inside the mask (Dirichlet) corresponding to the displacement field between the inner surface and this file. Note that the interior and exterior surfaces must be manifold, and therefore have no intersections. For the writing of Dirichlet's conditions, the .sol to be written should actually contain the morphing results.

merge.py

Merges several .meshe files into one.

```
python3 merge.py -i FILES -o OUTPUT
```

FILES : list of .mesh files to merge, supports wildcards

OUTPUT : .mesh merged file

morph.py

Initiates the morphing of a template mesh to a signed distance.

```
python3 morph.py -s SOL-FILE -t TEMPLATE -o OUTPUT
```

SOL-FILE : .sol file target (signed distance) for the morphing

TEMPLATE : .mesh template file to deform towards the signed distance

OUTPUT : .mesh morphed file

pca.py

Initiates a PCA to reconstruct an « unknown » mesh based on a set of meshes. Several actions can be performed with this script : compute the coefficients only, or rebuild a mesh in an existing database using n components. By default, the script computes the PCA on the input meshes, reconstructs the unknown mesh using the first 15 components.

```
python3 pca.py -t TRAINING -u UNKNOWN -o OUTPUT
```

TRAINING : list of .mesh files in order to compute their main components (PCA)

UNKNOWN : unknown mesh to be reconstructed in the created space

OUTPUT : output .mesh file

shell.py

Creates a shell.

```
python3 shell.py -i INPUT -o OUTPUT
```

INPUT : list of .mesh files to enclosed with a shell

OUTPUT : output .mesh file

signed.py

Computes the signed distance from a .mesh file, by creating or adapting a computation domain in advance.

```
python3 signed.py -i INPUT -o OUTPUT [-v VOLUME]
```

INPUT : .mesh file representing the surface to which we want to compute the distance.

OUTPUT : .mesh file that will contain the result

VOLUME : .mesh file containing tetrahedra and on which the signed distance will be calculated.

Note that by default, a volumetric mesh enclosing the object is created and adapted to the target object. This then allows `mshdist` to compute a signed distance on a mesh whose elements are smaller around the surface. If a volume is provided, it is used as a reference mesh, but is still remeshed to fit the surface. It would therefore be necessary to modify the script to directly calculate the signed distance on the volume provided, which would actually be equivalent to simply running `mshdist`.

split.py

Cuts a `.mesh` file in its middle on the X axis, keeping the part of the positive or negative x's. Based on blender to make a "clean" cut, this script is different from the others in that it must be executed via blender from the command line.

```
blender -background -python split.py - -i INPUT -o OUTPUT -x X
```

INPUT : .input mesh to be cut in its center (must therefore be centered in X)

OUTPUT : output file to write

X : +1 (to keep the x-positive part and make a symmetry) or -1 (left part, no other transformations)

Be careful, the files thus created are not centered in 0,0,0!

transform.py

Can be used to : scale to 1 (the maximum size of the object will be 1) and center an `.mesh` to 0.5,0.5,0.5 , simply scale and/or move a `.mesh` file, apply a transformation matrix to a mesh (e. g. from the ICP calculation).

```
python transform.py -i INPUT -o OUTPUT [-s sx sy sz] [-t tx ty tz] [-c] [-m MATRIX]
```

INPUT : Input `.mesh` file

OUTPUT : transformed `.mesh` file

sx, sy, sz : scale factor according to x, y and z

tx, ty, tz : translation according to x, y and z

c : Boolean flag to be used alone to scale 1 and translate an `.mesh` into 0.5,0.5,0.5

MATRIX : `.txt` file containing a transformation matrix to be applied to the object

warp.py

Performs the warping of a template sphere on another object, with the objective of closing this object.

```
python3 morph.py -i FILE -t TEMPLATE -o OUTPUT
```

FILE : `.mesh` file corresponding to the object to warp

TEMPLATE : `.mesh` template file to be deformed (a sphere)

OUTPUT : `.mesh` warped file



C. Anthropological Application

Sommaire

C.1	Context	193
C.2	The test case	194
C.3	Numerical results	195
C.3.1	Toothless skull with no nasal bone	195
C.3.2	Skull with the teeth and without the nasal bone	195
C.3.3	Skull with the teeth and the nasal bone	195
C.4	Conclusion	197

Application of our facial reconstruction to a real anthropological case

Work in collaboration with Martin Friess.

C.1 Context

As part of the FaciLe project, we have been brought to work with anthropologists specialized in skull studies and 3D cephalometry. They took part in the different aspects of the project : participation in scientific reflections and decisions, software expertise, presentations during the working group, contextualization, and numerical simulations. It is the latter that we highlight in this section.

The MNHN's collection of skulls, to which anthropologists have access, is huge. Unfortunately these skulls are not all in excellent condition, indeed, depending on their level of preservation, some bones may be missing, such as teeth or even the mandible. It is in this context that we became

interested in reconstructing the face, using the methods described in Chapter 7, of a skull whose we only had the cranial cavity left.

Once our reconstruction method had been developed, it was an opportunity to test it in a different context than for forensic medicine. This allowed us to check the effectiveness of our software.

C.2 The test case

In this context and in order to use our methods, anthropologists had to set up a simulation of the missing bones. A first step was to estimating the mandible from cranial landmarks. The missing mandible of the test skull was estimated following two major steps :

1. 39 calvarial and 33 mandibular landmarks were recorded on a reference sample of 72 complete modern human skulls, with the mandible in occlusion. The cranial landmarks were also recorded on the incomplete skull (test skull). After partial Procrustes superimposition (translation and rotation, but not scale), the missing mandibular landmarks were estimated using the Thin-plate spline function [87], implemented in the Morpho library [185].
2. The closest specimen (based on Procrustes distance from step 1) was chosen as visual template. A total of 512 calvarial landmarks and semilandmarks were recorded on both the template and the test skull, in order to capture finer anatomical details. After a partial Procrustes superimposition, this template was warped (using TPS) to the test skull. (This step also allowed to repair the broken nasal bones of the test skull)
3. Because the closest specimen did not feature a full dentition, and in order to avoid artefacts in the subsequent facial reconstruction process, a second template (calvarium+mandible) with full dentition was then warped to the completed test calvarium (step 2) + warped mandibular landmarks (step 1).

In all these tests we decided not to reconstruct the masseter muscle, because its reconstruction is based on the knowledge of the mandible shape, which is itself simulated and therefore less reliable for performing measurements.

In Figure C.1, we can visualize the skull in 3D before and after the missing bones have been placed. Surrounded by a pink ellipse the non-obvious reconstruction of the nasal bone.

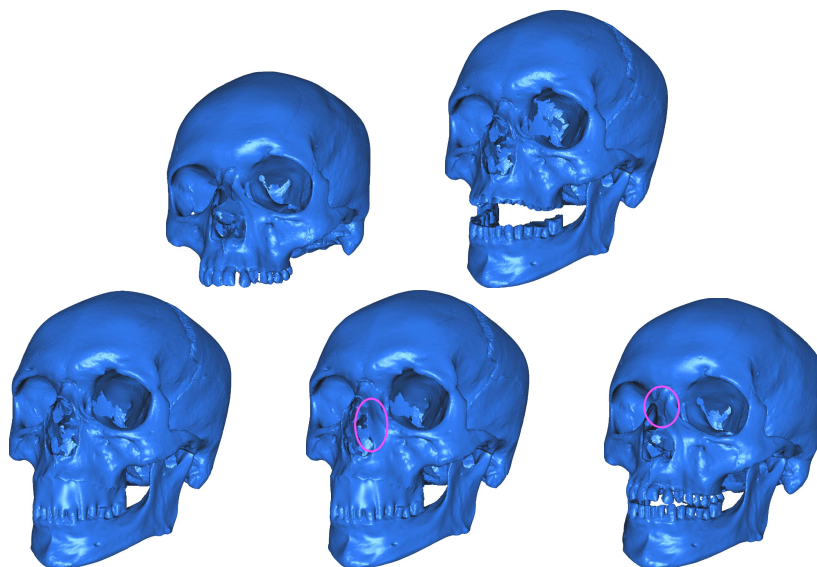


FIGURE C.1 – Comparison between the simple cranium and the whole skull with numerically simulated bones

We were able to carry out several tests in a very short restitution time thanks to the fully automated software presented in Appendix A. In fact the code can run several cases in parallel and a case is solved in less than 12 hours. This example therefore also illustrates the effectiveness of the software in a real case.

C.3 Numerical results

C.3.1 Toothless skull with no nasal bone

In this very first test, we consider as the starting skull for facial reconstruction : the original cranium to which only the mandible was added, as explain above. The results of this first simulation can be seen in Figure C.2 below :

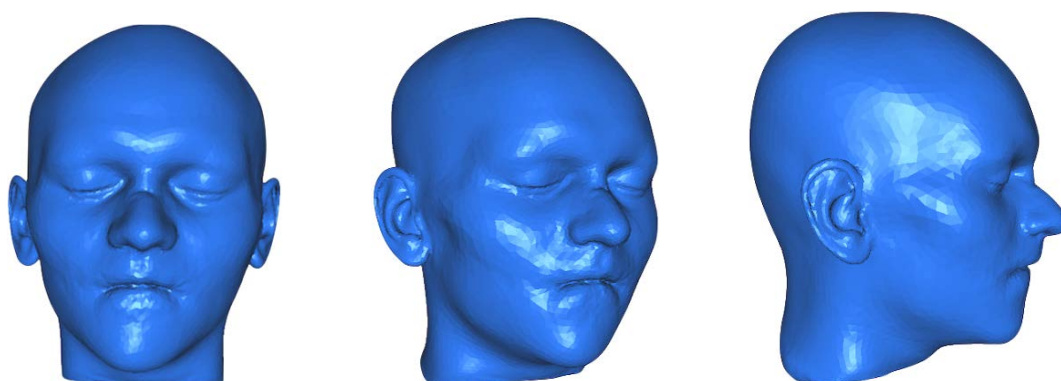


FIGURE C.2 – Simulation 1 : Face reconstructed from the skull and the mandible, i.e. without the teeth and the nasal bone

It can be seen that the absence of teeth and nasal bone generates artifacts.

With regard to the region of the teeth on the reconstructed face, it is easy to assume that the shape of this region of the face was not that one, during his lifetime. However, this simulates the face and profile of an edentulous person quite well. This presents a first argument to demonstrate that our method accurately transcribes the shape of the face according to the shape of the bone.

In the nose area, a breach can also be noticed. In our method, nose reconstruction is the least accurate. Indeed, since there is no bone directly underlying it, the morphing applied to the reference face is less precise at this level. The only bone involved is the nasal bone, which is unfortunately absent on this skull. In the same way as for teeth, the face obtained is visibly affected by the missing information and therefore gives us a bad result. However, this further confirms the basic assumption that our facial reconstruction is faithful to the underlying elements.

C.3.2 Skull with the teeth and without the nasal bone

As a first correction the teeth were added to the previous model, allowing us in a first comparison. The results can be viewed in Figure C.3 (below).

We immediately notice an improvement in the mouth area on this second reconstructed face. The presence of teeth therefore has a significant influence on reconstruction.

In the nose region, however, there is no improvement, but this also indicates a form of robustness of the algorithm. Indeed, apart from the teeth nothing was changed on the skull and therefore the rest of the face is almost identical to the first simulation.

C.3.3 Skull with the teeth and the nasal bone

In a second step, anthropologists also reconstructed the bone of the nose. However, these 3D simulations of the nasal bone are performed manually and require some adjustment. So we



FIGURE C.3 – Simulation 2 : Face reconstructed from the skull, the mandible and the teeth, i.e. without the nasal bone

performed two different cases, with two different nasal bone reconstructions.

The first test is based on a very simple reconstruction of the nasal bone, and keeps a small artifact in the nose (Figure C.4).



FIGURE C.4 – Simulation 3-a : Face reconstructed from the skull, the mandible, the teeth and the nasal bone

The second test is always performed on the same skull with a more complete nasal bone to obtain the most realistic face. There are no artifacts on the nose anymore (Figure C.5).



FIGURE C.5 – Simulation 3-b : Face reconstructed from the skull, the mandible, the teeth and the nasal bone

In this last test, the position of the mandible was also reassessed forward (Figure C.6, which explains the slight change in the shape of the chin, while confirming our assumptions, detailed in

the conclusion below.

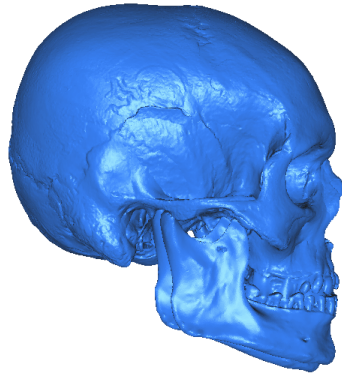


FIGURE C.6 – Comparison of the position of the mandible between simulations 3-a and -b

C.4 Conclusion

These four tests can lead us to different conclusions of interest for the facial reconstruction project as a whole.

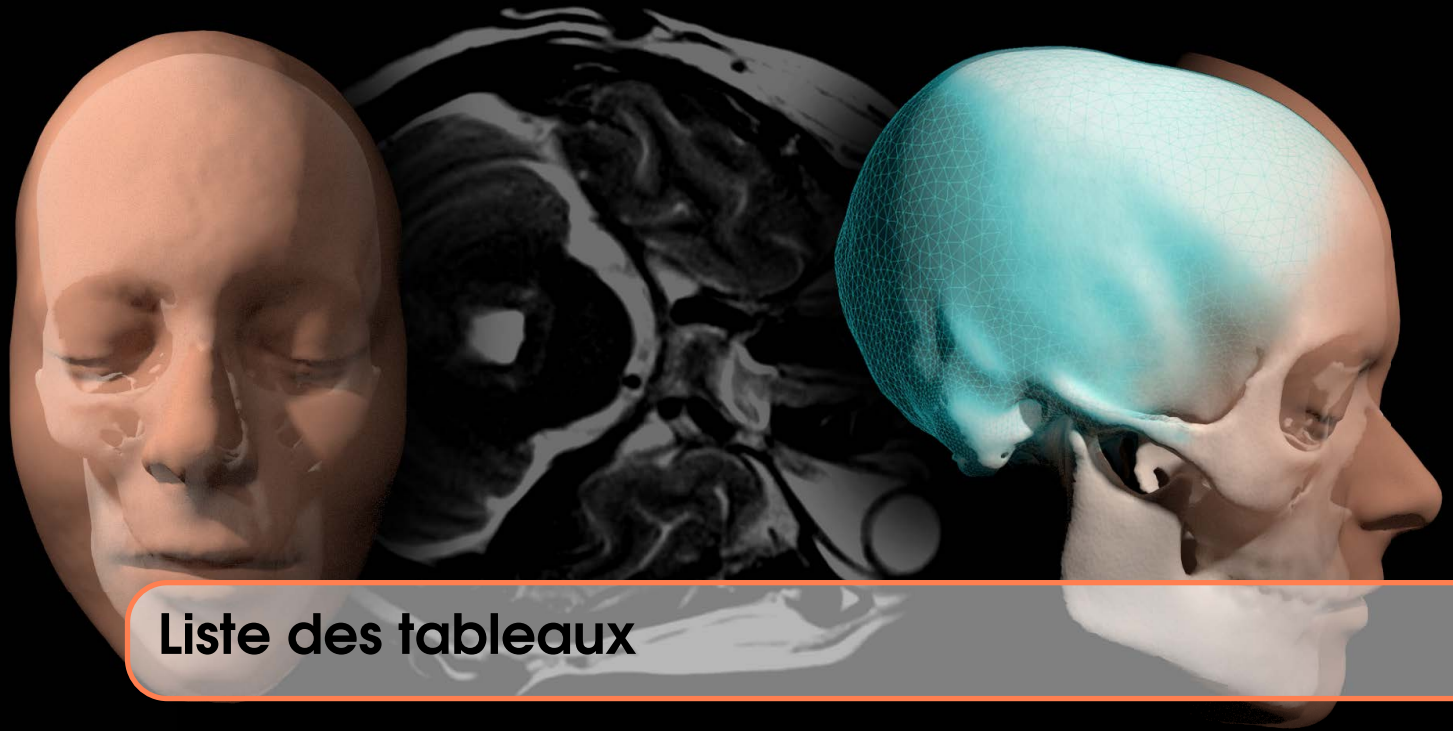
We can appreciate the ease with which these tests were set up : fully automatic, with the possibility of running them in parallel, it took less than 12 hours to obtain these results.

In addition, the stability of the simulations provided by the software is also very interesting : the overall shape of the face remains the same in all the simulations, showing that the change of a bone element alone does not affect the entire face.

Moreover, local changes in the bone shape (teeth, nose) also only locally affect the shape of the face, confirming the overall stability but also the fact that the software really takes into account the underlying elements of the bone skeleton.

This last very positive point in the case where the skull is complete allows us to attest to a certain precision of the method. However, in cases where the reconstruction of some bones is necessary for the process because they are poorly preserved (as is often the case in anthropology), a small modification can lead to a significant local modification of the shape of the face. It is therefore important to keep this aspect of the problem in mind. To solve this problem, numerical methods of automatic reconstruction of the shape, and not manual, are entirely possible, and remains an ongoing research approach.

It is important to note that the entire project in which the facial reconstruction software presented here is available on forensic medicine. Indeed, the works presented in this appendix are to be carried out from an anthropological point of view. The two disciplines having of course common points, but not the same objectives. Forensic medicine focuses on the identification of a deceased person, while anthropology makes hypotheses about the faces of the entire human lineage.



Liste des tableaux

1.1	Descriptive statistics of masseter measurements	75
1.2	Descriptive statistics of cephalometric measurements	75
1.3	Correlation coefficients between masseter and skeletal measurements	76
2.1	Discrepancies between reconstructions and target, using PCA algorithm	93
2.2	Discrepancies between reconstructions and target, using Greedy algorithm	93
3.1	Mean projection error	112
3.2	Mean reconstruction error	113
5.1	Segmentation time for the two methods with both operators	131
5.2	Descriptive statistic of the error of semi automatic segmentation	131
6.1	Comparison between the boundary and volume functionals	150
7.1	Description of the measurements made on the skull	162
7.2	Correlation between the RB of the mandibule and the masseter	164
7.3	Description of reconstruction errors	167
7.4	Description of survey results	170

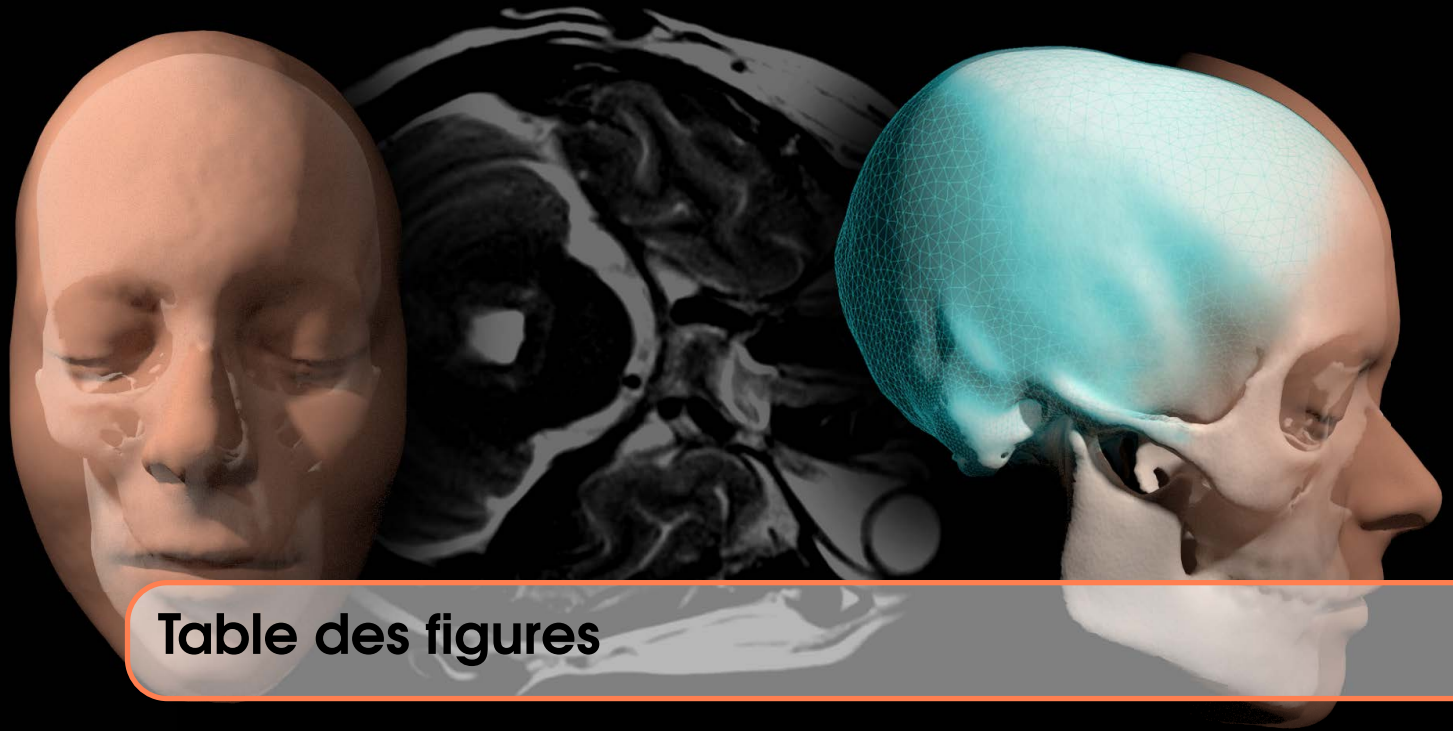


Table des figures

1	Représentations d'Ataï	11
2	Définition de la reconstruction faciale	12
3	Reconstruction faciale tridimensionnelle	13
4	Maillage 3D d'un crâne et d'un visage	14
5	Exemples de masques	14
6	Exemple 2D simple de morphing	15
7	Situation anatomique des muscles masséter et temporal	16
8	Reconstruction d'un muscle masséter via ACP	16
9	Image de scanner avec deux fenêtres d'acquisition	17
10	Exemple de segmentation d'un scanner	18
11	Application de validation de la reconstruction faciale	19
12	Selection de points - Segmentation semi-automatique	19
13	Exemple de différents landmarks céphalométriques	20
14	Maquette 3D du crâne et des muscles du visage	21
15	Les faisceaux du muscle masséter	21
16	Les mesures céphalométriques utilisées	22
17	Les deux fenêtres d'acquisition des images scanner	23
18	Remaillage d'un muscle masséter	24
19	Cinq muscles masséter identiques à un mouvement rigide près	25
20	Description schématique du warping	25
21	Les 5 premières composantes principales de notre base de données ...	26
22	Template non déformé, déformé et sa reconstruction	29
23	Décroissance des valeurs propres après ACP	29

24	Sélection des points à la frontière du muscle masséter	30
25	Représentation 3D d'un crâne et de son visage associé	31
26	Les deux logiciels de segmentation utilisés	31
27	Morphing 2D d'un disque en un lapin	33
28	Morphing 2D d'un disque en un lapin	34
29	Crânes plâtrés de Jericho (7000 av JC)	35
30	Méthode manuelle 2D et 3D de reconstruction faciale	35
31	Schéma de la base de données	36
32	Maillage tétraédrique d'un masque	37
33	Crânes fermés par warping	37
34	Reconstruction d'un visage	38
35	Two representations of Atai	39
36	Facial reconstruction definition	40
37	Three-dimensional facial reconstruction	41
38	3D mesh of a skull and of a face	42
39	Examples of masks	42
40	Simple 2D morphing example	43
41	Anatomical situation of the masseter and temporal muscle	44
42	Reconstruction of a masseter muscle via PCA	44
43	Scanner images with two different acquisition windows	45
44	Segmentation of the skull, the face, and the masseter muscles	46
45	Facial reconstruction validation application	47
46	Points identification - Semi-automatic segmentation	47
47	Example of different cephalometric landmarks	48
48	3D model of the skull and facial muscles	49
49	The beams of the masseter muscle	49
50	The cephalometric measurements used	50
51	The two scanner image acquisition windows	51
52	Remeshing of the masseter muscle	52
53	Five masseter muscles identical with the exception of a rigid movement	53
54	Schematic description of the warping algorithm	53
55	The first 5 main components of our database	54
56	Template undeformed, deformation and reconstruction	57
57	Decrease of eigenvalues after PCA	57
58	Selection of points at the muscle masseter boundary	58
59	3D representation of a skull and its associated face	59
60	The two segmentation software used	59
61	2D morphing of a disc into a rabbit	61
62	2D morphing of a disc into a rabbit	62
63	Flat skulls of Jericho (7000 BC)	62

64	Manual 2D and 3D facial reconstruction method	63
65	Schema of the database	64
66	Tetrahedral mesh of a mask	64
67	Closed skull with warping algorithm	65
68	Reconstruction of a face	65
1.1	Cephalometric landmarks and measurements	73
1.2	Measurements made on frontal plane and axial plane	74
1.3	Segmentation of the masseter muscle	75
1.4	Data Plots Showing Significant Correlation	76
2.1	2D cephalometric method	81
2.2	Masseter muscle segmentation	82
2.3	Automatic skull segmentation	82
2.4	Segmentation of the skull after removing the spine	83
2.5	Example of isosurface-cell intersection in the Marching Cubes algorithm	83
2.6	3D mesh of a masseter muscle	85
2.7	Alignment of a 3D pavement after using this method	88
2.8	Alignment of two masseters with an ellipsoid template	88
2.9	Warping a skull from a sphere	89
2.10	Ellipsoid map with elastic morphing to three masseter muscles	91
2.11	Decrease of the 10 first eigenvalues for our masseter muscles example	92
2.12	Reconstructed masseter muscle with POD and Greedy - 1	94
2.13	Reconstructed masseter muscle with POD and Greedy - 2	94
3.1	Definitions of voxels and segmentation	102
3.2	Exemples of segmentation	103
3.3	Reference configuration and a reconstruction	105
3.4	Illustration of the regularisation coefficient	106
3.5	Examples of generated shapes	106
3.6	Decrease of singular values with POD parametrisation	107
3.7	Examples of generated shapes	107
3.8	Visualisation of two results	108
3.9	Test case presented in Section 3.3 : Error mean and standard deviation	108
3.10	Visual representations of the first few real spherical harmonics	109
3.11	Example of shape generated with spherical harmonic functions	110
3.12	Shape generate with a parametrized spherical haromonic function	111
3.13	Exemple of shape generate with spherical haromonics function	111
4.1	Software interface with the 3 views	119
4.2	An example of points selection on an axial slice	119
4.3	The bounding box selection	120

4.4	Points cloud vs masseter mesh in the unit box	120
4.5	Schema of the head of our 3D image data	121
4.6	Cloud of points superimposed on the masseter mesh	122
4.7	Reconstruction in 3D	124
4.8	Projection of the reconstruction on the original dicom images	125
5.1	Segmentation of the masseter from the 3 scanner cross-sectional planes	129
5.2	Example of a point selection located on the masseter's periphery	130
5.3	Segmentation difficulties : Artifacts	131
5.4	The posterolateral contour of the masseter	132
5.5	The radiolucency shows the separation of the beams	132
6.1	Variation of a shape according to Hadamard's method.	142
6.2	Deformation of the template shape	145
6.3	Target and template shapes	146
6.4	Simple 2d examples for the boundary functional	147
6.5	Simple 2d examples for the volume functional	148
6.6	Signed distance and discrepancy on 3 examples	149
6.7	Three 2d examples for the boundary functional	151
6.8	Three 2d examples for the volume functional	152
6.9	An example in 3d with the volume functional - 1	153
6.10	An example in 3d with the volume functional - 2	154
7.1	Anatomical location of the masseter muscle and its three layers	158
7.2	CT-Scan segmented and the 3D surfacic mesh - Masseter	159
7.3	CT-Scan segmented and the 3D surfacic mesh - Skull/Face	160
7.4	RB reconstruction of a masseter muscle	161
7.5	Landmarks use for the measurements made on the skull	162
7.6	Exemple of measurements made in 3D	163
7.7	Mandible mesh model	163
7.8	Two examples of reconstructed masseter via machine learning	164
7.9	A skull with no muscle, the real muscle, and the reconstructed one	165
7.10	An example of a mask	165
7.11	A skull after warping	166
7.12	An example of reconstruction	166
7.13	Color map of the errors made on the reconstruction	167
7.14	Color map of the errors made on the reconstruction - 2	168
7.15	One example reconstruction with the three tested cases	169
7.16	Application of validation - 1	171
7.17	Application of validation - 2	172
7.18	Suggested face with secondary features	175

A.1	Reference configuration and a reconstruction	182
A.2	Decreasing of singular values and Error mean	183
C.1	Simulated bones of the Skull	194
C.2	Face reconstructed without the teeth and the nasal bone	195
C.3	Face reconstructed with the teeth, but without the nasal bone	196
C.4	Face reconstructed with all simulated bones - 1	196
C.5	Face reconstructed with all simulated bones - 2	196
C.6	Comparison of the position of the mandible	197



Bibliography

Books

- [3] Grégoire ALLAIRE. *Conception optimale de structures*. Tome 58. Mathematics & Applications, Springer-Verlag, Berlin, 2007 (cf. pages 15, 32, 43, 60, 90, 141, 142, 144).
- [5] Pierre ALLIEZ et al. *Recent advances in remeshing of surfaces*. Springer, 2008, pages 53–82 (cf. page 84).
- [28] SN BHATIA et BC LEIGHTON. *Manual of facial growth : a computer analysis of longitudinal cephalometric growth data*. Oxford University Press, Inc., 1993 (cf. page 80).
- [30] Fred L BOOKSTEIN. *Morphometric tools for landmark data : geometry and biology*. Cambridge University Press, 1997 (cf. pages 13, 40, 81).
- [32] Mario BOTSCH et al. *Polygon mesh processing*. AK Peters/CRC Press, 2010 (cf. pages 23, 51, 83).
- [42] Philippe G. CIARLET. *Mathematical Elasticity : Three-dimensional elasticity*. Elsevier, North-Holland, 1994 (cf. pages 145, 156).
- [96] Antoine HENROT et Michel PIERRE. *Variation et optimisation de forme*. Tome 48. Mathematics & Applications, Springer-Verlag, Berlin, 2005 (cf. pages 15, 32, 43, 60, 90, 141, 144).
- [107] British Standards INSTITUTION. *British standard glossary of dental terms*. British Standards Institution, 1983 (cf. pages 20, 48, 72).
- [108] Mehmet Yasar ISCAN et Maryan STEYN. *The human skeleton in forensic medicine*. Charles C Thomas Publisher, 2013 (cf. page 156).
- [112] Ian JOLLIFFE. *Principal component analysis*. Springer, 2011 (cf. page 81).
- [146] Stephen MANCUSI. *The police composite sketch*. Springer Science & Business Media, 2010 (cf. page 156).

- [157] Francois MURAT et Jacques SIMON. *Quelques résultats sur le contrôle par un domaine géométrique*. Publications du Laboratoire d'Analyse Numérique, 1974 (cf. pages 32, 60, 141).
- [216] G SUBSOL et G QUATREHOMME. *Automatic 3D facial reconstruction by feature-based registration of a reference head*. Sous la direction d'éditeurs. CLEMENT J Marks MM. Computer-graphic facial reconstruction. London : Elsevier. 2005, pages 79–101 (cf. page 156).
- [220] Karen T TAYLOR. *Forensic art and illustration*. CRC Press, 2000 (cf. pages 35, 63).
- [222] R TAYLOR et P CRAIG. *The wisdom of bones : facial approximation on the skull*. Sous la direction de Marks MK CLEMENT JG. Computer-graphic facial reconstruction. Boston (MA) : Elsevier Academic Press. 2005, pages 33–55 (cf. page 156).
- [230] P TU et al. *Face reconstructions using flesh deformation modes*. Sous la direction de Marks MK CLEMENT JG. Computer-graphic facial reconstruction. Boston (MA) : Elsevier Academic Press. 2005, pages 145–162 (cf. page 156).
- [237] Tim VALENTINE et Josh P DAVIS. *Forensic facial identification : Theory and practice of identification from eyewitnesses, composites and CCTV*. John Wiley & Sons, 2015 (cf. page 156).
- [255] Caroline WILKINSON et Christopher RYNN. *Craniofacial identification*. Cambridge University Press, 2012 (cf. page 156).

Articles

- [1] M AIRAN, L AIRAN S ans Sharma et et AL. “Correlating the ear length and ear width with mid facial height : a mophometric study”. In : *J Adv Med Dental Sci Res* 5 (2017), pages 19–21 (cf. page 157).
- [2] Paul ALJABAR et al. “Multi-atlas based segmentation of brain images : atlas selection and its effect on accuracy”. In : *Neuroimage* 46.3 (2009), pages 726–738 (cf. pages 27, 55, 103).
- [4] Eman ALLAM et al. “The Relationship Between Hard Tissue and Soft Tissue Dimensions of the Nose in Children : A 3D Cone Beam Computed Tomography Study”. In : 63 (2018), pages 1652–1660. ISSN : 0022-1198. DOI : 10.1111/1556-4029.13801 (cf. page 157).
- [6] Felix AMBELLAN et al. “Automated segmentation of knee bone and cartilage combining statistical shape knowledge and convolutional neural networks : Data from the Osteoarthritis Initiative”. In : *Medical image analysis* 52 (2019), pages 109–118 (cf. page 103).
- [7] Edward H ANGLE. “Classification of malocclusion”. In : *Dent. Cosmos*. 41 (1899), pages 350–375 (cf. pages 20, 48, 72).
- [8] Author ANONYMOUS. “Police find house used for murders”. In : *The New York Times*, 1916 Sept 26 Ed. (1916) (cf. page 156).
- [9] Author ANONYMOUS. “Reconstruct body to solve murders”. In : *The New York Times*, 1916 Sept 25 Ed. (1916) (cf. page 156).
- [10] Y ARIJI et al. “Three-dimensional morphology of the masseter muscle in patients with mandibular prognathism.” In : *Dentomaxillofacial Radiology* 29.2 (2000), pages 113–118 (cf. pages 22, 50, 157).
- [11] Michel A. AUDETTE, Frank P. FERRIE et Terry M. PETERS. “An algorithmic overview of surface registration techniques for medical imaging”. In : 4 (2000), pages 201–217. ISSN : 1361-8415. DOI : 10.1016/s1361-8415(00)00014-1 (cf. page 80).

-
- [12] Mohammed Faouzi AZAROUAL et al. “Relationship between dimensions of muscles of mastication (masseter and lateral pterygoid) and skeletal dimensions : study of 40 cases”. In : *International orthodontics* 12.1 (2014), pages 111–124 (cf. pages 22, 49, 50, 72, 77, 157).
- [13] Ruzena BAJCSY. “Multiresolution elastic matching”. In : 45 (1989), page 132. ISSN : 0734-189X. DOI : 10.1016/0734-189x(89)90082-0 (cf. pages 15, 42).
- [14] Ruzena BAJCSY et Stane KOVAČIČ. “Multiresolution Elastic Matching”. In : *Comput. Vision Graph. Image Process.* 46.1 (1989), pages 1–21 (cf. pages 32, 60, 140).
- [15] Timothy J. BAKER. “Mesh Movement and Metamorphosis”. In : (2001), pages 387–396 (cf. page 145).
- [16] Siqi BAO et Albert CS CHUNG. “Multi-scale structured CNN with label consistency for brain MR image segmentation”. In : *Computer Methods in Biomechanics and Biomedical Engineering : Imaging & Visualization* 6.1 (2018), pages 113–117 (cf. pages 27, 55, 102, 180).
- [17] John SH BAXTER et al. “The semiotics of medical image Segmentation”. In : *Medical image analysis* 44 (2018), pages 54–71 (cf. page 132).
- [18] Michael P BECHT et al. “Evaluation of masseter muscle morphology in different types of malocclusions using cone beam computed tomography”. In : *International Orthodontics* 12.1 (2014), pages 32–48 (cf. page 77).
- [19] HC BECKER et al. “Digital computer determination of a medical diagnostic index directly from chest X-ray images”. In : *IEEE Transactions on Biomedical Engineering* 3 (1964), pages 67–72 (cf. pages 27, 55, 102).
- [21] Mirza F. BEG et al. “Computing Large Deformation Metric Mappings via Geodesic Flows of Diffeomorphisms”. In : *International Journal of Computer Vision* 61.2 (2005), pages 139–157 (cf. pages 15, 42, 140).
- [22] Serge BELONGIE, Jitendra MALIK et Jan PUZICHA. “Shape matching and object recognition using shape contexts”. In : *IEEE transactions on pattern analysis and machine intelligence* 24.4 (2002), pages 509–522 (cf. pages 15, 42, 141).
- [23] Philip CM BENINGTON, John E GARDENER et Nigel P HUNT. “Masseter muscle volume measured using ultrasonography and its relationship with facial morphology”. In : *The European Journal of Orthodontics* 21.6 (1999), pages 659–670 (cf. page 77).
- [25] Florian BERNARD et al. “Shape-aware surface reconstruction from sparse 3D point-clouds”. In : *Medical image analysis* 38 (2017), pages 77–89 (cf. pages 28, 55, 104, 180).
- [26] Stefano BERRETTI et al. “Representation, analysis, and recognition of 3D humans : A survey”. In : *ACM Transactions on Multimedia Computing, Communications, and Applications (TOMM)* 14.1s (2018), page 16 (cf. page 80).
- [27] Paul J BESL et Neil D MCKAY. “Method for registration of 3-D shapes”. In : 1611 (1992), pages 586–607 (cf. page 89).
- [29] Christophe BONNEFOY, Luc CHIKHANI et Jacques DICHAMP. “Anatomie descriptive et fonctionnelle de l’articulation temporo-mandibulaire”. In : *Actualites Odonto-Stomatologiques* 265 (2013), pages 4–18 (cf. pages 21, 49, 158).
- [31] H P W BOOM et al. “A comparison of human jaw muscle cross-sectional area and volume in long- and short-face subjects, using MRI.” In : *Archives of oral biology* 53 (3 mar. 2008), pages 273–281. ISSN : 0003-9969. DOI : 10.1016/j.archoralbio.2007.08.013 (cf. pages 15, 22, 43, 50, 72, 157).

- [33] Alexander de BREBISSON et Giovanni MONTANA. “Deep neural networks for anatomical brain segmentation”. In : (2015), pages 20–28 (cf. pages 27, 55, 102, 180).
- [34] M. de BUHAN, C. NARDONI et L. URO. “Volumic and Boundary shape matching : comparison of two optimization methods”. In : (2019) (cf. pages 90, 165).
- [35] Maya de BUHAN et Chiara NARDONI. “A facial reconstruction method based on new mesh deformation techniques.” In : *Forensic sciences research* 3 (3 2018), pages 256–273. ISSN : 2471-1411. DOI : 10.1080/20961790.2018.1469185 (cf. pages 14, 36, 38, 42, 64, 66, 137, 150, 156–158, 165, 167, 170).
- [36] Maya de BUHAN et al. “An optimization method for elastic shape matching”. In : *Comptes Rendus Mathématique* 354.8 (2016), pages 783–787 (cf. pages 137, 140).
- [37] M BURGER. “A framework for the construction of level set methods for shape optimization and reconstruction”. In : *Interfaces and Free Boundaries* 5 (2003), pages 301–329 (cf. page 143).
- [38] A BUSATO et al. “Management and control of isotonic contraction generated stress : evaluation of masseter muscle deformation pattern by means of ecography”. In : *ORAL & implantology* 9.Suppl 1/2016 to N 4/2016 (2016), page 45 (cf. page 158).
- [39] Benjamin BUSTOS et al. “Feature-based similarity search in 3D object databases”. In : *ACM Computing Surveys (CSUR)* 37.4 (2005), pages 345–387 (cf. pages 82, 132).
- [40] Carlos E CARDENAS et al. “Advances in auto-segmentation”. In : 29.3 (2019), pages 185–197 (cf. pages 27, 55, 103).
- [41] Jean CEA. “Conception optimale ou identification de formes, calcul rapide de la dérivée directionnelle de la fonction coût”. In : 20 (1986), pages 371–402. ISSN : 0764-583X. DOI : 10.1051/m2an/1986200303711 (cf. pages 15, 43).
- [43] Peter CLAES et al. “Craniofacial reconstruction using a combined statistical model of face shape and soft tissue depths : methodology and validation”. In : *Forensic science international* 159 (2006), S147–S158 (cf. pages 34, 62, 156, 159).
- [44] Peter CLAES et al. “Computerized craniofacial reconstruction : conceptual framework and review”. In : *Forensic science international* 201.1-3 (2010), pages 138–145 (cf. pages 13, 40, 156, 157).
- [45] Olivier COMMOWICK et Grégoire MALANDAIN. “Efficient selection of the most similar image in a database for critical structures segmentation”. In : (2007), pages 203–210 (cf. pages 27, 55, 103).
- [46] Timothy F COOTES et Christopher J TAYLOR. “Combining point distribution models with shape models based on finite element analysis”. In : *Image and Vision Computing* 13.5 (1995), pages 403–409 (cf. page 81).
- [47] Timothy F COOTES et al. “Use of active shape models for locating structures in medical images”. In : *Image and vision computing* 12.6 (1994), pages 355–365 (cf. page 80).
- [48] Timothy F COOTES et al. “Active shape models-their training and application”. In : *Computer vision and image understanding* 61.1 (1995), pages 38–59 (cf. page 81).
- [49] Emily A. EA CRAIG. “Commentary on : Stephan CN. Facial approximation : globe projection guideline falsified by exophthalmometry literature. *J Forensic Sci* 2002;47(4) :730–5.” In : 48 (2003), page 2002319. ISSN : 0022-1198. DOI : 10.1520/jfs2002319 (cf. page 157).

-
- [50] Charles DAPOGNY, Cécile DOBRZYNSKI et Pascal FREY. “Three-dimensional adaptive domain remeshing, implicit domain meshing, and applications to free and moving boundary problems”. In : *Journal of computational physics* 262 (2014), pages 358–378 (cf. pages 23, 51, 84, 159).
- [51] Charles DAPOGNY et Pascal FREY. “Computation of the signed distance function to a discrete contour on adapted triangulation”. In : *Calcolo* 49.3 (2012), pages 193–219 (cf. page 148).
- [52] Charles DAPOGNY et al. “GEOMETRICAL SHAPE OPTIMIZATION IN FLUID MECHANICS USING FREEFEM++”. In : *Preprint* (2017) (cf. pages 144, 147).
- [53] J DELAIRE. “L’analyse architecturale et structurale cranio-faciale (de profil). Principes théoriques. Quelques exemples d’emploi en chirurgie maxillo-faciale”. In : *Rev. Siom.*, 1978; 79 : 1 33 (1978) (cf. page 80).
- [54] Alexei DEMYANOV. “On the solution of min-sum-min problems”. In : *Journal of Global Optimization* 31.3 (2005), pages 437–453 (cf. page 123).
- [55] Qingqiong DENG et al. “A regional method for craniofacial reconstruction based on coordinate adjustments and a new fusion strategy”. In : *Forensic science international* 259 (2016), pages 19–31 (cf. page 157).
- [56] Girard J DIPIETRO et James R MOERGELI JR. “Significance of the Frankfort-mandibular plane angle to prosthodontics”. In : *The Journal of prosthetic dentistry* 36.6 (1976), pages 624–635 (cf. pages 22, 50, 72, 77, 157).
- [57] Cécile DOBRZYNSKI et Pascal FREY. “Anisotropic Delaunay mesh adaptation for unsteady simulations”. In : (2008), pages 177–194 (cf. pages 23, 51, 84, 159).
- [58] Akio DOI et Akio KOIDE. “An efficient method of triangulating equi-valued surfaces by using tetrahedral cells”. In : *IEICE TRANSACTIONS on Information and Systems* 74.1 (1991), pages 214–224 (cf. page 83).
- [59] Kunio DOI. “Overview on research and development of computer-aided diagnostic schemes”. In : 25.5 (2004), pages 404–410 (cf. pages 27, 55, 102).
- [60] Kunio DOI. “Current status and future potential of computer-aided diagnosis in medical imaging”. In : *The British journal of radiology* 78.suppl_1 (2005), s3–s19 (cf. pages 27, 55, 102).
- [61] Kunio DOI. “Diagnostic imaging over the last 50 years : research and development in medical imaging science and technology”. In : *Physics in Medicine & Biology* 51.13 (2006), R5 (cf. page 27).
- [62] Kunio DOI. “Computer-aided diagnosis in medical imaging : historical review, current status and future potential”. In : *Computerized medical imaging and graphics* 31.4-5 (2007), pages 198–211 (cf. pages 27, 28, 55, 56, 80, 102).
- [63] Kunio DOI et al. “Computer-aided diagnosis in radiology : potential and pitfalls”. In : *European journal of radiology* 31.2 (1999), pages 97–109 (cf. page 27).
- [64] Eve DONNELLY. “Methods for assessing bone quality : a review”. In : *Clinical Orthopaedics and Related Research®* 469.8 (2011), pages 2128–2138 (cf. page 80).
- [65] Hélène F. DORFLING et al. “Facial approximations : Characteristics of the eye in a South African sample”. In : 286 (2018), pages 46–53. ISSN : 0379-0738. DOI : 10.1016/j.forsciint.2018.02.029 (cf. page 157).
- [66] Fuqing DUAN et al. “Craniofacial reconstruction based on multi-linear subspace analysis”. In : *Multimedia Tools and Applications* 73.2 (2014), pages 809–823 (cf. page 157).

- [67] Paul DUPUIS, Ulf GRENANDER et Michael I MILLER. “Variational problems on flows of diffeomorphisms for image matching”. In : *Quarterly of applied mathematics* (1998), pages 587–600 (cf. pages 15, 42, 140).
- [68] Chenyang Xu DZUNG L. PHAM et Jerry L. PRINCE. “CURRENT METHODS IN MEDICAL IMAGE SEGMENTATION”. In : *Annual Review of Biomedical Engineering, Volume 2* (2000) (cf. pages 102, 116, 180).
- [69] Hv EGGELING. “Die Leistungsfähigkeit physiognomischer Rekonstruktionsversuche auf Grundlage des Schädels”. In : *Archiv Anthropol* 12 (1913), pages 44–47 (cf. page 156).
- [70] Bradley J ERICKSON et Brian BARTHOLMAI. “Computer-aided detection and diagnosis at the start of the third millennium”. In : *Journal of digital imaging* 15.2 (2002), pages 59–68 (cf. pages 27, 55, 102).
- [72] Daniel FREEDMAN et al. “Model-based segmentation of medical imagery by matching distributions”. In : *IEEE transactions on medical imaging* 24.3 (2005), pages 281–292 (cf. pages 27, 55, 103).
- [73] Jaime L FRIAS, Ann L WILSON et Gregory J KING. “A cephalometric study of fetal alcohol syndrome”. In : *The Journal of pediatrics* 101.5 (1982), pages 870–873 (cf. pages 21, 49).
- [74] Betty Pat GATLIFF. “Facial sculpture on the skull for identification”. In : 5 (1984), pages 327–332. ISSN : 0195-7910. DOI : 10 . 1097 / 00000433 - 198412000 - 00009 (cf. pages 156, 157).
- [75] TR GEBECK. “Analysis—concepts and values. Part I.” In : *Journal of the Charles H. Tweed International Foundation* 17 (1989), pages 19–48 (cf. pages 20, 48, 72).
- [76] Mikhail GERASIMOV. “The face finder”. In : (1971) (cf. pages 35, 63, 156, 157).
- [77] MM GERASIMOV. “The reconstruction of the face from the basic structure of the skull”. In : *Russia : Publisher Unknown* (1955) (cf. pages 35, 63, 157).
- [78] Thomas GIETZEN et al. “A method for automatic forensic facial reconstruction based on dense statistics of soft tissue thickness”. In : *PloS one* 14.1 (2019), e0210257 (cf. page 157).
- [79] N GIONHAKU et AA LOWE. “Relationship between jaw muscle volume and craniofacial form”. In : *Journal of Dental Research* 68.5 (1989), pages 805–809 (cf. page 78).
- [81] Joan GLAUNES, Alain TROUVÉ et Laurent YOUNES. “Diffeomorphic matching of distributions : A new approach for unlabelled point-sets and sub-manifolds matching”. In : 2 (2004) (cf. page 140).
- [82] Joan GLAUNÈS, Alain TROUVÉ et Laurent YOUNES. “Modeling planar shape variation via Hamiltonian flows of curves”. In : *Statistics and analysis of shapes* (2006), pages 335–361 (cf. page 140).
- [83] Joan GLAUNÈS et al. “Large deformation diffeomorphic metric curve mapping”. In : *International journal of computer vision* 80.3 (2008), pages 317–336 (cf. page 140).
- [84] Frédéric de GOURNAY. “Velocity extension for the level-set method and multiple eigenvalues in shape optimization”. In : *SIAM journal on control and optimization* 45.1 (2006), pages 343–367 (cf. page 143).
- [85] Ulf GRENANDER et Michael I MILLER. “Computational anatomy : An emerging discipline”. In : *Quarterly of applied mathematics* 56.4 (1998), pages 617–694 (cf. page 140).
- [86] Xianfeng GU et Baba C VEMURI. “Matching 3d shapes using 2d conformal representations”. In : (2004), pages 771–780 (cf. page 141).

-
- [87] P GUNZ, P MITTEROECKER et F. L. BOOKSTEIN. “Semilandmarks in Three Dimensions, in Modern Morphometrics in Physical Anthropology.” In : *New York : Kluwer Academic/Plenum Publishers*. (2005). Sous la direction de D. E. SLICE, pages 73–98 (cf. page 194).
- [88] P GUYOMARC’H et CN STEPHAN. “The validity of ear prediction guidelines used in facial approximation”. In : *J Forensic Sci* 57 (2012), pages 1427–1441 (cf. page 157).
- [89] Pierre GUYOMARC’H et al. “Anatomical Placement of the Human Eyeball in the Orbit-Validation Using CT Scans of Living Adults and Prediction for Facial Approximation*^{*}. ANATOMICAL PLACEMENT OF THE HUMAN EYEBALL”. In : 57 (2012), pages 1271–1275. ISSN : 0022-1198. DOI : 10.1111/j.1556-4029.2012.02075.x (cf. page 157).
- [90] Pierre GUYOMARC’H et al. “Anthropological Facial Approximation in Three Dimensions (AFA3D) : Computer-Assisted Estimation of the Facial Morphology Using Geometric Morphometrics”. In : 59 (2014), pages 1502–1516. ISSN : 0022-1198. DOI : 10.1111/1556-4029.12547 (cf. page 156).
- [91] William D HAGLUND et Donald T REAY. “Use of facial approximation techniques in identification of Green River serial murder victims.” In : *The American journal of forensic medicine and pathology* 12.2 (1991), pages 132–142 (cf. pages 35, 36, 63, 156).
- [92] Steven HAKER et al. “Optimal mass transport for registration and warping”. In : *International Journal of computer vision* 60.3 (2004), pages 225–240 (cf. page 141).
- [93] AG HANNAM et WW WOOD. “Relationships between the size and spatial morphology of human masseter and medial pterygoid muscles, the craniofacial skeleton, and jaw biomechanics”. In : *American Journal of Physical Anthropology* 80.4 (1989), pages 429–445 (cf. page 78).
- [94] Tobias HEIMANN et Hans-Peter MEINZER. “Statistical shape models for 3D medical image segmentation : a review”. In : *Medical image analysis* 13.4 (2009), pages 543–563 (cf. pages 27, 28, 55, 56, 102, 103, 180).
- [95] Andrew G HENDRICKX et al. “Teratological and radiocephalometric analysis of craniofacial malformations induced with retinoic acid in rhesus monkeys (*Macaca mulatta*)”. In : *Teratology* 22.1 (1980), pages 13–22 (cf. pages 21, 49).
- [97] Masaki HILAGA et al. “Topology matching for fully automatic similarity estimation of 3D shapes”. In : (2001), pages 203–212 (cf. page 141).
- [99] Harold HOTELLING. “The Generalization of Student’s Ratio”. In : 2 (1931), pages 360–378. ISSN : 0003-4851. DOI : 10.1214/aoms/1177732979 (cf. page 130).
- [100] Harold HOTELLING. “Analysis of a complex of statistical variables into principal components.” In : *Journal of educational psychology* 24.6 (1933), page 417 (cf. page 81).
- [101] Yongli HU et al. “Craniofacial reconstruction based on a hierarchical dense deformable model”. In : *EURASIP Journal on Advances in Signal Processing* 2012.1 (2012), page 217 (cf. page 157).
- [102] Maria Isabel HUETE et al. “Past, present, and future of craniofacial superimposition : Literature and international surveys”. In : *Legal Medicine* 17.4 (2015), pages 267–278 (cf. pages 34, 62).
- [103] John R HURLEY et Raymond B CATTELL. “The Procrustes program : Producing direct rotation to test a hypothesized factor structure”. In : *Behavioral science* 7.2 (1962), pages 258–262 (cf. page 81).

- [104] Tim J HUTTON, Sue CUNNINGHAM et Peter HAMMOND. “An evaluation of active shape models for the automatic identification of cephalometric landmarks”. In : *The European Journal of Orthodontics* 22.5 (2000), pages 499–508 (cf. pages 80, 81).
- [105] Juan Eugenio IGLESIAS et Mert R SABUNCU. “Multi-atlas segmentation of biomedical images : a survey”. In : *Medical image analysis* 24.1 (2015), pages 205–219 (cf. pages 27, 28, 55, 56, 81, 103, 180).
- [106] B. E. N. G. T. INGERVALL et B. I. R. G. I. T. THILANDER. “Relation between facial morphology and activity of the masticatory muscles. An electromyographic and radiographic cephalometric investigation”. In : 1 (1974), pages 131–147. ISSN : 0305-182X. DOI : 10.1111/j.1365-2842.1974.tb00771.x (cf. page 72).
- [109] MY ISCAN, RP HELMER et Murray K MARKS. “Forensic Analysis of the Skull : Craniofacial Analysis, Reconstruction, and Identification”. In : *Human Biology* 68.2 (1996), pages 325–330 (cf. pages 156, 158).
- [110] Manaswini JENA, Smita Prava MISHRA et Debahuti MISHRA. “A Survey on Applications of Machine Learning Techniques for Medical Image Segmentation”. In : *International Journal of Engineering & Technology* 10.x (2018), pages xxx–xxx (cf. pages 27, 28, 55, 103).
- [113] Sarang C JOSHI et Michael I MILLER. “Landmark matching via large deformation diffeomorphisms”. In : *IEEE Transactions on Image Processing* 9.8 (2000), pages 1357–1370 (cf. page 140).
- [114] Alexander JUERCHOTT et al. “In vivo reliability of 3D cephalometric landmark determination on magnetic resonance imaging : a feasibility study”. In : *Clinical oral investigations* (2019), pages 1–11 (cf. page 80).
- [115] Yan KANG, Klaus ENGELKE et Willi A KALENDER. “A new accurate and precise 3-D segmentation method for skeletal structures in volumetric CT data”. In : *IEEE transactions on medical imaging* 22.5 (2003), pages 586–598 (cf. pages 27, 55, 102, 180).
- [116] S KILIARIDIS et P KÄLEBO. “Masseter muscle thickness measured by ultrasonography and its relation to facial morphology”. In : *Journal of dental research* 70.9 (1991), pages 1262–1265 (cf. pages 22, 50, 77, 78, 159).
- [117] Stavros KILIARIDIS et al. “Ultrasonographic thickness of the masseter muscle in growing individuals with unilateral crossbite”. In : *The Angle Orthodontist* 77.4 (2007), pages 607–611 (cf. page 78).
- [118] Sang-Rok KIM et al. “Three-dimensional prediction of the human eyeball and canthi for craniofacial reconstruction using cone-beam computed tomography”. In : 261 (2016), 164.e1–164.e8. ISSN : 0379-0738. DOI : 10.1016/j.forsciint.2016.01.031 (cf. page 157).
- [119] Sung-Ho KIM et Kyung-Yong CHUNG. “Medical information service system based on human 3D anatomical model”. In : *Multimedia Tools and Applications* 74.20 (2015), pages 8939–8950 (cf. page 80).
- [120] N KITAI et al. “Human masticatory muscle volume and zygomatico-mandibular form in adults with mandibular prognathism”. In : *Journal of dental research* 81.11 (2002), pages 752–756 (cf. page 78).
- [121] Vladimir A KNYAZ et al. “Virtual face reconstruction based on 3D skull model”. In : 4661 (2002), pages 182–190 (cf. page 159).

-
- [122] Leif P KOBBELT et al. “Feature sensitive surface extraction from volume data”. In : (2001), pages 57–66 (cf. page 83).
- [123] Büchly W KOLLMANN J. “Die Persistenz der Rassen und die reconstruction der Physiognomie prahistorischer Schädel”. In : *Archiv Anthropol* 25 (1898), pages 329–359 (cf. page 156).
- [124] Wilton Marion KROGMAN et MY ISCAN. “The Human Skeleton in Forensic”. In : *Medicine* (1962), pages 301–327 (cf. pages 35, 63).
- [125] MUNUTSUGU KUBOTA et al. “Maxillofacial morphology and masseter muscle thickness in adults”. In : *The European Journal of Orthodontics* 20.5 (1998), pages 535–542 (cf. pages 22, 50, 77, 78).
- [126] Jinsa KURUVILLA et K GUNAVATHI. “Lung cancer classification using neural networks for CT images”. In : *Computer methods and programs in biomedicine* 113.1 (2014), pages 202–209 (cf. pages 28, 55, 103).
- [127] Hans LAMECKER et al. “A 3D statistical shape model of the pelvic bone for segmentation”. In : 5370 (2004), pages 1341–1351 (cf. pages 27, 55, 103).
- [128] Sung Min LEE et al. “Automatic 3D cephalometric annotation system using shadowed 2D image-based machine learning”. In : *Physics in Medicine & Biology* 64.5 (2019), page 055002 (cf. page 80).
- [129] Won-Joon LEE, Caroline M. WILKINSON et Hyeon-Shik HWANG. “An Accuracy Assessment of Forensic Computerized Facial Reconstruction Employing Cone-Beam Computed Tomography from Live Subjects. AN ACCURACY ASSESSMENT OF FORENSIC COMPUTERIZED FACIAL RECONSTRUCTION”. In : 57 (2012), pages 318–327. ISSN : 0022-1198. DOI : 10.1111/j.1556-4029.2011.01971.x (cf. page 156).
- [130] Bruno LÉVY. “A numerical algorithm for L2 semi-discrete optimal transport in 3D”. In : *ESAIM : Mathematical Modelling and Numerical Analysis* 49.6 (2015), pages 1693–1715 (cf. pages 15, 42, 141).
- [131] Geert LITJENS et al. “A survey on deep learning in medical image analysis”. In : *Medical image analysis* 42 (2017), pages 60–88 (cf. pages 28, 56, 102, 180).
- [132] Gwilym S LODWICK et al. “Computer diagnosis of primary bone tumors : A preliminary report”. In : *Radiology* 80.2 (1963), pages 273–275 (cf. pages 27, 55, 102).
- [133] Antonio M LÓPEZ et al. “Evaluation of methods for ridge and valley detection”. In : *IEEE Transactions on Pattern Analysis and Machine Intelligence* 21.4 (1999), pages 327–335 (cf. pages 27, 55, 102, 180).
- [134] William E LORENSEN et Harvey E CLINE. “Marching cubes : A high resolution 3D surface construction algorithm”. In : 21.4 (1987), pages 163–169 (cf. pages 23, 51, 83, 84).
- [135] Alan A LOWE et al. “Facial morphology and obstructive sleep apnea”. In : *American Journal of Orthodontics and Dentofacial Orthopedics* 90.6 (1986), pages 484–491 (cf. pages 21, 48).
- [136] Lok Ming LUI et al. “Optimized conformal surface registration with shape-based landmark matching”. In : *SIAM Journal on Imaging Sciences* 3.1 (2010), pages 52–78 (cf. page 141).
- [137] Y. MADAY, D. LOMBARDI et L. URO. “Fast semi-automatic segmentation based on reduced basis”. In : *C. R. Acad. Sci. Paris* (2019) (cf. page 82).
- [138] Dennis MADSEN et al. “Probabilistic joint face-skull modelling for facial reconstruction”. In : (2018), pages 5295–5303 (cf. pages 156, 157).

- [139] S Sara MAHDAVI et al. "Semi-automatic segmentation for prostate interventions". In : *Medical Image Analysis* 15.2 (2011), pages 226–237 (cf. page 133).
- [140] Ravi Kumar MAHTO et al. "Variation of Cranial Base Morphology among Different Sagittal Skeletal Malocclusion—A Cephalometric Study in Nepalese Population". In : *Journal of Pierre Fauchard Academy (India Section)* 33.1 (2019), pages 19–24 (cf. pages 21, 48).
- [141] Tahir MAJEED et al. "A shape prior-based MRF model for 3D masseter muscle segmentation". In : 8314 (2012), 831400 (cf. pages 128, 132).
- [142] Tahir MAJEED et al. "Using a flexibility constrained 3D statistical shape model for robust MRF-based segmentation". In : (2012), pages 57–64 (cf. pages 128, 132).
- [143] K MALA, V SADASIVAM et S ALAGAPPAN. "Neural network based texture analysis of CT images for fatty and cirrhosis liver classification". In : *Applied Soft Computing* 32 (2015), pages 80–86 (cf. pages 28, 55, 103).
- [144] P MALA. "Pronasale position : an appraisal of two recently proposed methods for predicting nasal projection in facial reconstruction". In : *J Forensic Sci* 58 (2013), pages 957–963 (cf. page 157).
- [145] P MALA et J VELEMINSKA. "Vertical lip position and thickness in facial reconstruction : a validation of commonly used methods for predicting the position and size of lips." In : *J Forensic Sci* 61 (2016), pages 1046–1054 (cf. page 157).
- [147] F. MARCHAL et al. "La restitution des têtes osseuses d'Atai et de son compagnon". In : 28 (2016), pages 100–105. ISSN : 0037-8984. DOI : 10.1007/s13219-016-0142-4 (cf. pages 11, 39).
- [148] C MARÉCAUX et al. "A new 3D cephalometric analysis for planning in computer aided orthognatic surgery". In : 61 (2003) (cf. page 80).
- [149] Sergey V MATVEYEV. "Approximation of isosurface in the marching cube : ambiguity problem". In : (1994), pages 288–292 (cf. page 83).
- [150] Phillip H MEYERS et al. "Automated computer analysis of radiographic images". In : *Radiology* 83.6 (1964), pages 1029–1034 (cf. pages 27, 55, 102).
- [151] Malay MITRA et RK SAMANTA. "Cardiac arrhythmia classification using neural networks with selected features". In : *Procedia Technology* 10 (2013), pages 76–84 (cf. pages 28, 55, 103).
- [152] Nobutaka MITSUHASHI et al. "BodyParts3D : 3D structure database for anatomical concepts". In : *Nucleic acids research* 37.suppl_1 (2008), pages D782–D785 (cf. page 80).
- [153] Sachio MIYASAKA et al. "The computer-aided facial reconstruction system". In : *Forensic science international* 74.1-2 (1995), pages 155–165 (cf. pages 34, 62, 156).
- [154] J. MONTAGNAT, H. DELINGETTE et N. AYACHE. "A review of deformable surfaces : topology, geometry and deformation". In : 19 (2001), pages 1023–1040. ISSN : 0262-8856. DOI : 10.1016/s0262-8856(01)00064-6 (cf. page 80).
- [155] Claudio MONTANI, Riccardo SCATENI et Roberto SCOPIGNO. "A modified look-up table for implicit disambiguation of marching cubes". In : *The visual computer* 10.6 (1994), pages 353–355 (cf. page 83).
- [156] R MULLERMULLER et al. "Morphometric Analysis of Human Bone Biopsies : A Quantitative Structural Comparison of Histological Sections and Micro-Computed Tomography-Comparison of high-resolution computed tomography and histologic sections". In : *Bone* 23.1 (1998), pages 59–66 (cf. page 80).

-
- [159] Kamal NASREDDINE, Abdesslam BENZINOUE et Ronan FABLET. “Variational shape matching for shape classification and retrieval”. In : *Pattern Recognition Letters* 31.12 (2010), pages 1650–1657 (cf. page 140).
- [160] Bala Chakravarthy NEELAPU et al. “Craniofacial and upper airway morphology in adult obstructive sleep apnea patients : A systematic review and meta-analysis of cephalometric studies”. In : *Sleep medicine reviews* 31 (2017), pages 79–90 (cf. pages 21, 48).
- [161] Gregory M NIELSON et Bernd HAMANN. “The asymptotic decider : resolving the ambiguity in marching cubes”. In : (1991), pages 83–91 (cf. page 83).
- [162] Märta OLOW-NORDENRAM. “Maxillonasal dysplasia (Binder’s syndrome). A study of craniofacial morphology, associated malformations and familial relations.” In : *Swedish dental journal. Supplement* 47 (1987), pages 1–38 (cf. pages 21, 49).
- [163] H OPDEBEECK et WH BELL. “The short face syndrome”. In : *American Journal of Orthodontics* 73.5 (1978), pages 499–511 (cf. pages 72, 157).
- [164] Sohyun PARK et al. “The impacts of three-dimensional anatomical atlas on learning anatomy”. In : 52 (2019), page 76. ISSN : 2093-3665. DOI : 10.5115/acb.2019.52.1.76 (cf. page 80).
- [165] Connie L. PARKS et Keith L. MONSON. “Automated facial recognition and candidate list rank change of computer generated facial approximations generated with multiple eye orb positions”. In : 266 (2016), pages 396–398. ISSN : 0379-0738. DOI : 10.1016/j.forsciint.2016.06.023 (cf. page 157).
- [166] Connie L. PARKS et Keith L. MONSON. “Biometric correspondence between reface computerized facial approximations and CT-derived ground truth skin surface models objectively examined using an automated facial recognition system”. In : 286 (2018), pages 8–11. ISSN : 0379-0738. DOI : 10.1016/j.forsciint.2018.02.019 (cf. page 170).
- [167] Connie L. PARKS et Keith L. MONSON. “Recognizability of computer-generated facial approximations in an automated facial recognition context for potential use in unidentified persons data repositories : Optimally and operationally modeled conditions”. In : 291 (2018), pages 272–278. ISSN : 0379-0738. DOI : 10.1016/j.forsciint.2018.07.024 (cf. page 170).
- [168] Connie L. PARKS, Adam H. RICHARD et Keith L. MONSON. “Preliminary performance assessment of computer automated facial approximations using computed tomography scans of living individuals”. In : 233 (2013), pages 133–139. ISSN : 0379-0738. DOI : 10.1016/j.forsciint.2013.08.031 (cf. page 156).
- [169] Pascal PAYSAN et al. “A 3D face model for pose and illumination invariant face recognition”. In : (2009), pages 296–301 (cf. page 157).
- [170] Dzung L PHAM, Chenyang XU et Jerry L PRINCE. “Current methods in medical image segmentation”. In : *Annual review of biomedical engineering* 2.1 (2000), pages 315–337 (cf. pages 27, 55, 102, 180).
- [171] Manuel PINHEIRO et al. “A 3D cephalometric protocol for the accurate quantification of the craniofacial symmetry and facial growth”. In : *Journal of biological engineering* 13.1 (2019), page 42 (cf. page 80).
- [172] Benjamin J POMIDOR, Jana MAKEDONSKA et Dennis E SLICE. “A landmark-free method for three-dimensional shape analysis”. In : *PloS one* 11.3 (2016), e0150368 (cf. page 81).
- [173] Arish A QAZI et al. “Auto-segmentation of normal and target structures in head and neck CT images : A feature-driven model-based approach”. In : *Medical physics* 38.11 (2011), pages 6160–6170 (cf. pages 27, 55, 103).

- [174] Gérald QUATREHOMME et al. “A fully three-dimensional method for facial reconstruction based on deformable models”. In : *Journal of Forensic Science* 42.4 (1997), pages 649–652 (cf. pages 156, 159).
- [175] Mohd Shafry Mohd RAHIM et al. “3D bones segmentation based on CT images visualization”. In : (2017) (cf. pages 27, 55, 102, 180).
- [176] N RAMESH, J-H YOO et IK SETHI. “Thresholding based on histogram approximation”. In : *IEE Proceedings-Vision, Image and Signal Processing* 142.5 (1995), pages 271–279 (cf. pages 27, 55, 102, 180).
- [177] P RANJANOMENNAHARY et al. “Comparison of radiograph-based texture analysis and bone mineral density with three-dimensional microarchitecture of trabecular bone”. In : *Medical Physics* 38.1 (2011), pages 420–428 (cf. page 80).
- [178] Yousef REZAEI TABAR et Ilkay ULUSOY. “The effect of labeled/unlabeled prior information for masseter segmentation”. In : *Mathematical Problems in Engineering* 2013 (2013) (cf. page 128).
- [179] AF RIDEL, F DEMETER et J et al. LIEBENBERG. “Skeletal dimensions as predictors for the shape of the nose in a South African sample : a cone-beam computed tomography (CBCT) study”. In : *Forensic Sci Int* 289 (2018), pages 18–26 (cf. page 157).
- [180] Torsten ROHLFING et al. “Quo vadis, atlas-based segmentation ?” In : (2005), pages 435–486 (cf. pages 27, 55, 103).
- [181] Stefanie ROSENHAIN et al. “A preclinical micro-computed tomography database including 3D whole body organ segmentations”. In : *Scientific Data* 5 (2018), page 180294 (cf. page 80).
- [182] Christopher RYNN et Caroline M. WILKINSON. “Appraisal of traditional and recently proposed relationships between the hard and soft dimensions of the nose in profile”. In : 130 (2006), pages 364–373. ISSN : 0002-9483. DOI : 10.1002/ajpa.20337 (cf. page 157).
- [183] M SARITHA, K Paul JOSEPH et Abraham T MATHEW. “Classification of MRI brain images using combined wavelet entropy based spider web plots and probabilistic neural network”. In : *Pattern Recognition Letters* 34.16 (2013), pages 2151–2156 (cf. pages 28, 55, 103).
- [184] Stephen A SCHENDEL et al. “The long face syndrome : vertical maxillary excess”. In : *American journal of orthodontics* 70.4 (1976), pages 398–408 (cf. pages 72, 157).
- [185] S SCHLAGER. “Morpho - Calculations and visualisations related to Geometric Morphometrics”. In : (2014). URL : <http://sourceforge.net/projects/morpho-rpackage> (cf. page 194).
- [186] JJ SCIOTE et al. “Masseter function and skeletal malocclusion”. In : *Revue de stomatologie, de chirurgie maxillo-faciale et de chirurgie orale* 114.2 (2013), pages 79–85 (cf. page 77).
- [187] Heiko SEIM et al. “Automatic Segmentation of the Pelvic Bones from CT Data Based on a Statistical Shape Model.” In : *VCBM* 8 (2008), pages 93–100 (cf. pages 27, 55, 103).
- [188] Tanya SELLA-TUNIS et al. “Human mandibular shape is associated with masticatory muscle force”. In : 8 (2018). ISSN : 2045-2322. DOI : 10.1038/s41598-018-24293-3 (cf. page 72).
- [189] Neeraj SHARMA et Lalit M AGGARWAL. “Automated medical image segmentation techniques”. In : *Journal of medical physics/Association of Medical Physicists of India* 35.1 (2010), page 3 (cf. page 180).

-
- [190] Sarah SHRIMPSON et al. “A spatially-dense regression study of facial form and tissue depth : towards an interactive tool for craniofacial reconstruction”. In : *Forensic science international* 234 (2014), pages 103–110 (cf. page 157).
- [191] Wuyang SHUI et al. “A PCA-Based method for determining craniofacial relationship and sexual dimorphism of facial shapes”. In : *Computers in biology and medicine* 90 (2017), pages 33–49 (cf. page 157).
- [192] Konrad SIMON et Ronen BASRI. “Elasticity-based matching by minimising the symmetric difference of shapes”. In : 12 (2018), pages 412–423. ISSN : 1751-9632 (cf. pages 32, 60, 140).
- [193] Konrad SIMON et al. “A linear elastic force optimization model for shape matching”. In : *Journal of Mathematical Imaging and Vision* 51.2 (2015), pages 260–278 (cf. pages 15, 32, 42, 60, 140).
- [194] Porntip P SIRIWAT et Joseph R JARABAK. “Malocclusion and facial morphology is there a relationship? An epidemiologic study”. In : *The Angle Orthodontist* 55.2 (1985), pages 127–138 (cf. pages 21, 48).
- [195] Beni SOLOW. “The pattern of craniofacial associations : A morphological and methodological correlation and factor analysis study on young male adults”. In : *Acta Odontol Scand* 24 46 (1966), pages 123–135 (cf. pages 20, 48, 72).
- [197] Detlev STALLING, Malte WESTERHOFF, Hans-Christian HEGE et al. “Amira : A highly interactive system for visual data analysis”. In : *The visualization handbook* 38 (2005), pages 749–67 (cf. pages 31, 59, 74, 83, 129, 159).
- [198] Murphy SJ. STEPHAN CN. “Mouth width prediction in craniofacial identification : cadaver tests of four recent methods, including two techniques for edentulous skulls”. In : *J Forensic Odonto-Stomatol* 27 (2008), pages 2–7 (cf. page 157).
- [199] C. N. STEPHAN. “Anthropological facial ‘reconstruction’ – recognizing the fallacies, ‘unembracing’ the errors, and realizing method limits”. In : 43 (2003), pages 193–200. ISSN : 1355-0306. DOI : 10.1016/s1355-0306(03)71776-6 (cf. page 156).
- [200] C. N. STEPHAN et R. S. ARTHUR. “Assessing facial approximation accuracy : How do resemblance ratings of disparate faces compare to recognition tests?” In : 159 (2006), S159–S163. ISSN : 0379-0738. DOI : 10.1016/j.forsciint.2006.02.026 (cf. page 169).
- [201] Carl N. STEPHAN. “Facial Approximation : Globe Projection Guideline Falsified by Exophthalmometry Literature”. In : 47 (2002), 15457J. ISSN : 0022-1198. DOI : 10.1520/jfs15457j (cf. page 157).
- [202] Carl N. STEPHAN. “Beyond the Sphere of the English Facial Approximation Literature : Ramifications of German Papers on Western Method Concepts*”. In : 51 (2006), pages 736–739. ISSN : 0022-1198. DOI : 10.1111/j.1556-4029.2006.00175.x (cf. pages 156, 157).
- [203] Carl N STEPHAN. “The human masseter muscle and its biological correlates : a review of published data pertinent to face prediction”. In : *Forensic science international* 201.1-3 (2010), pages 153–159 (cf. pages 36, 64, 72, 157).
- [204] Carl N STEPHAN. “Facial approximation—from facial reconstruction synonym to face prediction paradigm”. In : *Journal of forensic sciences* 60.3 (2015), pages 566–571 (cf. pages 156, 157).
- [205] Carl N. STEPHAN et Jody CICOLINI. “The reproducibility of facial approximation accuracy results generated from photo-spread tests”. In : 201 (2010), pages 133–137. ISSN : 0379-0738. DOI : 10.1016/j.forsciint.2010.02.028 (cf. page 169).

- [206] Carl N. STEPHAN et Paavi L. DAVIDSON. “The Placement of the Human Eyeball and Canthi in Craniofacial Identification”. In : 53 (2008), pages 612–619. ISSN : 0022-1198. DOI : 10.1111/j.1556-4029.2008.00718.x (cf. page 157).
- [207] Carl N. STEPHAN et Matthew DEVINE. “The superficial temporal fat pad and its ramifications for temporalis muscle construction in facial approximation”. In : 191 (2009), pages 70–79. ISSN : 0379-0738. DOI : 10.1016/j.forsciint.2009.06.016 (cf. page 158).
- [208] Carl N. STEPHAN et Maciej HENNEBERG. “Building Faces from Dry Skulls : Are They Recognized Above Chance Rates?” In : 46 (2001), 14993J. ISSN : 0022-1198. DOI : 10.1520/jfs14993j (cf. pages 156, 169).
- [209] Carl N. STEPHAN et Maciej HENNEBERG. “Predicting Mouth Width from Inter-Canine Width—A 75% Rule”. In : 48 (2003), page 2002418. ISSN : 0022-1198. DOI : 10.1520/jfs2002418 (cf. page 157).
- [210] Carl N. STEPHAN, Anne J. R. HUANG et Paavi L. DAVIDSON. “Further Evidence on the Anatomical Placement of the Human Eyeball for Facial Approximation and Craniofacial Superimposition”. In : 54 (2009), pages 267–269. ISSN : 0022-1198. DOI : 10.1111/j.1556-4029.2008.00982.x (cf. page 157).
- [211] Carl N. STEPHAN et Ellie K. SIMPSON. “Facial soft tissue depths in craniofacial identification (part I) : an analytical review of the published adult data”. In : *Journal of Forensic Sciences* 53.6 (2008), pages 1257–1272 (cf. page 157).
- [212] Carl N. STEPHAN et al. “An overview of the latest developments in facial imaging”. In : *Forensic sciences research* 4.1 (2019), pages 10–28 (cf. page 156).
- [213] RAP STRAPASSON, LM HERRERA et RFH MELANI. “Forensic facial reconstruction : relationship between the alar cartilage and piriform aperture”. In : *J Forensic Sci* 62 (2017), pages 1460–1465 (cf. page 157).
- [214] STUDENT. “The Probable Error of a Mean”. In : 6 (1908), page 1. ISSN : 0006-3444. DOI : 10.2307/2331554 (cf. page 130).
- [215] Zhengyu SU et al. “Optimal mass transport for shape matching and comparison”. In : *IEEE transactions on pattern analysis and machine intelligence* 37.11 (2015), pages 2246–2259 (cf. page 141).
- [217] Ronald M. SUMMERS. “Road maps for advancement of radiologic computer-aided detection in the 21st century”. In : *Radiology* 229.1 (2003), pages 11–13 (cf. pages 27, 55, 102).
- [218] Alexander TACK et Stefan ZACHOW. “Accurate automated volumetry of cartilage of the knee using convolutional neural networks : data from the osteoarthritis initiative”. In : (2019), pages 40–43 (cf. page 103).
- [221] KT TAYLOR et BP GATLIFF. “Skull protection and preparation for reconstruction”. In : *Forensic Art and Illustration : Boca Raton USA : CRC Press LLC* (2001) (cf. page 156).
- [223] J-P THIRION. “Image matching as a diffusion process : an analogy with Maxwell’s demons”. In : *Medical image analysis* 2.3 (1998), pages 243–260 (cf. pages 27, 55, 103).
- [224] Paul M. THOMPSON et Arthur W. TOGA. “Detection, visualization and animation of abnormal anatomic structure with a deformable probabilistic brain atlas based on random vector field transformations”. In : *Medical image analysis* 1.4 (1997), pages 271–294 (cf. page 81).
- [225] Françoise TILOTTA et al. “Construction and analysis of a head CT-scan database for craniofacial reconstruction”. In : *Forensic science international* 191.1-3 (2009), 112–e1 (cf. pages 17, 45).

- [226] F TILOTTA-YASUKAWA et al. “Contribution à la reconstitution faciale en médecine légale : Étude préliminaire d’une méthode tridimensionnelle à partir de l’imagerie numérique”. In : *Morphologie* 90.289 (2006), page 106 (cf. pages 17, 45).
- [227] Kathrin TINGELHOFF et al. “Comparison between manual and semi-automatic segmentation of nasal cavity and paranasal sinuses from CT images”. In : (2007), pages 5505–5508 (cf. page 132).
- [228] Viviana TORO-IBACACHE, Victor ZAPATA MUÑOZ et Paul O’ HIGGINS. “The Predictability from Skull Morphology of Temporalis and Masseter Muscle Cross-Sectional Areas in Humans”. In : *The Anatomical Record* 298.7 (2015), pages 1261–1270 (cf. page 72).
- [229] PH TU et al. “Towards a statistical basis for facial deformation modes in reconstruction”. In : *Forensic Sci Int* 136 (2003), pages 168–169 (cf. page 156).
- [231] W. D. TURNER et al. “A novel method of automated skull registration for forensic facial approximation”. In : 154 (2005), pages 149–158. ISSN : 0379-0738. DOI : 10.1016/j.forsciint.2004.10.003 (cf. page 156).
- [232] Douglas H. UBELAKER et Gene O’DONNELL. “Computer-Assisted Facial Reproduction”. In : 37 (1992), 13223J. ISSN : 0022-1198. DOI : 10.1520/jfs13223j (cf. page 156).
- [233] Herbert ULLRICH et Carl N STEPHAN. “On Gerasimov’s plastic facial reconstruction technique : new insights to facilitate repeatability.” In : *Journal of forensic sciences* 56 (2 mar. 2011), pages 470–474. ISSN : 1556-4029. DOI : 10.1111/j.1556-4029.2010.01672.x (cf. pages 156, 157).
- [234] H UTSUNO, T KAGEYAMA et K et al. UCHIDA. “Establishment of a prediction method for the mid-facial region of unknown human Mongoloid skeletal remains”. In : *Forensic Sci Int* 288 (2018), pages 287–303 (cf. page 157).
- [235] Marc VAILLANT et Joan GLAUNÈS. “Surface matching via currents”. In : (2005), pages 1–5 (cf. page 140).
- [236] Tim VALENTINE et Josh P DAVIS. “Forensic facial identification : a practical guide to best practice”. In : *Forensic Facial Identification : Theory and Practice of Identification from Eyewitnesses, Composites and CCTV*. Chichester : John Wiley & Sons (2015), pages 323–347 (cf. page 156).
- [238] PH VAN SPRONSEN et al. “Comparison of jaw-muscle bite-force cross-sections obtained by means of magnetic resonance imaging and high-resolution CT scanning”. In : *Journal of Dental Research* 68.12 (1989), pages 1765–1770 (cf. page 78).
- [239] PH VAN SPRONSEN et al. “Relationships between jaw muscle cross-sections and craniofacial morphology in normal adults, studied with magnetic resonance imaging”. In : *Eur J Orthod* 13.5 (1991), pages 351–61 (cf. page 78).
- [240] Dirk VANDERMEULEN et al. “Computerized craniofacial reconstruction using CT-derived implicit surface representations”. In : *Forensic science international* 159 (2006), S164–S174 (cf. pages 156, 159).
- [242] P. VANEZIS et al. “Application of 3-D computer graphics for facial reconstruction and comparison with sculpting techniques”. In : 42 (1989), pages 69–84. ISSN : 0379-0738. DOI : 10.1016/0379-0738(89)90200-4 (cf. page 156).
- [243] P. VANEZIS et al. “Facial reconstruction using 3-D computer graphics”. In : 108 (2000), pages 81–95. ISSN : 0379-0738. DOI : 10.1016/s0379-0738(99)00026-2 (cf. page 156).
- [244] Remco C VELTKAMP. “Shape matching : Similarity measures and algorithms”. In : (2001), pages 188–197 (cf. pages 15, 32, 42, 60, 140).

- [245] Sen WANG et al. “3D surface matching and recognition using conformal geometry”. In : 2 (2006), pages 2453–2460 (cf. page 141).
- [246] WA WEIJS et B HILLEN. “Relationships between masticatory muscle cross-section and skull shape”. In : *Journal of Dental Research* 63.9 (1984), pages 1154–1157 (cf. page 78).
- [247] WA WEIJS et B HILLEN. “Physiological cross-section of the human jaw muscles”. In : *Cells Tissues Organs* 121.1 (1985), pages 31–35 (cf. page 77).
- [248] Rüdiger WESTERMANN, Leif KOBBELT et Thomas ERTL. “Real-time exploration of regular volume data by adaptive reconstruction of isosurfaces”. In : *The Visual Computer* 15.2 (1999), pages 100–111 (cf. page 83).
- [249] Anders WESTERMARK, Stefan ZACHOW et Barry L EPPLEY. “Three-dimensional osteotomy planning in maxillofacial surgery including soft tissue prediction”. In : *Journal of Craniofacial Surgery* 16.1 (2005), pages 100–104 (cf. page 78).
- [250] Jane WILHELMS et Allen VAN GELDER. “Octrees for faster isosurface generation”. In : *ACM Transactions on Graphics (TOG)* 11.3 (1992), pages 201–227 (cf. page 83).
- [252] Caroline WILKINSON. “Computerized forensic facial reconstruction”. In : *Forensic Science, Medicine, and Pathology* 1.3 (2005), pages 173–177 (cf. pages 12, 13, 40, 156).
- [253] Caroline WILKINSON. “Facial reconstruction—anatomical art or artistic anatomy?” In : *Journal of anatomy* 216.2 (2010), pages 235–250 (cf. pages 35, 63).
- [254] Caroline M. WILKINSON et Sophie A. MAUTNER. “Measurement of Eyeball Protrusion and Its Application in Facial Reconstruction”. In : 48 (2003), page 2002053. ISSN : 0022-1198. DOI : 10.1520/jfs2002053 (cf. page 157).
- [256] CM WILKINSON, M MOTWANI et E CHIANG. “The relationship between the soft tissues and the skeletal detail of the mouth”. In : *J Forensic Sci* 48 (2003), pages 728–732 (cf. page 157).
- [257] C WILKINSON et al. “A blind accuracy assessment of computer-modeled forensic facial reconstruction using computed tomography data from live subjects”. In : *Forensic Sci Med Pathol* (2006), 2 :179–187 (cf. page 156).
- [258] Daniel J WITHEY et Zoltan J KOLES. “Medical image segmentation : Methods and software”. In : (2007), pages 140–143 (cf. pages 27, 55, 102, 180).
- [259] Jinzhong YANG et al. “Atlas ranking and selection for automatic segmentation of the esophagus from CT scans”. In : *Physics in Medicine & Biology* 62.23 (2017), page 9140 (cf. pages 27, 55, 103).
- [260] Chung-Chih YU, Philip Kuo-Ting CHEN et Yu-Ray CHEN. “Botulinum toxin A for lower facial contouring : a prospective study”. In : *Aesthetic plastic surgery* 31.5 (2007), pages 445–451 (cf. pages 21, 49, 72, 157, 158).
- [261] Katrina ZEPA et al. “Three-dimensional evaluation of musculoskeletal in Class II and Class III patients.” In : *Stomatologija* 11 (1 2009), pages 15–20. ISSN : 1392-8589 (cf. page 77).
- [262] Jing ZHANG et al. “Fast segmentation of bone in CT images using 3D adaptive thresholding”. In : *Computers in biology and medicine* 40.2 (2010), pages 231–236 (cf. pages 27, 55, 102, 180).
- [263] Hong-Kai ZHAO, Stanley OSHER et Ronald FEDKIW. “Fast surface reconstruction using the level set method”. In : *IEEE Workshop on Variational and Level Set Methods in Computer Vision* 59 (2001), pages 194–201 (cf. page 144).

Phd Thesis

- [20] Mirza F. BEG. “Variational and computational methods for flows of diffeomorphisms in image matching and growth in computational anatomy”. Johns Hopkins University, 2004 (cf. page 140).
- [24] Maxime BERAR. “Modèles Statistiques de la forme d’organes du corps humain. Application à la reconstruction faciale”. Thèse de doctorat. INPG, 2007 (cf. page 80).
- [80] Joan GLAUNÈS. “Transport par difféomorphismes de points, de mesures et de courants pour la comparaison de formes et l’anatomie numérique”. Université Paris 13, 2005 (cf. page 140).
- [158] Chiara NARDONI. “Mesh deformation strategies in shape optimization. Application to forensic facial reconstruction”. Paris 6, 2017 (cf. pages 12–15, 25, 40–43, 53, 90, 137, 165).

Misc

- [71] Raymond J. EVENHOUSE, Mary RASMUSSEN et Lewis L. SADLER. *Computer-aided forensic facial reconstruction*. 1991. DOI : 10.1117/12.48078 (cf. page 156).
- [98] John Darrell Van HORN et Arthur W. TOGA. *Brain Atlases : Their Development and Role in Functional Inference*. 2016. DOI : 10.1007/978-1-4939-5611-1_9 (cf. page 80).
- [111] PRAG JOHN et Richard NEAVE. *Making Faces Using Forensic and Archaeological Evidence*. 1997 (cf. pages 12, 34, 35, 40, 62, 156).
- [196] Thomas S SPISZ et IN BANKMAN. *Handbook of medical imaging*. 2000 (cf. pages 27, 55, 102, 180).
- [219] Karen TAYLOR. *Two-Dimensional Facial Reconstruction from the Skull*. 2000. DOI : 10.1201/9781420036954.ch12 (cf. page 156).
- [241] Dirk VANDERMEULEN et al. *Automated facial reconstruction*. 2012. DOI : 10.1017/cbo9781139049566.017 (cf. page 156).
- [251] Caroline WILKINSON. *Forensic Facial Reconstruction*. 2004. DOI : 10.1017/cbo9781107340961 (cf. page 156).